Singlet-Triplet qubits and spin-orbit interaction in 2-dimensional Ge hole gases

by

Daniel Jirovec

October, 2021

A Thesis
Presented to the Faculty of the Graduate School of the
Institute of Science and Technology Austria, Klosterneuburg, Austria
in Partial Fulfillment of the Requirements for the Degree
Doctor of Philosophy

IST AUSTRIA
Institute of Science and Technology

The dissertation of Daniel Jirovec, titled *Singlet-Triplet qubits and spin-orbit interaction in 2-dimensional Ge hole gases*, is approved by:

Supervisor: Georgios Katsaros, IST Austria, Klosterneuburg, Austria

Signature: ____________________________

Committee Member: Maksym Serbyn, IST Austria, Klosterneuburg, Austria

Signature: ____________________________

Committee Member: Menno Veldhorst, University of Technology Delft, Delft, The Netherlands

Signature: ____________________________

Exam Chair: Christoph Lampert, IST Austria, Klosterneuburg, Austria

Signature: ____________________________

IST Austria Thesis, ISSN: 2663-337X

I hereby declare that this thesis is my own work and that it does not contain other people's work without this being so stated; this thesis does not contain my previous work without this being stated, and the bibliography contains all the literature that I used in writing the dissertation.

I declare that this is a true copy of my thesis, including any final revisions, as approved by my thesis committee, and that this thesis has not been submitted for a higher degree to any other university or institution.

I certify that any republication of materials presented in this thesis has been approved by the relevant publishers and co-authors.

Signature: ______________________________

Daniel Jirovec
October, 2021

Abstract

Quantum information and computation has become a vast field paved with opportunities for researchers and investors. As large multinational companies and international funds are heavily investing in quantum technologies it is still a question which platform is best suited for the task of realizing a scalable quantum processor.

In this work we investigate hole spins in Ge quantum wells. These hold great promise as they possess several favorable properties: a small effective mass, a strong spin-orbit coupling, long relaxation time and an inherent immunity to hyperfine noise. All these characteristics helped Ge hole spin qubits to evolve from a single qubit to a fully entangled four qubit processor in only 3 years. Here, we investigated a qubit approach leveraging the large out-of-plane g-factors of heavy hole states in Ge quantum dots. We found this qubit to be reproducibly operable at extremely low magnetic field and at large speeds while maintaining coherence. This was possible because large differences of g-factors in adjacent dots can be achieved in the out-of-plane direction. In the in-plane direction the small g-factors, on the other hand, can be altered very effectively by the confinement potentials. Here, we found that this can even lead to a sign change of the g-factors. The resulting g-factor difference alters the dynamics of the system drastically and produces effects typically attributed to a spin-orbit induced spin-flip term.

The investigations carried out in this thesis give further insights into the possibilities of holes in Ge and reveal new physical properties that need to be considered when designing future spin qubit experiments.

Acknowledgments

In 2017 my PhD journey started and I interacted with so many kind, smart and helpful people that I hope they will forgive me if I do not manage to include all of them by name.

First and foremost a great thank you to the Nanofabrication facility staff around Salvo, Juan, Lubuna and Arkadiusz who have helped setting up the cleanroom and getting it running. A special thanks to Philip and Ivan whom I think I bothered more than anyone else and who have been invaluable in developing the oxide and the etching recipe.

Next, a big thank you to the electronic workshop and especially Thomas and Peter who have single handedly wired all of the fridges and probes and who always fulfilled all our wished when it came to equipment in the lab. From repairing DAC cards to making gyrators and assembling PCBs they always did an amazing job.

A big thank you to all the external collaborators. The "Como" people, Danny Chrastina, Andrea Ballabio, Giovanni Isella, Jacopo Frigerio, Giulio Tavani and Stefano Calcaterra who grew our heterostructures, characterized their mobilities and always gave us great support. The XRD measurements and mobility characterizations of Chapter 5 were performed by Danny, Andrea, Giulio and Stefano.

The "Konstanz" people with Philipp M. Mutter and Guido Burkard who very patiently explained us the theory we failed to understand. Philipp in particular wrote the theory part of both our papers and they are featured in Chapter 2, 5 and especially in Chapter 6. The "Barcelona" people with Jordi Arbio and Marc Botifoll who provided us with amazing TEM images and strain analysis. The TEM images in Chapter 4 and 5 were done by them.

I still owe a thank you also to my supervisors during my Master's thesis: Hendrick and Lars who taught me the tough reality of experimental physics and how to deal with noise.

I am very thankful also to Amir Yacoby for a very fruitful discussion about singlet-triplet qubits during his zoom visit in December 2020.

Thank you to Menno and Maksym for co-supervising and reading my thesis!

A great thank you to the Katsaros group and here let me try to be ordered: Jason (my first, very quiet yet fun office mate), Praveen (my youngest office mate), Alberto (the forgotten office mate), Konrad (ye boy), Josh (whadup), Marin (lunch is at 12:30), Oliver (freaking qual and etching and track course), Luka (stud'nt) and Kushagra (our flowerboy), Lada (for her positive attitude), Hannes (for his stoic appearance), Josip (see below), Marco (little parks), Marian (for being the best new Hannes), Chaitrali (subscribe to card, unsubscribe to card), Robin (our spy), Jaime (the espanish dude), Stavroula (never matching outfit), Max (for his amazing tables), Yona (a new hope), Frederico (guess Portugal still lost), Matthias (the german dude), Andrea (Team hole gas), Alessandro (baby, I disagree).

Finally I would like to thank Josip for his enormous efforts in building up the lab, his immense patience in understanding and explaining the Zurich instrument devices and for basically providing PCBs and reflectometry to the whole lab: you are the real MVP.

A big thank you to Giorgos who believed in me when I was not anymore. He always teased us by saying: "it is going to work!" and of course he was right. It was great fun working with him and he taught me what real leaders are all about, not leading, but inspiring! The famous short term pessimist and long term optimist...

Last but not least a big thank you to Cerag for supporting me and not getting tired of me during our quarantine times when I was constantly measuring and forgetting about dinner, the dog, or her...

About the Author

I studied general physics at the university of Pisa where I completed my bachelor's degree in 2014. I then moved to Aachen to RWTH for my master's degree with a focus on Nanoelectronics. Here I discovered my passion for spin qubits working on my master thesis in the group of Hendrik Bluhm. I completed my master in 2016 and started in early 2017 at IST Austria first as an intern and then as a PhD student.

List of Publications

1. 30 GHz-voltage controlled oscillator operating at 4 K
   Hollmann A, Jirovec D, Kucharski M, Kissinger D, Fischer G, Schreiber LR.
   Review of Scientific Instruments **89**(11), 114701 (2018)

2. Asessing the potential of Ge/SiGe quantum dots for singlet-triplet qubits
   A. Hofmann, D. Jirovec, M. borovkov, I. Prieto, A. Ballabio, J. Frigerio, D. Chrastina, G. Isella and G. Katsaros
   Preprint at https://arxiv.org/pdf/1910.05841.pdf

3. Enhancement of Proximity Induced Superconductivity in a Planar Ge Hole Gas
   K. Aggarwal, A. Hofmann, D. Jirovec, I. Prieto, A. Sammak, M. Botifoll, S. Marti-Sanchez, M. Veldhorst, G. Scapucci, J. Danon and G. Katsaros
   Phys. Rev. Research **3**, L022005 (2021)

4. A singlet-triplet hole spin qubit in planar Ge
   D. Jirovec, A. Hofmann, A. Ballabio, P. M. Mutter, G. Tavani, M. Botifoll, A. Crippa, J. Kukučka, O. Sagi, F. Martins, J. Saez-Mollejo, I. Prieto, M. Borovkov, J. Arbiol, D. Chrastina, G. Isella and G. Katsaros
   Nat. Materials **20**, 1106-1112 (2021)

5. Cross-architecture Tuning of Silicon and SiGe-based Quantum Devices Using Machine Learning
   B. Severin, D. T. Lennon, L. C. Camenzind, F. Vigneau, F. Fedele, D. Jirovec, A. Ballabio, D. Chrastina, G. Isella, M. de Kruijf, M. J. Carballido, S. Svab, A. V. Kuhlmann, F. R. Braakman, S. Geyer, F. N. M. Froning, H. Moon, M. A. Osborne, D. Sejdinovic, G. Katsaros, D. M. Zumbühl, G. A. D. Briggs and N. Ares
   Preprint at https://arxiv.org/pdf/2107.12975.pdf

Table of Contents

Abstract vii

Acknowledgments viii

About the Author x

List of Publications xi

List of Tables xiv

List of Figures xv

1 Introduction xviii
- 1.1 Thesis outline . . . 3

2 Theoretical concepts 5
- 2.1 Semiconductors . . . 5
- 2.2 Qubits . . . 17

3 Fabrication and Setup 26
- 3.1 Setup . . . 27
- 3.2 Fabrication . . . 29

4 Ge hole gases: from Hall bars to reflectometry charge sensing 36
- 4.1 The 6770 series: 2017 . . . 37
- 4.2 The 10440 series: 2017-2018 . . . 40
- 4.3 The 10660 series: 2019-today . . . 40
- 4.4 The 10720 series: 2020- today . . . 56

5 A hole singlet triplet qubit in Ge 57
- 5.1 Overview . . . 57
- 5.2 Device . . . 58

5.3 Pauli spin blockade and spin funnel 59
5.4 g^--driven oscillations 61
5.5 Exchange-driven rotations and noise 62
5.6 Echo 66
5.7 Conclusion 66
5.8 Methods 68
5.9 Supplementary information 69

6 Dynamics of hole singlet triplet qubits with large g-factor differences 85
6.1 Introduction 85
6.2 Funnel as a function of magnetic field angle 86
6.3 g-factor anisotropy extraction through singlet-triplet oscillations 88
6.4 t_{SO} extraction with single Landau-Zener passages 91
6.5 Funnel Simulations and l_{SO} 93
6.6 Conclusion 93
6.7 Supplementary Information 95

7 Future Directions 110
7.1 Gate fidelity 111
7.2 Auto-tuning 113

8 Conclusion 114

Bibliography 116

A Appendix 131
A.1 Simulations and scripts 131

List of Tables

3.1 Fabrication Recipe 30

List of Figures

2.1 Band gap of metals, semiconductors and insulators 6
2.2 Bandstructure of GaAs, Si and Ge 7
2.3 Band alignement of heterojunctions 8
2.4 Single Quantum Dot 11
2.5 Double Quantum Dots 13
2.6 Pauli spin blockade principle 15
2.7 Bloch sphere 18
2.8 Loss DiVincenzo qubit schematic 21
2.9 Singlet-Triplet qubit operation 25

3.1 Experimental Setup 28
3.2 Fabrication Schematics 32
3.3 Optical and SEM image 33
3.4 Test at 4 K 34
3.5 Sample for Cooldown 35

4.1 SEM and data of the first 6777 sample 38
4.2 Shubnikov-de Haas oscillations and quantum Hall effect in the 6777 wafer 39
4.3 TEM of the 1066x series 41
4.4 Heterostructure layer stack and simulations 42
4.5 Mobilites of 1066x series 43
4.6 10662 sample layout and single quantum dots. 44
4.7 Double quantum dots as a function of center barrier voltage 45
4.8 Signature of PSB 45
4.9 Kondo peak 47
4.10 Kondo versus temperature 48
4.11 Kondo versus magnetic field 48
4.12 Charge Sensing 49
4.13 Heliox Setup 52

4.14 Gate Reflectometry 53
4.15 Ohmic Reflectometry 54
4.16 Coulomb oscillations in reflectometry 55

5.1 Heterostructure and gate layout 58
5.2 Pauli spin blockade and dispersion relation 60
5.3 g^--driven rotations 63
5.4 Exchange-rotations at $B = 1\,\text{mT}$ and $V_{\text{CB}} = 910\,\text{mV}$ 64
5.5 Spin Echo at B = 1 mT 67
5.6 Simulations performed in Qutip 69
5.7 TEM and XRD of the 10721 heterostructure 71
5.8 Bias triangles and lever arm extraction 72
5.9 Stability diagram recorded from the current through the charge sensor and differentiated . 73
5.10 Exchange oscillations for $V_{CB} = 950\,\text{mV}$ at $1\,\text{mT}$ 73
5.11 g^- and t_C as a function of V_{LB} and V_{RB}. 74
5.12 Spin-funnel acquired at the transition $(3, 2n + 1) \leftrightarrow (2, 2n + 2)$ 74
5.13 Data from second and third device 75
5.14 Frequency, T_2^* and Q-factor 76
5.15 $S - T_-$ avoided crossing 77
5.16 Echo oscillations as a function of δt 79
5.17 Pulsing schematics 80
5.18 T_1 in the measurement point at different magnetic field 81
5.19 X-rotations 82
5.20 Z-rotations 1 83
5.21 Z-rotations 2 83
5.22 Z-rotations 3 84

6.1 Funnels vs magnetic field direction 87
6.2 Singlet-triplet oscillations vs magnetic field direction 89
6.3 t_{SO} extraction through LZ passages 92
6.4 Funnel Simulations 94
6.5 Stability Diagram 95
6.6 Exchange oscillations 96
6.7 In-plane $S - T$ oscillations 97
6.8 $S - T$ oscillations vs angle of magnetic field 98
6.9 Funnel for all magnetic field directions 100
6.10 Level velocity and triplet initialization 101

6.11 Relaxation of T_0 state 101
6.12 Spectral leakage due to improper initializaton 103

7.1 The GRAPE principle 112

1 Introduction

In 1981, during a memorable keynote speech held by Richard Feynman [1], he posed a visionary question: "can we simulate quantum physics with quantum physics?". In other words: is it possible to control quantum mechanical objects to a degree in which it becomes possible to reproduce naturally occurring quantum phenomena. The idea of the quantum computer was born. Feynman's keynote speech was published in 1982, the same year that saw the birth of companies like Adobe, Electronics Arts (EA) and LucasArts. It was a time when IBM just joined the race to build PCs and the first "portable" devices were brought on the market. Feynman witnessed the evolution of the classical computer from a room filling and costly device developed during World War II to the personal computer that could be purchased by anyone. This was possible because of the invention of the transistor, a piece of Ge and some Au contacts, by Bratton, Bardeen and Shockley [2]. However, Si replaced Ge rather quickly because of its much more stable naturally forming oxide layer. But it was with the invention of the scalable integrated circuit in 1957 by Fairchild Semiconductor that the true potential of calculators was unleashed [3]. One of the founders of Fairchild semiconductors was Gordon Moore. In 1965 he made a prediction that the number of transistors on a chip of a computer would double every 18 months [4]. Moore's law would not only hold for the next 6 decades, it would be taken as a goal for companies like Intel to fulfill it. It is without a doubt that Moore's law is the reason why the scientific progress of the last few decades grew exponentially. With the advent of ever more complex machines, more calculating power, more automation it is now possible to shrink down the transistor to a few atoms. However, Moore's law will soon come to an end as quantum effects like tunneling become evident and ruin device performance. While there is still room for improvement of calculators beyond simple miniaturization, as shown impressively by Apple with their ARM based chips [5], the need for alternative computing methods also starts to grow. This is also because there exist a class of complex problems which can not be efficiently solved on a classical machine. A quantum computer as envisioned by Feynman would violate the Thuring theorem [6, 7] and Shor [8] demonstrated in 1994 that, by leveraging quantum mechanical properties, it is possible to efficiently find the prime factors of a number. The computational complexity of finding the prime factors of a large number are at the basis of many cryptographic schemes which are put under threat by potential quantum computers.

Today we are in the noisy intermediate scale quantum (NISQ) technology era, where small prototype quantum processors can solve rudimentary quantum algorithms [9, 10]. These prototypes are assembled from a handful of basic building blocks called qubits. A qubit is essentially the quantum mechanical analog of a bit. However, its quantum mechanical nature enables computational steps impossible on a classical machine. Exclusively quantum mechanical properties such as entanglement and superposition are the ground stone for the ever growing field of quantum information [11]. Several material systems have been proposed, and many also demonstrated, for qubit implementation. The most promising platforms include ion traps [12], photons [13], supercondcting [10] and semiconducting qubits [14, 15]. All qubit platforms, even the more exotic Majorana qubits [16], have seen major investments from international Tech giants such as Microsoft, IBM, Intel, Google and many others. The economic interest in a reliable quantum computing technology is pushing the field to new heights and in 2019 quantum advantage was demonstrated in a 53 superconducting qubit processor [17]. However, the fragile nature of quantum mechanics makes device design and manufacturing complicated. Each mentioned platform comes with advantages, but also disadvantages that need to be compensated for. The main issue, for all platforms, is reproducibility and scalability. It is clear that, in order to achieve a scalable quantum computer, an invention like the integrated circuit must arise.

It this work we will discuss spin-qubits in more detail. These were proposed by Loss and Divincenzo [18], Kane [19] and Levy [20] in the late 1990s and early 2000s. Spin qubits typically have long relaxation times giving them a major edge over supercondcuting qubits. Moreover, the size of a single qubit is on the order of a few 100s of nm compared to the several μms of superconducting circuits. The first successful implementations were demonstrated in 2005 in the Yacoby group [21] for the Levy proposal and in 2006 in the Vandersypen group [22] for the Loss-DiVincenzo proposal in GaAs. However, the nuclear spins present in the host material made the spin qubit very short lived with dephasing times of 10 ns. Later, this was partially addressed by dynamic nuclear polarization (DNP) [23], a technique that allows to stabilize the nuclear spin bath. I personally find this technique incredible as it shows the level of understanding and control that we already gained on the dynamics of the quantum world. However, DNP is only a partial solution and helped GaAs to remain an interesting platform for proof of concept. Si, as a group IV element, is almost nuclear spin free and can be isotopically purified to yield very "quiet" qubit materials. This lead to the demonstration of long coherence times and high fidelity single qubit gates [24–26]. The fidelity of a quantum gate describes how many errors per operation are made. A high fidelity corresponds to a low error rate. As a quantum computer should work without errors, scientists have developed quantum error correction protocols which encode a logical qubit in several physical qubits [27, 28]. The higher the fidelity, the lower the amount of physical qubits necessary to obtain an error corrected logical qubit. As an example, in the surface code architecture a single qubit gate fidelity of 99.9% would require 3600 physical qubits for a single logical qubit.

While Si is an almost ideal spin qubit environment, there are other aspects of the material system that make upscaling challenging. For example, the large effective mass for electrons in Si forces small device sizes bringing nano-fabrication techniques to their limit [15]. This leads to a high device variability and more difficulties in controlling the tunnel coupling between adjacent spins and lowers two-qubit gate fidelity. In fact, first two-qubit devices in Si formed at least one of the quantum dots in an unexpected position and featured fidelities below the threshold required for fault tolerant quantum computation [29,30]. Switching to holes as the main charge carriers in semiconductors offers several advantages over electrons. The larger spin-orbit interaction allows all electrical manipulation of spin qubits [31]. Moreover, due to the p-type wave function, the contact hyperfine interaction is suppressed [32]. In GaAs, progress for hole devices is hampered by the larger effective mass than for electrons [33]. In Si all electrical control of hole devices was demonstrated in a CMOS compatible foundry process [34]. Holes in Ge, on the other hand, have seen an unprecedented evolution from single spin qubits in 2018 [35] to a 4-qubit processor in early 2021 [36]. Arguably, holes in Ge are so successful because they combine the best of both GaAs and Si: a small effective mass [37] eases fabrication constraints and makes the devices more reproducible but the material has only a small amount of nuclear spins making it a more quiet qubit environment [38]. At the time of writing, Ge is the material that holds the highest two-qubit gate fidelity for spin-qubits [39], the fastest single qubit manipulation time [40] and the most entangled qubits in one single device [36]. Ge also makes contact to most metals and can even be proximitized with superconductors making it interesting for the exploration of semiconductor-superconductor hybrid devices [41,42]. It is hard to find a material system that is better suited for hosting spin-qubits. Time will tell whether Ge will take over the semiconductor world again. We, therefore, opted for Ge as the material for our qubit experiments and explored the properties of coupled hole spins.

1.1 Thesis outline

This thesis is centered around Ge hole gases and the development of a singlet-triplet qubit. In Chapter 2 I will give an overview of the theoretical concepts used throughout the thesis. I will introduce semiconductors and their properties like mobility and effective mass, give a quick resume on quantum dots and qubits and finish by explaining the Loss-DiVincenzo proposal as opposed to the singlet-triplet qubit. Chapter 3 introduces the experimental setup and the fabrication techniques. In particular, I will give a step by step instruction of the fabrication and testing procedure leading to the main experiments. In Chapter 4 I will discuss the development of hole gases in our group and what we learned from each heterostructure: how to make quantum dots, how to measure g-factors and how to perform charge sensing. Chapter 5 represents the culmination of all the struggles as we managed to develop a singlet-triplet qubit in Ge, the first of its kind for holes. Here, we explored the many favorable properties of heavy hole states for qubits which lead to fast manipulation at low out of plane fields with coherence times exceeding 150 µs. Despite the singlet-triplet qubit, I believe that Chapter 6 is even more interesting as we observed the behavior of the qubit in other magnetic field directions with rather surprising outcomes. In fact, we found that the shape of the quantum dots can alter the effective g-factors so significantly that it can even change sign. Chapter 7 concludes this work with an overview and a reflection on the results of this work. Furthermore, future research directions in our group are discussed such as gate optimization and automated tuning of quantum dots.

2 Theoretical concepts

In this chapter I will cover the basic concepts of semiconductors, band structures and mobility, single and double quantum dots as well as give a brief introduction to qubits. After introducing the DiVincenzo criteria I will present two spin qubit proposals: the single spin qubit and the singlet-triplet qubit.

2.1 Semiconductors

Materials can usually be classified in three categories for transport: metals, semiconductors and insulators (see Fig. 2.1) [43]. Metals conduct electric charge well at room temperature and even better at low temperatures. Insulators do not exhibit any conductivity at room temperature whereas semiconductors show a conductivity that depends on temperature. The electronic states (or bands) in a metal are filled up to the Fermi energy at zero temperature (E_F). The occupation number of electrons in the conduction band as well as the empty states in the valence band of a metal at finite temperature are determined by the Fermi distribution function:

$$f(E,T) = \frac{1}{1 + \exp\left(\frac{E - E_F}{k_B T}\right)} \tag{2.1}$$

where k_B is the Boltzmann constant, T the temperature and E is the energy of the state.

The Fermi energy is easily confused with the "Fermi level" or "electro-chemical potential" describing the thermodynamic work necessary to add an electron to a solid-state body as it is usually also denoted as E_F. In the following we will denote it as μ_e. The empty bands above μ_e, in the conduction band, allow electronic transport. Also the empty states below μ_e, in the valence band, contribute to the conductivity via hole transport. In insulators the valence band is completely occupied by electrons and, thus, no charge reconfiguration by means of an electric field is possible. As the gap to the conduction band is usually $E_g > 4\,\text{eV}$ no thermal excitation can push electrons to the conduction band and, therefore, no transport occurs. Semiconductors typically have $0.4\,\text{eV} < E_g < 4\,\text{eV}$ and thermal excitations can push electrons into the conduction band allowing transport to happen. Semiconductors are incredibly versatile and find various applications due to their unique properties. These include the already mentioned

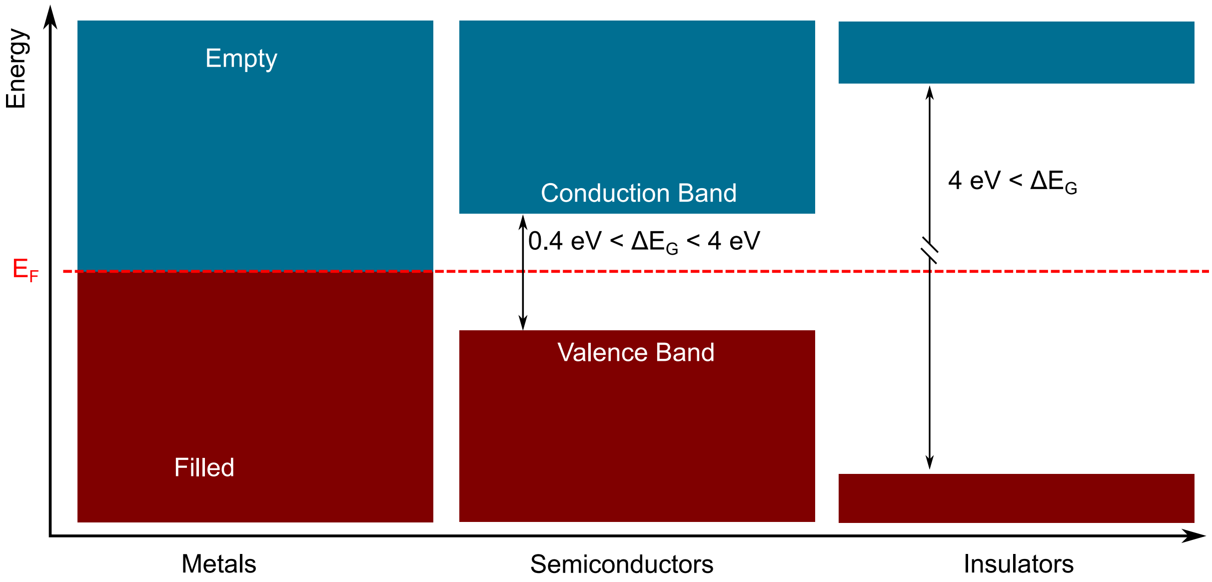

Figure 2.1: Band gap of metals, semiconductors and insulators. In metals all bands up until the Fermi level E_F are filled with electrons (at zero temperature). Charges can easily occupy states in the empty conduction band and participate in transport. For semiconductors there is typically a band gap ΔE_G of 0.4 to $4\,\mathrm{eV}$. Hence, electrons in the valence band require some energy to be transferred to the conduction band. Thermal excitations, for example, can provide such an energy. Insulators, on the other hand, typically display band gaps of $> 4\,\mathrm{eV}$ and thermal excitations are not sufficient to induce an appreciable conductivity.

conductivity dependent on temperature. Moreover, semiconductors can be doped with foreign atoms to induce excess electrons or holes and, thereby, enhance the charge carrier density. Furthermore, the field effect can be harvested where the charge carrier concentration can be changed by means of an externally applied electric field. There are a variety of semiconductors available and, depending on the needs, they offer advantages over the others. Elementary semiconductors like Ge and, especially, Si find applications in integrated circuits. Compound semiconductors, like SiC (group IV-IV), GaAs (group III-V) and ZnS (group II-VI) can be interesting for optoelectronis and high speed electronics [44]. Alloys of the above mentioned semiconductors can further be tailored to the specific needs of the experimentalist.

2.1.1 Band structure

The bandstructure of Si, Ge and GaAs is depicted in Fig. 2.2 [45–47]. Notice that Si and Ge have an indirect bandgap, that is the maximum of the valence band at the Γ point is not aligned with the minimum of the conduction band in k-space. GaAs, on the other hand, has a direct bandgap which is favourable for optoelectronics as photons can excite an electron from the valence band directly into the conduction band without any additional momentum transfer. The band structure reveals an important property of the material. In fact, one can derive the effective mass m^* of a charge carrier in the material through:

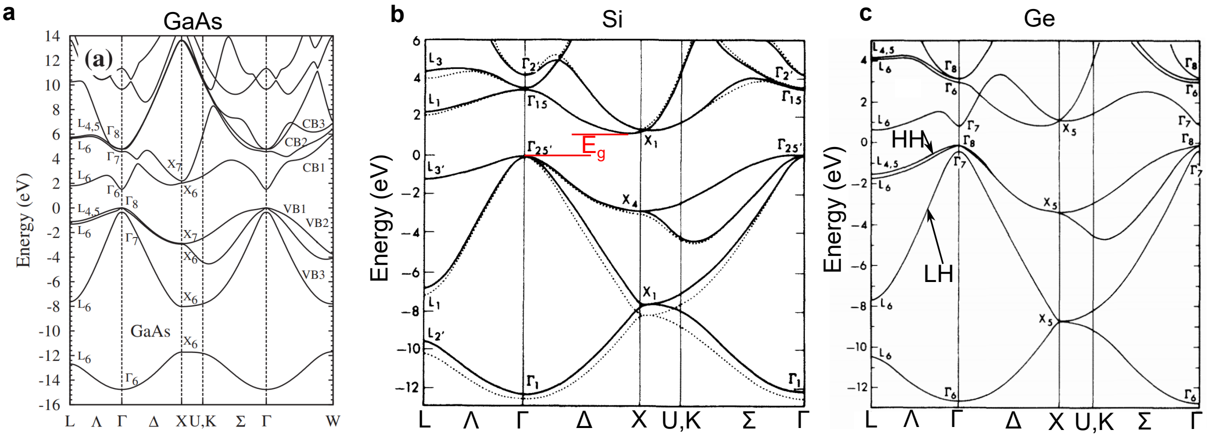

Figure 2.2: Bandstructure of GaAs, Si and Ge. a) Band structure of GaAs [45]. The band gap is direct as the maximum of the valence band is aligned with the minimum of the conduction band at the Γ point in k-space. b) Bandstructure of Si [46]. The band gap is indirect as the minimum of the conduction band is not aligned with the maximum of the valence band. c) Similarly the bandstructure of Ge [47]) displays an indirect bandgap. The arrows indicate the heavy hole (HH) and light hole (LH) band which will be discussed further below.

$$m^* = \left(\frac{1}{\hbar^2} \frac{d^2E}{dk^2} \right)^{-1}. \tag{2.2}$$

The effective mass is dependent on the inverse of the curvature of the band and is a consequence of the periodic potential of the crystal lattice. For many practical applications it is sufficient to consider the region close to the conduction band minimum or valence band maximum. Here, generally the parabolic approximation is valid and the kinetic energy of a charge can be written as

$$E = \frac{\hbar^2 k^2}{2m^*}. \tag{2.3}$$

Therefore, one obtains a constant effective mass which is generally valid around the conduction band minimum or valence band maximum.

2.1.2 Heterostructures

Semiconductors that possess the same lattice structure can be combined epitaxially to yield more complex and versatile devices [48]. These layered structures are typically grown by molecular beam epitaxy (MBE) or chemical vapor deposition (CVD). Ideally, two different semiconductors with the same lattice constant but different band gaps are combined. However, only few such semiconductor combinations exist, an example being AlAs and GaAs with lattice constants differing by less than 1%. When semiconductors with differing lattice constants are brought together this causes strain and defects to appear depending on the mismatch. As can be seen by the band alignement in Fig. 2.3 charge carriers are accumulated close to the interface between the semiconductors. Therefore, a defect-free interface is of

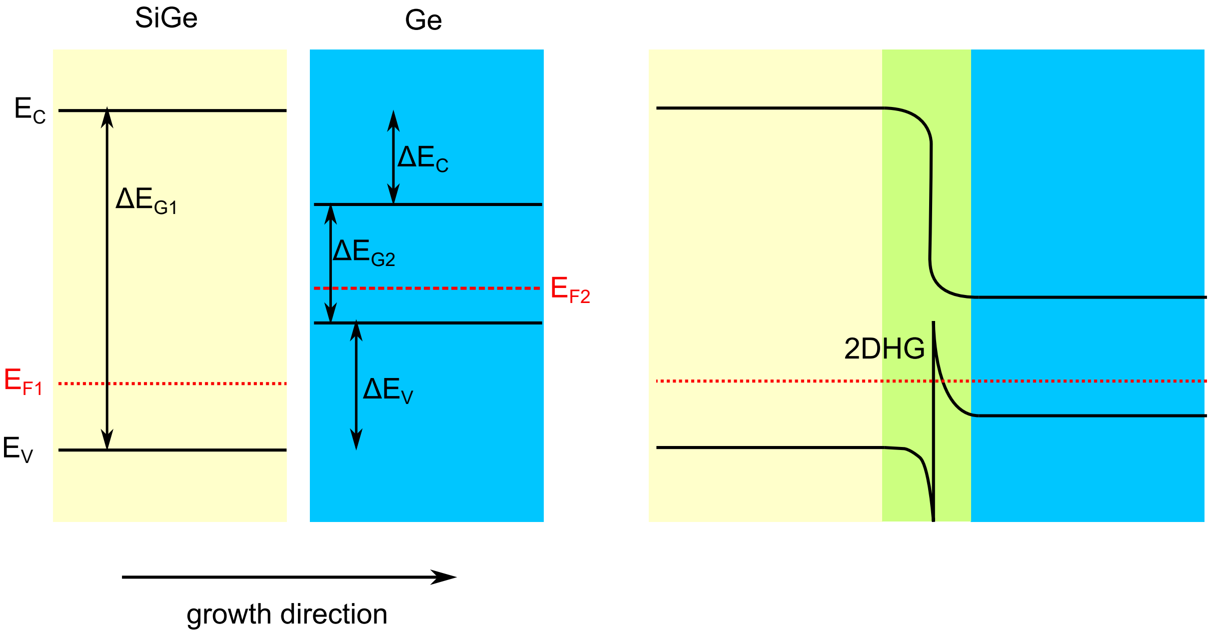

Figure 2.3: Band alignement of heterojunctions. Left: two semiconductors (for example SiGe and Ge) have a different Fermi energy E_F and different band gap. Right: when brought into contact the Fermi energies align and the conduction and valence band bend to form a trapping potential, for holes in this example, at the interface. This trapping potential causes a quantization of the momentum in the growth direction.

great advantage for transport and is also the reason why GaAs/AlGaAs heterostructures were the first to be successfully grown.

By sandwitching one semiconductor between another type of semiconductor it is possible to obtain 2 dimensional carrier gases. Depending on the nature of the active region (the inner semiconductor) and the barriers (the outer semiconductors) the resulting potential is either confining electrons, confining holes, confining both electrons and holes or acting as a barrier for both. In this work we will treat heterostrucures where Ge is the active layer and it is sandwitched between Si$_{0.3}$Ge$_{0.7}$ yielding a deep trapping potential for holes.

2.1.3 Mobility, Quantum Hall Effect and Landau Levels

In a semiclassical model of transport charge carriers subject to an electric field E will drift with a drift velocity:

$$v_d = \mu E \tag{2.4}$$

where μ is the mobility. The mobility thus expresses the inertia of charge carriers when an electric field is applied and macroscopically describes the amount of scattering centers in the semiconductor. In fact one finds that μ is proportional to τ_e where τ_e is the scattering time of a particle in a medium. A straightforward way to extract the mobility of a device is to harvest the Hall effect [49]. Assume a conductor of width w, length L and thickness t with $L, w \gg t$, basically our two dimensional carrier gas introduced before. Applying a magnetic field B perpendicular to the sample causes the charged particles to bend their trajectory according to the Lorentz force

$$\mathbf{F}_L = q(\mathbf{E} + \mathbf{v} \times \mathbf{B}) \tag{2.5}$$

where q is the charge of the particle. As electrons have opposite charge than holes and propagate in the opposite direction both holes and electrons are pushed towards the same side of the device in hole and electron conductors. This causes a potential drop to appear as charges accumulate more on one side of the sample. The voltage drop is know as the Hall voltage V_H. We can determine V_H by substituting $E = \frac{V_H}{w}$, $v = \frac{L}{t} = \frac{LI}{Q} = \frac{LI}{nV_S q} = \frac{LI}{nwLqd}$ in equation 2.5 and putting $F_L = 0$. Here I is the current, Q the overall charge,V_S the volume and n the charge carrier density in 2 dimensions. We therefore find

$$V_H = -\frac{IB}{ndq} = \frac{-IB}{n_S q} \tag{2.6}$$

where we defined $n_S = nd$ as the sheet carrier density. Therefore, measuring V_H with an applied current I and magnetic field B allows to infer the sheet carrier density

$$n_S = -\frac{IB}{q|V_H|} \tag{2.7}$$

Also the mobility can be extracted by observing that

$$\mu = n_S q \mu \frac{1}{n_S q} = \frac{1}{q n_S R_S} = \frac{|V_H|}{R_S I B} \tag{2.8}$$

where we introduced the sheet resistance $R_S = \frac{I}{V}$. The sheet resistance can be measured using the Van der Pauw technique.

The above discussion holds for small magnetic fields. However, in 2 dimensional systems at higher magnetic fields the solutions to the Schrödinger equation reveal other characteristic effects. In fact, the density of states of free electrons is replaced by a series of δ-functions known as Landau levels [43]. These contain a number of degenerate states with different momentum k. The boundary conditions set by the sample size reveal that the number of states in a Landau level per unit area is $n_B = \frac{eB}{h}$. The filling factor $\nu = \frac{n_S}{n_B}$ describes how many Landau levels are filled. At determined fields $B_n = \frac{hn_S}{en}$ the filling factor assumes integer values and all Landau levels below the Fermi energy are filled. At these fields the longitudinal resistance is minimized as only edge channels contribute to the conductance. When the Fermi energy lies in a Landau level (ν not integer) the resistance increases. This effect in known as Shubnikov de Haas oscillations [50] because the longitudinal resistance oscillates as a function of the applied magnetic field. Interestingly, the transversal resistance $R_{xy} = \frac{B}{qn_S}$ also assumes quantized values for $B = B_n$:

$$R_{xy}^{-1} = \left(\frac{e^2}{h}\right) n \tag{2.9}$$

These plateaus of transversal resistance, therefore, appear exactly at the same magnetic field as the longitudinal resistance minimum and are a signature of the integer Quantum Hall effect [51]. In chapter 3 we will see that we observed both the Quantum Hall effect and Shubnikov de Haas oscillations in doped and undoped heterostructures and inferred the charge carrier density and mobility.

2.1.4 Quantum dots

Interesting transport phenomena can be observed upon reducing the dimensionality of the semiconductor even further than 2 dimensions. This can be achieved in a variety of ways. For example, nanowires are 1 dimensional structures that can be self-assembled, as is the case for Ge hut wires [52], or grown starting from a metallic nanoparticle that acts as catalyst [53]. Similarly, 0 dimensional structures, so called quantum dots (QD), can be self-assembled due to a combination of strain and surface energy [54] (see Fig. 2.4b). Alternatively, surface gates can be used to deplete or accumulate charge carriers in a 2 dimensional carrier gas to form 1D or 0D structures [14]. Quantum dots are often referred to as artificial atoms because they similarly exhibit discrete electronic energy levels due to the tight confinement in all spacial directions. Moreover, coupling more quantum dots together allows to form artificial molecules with hybridized states as we will see in the following.

Single Quantum Dots

Charges of the same sign repel each other due to Coulomb interaction. Therefore, in QDs, the energy necessary to add an additional charge on the QD E_{add} is equal to the charging energy E_C. Moreover, when the size of the QD approaches the wavelength of the charge carrier orbital effects become evident and an additional energy splitting E_{orb} appears. Treating the QD as a particle in the box system reveals that this orbital energy $E_{orb} \approx \frac{1}{m^* L^2}$, where L is the size of the box. Therefore, to obtain a large orbital spacing it is necessary to keep the product $m^* L^2$ small. As we will see, heavy holes in planar Ge have a particularly small effective mass in the direction parallel to the quantum well in heterostructures allowing the dimensions of the QD to be larger than for electrons in Si [15]. The relaxed fabrication constraints are one of the reasons why Ge has become such a successful quantum material.

The electrochemical potential $\mu_e(N)$ (not to be confused with the mobility) describes the energy necessary to add the N-th charge to the quantum dot:

$$\mu_e(N) = U(N) - U(N-1) \tag{2.10}$$

where $U(N)$ is the total energy of the dot containing N charges. The addition energy can be conveniently written as $E_{add} = \mu_e(N+1) - \mu_e(N) = E_C + E_{orb}$. As charges in the QD can not be created from nothing, QDs are typically coupled to one or more reservoirs. To observe transport actually a source and drain reservoir with electrochemical potential μ_S and μ_D, respectively, are present. The QD is separated from source and drain by tunnel barriers and the electrochemical potential in the dot is controlled by an external gate voltage capacitively coupled to the dot. The circuit diagram of this system is depicted in Fig 2.4a. Applying a bias to source and drain, $eV_{SD} = \mu_S - \mu_D$, now allows charge to flow. Electrons flow from higher electrochemical potential to lower potential. Correspondingly, holes flow from lower to higher potential. Transport can only occur if $\mu_D < \mu_e(N) < \mu_S$ (or $\mu_D > \mu_e(N) > \mu_S$). Otherwise, transport is blocked. This phenomenon is known as Coulomb Blockade and the level alignment

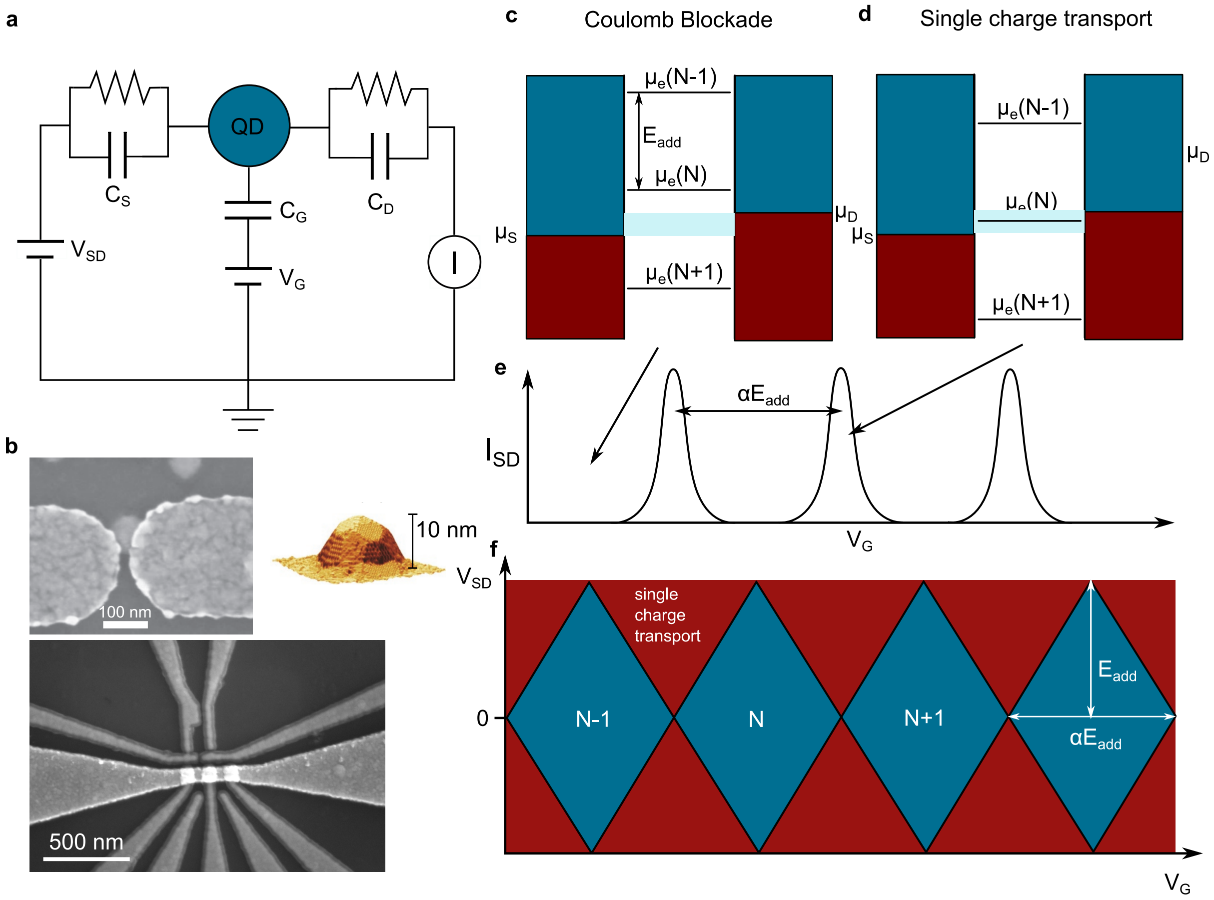

Figure 2.4: Single quantum dot. a) Schematics of a single QD circuit. The QD is tunnel coupled to a source and drain lead and the tunneling is characterized by C_S and C_D, respectively in parallel with a resistor. A bias voltage V_{SD} can be applied between source and drain and the current I can be measured. The charges in the QD can be controlled by a gate voltage V_G capacitively coupled through C_G to the dot. b) Examples of a self-assembled Ge quantum dot (a dome [54]) and a gate defined quantum dot. c) Electrochemical potentials for a QD in Coulomb blockade. Inside the source drain window (light blue) there is no level available for transport. The current is blocked. d) Single charge transport window. One level is available in the source-drain window for transport. Electrons flow from higher to lower electrochemical potential, holes do the opposite. e) Schematics of I_{SD} as a function of V_G. The current is 0 in Coulomb blockade while it peaks when levels are within the source drain window. The distance between the peaks is proportional to the addition energy. f) Stability diagram of a QD. V_{SD} changes the bias window while V_G controls the levels in the dot. The result is a regular pattern of Coulomb diamonds. The height of a diamond corresponds to E_{add}.

is depicted in Fig. 2.4c while charge transport happens in Fig. 2.4d. Fig. 2.4e schematically draws the current through the QD as a function of gate voltage. The spread of the current peaks is due to the thermal broadening of the leads, described by the Fermi distribution function, and the lifetime of the charges is the dot, determined by the couplings to the leads.

When the bias voltage is opened the transport window is increased. Sweeping both gate and bias voltage gives rise to so-called Coulomb Diamonds as can be seen schematically in Fig. 2.4f. Inside the diamond the current is blocked as the system is in Coulomb Blockade and the charge number in the dot is fixed. Outside the diamond single charge transport takes place as one energy level of the dot falls within the bias window. The slope of the diamond edges are $-\frac{qC_G}{C_{tot}-C_S}$ and $(\frac{qC_G}{C_S})$ for the left (right) edge. Here C_G is the gate capacitance, C_S is the source capacitance and $C_{tot} = C_G + C_S + C_D$ is the total capacitance. The height of the diamond is $E_{add} = eV_{SD}$ and the length is $\delta V_G = E_{add}/\alpha_G$, where $\alpha_G = qC_G/C_{tot}$ is the gate lever arm. In other words, the lever arm transforms a gate voltage to an energy change in the quantum dot and is measured in eV/V. The presence of higher orbitals can also be observed in this charge stability diagram as a step-like increase in the current when such a level falls within the bias window (not shown in the schematics). If one records the current as a function of an external parameter like the magnetic field this can be used, for example, to investigate the Zeeman splitting. As the addition energy becomes $E_{add} = E_C + E_Z = E_C \pm \frac{g\mu_B B}{2}$, where + corresponds to one spin state (for example $\uparrow$) and - to the other spin state (for example $\downarrow$),the current increase step moves to a different bias voltage.

Double Quantum Dots

Adding a second quantum dot in series to the first one gives rise to a double quantum dot (DQD) system (Fig. 2.5a) [55]. Now μ_{e1} (μ_{e2}) describes the electrochemical potential in dot 1 (2) controlled by $V_{G1(2)}$. Elastic transport through the dot is allowed when $\mu_S < \mu_{e1} = \mu_{e2} < \mu_D$ (or $\mu_S > \mu_{e1} = \mu_{e2} > \mu_D$) (Fig. 2.5b). The resulting stability diagram is depicted in (Fig. 2.5c). Here we assumed no mutual capacitance C_m between the dots and no lever arm of gate 1 on dot 2 and vice versa ($\alpha_{12(21)} = 0$). When $C_m > 0$ and $\alpha_{12(21)} > 0$, which is normally the case for real systems, the charge stability lines become tilted and give rise to a characteristic honeycomb pattern (Fig. 2.5d). Transport is only allowed at the triple points, which come in pairs, where all the electrochemical potentials are aligned. Inside a honeyomb the charge number is fixed. Transport at the triple points can happen in two ways: in the upper triple point an electron from the right dot exits to the drain, an electron from the left jumps to the right dot and is replaced by and electron from the left lead. This corresponds to an effective hole transfer from right to left. In the lower tiple point first an electron enters the double dot from the left lead, is transferred to the right dot and subsequently to the right lead. This is an effective electron transfer from the left to the right lead. Increasing the bias voltage results in the triple points evolving to bias triangles. The alignment of the electrochemical potentials in each dot is depicted in Fig. 2.5e.

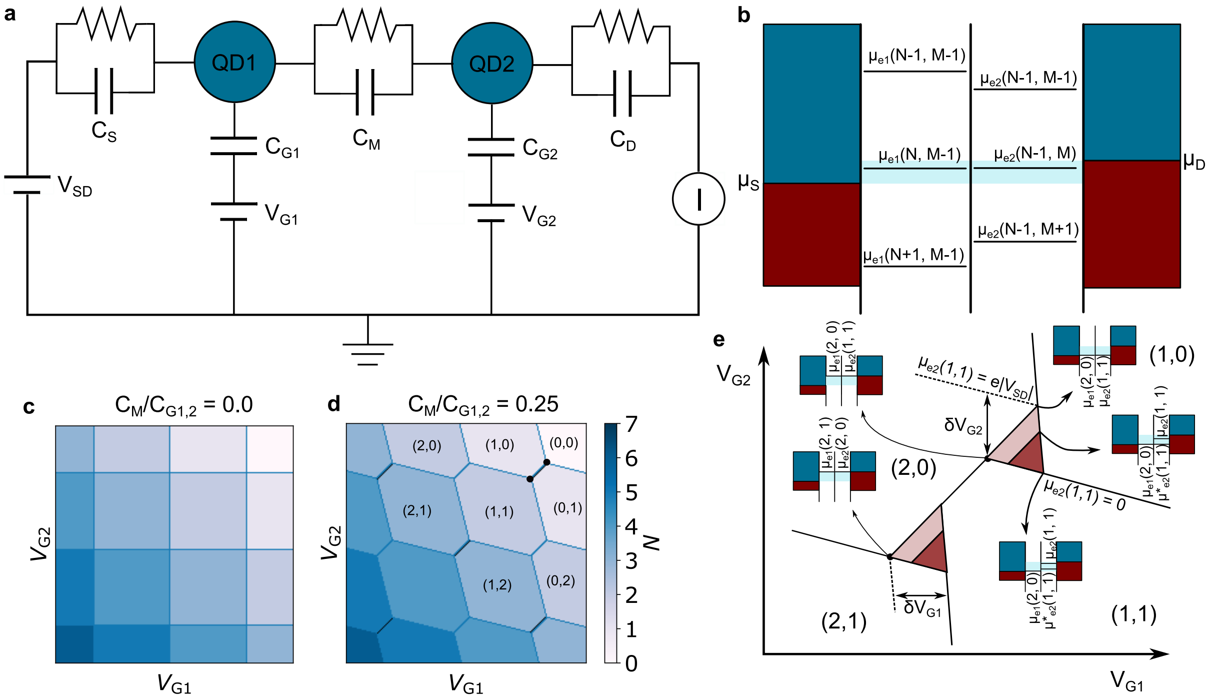

Figure 2.5: Double quantum dots. a) Circuit schematic of a double quantum dot. We now simply have two tunnel coupled quantum dots that are individually controlled by their respective gate voltages. b) Electrochemical potentials in the two quantum dots. Transport is facilitated when the levels in both QDs are aligned and inside the bias window. c) Stability diagram with mutual capacitance $C_M = 0$ and zero bias. Here each gate controls only the level in the respective dot. Charge transitions appear as horizontal and vertical lines. d) Stability diagram with $C_M/C_{G1,2} = 0.25$. Now each gate influences not only its respective dot but also the other dot leading to more diagonal charge transitions. The black dots mark a pair of triple points. Here, the levels of both dots are aligned and transport can occur. e) Bias triangles appear in place of triple points when a bias is opened. The respective electrochemical potentials are highlighted for each vertex of a triangle. $\delta V_{G1,2}$ can be used to extract the lever arm of the gates when the applied bias is known.

The base line of such a triangle corresponds to the region where the electrochemical potentials of two levels in the dots are aligned and are within the bias window. In general, lines of increased current appear when any two levels in the two dots are aligned and within the bias window. Moreover, one generally observes an increased current in the bias triangles also when the levels in the dots are not aligned. This is due to inelastic scattering processes where the energy difference between the levels is compensated by energy transfer to phonons for example. Moreover, for very transparent tunnel barriers, also the transitions to the leads can become visible in current. As we will see, DQDs in a magnetic field are particularly useful for operating spin qubits as they offer an easy way to read out the qubit spin state.

Exchange interaction and Pauli spin blockade

Fermionic states in a double quantum dot are not only characterized by their spatial localization but also by their spin. Two-spin systems can have 4 possible states: 3 triplets corresponding to a total angular momentum $\mathbf{S} = 1$ and 1 singlet state with total angular momentum $\mathbf{S} = 0$:

$$|S\rangle = \frac{|\uparrow\downarrow\rangle - |\downarrow\uparrow\rangle}{\sqrt{2}} \tag{2.11}$$

$$|T_+\rangle = |\uparrow\uparrow\rangle \tag{2.12}$$

$$|T_0\rangle = \frac{|\uparrow\downarrow\rangle + |\downarrow\uparrow\rangle}{\sqrt{2}} \tag{2.13}$$

$$|T_-\rangle = |\downarrow\downarrow\rangle \tag{2.14}$$

where the three triplet states have their spin projection in the quantization axis $S_Z = +1, 0, -1$, respectively. For the singlet state the spin component to the wavefunction is anti-symmetric while it is symmetric for the triplet states. As fermions the total wavefunction of these states has to be anti-symmetric leading to a symmetric spatial wavefunction for the singlet and an anti-symmetric one for the triplets. We denote the total singlet (triplet) state as $S(n_L, n_R)$ ($T_{\pm,0}(n_L, n_R)$) with $n_{L,R}$ the number of spins in the left and right QD, respectively. Due to the large wave function overlap for spins in the same dot the singlet-triplet splitting E_{ST}^{02} is of the order of meV. Usually we operate our QDs in regimes where the orbital level spacing is much larger than any other relevant energy scale. Hence, $T(2,0)$ states, where both charges are in one dot, are energetically very unfavourable and can be safely neglected in the scope of this work.

In the (1,1) charge configuration the singlet triplet splitting is typically referred to as the exchange interaction J. The wavefunction overlap between the spins is controlled by the relative energy detuning ϵ. Throughout this work the T_0 energy is always 0 and the singlet energy is $E_S = -J$, and $\epsilon = 0$ at the charge symmetry point ($(2,0) \Longleftrightarrow (1,1)$). For a tunnel coupling t_C the exchange energy takes the form:

$$J(t_C, \epsilon) = \sqrt{\frac{\epsilon^2}{4} + 2t_C^2} - \frac{\epsilon}{2} \tag{2.15}$$

While tunneling is blocked for spins in the triplet configuration, singlet states are free to tunnel between the $S(1,1)$ and $S(2,0)$ regime. This allows to map the spin state to the charge state: a triplet state will maintain the (1,1) charge configuration while a singlet will have the (2,0) charge configuration when actively lowering the energy of the left dot with respect to the right one. This phenomenon is known as Pauli spin blockade [56]. PSB can be observed either in DC by a vanishing base line of a bias triangle in one bias direction or by quickly pulsing the system through different charge configurations and monitoring the response of a charge sensor [57]. Fig. 2.6 schematically shows two pulse schemes that

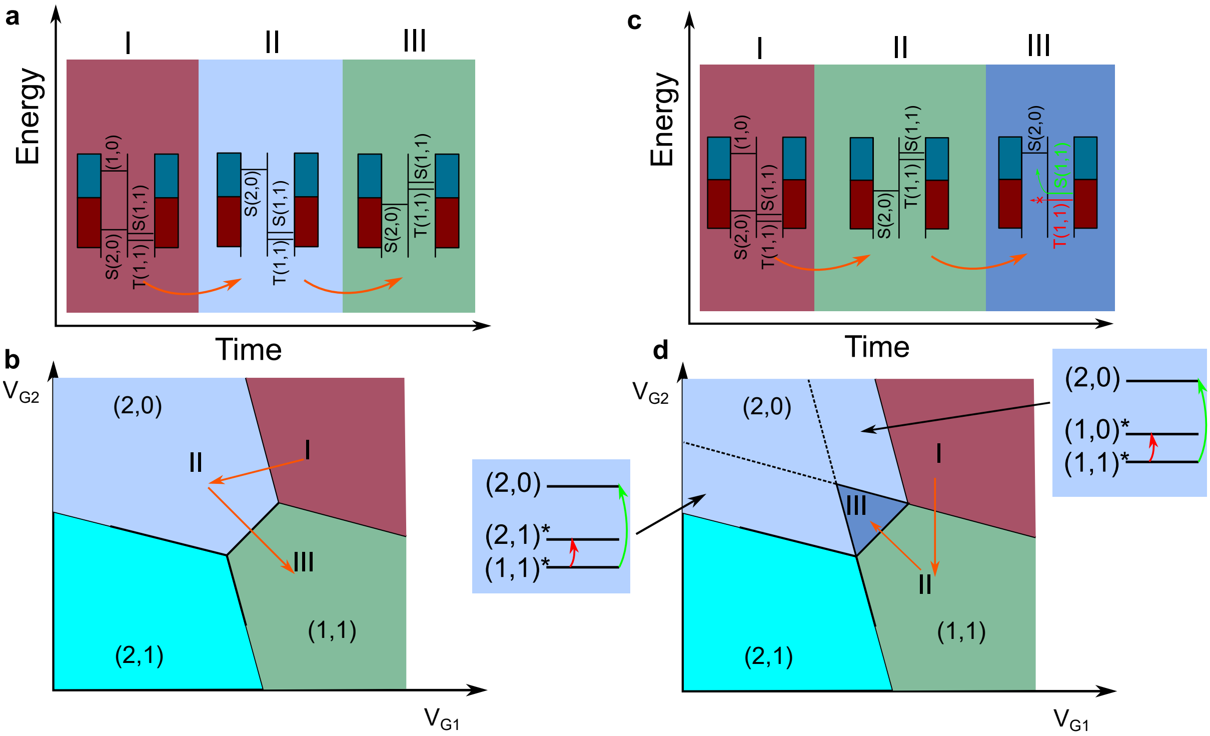

Figure 2.6: Pauli spin blockade principle. a) Pulse sequence allowing transport. The system is initialized in (1,0) at point I. A pulse then pushes the system to (2,0) where another hole is loaded to the left dot. Since the $T(2,0)$ state is far off in energy only an $S(2,0)$ state can be loaded. Another pulse to (1,1) allows a spin to be transferred to the $S(1,1)$ state. b) Stability diagram at 0 bias. The arrow highlights the direction of the pulses in a). c) Inverse pulse sequence. This time after initialization in (1,0) the system is pulsed to (1,1) where either a $S(1,1)$ or a $T(1,1)$ will form. A pulse to (2,0) into the marked triangular region will allow only the $S(1,1)$ to be transferred to a $S(2,0)$ while spin conservation will block the $T(1,1)$ state. d) Stability diagram at 0 bias with inverse pulsing. Blockade occurs in the triangular region close to the charge symmetry point. The dashed lines mark the regions where tunneling to the leads to exchange the spin state is energetically favorable as the $(2,1)^*$ and $(1,0)^*$ lie in between the energy of the (1,1)* and the $S(2,0)$ state. The * symbol denotes the fact that these are excited states in the (2,0) charge region.

can detect PSB in charge sensing. In both cases the system in initialized in (1,0). For a counterclockwise pulsing around a triple point (Fig. 2.6a,b) the system is the pulsed to (2,0) where a $S(2,0)$ state will form owing to the fact that the $T(2,0)$ state lies much higher in energy. A consequent pulse to (1,1) will transfer the $S(2,0)$ state to another singlet: $S(1,1)$. For clockwise pulsing (Fig. 2.6c,d), on the other hand, in the (1,1) region either a $S(1,1)$ or a $T(1,1)$ state can be initialized. Therefore, a pulse to (2,0) will only allow a $S(1,1)$ to be transferred while a $T(1,1)$ state remains blocked. In the stability diagram a triangular region appears in which PSB occurs. Read-out can be performed in this region allowing to infer the spin state of the system via spin-to-charge conversion [58]. Outside the triangle tunneling to the leads lifts PSB as a spin can be flipped. Other effects such as SOI or the hyperfine interaction can also lift the blockade inside the triangular region leading to a decay of the triplet state with a characteristic timescale set by the relaxation time T_1.

2.1.5 Luttinger-Kohn Hamiltonian

As we will focus mainly on holes in this work it is a good point to introduce the Luttinger-Kohn Hamiltonian which describes the band structure of the valence band of commonly used semiconductors close to the Γ-point. From the band structure of Si and Ge (Fig. 2.2) we observe that 2 bands, the heavy hole (HH) and light hole (HH) band, are degenerate at the Γ-point with a third band, the split-off (SO) band, lower in energy. Strain, confinement and the spin orbit interaction lift the degeneracy of the HH and LH band. As holes are fermions they possess a spin of $S = \pm\frac{1}{2}$. Moreover, the HH and LH band have a p-type orbital character which means they carry an additional angular momentum $L = 1$. The total angular momentum for HH and LH is therefore $\mathbf{J} = \mathbf{L} + \mathbf{S} = \frac{3}{2}$. The projection along the z-axis for HH is $j_Z = \pm\frac{3}{2}$ while for LH it is $j_Z = \pm\frac{1}{2}$. For the systems investigated here the SO band is usually far off in energy and we can ignore it. The Hamiltonian for HH and LH in a magnetic field in the 2 dimensional limit can be written block form as:

$$H = \begin{pmatrix} H_{HH} & H_{HL} \\ H_{LH} & H_{LL} \end{pmatrix} \tag{2.16}$$

Each term in the Hamiltonian is a 2x2 matrix with:

$$H_{HH/LH} = \frac{\gamma_1 \pm \gamma_2}{2m^*}(k_x^2 + k_y^2) + \frac{\gamma_1 \mp 2\gamma_2}{2m^*}k_z^2 + \frac{1}{2}\mu_B \boldsymbol{\sigma} g_{H/L}\mathbf{B} + U(x,y) + V_{H/L}(z) \tag{2.17}$$

here γ_1, γ_2 are material specific parameters and come from the Luttinger-Kohn Hamiltonian, σ is the spin operator contained in the magnetic field dependent term, $U(x,y)$ is the confinement potential in the x,y direction and $V_{H/L}$ is the confinement of heavy and light holes in the z-direction. One can define the effective mass for HH and LH as

$$\frac{1}{m^*_{HH/LH}} = \frac{\gamma_1 \pm \gamma_2}{2m^*} \tag{2.18}$$

For bulk Ge $\gamma_1 = 13.35$ and $\gamma_2 = 4.25$. Therefore, one can see that in the 2 dimensional limit the heavy hole mass is actually lighter than the light hole mass in the direction of transport, a characteristic that becomes very useful when fabricating devices. In formula 2.17 $g_{H/L}$ denotes the effective heavy and light hole g-tensor respectively. One finds that

$$g_H = \begin{pmatrix} 3q & 0 & 0 \\ 0 & 3q & 0 \\ 0 & 0 & -6\kappa - \frac{27}{2}q \end{pmatrix} = \begin{pmatrix} 0.21 & 0 & 0 \\ 0 & 0.21 & 0 \\ 0 & 0 & -21.405 \end{pmatrix} \tag{2.19}$$

$$g_L = \begin{pmatrix} 4\kappa + 10q & 0 & 0 \\ 0 & 4\kappa + 10q & 0 \\ 0 & 0 & 2\kappa + \frac{1}{2}q \end{pmatrix} = \begin{pmatrix} 14.34 & 0 & 0 \\ 0 & 14.34 & 0 \\ 0 & 0 & 7.26 \end{pmatrix} \tag{2.20}$$

where $\kappa = 3.41$ and $q = 0.07$ are again material specific parameters and the g-tensor is expressed in (x,y,z) coordinates. As one can see the out-of-plane g-factor of HH is very large, while it is small for LH. In plane, the HH g-factor vanishes while the LH g-factors become dominant. Thus, to determine the character of a hole, one can measure the g-factor anisotropy between in-plane and out-of-plane magnetic field direction.

The HH-LH mixing is found to be

$$H_{HL} = H_{LH}^{\dagger} = \frac{i\sqrt{3}\gamma_3}{m}(k_x\sigma_y + k_y\sigma_x)k_z \tag{2.21}$$

where γ_3 is another material specific parameter. We can see that the HH-LH mixing couples spin to momentum as a spin orbit interaction does.

The HH-LH mixing term entails that a hole in a semiconductor under strain is generally a mixture of HH and LH ($|\Psi\rangle = \alpha\,|\Psi_{HH}\rangle + \beta\,|\Psi_{LH}\rangle$) and the effective g-factor will reflect this by assuming a value in between the purely HH and purely LH one.

2.2 Qubits

A qubit, short for quantum bit, is the quantum mechanical analog to a classical bit. Similarly to a classical bit that can be in two states, 0 and 1, a qubit can be in the states $|0\rangle$ and $|1\rangle$. However, the quantum mechanical nature of the qubit allows it to be found also in any superposition of the aforementioned basis states. Such a superposition is generally denoted as $|\Psi\rangle = \cos\left(\frac{\theta}{2}\right)|0\rangle + \sin\left(\frac{\theta}{2}\right)\exp(i\phi)\,|1\rangle$ with $0 < \theta < \pi$ and $0 < \phi < 2\pi$. A general qubit state can therefore be mapped on the surface of a sphere with unit radius. The polar angle of this state is θ while the azimuthal angle is denoted ϕ. An image of this so called Bloch sphere is depicted in Fig. 2.7. The polar angle θ describes the amount of overlap between the qubit states and is simply the projection of the state along the z-axis. Similarly, the angle ϕ describes the projection along the x and y axis.

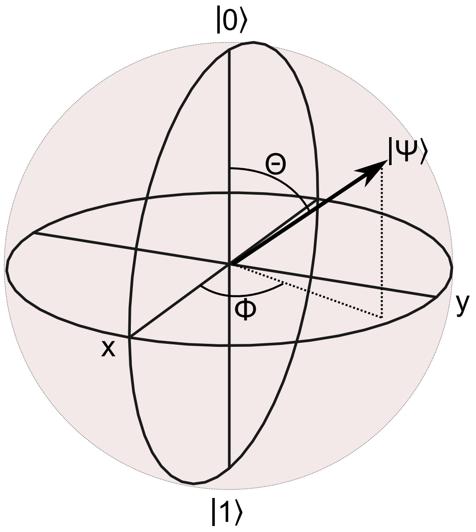

Figure 2.7: Bloch sphere representation of a qubit state $|\Psi\rangle$. The polar angle θ describes the amount of overlap between the qubit basis states $|0\rangle$ and $|1\rangle$. The azimuthal angle ϕ describes the projection on the x and y axis.

2.2.1 Time evolution

In quantum mechanics the state dynamics is governed by the Schrödinger equation.

$$i\hbar\,|\Psi(t)\rangle = H\,|\Psi(t)\rangle \tag{2.22}$$

which has the solution

$$|\Psi(t)\rangle = \exp\left(-\frac{iHt}{\hbar}\right)|\Psi(0)\rangle \tag{2.23}$$

If we assume a simple Hamiltonian with eigenenergies E_0 and E_1 for the eigenstates $|0\rangle$ and $|1\rangle$, respectively, the state at time t takes the form:

$$\begin{aligned} |\Psi(t)\rangle &= \cos\left(\frac{\theta}{2}\right)\exp\left(-\frac{iE_0t}{\hbar}\right)|0\rangle + \sin\left(\frac{\theta}{2}\right)\exp(i\phi)\exp\left(-\frac{iE_1t}{\hbar}\right)|1\rangle \\ &= \exp\left(-\frac{iE_0t}{\hbar}\right)\left(\cos\left(\frac{\theta}{2}\right)|0\rangle + \sin\left(\frac{\theta}{2}\right)\exp\left(i(\phi - \frac{i(E_1-E_0)t}{\hbar})\right)\right)|1\rangle \end{aligned} \tag{2.24}$$

Since a global phase can be neglected for a quantum state, from (2.24) we can see the effect of the Hamiltonian on its eigenstates $|0\rangle$ and $|1\rangle$. The polar angle is unaffected by the time evolution and only the azimuthal angle changes depending on the eigenenergies and the time. Hence, a Hamiltonian rotates a state around an axis defined by its eigenstates about an angle that depends on the eigenenergies and the time it is applied. To achieve full qubit control two non colinear Hamiltonians and precisely timed switching needs to be available.

2.2.2 Relaxation, dephasing and decoherence

As qubits are quantum states they are very fragile and can be easily disturbed by their environment. The disurbing interactions can happen through spin-phonon interaction, spin-spin interaction and charge noise. Processes that can flip the spin state from the excited state to the ground state are know as relaxation processes and are described by an average decay time T_1. One way of measuring this average relaxation time is to prepare a qubit in the excited state and wait for it to decay and then average over many experimental runs. At each run, a spin will decay at a random time and the average of all decay times will be T_1. Relaxation times for holes were predicted to be rather short due to the SOI coupling HH and LH subbands [59]. However, theoretical proposals and experimental realizations [60] showed that a long T_1 can still be obtained for holes in QDs.

Processes that alter the phase of a superposition state are known as decoherence processes and are typically described by a time T_2. Averaging many single shot experiments will give rise to an effective spin ensemble measurement where the system is sensitive to fluctuations of its environment on the timescale of the experiment. The characteristic decay time is known as inhomogeneous dephasing time and is denoted T_2^*. For holes in Ge the main source of decoherence are trapped charges giving rise to 2 level system fluctuations with a characteristic $1/f$ noise spectral density. However, also the special Ising-type hyperfine interaction for HH states [32] is predicted to contribute to the decoherence. Isotopic purification can help to reduce this noise contribution.

2.2.3 Di Vincenzo criteria

The general requirements for a qubit were known and around since quite some time before DiVincenzo summarized them in probably one of the most influential papers for the field of quantum computation [61]. His 5 requirements are actively driving research in the field of experimental quantum computation. The first criterion states that a quantum computer should essentially be a "scalable physical system with well characterized qubits". This very broad first statement limits qubit candidates to any two level system. Many proposals for the realization of qubits exist and have been demonstrated experimentally but the keyword "scalable" is often overlooked. The second criterion states that it has to be possible to initialize the system in a well known state, such as $|000...\rangle$. Simply put, the system should be in the ground state, or at least always the same state, at the beginning of the calculation. The third criterion covers decoherence. The quantum information should be preserved for long enough time, much longer than the relevant gate operation time. Often in literature systems are praised for their long coherence times because the systems are well isolated from their environment. However, this also causes manipulation speeds to be slow. On the other hand, very fast operation unavoidably results in shorter coherence times because the system interacts strongly with its environment. It is, therefore, prudent to always consider the ratio of coherence time and gate time to obtain a comparable quantity that is meaningful over different qubit implementations. The fourth criterion postulates the existence of

a universal set of quantum gates. Classically it can be proven that a single gate, the "NAND" (or the "NOR") gate is universal and can, if used in the correct sequence, mimic any other logic gate. It turns out that in quantum computation a universal set of quantum gates is given by the single qubit Pauli operators in combination with one two-qubit gate, the CNOT. Other implementations also exist. For example the 3-fold Toffoli gate alone is also universal [61]. The last criterion states that a "qubit specific measurement capability" has to be available. Indeed, there needs to be a way to extract information from the system in order to learn the outcome of a computation.
Having outlined the general criteria for a qubit platform we now introduce spin qubit platforms and emphasize their strenghts and weaknesses.

2.2.4 The Loss-DiVincenzo qubit

The most straight-forward and intuitive implementation of a qubit is the Loss-DiVincenzo (LD) proposal [18]. Here, a series of spin-1/2 particles are confined in adjacent quantum dots (Fig. 2.8a). Each spin-1/2 particle constitutes an individual qubit. Metallic surface gates generate a highly tunable trapping potential and a magnetic field splits the spin states due to the Zeeman Hamiltonian $H_Z = -\mu\mathbf{B}$, where $\mu = \frac{eg}{2m}\mathbf{S}$ is the particle's magnetic moment, e is the electron charge, m the particle's mass, g the effective g-factor in the magnetic field direction and $\mathbf{S} = \frac{\hbar}{2}\sigma$ is the spin vector. $\hbar$ is the reduced Planck constant and $\sigma = (\sigma_x, \sigma_y, \sigma_z)$ is the Pauli vector. The Hamiltonian then takes the form $H_Z = \frac{1}{2}g\mu_B\mathbf{B}\sigma$ with $\mu_B = \frac{e\hbar}{2m}$ being the Bohr magneton. The eigenstates of this Hamiltonian are $|\uparrow\rangle$ with eigenvalue $-\frac{1}{2}g\mu_B\mathbf{B}$ and $|\downarrow\rangle$ with eigenvalue $+\frac{1}{2}g\mu_B\mathbf{B}$. The spin up $|\uparrow\rangle$ and spin down $|\downarrow\rangle$ are the $|0\rangle$ and $|1\rangle$ qubit states, respectively, and can be directly mapped to the Bloch sphere picture. In fact, now θ and ϕ simply describe in what direction the spin state is pointing on the Bloch sphere. Single qubit operations are achieved by applying resonant microwave excitations (Fig. 2.8b) either via alternating magnetic fields [22] or via electric fields if spin orbit interaction is present [62]. Qubit to qubit interaction is achieved by tuning the wave-function overlap of adjacent spin qubits [29]. The resulting exchange interaction can be used to selectively address a qubit depending on the state of the other (Fig. 2.8c). In fact, the exchange interaction gives rise to 4 states ($|\uparrow\uparrow\rangle$,$|\uparrow\downarrow\rangle$, $|\downarrow\uparrow\rangle$, $|\downarrow\downarrow\rangle$) with different energy splittings symbolized by the differently colored waves. Selecting the wanted transition frequency will, therefore, drive the desired state transitions.

The main source of decoherence for this kind of qubit are fluctuations in the magnetic field experienced by the spin particles. In real devices the host material consists of atoms that can carry a nuclear spin. The collective fluctuations of the directions of these nuclear spins generates an average magnetic field experienced by the qubit spin known as the Overhauser field. Early spin qubit attempts were engineered in AlGaAs/GaAs heterostructures because lattice matching of the two materials enables low defect, high mobility host materials. However, being a group III-V compound, all the naturally occurring isotopes of Ga and As carry a nuclear spin (see Fig. 2.8d). To this day this is the main argument against GaAs

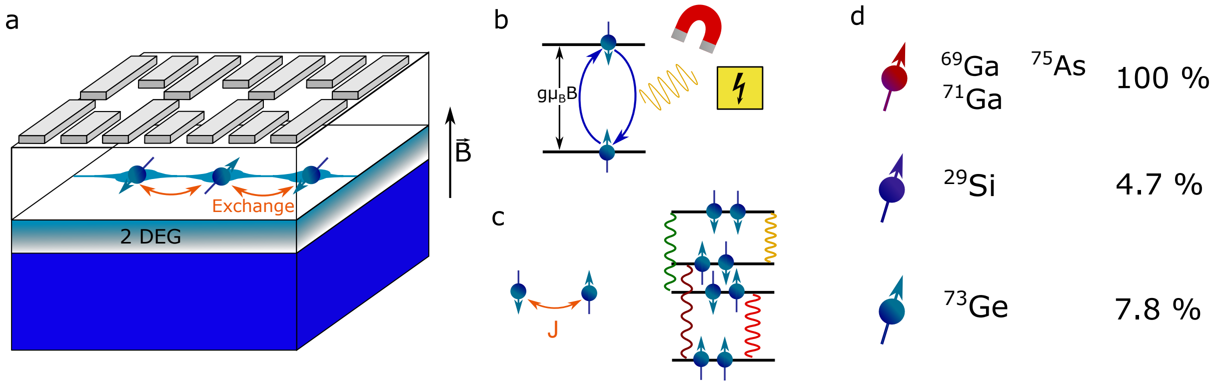

Figure 2.8: Loss DiVincenzo qubit schematics. a) Quantum dots are confined in a 2 dimensional electron gas by means of epitaxy and surface gate voltages. A magnetic field B separates the spin states energetically. The spins experience an energy shift due to the nearest neighbour exchange interaction. b) Schematics of the Zeeman splitting of two spins. Transitions can be driven by resonant AC magnetic or electric fields if a SOI interaction is present. c) The exchange interaction between two spins results in 4 energy levels with different energy splittings. Hence, 4 different resonant drives can be used to induce state transitions. Two-qubit gates can easily be accomplished harvesting this property. d) The main decoherence mechanisms for Loss DiVincenzo qubits are fluctuations in the magnetic field caused by the random overhauser field of the nuclei in the host material. In GaAs all the atoms possess nuclear spin and result in decoherence times of $10\,\mathrm{ns}$. Si and Ge have only one isotope carrying nuclear spin are are, therefore, much better suited for hosting spin qubits. Moreover, these materials can be isotopically purified to yield almost nuclear spin-free materials.

as a qubit material despite great advances in dynamic nuclear polarization. Group IV semiconductors like Si and Ge, on the other hand, possess only a small amount of nuclear spin carrying isotopes [15]. The main difficulty of these materials is that no lattice matching can be achieved for SiGe compounds. Hence, SiGe heterostructures often suffer from interface defects and rather low mobilities compared to GaAs. Nevertheless, the low amount of nuclear spins, which can be further reduced by isotopic purification, has enabled record coherence times for electrons in Si [24,25]. Moreover, fault tolerant single qubit fidelities have been demonstrated exceeding 99.9% (less than 1 error for every 1000 operations) [26]. Two qubit gate fidelities, however, have failed to reach fault tolerant levels mainly because the slow driving speed leads to long gate times and dephasing and charge noise reduce fidelity. Moreover, the 6-fold degeneracy of the conduction band in Si is split by confinement and gives rise to valley states that can interfere with the qubit states [63]. In spite of all these challenges, Si still holds great promise for future scale up.

Holes in Ge have recently emerged as an alternative to electrons in Si. Several key features are beneficial for this material in respect to Si but also GaAs. The main advantages of holes, particularly in Ge, for spin qubits are:

- a small effective mass and, therefore, relaxed fabrication contraints;
- a high mobility, in fact the highest hole mobility of all known semiconductors;
- a p-type wavefuntion and, therefore, resilience to contact hyperfine interaction;
- a large SOI and, therefore, fast all electrical operation;
- Fermi level pinning and, therefore, easy ohmic contact formation to almost all metals without the need for ion implantation;
- a low abundance of nuclear spins and further isotopical purification available.

All these characteristics lead to the demonstration of the first LD qubit in Ge hutwires in 2018 in our group [30] followed by a steep progress in the field and the demonstration of single qubits in SiGe/Ge heterostructures [60] and core-shell nanowires [40], fault tolerant two qubit gates in heterostructures [39] and recently even a four qubit processor, again in heterostructures [36]. In fact, Ge might just be the first material to follow Moore's law for quantum bits.

2.2.5 The Singlet Triplet Qubit

The singlet-triplet qubit operates with similar premises to the LD proposal, with the difference that 2 spins, instead of one, are used to encode a single qubit. The advantage of the singlet-triplet qubit becomes evident when considering the $S_z = 0$ subspace formed by S and T_0 as these are independent of the external overall magnetic field. Hence, the magnetic field fluctuations affecting the Loss DVincenzo qubit are, in principle, absent. In this context one speaks about "protected" or "decoherence-free" subspaces [64]. One key requirement is the ability to switch the exchange interaction between the spins on and off rapidly. Another requirement is that the two spins experience a slightly different Zeeman splitting [20]. Here, two possible ways to obtain this difference exist: a difference in the effective magnetic field (ΔB) or a difference in the effective g-factors (Δg). Early attempts in GaAs for example, leveraged on the random local nuclear Overhauser field to obtain singlet triplet oscillations [21]. However, the large amount of uncontrolled nuclei still presented a major decoherence channel. With dynamic nuclear polarization the Overhauser field can be stabilized and the dephasing time of GaAs singlet-triplet qubits was extended by one order of magnitude [23]. First attempts in Si also leveraged on the small hyperfine component present in the material [65]. However, this approach was quickly replaced by engineering magnetic field gradients with micro-magnets [66]. Both approaches indeed maintain the decoherence free subspace for the qubit. Another approach is to leverage the SOI of the material. This can cause small variations in the g-factors experienced by two spins in different locations. In Si, this has lead to the demonstration of singlet triplet qubits with g-factor differences in the order of 0.002 [67–70]. However, the presence of an explicit dependence on the B-field destroys the protected subspace. In the following we will describe the Hamiltonian of a hole $S-T_0$ qubit.

We assume a heavy-hole double quantum dot system to be in the (1,1)-(2,0) regime such that the (0,2) charge configuration and all triplet states consisting of a doubly occupied dot are split off energetically and may be neglected. Hence, the Hilbert space under consideration is spanned by the (2,0) singlet $|S_{20}\rangle$, the (1,1) singlet $|S\rangle$ and the three (1,1) triplet states $|T_{0,\pm}\rangle$. The two singlet states are detuned by an amount $\epsilon = U - \tilde{\epsilon}$, where U is the charging energy and $\tilde{\epsilon}$ is the energy difference between the two dots in the one-particle picture. At positive detunings, $\epsilon > 0$, the (1,1) singlet is energetically favourable. The parts of the Hamiltonian describing the basic DQD system and the spin-orbit interaction (SOI) read, respectively,

$$H_0 = \epsilon |S_{20}\rangle\langle S_{20}| + \sqrt{2} t_c \left(|S_{20}\rangle\langle S| + |S\rangle\langle S_{20}| \right), \tag{2.25}$$

$$H_{\text{SO}} = t_{\text{SO}} \sum_{\pm} \left(|S_{20}\rangle\langle T_\pm| + |T_\pm\rangle\langle S_{20}| \right), \tag{2.26}$$

where t_c is the one-particle tunneling element and t_{SO} parametrizes spin-flip tunneling events induced by the SOI. The unpolarized triplet does not appear in Eq. (2.26) as the SOI of Ge hole states in similar systems has been found to couple the singlet in the (2,0) configuration to the polarized triplets only [71].

When applying an out-of-plane magnetic field of magnitude B and taking into account site-dependent g-tensors, the Hamiltonian of the system contains a Zeeman term of the form [72],

$$H_Z = \frac{\mu_B B}{2} \sum_{d \in \{L,R\}} g_d \sigma_z^d, \tag{2.27}$$

where σ_z^d is the Pauli matrix along the quantization axis and g_d labels the out-of-plane g-factor in the left ($d = L$) and right ($d = R$) dot.

In the presence of a finite tunnel coupling t_c the singlets form hybridized states according to Eq. (2.25),

$$\begin{aligned} |S_G\rangle &= \cos\frac{\Omega}{2}|S\rangle + \sin\frac{\Omega}{2}|S_{20}\rangle, \\ |S_E\rangle &= \cos\frac{\Omega}{2}|S_{20}\rangle - \sin\frac{\Omega}{2}|S\rangle, \end{aligned} \tag{2.28}$$

with the mixing angle $\Omega = -\arctan\left(\frac{2\sqrt{2}t_c}{\epsilon}\right)$. Consequently, the total Hamiltonian $H = H_0 + H_{\mathsf{SO}} + H_Z$ reads in the basis $\{|S_E\rangle, |S_G\rangle, |T_+\rangle, |T_0\rangle, |T_-\rangle\}$,

$$H = \begin{pmatrix} \frac{\epsilon}{2} + \sqrt{\frac{\epsilon^2}{4} + 2t_c^2} & 0 & t_{\mathsf{SO}}\cos\frac{\Omega}{2} & -\frac{\Delta g\mu_B B}{2}\sin\frac{\Omega}{2} & t_{\mathsf{SO}}\cos\frac{\Omega}{2} \\ 0 & \frac{\epsilon}{2} - \sqrt{\frac{\epsilon^2}{4} + 2t_c^2} & t_{\mathsf{SO}}\sin\frac{\Omega}{2} & \frac{\Delta g\mu_B B}{2}\cos\frac{\Omega}{2} & t_{\mathsf{SO}}\sin\frac{\Omega}{2} \\ t_{\mathsf{SO}}\cos\frac{\Omega}{2} & t_{\mathsf{SO}}\sin\frac{\Omega}{2} & \frac{\Sigma g\mu_B B}{2} & 0 & 0 \\ -\frac{\Delta g\mu_B B}{2}\sin\frac{\Omega}{2} & \frac{\Delta g\mu_B B}{2}\cos\frac{\Omega}{2} & 0 & 0 & 0 \\ t_{\mathsf{SO}}\cos\frac{\Omega}{2} & t_{\mathsf{SO}}\sin\frac{\Omega}{2} & 0 & 0 & -\frac{\Sigma g\mu_B B}{2} \end{pmatrix}, \tag{2.29}$$

where Σg (Δg) denotes the sum (difference) of out-of-plane g-factors. The energy spectrum resulting from this Hamiltonian is displayed in Fig. 2.9c. In the regime $\frac{t_c}{\epsilon} \ll 1$, one has $\sin\frac{\Omega}{2} \approx 0$ and $\cos\frac{\Omega}{2} \approx 1$, allowing us to work in the approximately decoupled subspace spanned by the ground state singlet $|S_G\rangle$ and the unpolarized triplet $|T_0\rangle$.

The Hamiltonian for a $S - T_0$ qubit in the basis $|S_G\rangle = |S\rangle, |T_0\rangle$ then reads:

$$H = \begin{pmatrix} -J(\epsilon) & \Delta E_Z \\ \Delta E_Z & 0 \end{pmatrix} \tag{2.30}$$

where ΔE_Z is the Zeeman energy difference in the two dots. As we saw in a previous section the exchange interaction depends on the relative energy detuning ϵ. When ϵ is large we obtain $J(\epsilon) \ll \Delta E_Z$ and the Hamiltonian is $H \approx \Delta E_Z \sigma_X$. This corresponds to a rotation around the x-axis of the Bloch sphere. When ϵ is small, $J(\epsilon) \gg \Delta E_Z$ and $H \approx -1 - J(\epsilon)\sigma_Z$. The state therefore revolves around the z-axis. Hence, to obtain two non-collinear Hamiltonians one needs to be able to turn the exchange interaction on and off. This is easily accomplished in gate defined quantum dots by adjusting the relative energy detunings between two adjacent dots. Fig. 2.9 highlights the operation principle of a singlet triplet qubit switching between high ϵ (a) where the Zeeman term is dominant and low ϵ (b) where the exchange interaction is dominant. The key advantage of the singlet-triplet qubit is the ability to drive the qubit all electrically with pulses that are slower than 1 GHz reducing the costs of equipment and making operation easier. Two main disadvantages are the effects of charge noise on $J(\epsilon)$ and the inability to switch ΔE_Z rapidly. The latter condition means that the two axis of rotation will never be perpendicular to each other. Thus, quantum gates require composite pulses to be applied [73,74]. Nevertheless, high fidelity operation of single qubits have been demonstrated with pulse engineering [75]. Charge noise on

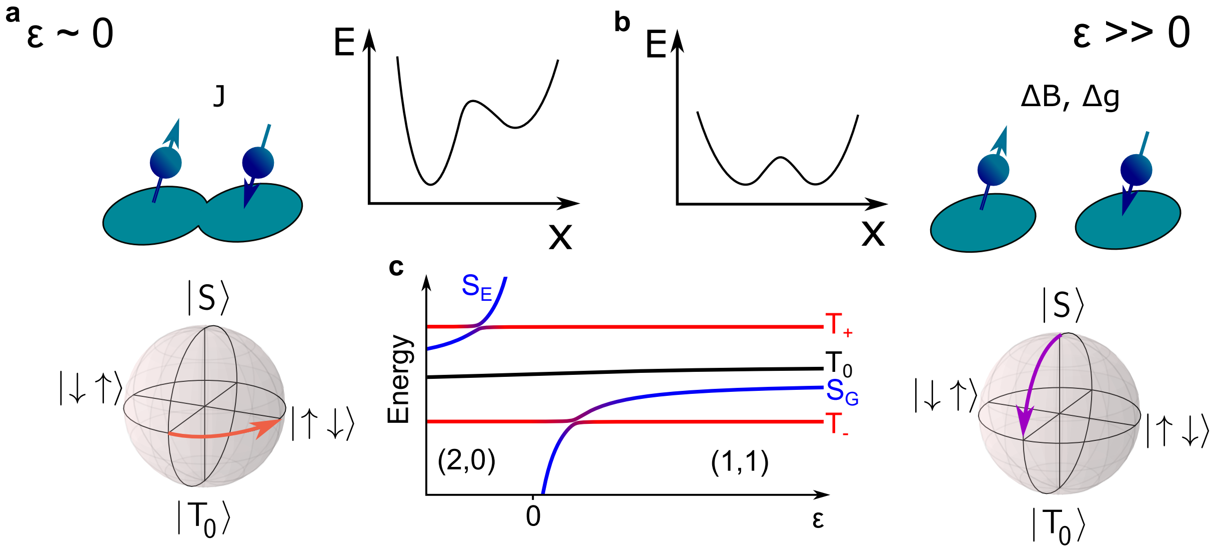

Figure 2.9: $S-T_0$ qubit operation schematics. a) For small ϵ the potential is now tilted and the exchange interaction dominates as the spins are forced closer together. This causes a precession around the qubit' z-axis. b) At large ϵ the spins are separated in the two dots and the exchange interaction is small. A schematic of the potential landscape is depicted on the right. The Zeeman energy difference caused by magnetic field gradients or g-factor differences results in $S-T_0$ oscillations as highlighted on the Bloch-sphere on the bottom. c) Energy level diagram calculated for the model in Eq. 2.29.

J can efficiently be suppressed by symmetric operation [76] or by resonantly driving the qubit at optimal working points [77, 78]. Resonant driving also makes the realization of quantum gates straight-forward as for the LD qubit.

Two-qubit gates can be achieved by leveraging the dipole moment of a $S-T_0$ qubit during exchange oscillations. As the charge distribution of the S and T_0 state are different and dependent on ϵ, an adjacent capacitively coupled qubit will experience a different electrostatic environment depending on the state of the first qubit allowing conditional rotations to be performed [79]. Similarly, one can exploit this feature in resonantly driven $S-T_0$ qubits to achieve high-fidelity entangling gates [77].

3 Fabrication and Setup

In this section I will discuss the fabrication process and the measurement setup used in most of the experiments. I adapted the first part from the methods section of our singlet triplet qubit paper [80] and I expanded it to discuss several aspects of the setup in more detail. I also adapted the second section from the supplementary information of the same paper and I expanded it by a detailed table that shows the recipe steps and a figure to sketch the processes involved. Moreover, I briefly discuss our method for testing the status of a fabricated device at 4K.

3.1 Setup

Most of the measurements in this thesis were carried out in one dilution refrigerator from Leiden cryogenics which we call "Smurf" (simply because it is blue). Some measurements were, however, carried out in a Bluefors fridge and some in another Leiden fridge. Each refrigerator is slightly different but the main principles apply to all which is why I decided to only include the setup in which I conducted most of the experiment. Fig. 3.1 schematically depicts all the elements used in the setup, except the 9/3 T vector magnet around the sample area. Fast gate lines are connected to the desired gate via one of 10 available connections. The signals are applied via a Zurich Instruments HDAWG with a maximum output of 5 V and a sampling rate of 2.4 GHz. As thermal noise from room temperature would drastically deteriorate the performance of the device, the signal is heavily attenuated before reaching the sample. At each stage a certain cooling power is available, that reduces towards the mixing chamber (MC). It is, therefore, crucial to attenuate the signal by the right amount at the right stage. The black rectangles in Fig. 3.1 depict attenuators and the number inside specifies the attenuation in dB. An attenuator with 0 dB serves as a thermal anchor for the cable and thermalizes the electrons inside to the temperature of the specific stage. On the printed circuit board (PCB, green box), the signal is merged with the DC voltage through a bias-T and applied directly to a gate of the device.

The reflectometry circuit features a directional coupler (mini-circuits ZFDC-20-50-S+). Here the signal

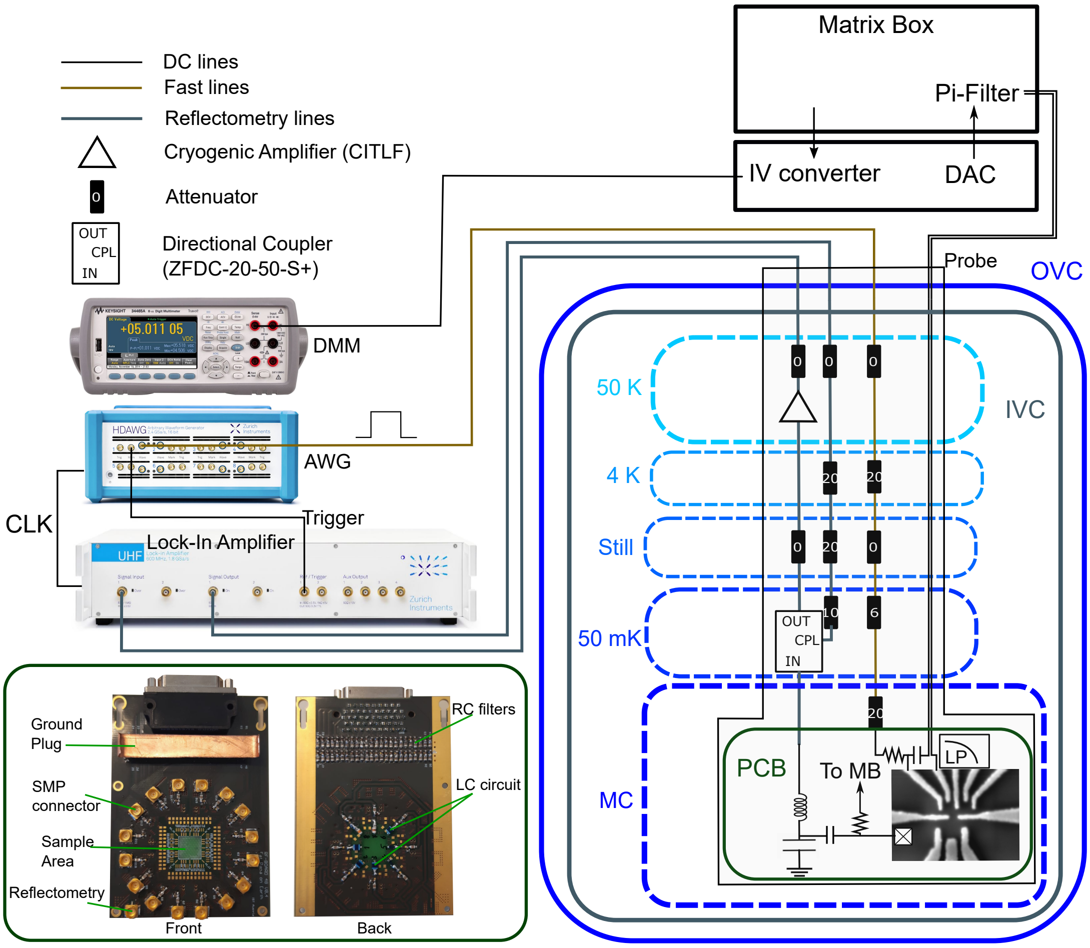

Figure 3.1: Schematics of the setup. The cryostat is sketched on the right. The outer vacuum chamber (OVC) contains the inner vacuum chamber (IVC) which itself contains the remaining shields and fridge plates. The different fridge stages are depicted as dashed boxes and their respective temperatures or names are reported. The Mixing chamber contains the PCB with the sample. The PCB (bottom left) called "Fat Papa" hosts 48 low pass filtered DC lines, 16 high frequency lines with respective SMP connectors, 8 LC circuits and a ground plug. Also, on the PCB bias-Ts add high frequency and DC signals for reflectometry and fast pulsing. All high frequency lines are attenuated at several stages to ensure a low electron temperature yet a large enough signal to still arrive at the sample. This is accomplished via attenuators (black boxes) of different values. The values in dB are adapted to the cooling power of the different stages. A 0 dB attenuator serves as a thermal anchor. Through these lines the Zurich Instruments HDAWG can apply fast pulses to the gates. Also the reflectometry lines are attenuated and the input line is fed into the coupling port of a directional coupler, reflected at the sample and rerouted through the coupler to the output. Here, a cryogenic amplifier enhances the signal which is then demodulated by the Zurich Instruments UHFLI. The DC voltages are provided by the Delft electronic IVVI rack (upper right). The DAC outputs a voltage in the range from 0-4V (when positive polarity is selected). The DAC outputs are connected to the matrix box which connects to the probe via two 24 pin Fisher connectors. Currents can also be read out by feading the signal into an IV converter and sending the outcoming signal to a digital multimeter.

from the Lock-in amplifier enters the coupling port (CPL), gets transmitted to the input port (IN), reflects at the LC resonator depending on the matching conditions, re-enters the coupler through the input port and gets transmitted to the output port (OUT) and from there to RT via a superconducting cable to minimize losses. As no attenuation is desired anymore, the cable from the output port is only thermally anchored to the fridge plates. At the 50 K stage, a cryogenic RF-amplifier enhances the signal which is then demodulated at room temperature by the Zurich Instrument Lock-in amplifier (UHFLI). Also for the reflectometry signal a bias-T is used to merge it with the DC signal and apply it to an Ohmic contact or a gate.

DC signals are applied via the Delft electronics IVVI rack. Up to 16 DACs with a range of $4\,\mathrm{V}$ (either $\pm2\,\mathrm{V}$ or 0 to $+4\,\mathrm{V}$ or $-4\,\mathrm{V}$) can be routed to the Matrix box where they pass through pi-filters and are connected to the probe by a 24 pin Fischer connector. In the probe, the DC lines are thermally anchored to the fridge stages and organized in twisted pairs in order to minimize noise. Several low-pass filter stages attenuate the high frequency component of the thermal noise. Currents from the sample can also be routed from the matrix box (to MB) to an IV-converter where they are amplified and can then be read out via a Keysight 34465a digital multimeter (DMM).

Fig. 3.1 also depicts the printed circuit board (PCB, green box in bottom left) called "Fat Papa". It can host up to 48 DC connections, 16 high frequency lines (front) and 8 LC-resonators (back). Surface mount SMP connectors allow us to plug the lines in the probe directly to the PCB where they are routed to the corresponding bonding pad. A ground plug shorting all contacts to ground on the front side of the PCB serves as a protection during bonding and is removed after the PCB is plugged into the probe via the 51 pin D-SUB connector.

Fat Papa was designed mostly by Josip Kukucka. The wiring of the probe with all the attenuating and amplifying stages was made possible by Thomas Adletzberger.

3.2 Fabrication

All our wafers are provided by the group of Giovanni Isella and are grown by Andrea Ballabio (cite ballabio). The growth process is a low energy plasma enhanced chemical vapour deposition (LEPECVD). Here, the precursor gases Silane (SiH_4) and Germane (GeH_4) are forced by the plasma to separate into Si and H or Ge and H, respectively. This aids the deposition process and ensures that the composition of the wafer is dependent solely on the concentration of the precursor gases in the chamber rather than the temperature of the substrate as is normally the case for conventional CVD. The wafer consists of a virtual substrate with 70% Ge, a 20 nm thick quantum well, a 20 nm $Si_{30\%}Ge_{70\%}$ barrier layer and a 2 nm sacrificial Si layer. The last layer serves to protect the structure and will form the native silicon oxide (SiO_2). More details about the wafer growth can be found in chapter 5.

Once the wafers are in our hands we proceed to cut them into $6 \times 6\,\mathrm{mm}$ pieces for further processing.

Step	Process	Remarks
Cleaning	-30 s Acetone at 50℃ -30 s rinse in IPA -blow dry with nitrogen gun	check sample under microscope for scratches or dirt
Markers and Ohmics	-Spin PMMA 950K 4% at 6000 rpm -bake at 180 ℃ for 5 min -expose pattern "Markers and Ohmics", dose 430 $\mu\mathrm{C}/\mathrm{cm}^2$ -develop Water:IPA 3:7 1 min, rinse IPA 30 s -argon milling 2x2 min -deposit 60 nm of Pt under 5° angle liftoff 10 min Acetone at 50 ℃	angle is crucial can also be faster than 10 min
Mesa	-Spin CSAR 13% at 6000 rpm -bake at 150 ℃ for 1 min -expose pattern "Mesa", dose $300\,\mu\mathrm{C}/\mathrm{cm}^2$ -develop with CSAR developper 1 min, rinse IPA 30 s -etch mesa with recipe JuAg SF6CHF3O2 for 90 s -clean sample in DMSO 80 ℃ for 1 h	etches about 90 nm or as long as needed
Oxide	- HF dip for 10 s, 10 s water, 10 s nitrogen gun - quickly place sample in ALD load lock - deposit 20 nm (200 cycles) of $\mathrm{Al_2O_3}$ at 300 ℃ - check refraction coefficient and thickness in ellipsometer	
Thin Gates	- spin PMMA 950K 3% 4000 rpm - bake 180 ℃ for 5 min - expose "Thin gates" beam 0.5 nA aperture 200, dose 385$\mu\mathrm{C}/\mathrm{cm}^2$ - develop Water:IPA 3:7 1 min, rinse IPA 30 s - deposit Ti/Pd 3/27 nm - liftoff 1 h DMSO at 80 ℃ - Pipette to remove metal more effectively	Ti ensures sticking of Pd or as long as needed
Rough Gates	- spin PMMA 950K 2% 4000 rpm - bake 180 ℃ for 5 min - expose "Thin gates" beam 50 nA, dose 450$\mu\mathrm{C}/\mathrm{cm}^2$ - develop Water:IPA 3:7 1 min, rinse IPA 30 s - deposit Ti/Pd 3/97 nm -liftoff 1 h DMSO at 80 ℃ - Pipette to remove metal more effectively	Ti ensures sticking of Pd or as long as needed

Table 3.1: Step by step fabrication protocol for double quantum dot samples. It is crucial to follow the development and rinse times to ensure clean surfaces before the next step.

On a single chip we fit 4 devices. All the fabrication steps are summarized in table 3.1. They can be summarized in 4 main steps:

- Markers and Ohmic contacts;
- Mesa etching;
- Oxide deposition;
- Gate patterning and evaporation.

3.2.1 Markers and Ohmic contacts

The "Markers" step serves to pattern markers on the sample surface for alignment of different exposures in the electron beam lithography system (EBPG 5150 from Raith, ebeam). However, in order to safe one exposure, we also pattern the Ohmic contacts onto the sample at this step. Before metal deposition we, therefore, perform an Argon milling step in the high vacuum (HV) electron beam evaporator (Plassys MEB 550S) in order to remove the native oxide and parts of the barrier layer without breaking the vacuum. Subsequently the metal is evaporated under an angle of 5°. This has proven to enhance the reproducibility of our Ohmic contacts and has lowered the contact resistance significantly. The metal of our choice is Pt since it is easy to lift, very reflective for scanning electron microscopy due to its weight (and, therefore, eases marker search in the ebeam) and creates a good ohmic contact to Ge due to its large work function.

3.2.2 Mesa etching

In a second step we etch the mesa after patterning it in the ebeam. Here we rely on a reactive ion etching (RIE) process and etch away about 90 nm of the wafer (Oxford Instruments PlasmaPRO 100 Cobra). In fact, it would be sufficient to etch just below the QW.

3.2.3 Oxide deposition

After etching we remove the native oxide completely by performing a dip in buffered hydrofluoric acid (BHF) and subsequently place a 20 nm aluminium oxide (Al_2O_3) layer on the device via atomic layer deposition (Oxford Instruments FlexAL ALD). This process is performed at 300 ℃ and, therefore, performs an unintentional annealing of the Ohmic contacts which further reduces contact resistance.

3.2.4 Gate patterning and evaporation

In the last step the gates are patterned and evaporated on the sample. The gate layer is split into thin and rough gates. The thin gates are placed only on top of the non-etched part (the mesa) and are

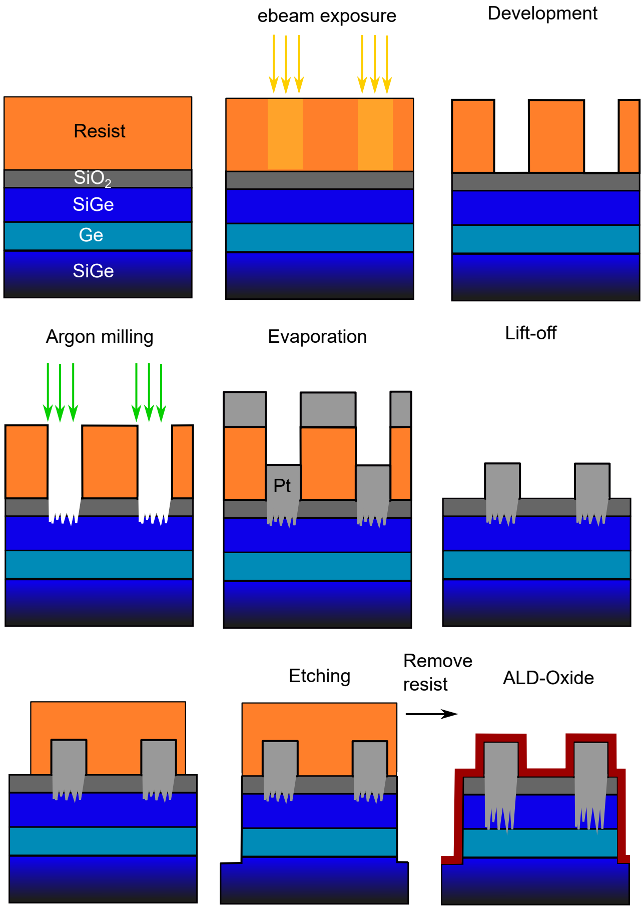

Figure 3.2: Schematics of the different fabrication steps. First we spin resist on the sample surface. The resist is either PMMA or CSAR. Then we expose the sample in the ebeam. The impinging electrons cause the polymer chains in the resist to break and, therefore, change their chemical properties. Depending on the resist the dose, so the amount of charge per surface area, necessary to break the chains changes. After exposure the sample is developed in a resist-specific developer. In the exposed areas the resist is removed. For Ohmic contacts an Argon milling step is necessary to remove the native oxide and parts of the upper barrier. Subsequently, we evaporate the metal. During lift-off the resist is removed and only the metal parts sticking on the sample surface remain. For Mesa etching we proceed similar to before by spinning resist and exposing the pattern in the ebeam. Then we etch the sample in a RIE process. After etching and removing the resist, we dip the sample in buffered HF as then deposit the gate oxide via ALD.

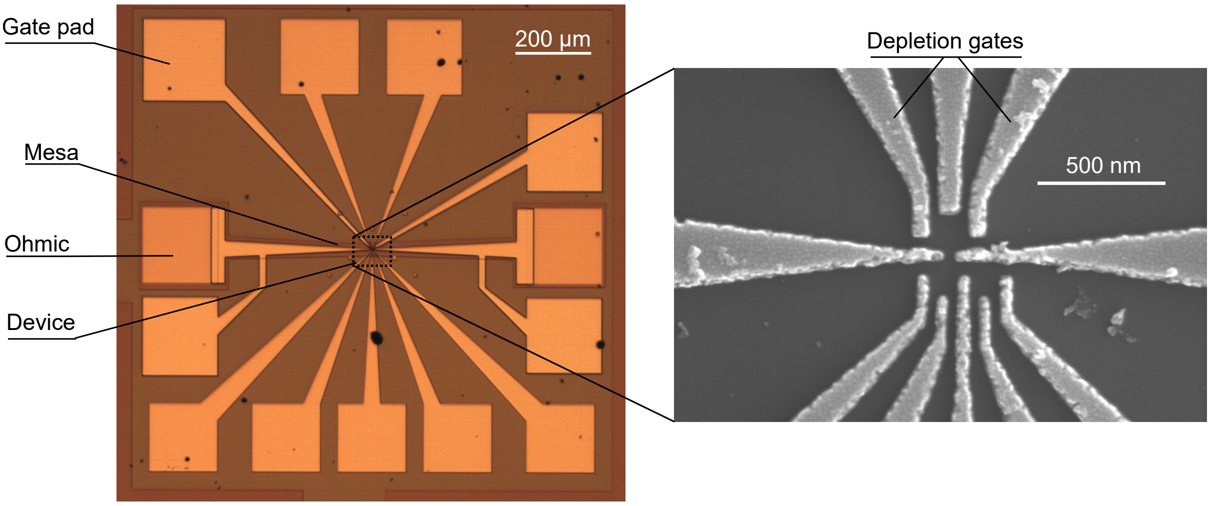

Figure 3.3: Left: Optical microscope image of a finished device with all the gate layers, Ohmic contacts and the mesa. The gates are visible in bright colors while the mesa appears gray. Right: SEM image of the gate layout of a device acquired from a dose test. Dose tests are performed for new gate layouts to determine the correct exposure parameters. For devices that need to be measured no SEM is performed prior to the cooldown. This is because the incoming electrons charge up the gate oxide and induce more charge noise in the system.

located at the center of the device. Their width is $\approx 30\,\mathrm{nm}$ and we opted for keeping the thickness also around this value for easier liftoff. In order to bond the gates we need to have access to large enough bond pads that should not be placed on top of the Mesa as the force of the bonding would most likely lead to leakage. Therefore, the rough gate layer is employed to guide the gates off the mesa and outward. As this layer needs to overcome the Mesa height it is around $100\,\mathrm{nm}$ in thickness. Once the last layer of gates is lifted the sample is ready for inspection under the optical microscope (Fig. 3.3). Here, we can already spot imperfections in the fabrication process. Effectively, one such inspection step is performed after each ebeam exposure and after each liftoff step.

3.2.5 Sample test at $4\,\mathrm{K}$

If the sample passes the visual inspection we bond one or more of the devices on a DC printed circuit board and cool it down in a liquid ^{4}He dewar (Fig. 3.4a). At $4\,\mathrm{K}$, the temperature of liquid ^{4}He, we first test the conductivity of the Ohmic contacts (Fig. 3.4b). We quickly realized that most of our heterostructures conduct even without any additional top gate voltage to accumulate charge carriers. From Hall bar measurements in different configurations we can conclude that a layer of trapped charges in the ALD oxide is the most plausible reason for this charge carrier density. We then test all the gates for leakage up to typically $4\,\mathrm{V}$ (Fig. 3.4c). If no gates leak we test for pinch-off (Fig. 3.4d). Here, we apply a small bias voltage to the Ohmic contact and measure the current through the device. A gate, or a combination of gates, pinches the channel if by increasing the voltage on the gate(s) the current through the sample

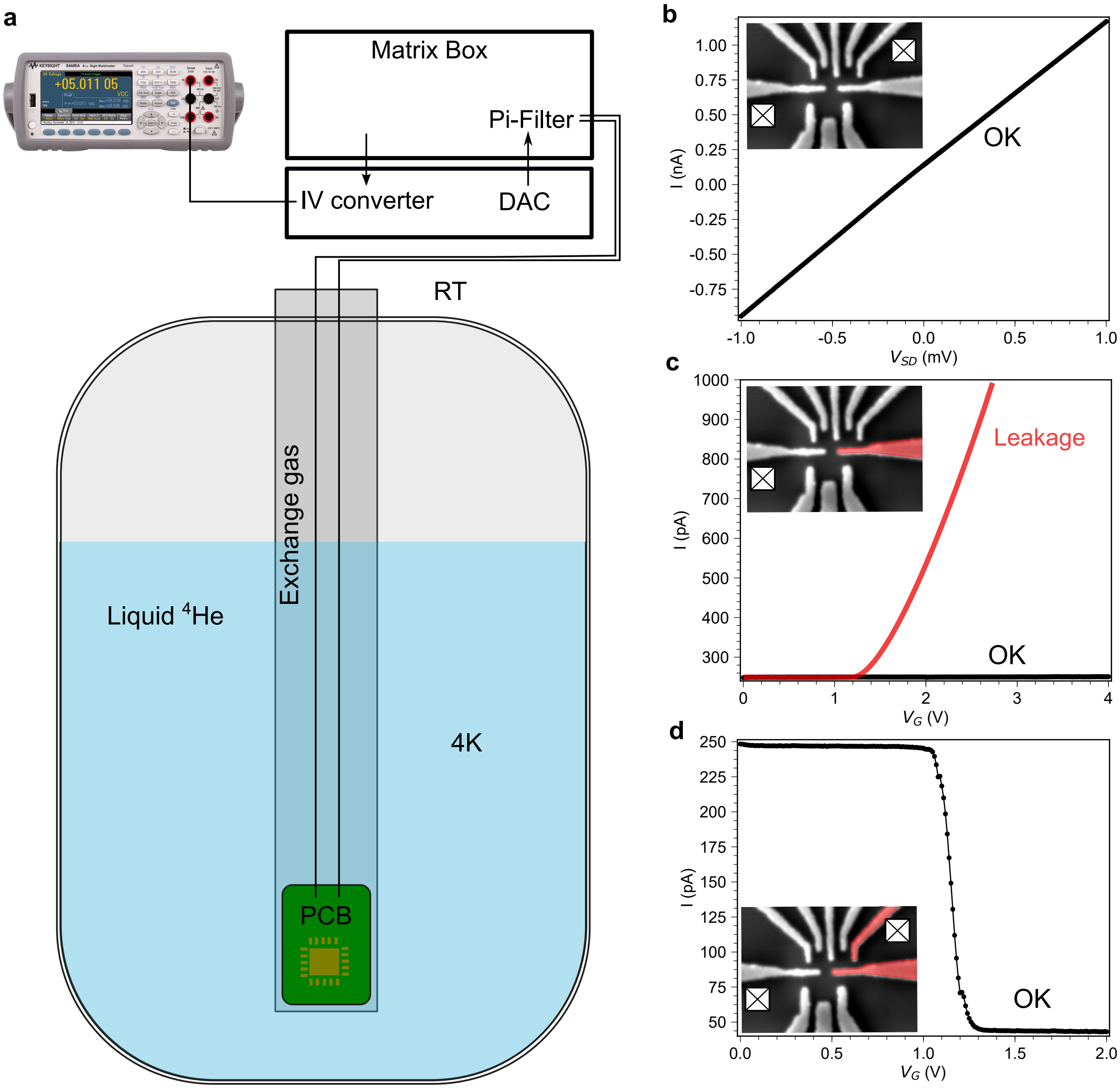

Figure 3.4: a) The setup for 4 K characterization consists of a big liquid ^{4}He tank in which we can insert our probe stick. The probe stick hosts a DC PCB and 24 DC lines. For cool-down the probe is pumped out to generate vacuum and then a small amount of exchange gas is inserted. This ensures proper thermalization. At room temperature the experimental apparatus consists of a Delft electronics rack and a DMM for current measurements. b) Ohmic contact characterization. Here we apply a voltage between two Ohmic contacts V_{SD} and record the current. A linear dependence is a confirmation of Ohm's law and shows the correct behavior of the contacts. c) Leakage test. Gates should be electrically isolated from the hole gas and each other. Here we measure the current between a gate (marked in red in the inset) and an Ohmic contact. If the current as a function of gate voltage V_G does not increase (black line) the gate is OK. If, however, the current increases significantly with V_G the gate is leaky and can not be used. Similarly, if we measure a current between gates these can not be used for tuning. d) In a last step we test for pinchoff. We record the current between two ohmic contacts applying a voltage V_{SD}. We then sweep one or more gate voltages using a combination of gates that can block the current path (for example the gates marked in red in the inset). If the current drops with V_G the gates are pinching. If all Ohmic contacts and all gates are working, the sample is ready for the real experiment.

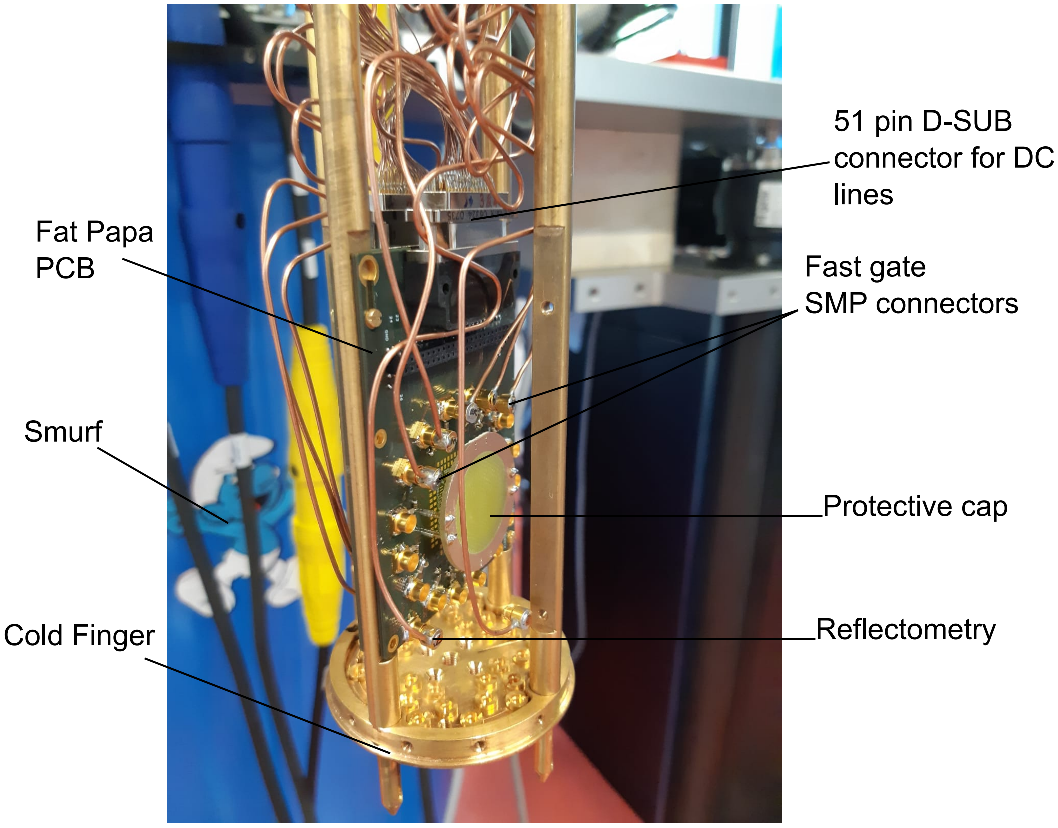

Figure 3.5: Picture of the cold finger just before loading into the fridge. In the background one can see the smurf sticker on our fridge. Several components of the Fat Papa PCB are highlighted. The device is bonded to the PCB but is not visible in the picture as it is hidden behind the protective cap. This is to ensure that no bonding wires are accidentally ripped off while connecting all the fast gate lines.

is blocked. Like this we can test the functionality of all the gates.

3.2.6 Cooldown for experiment

If the sample passes all the tests it can be carefully transferred to a PCB equipped with RF-reflectometry and fast gate circuitry like "Fat Papa" (Fig. 3.5). During un-bonding and re-bonding it is crucial to ground all the gates and oneself in order to prevent any static discharge from ruining the gates. Fat Papa is then connected to the cold finger of the probe and the fast gate and reflectometry lines are connected as well. Finally, the probe is loaded into the cryostate via a top-loading mechanism and is cooled down to 20 mK in less than 24 h. At this point the fun starts!

4 Ge hole gases: from Hall bars to reflectometry charge sensing

From 2017 to today we collaborate with the group of Giovanni Isella in Como to obtain high quality Ge/SiGe heterostructures. When I joined the Nanoelectronics group the last master student working on hole gases had left to try her fortune in industry. Her legacy was a project in its infancy which witnessed rather switchy devices on several heterostructures. The most reliable parts of the fabrication recipe of that time were the mesa etching and the ohmic contact creation. In this chapter I will go through the small steps we took to improve the heterostructures (although we only characterized them, Giovanni's group is really to thank for the outstanding development!). Interestingly, each generation of wafers helped us in understanding the system more and more. In Sec. 4.1 I will show first mobility measurements and single dot formation in a doped heterostructure. In Sec. 4.2 we switched to undoped heterostructures but with little success such that we were not able to progress. With the new generation of heterostructures in Sec. 4.3 we finally developed reliable double quantum dots and measured for the first time in our the g-factor anisotropy of 2 dimensional hole gases via the Kondo effect. Furthermore, we succeeded in charge sensing and reflectometry measurements.

4.1 The 6770 series: 2017

The 6770 series was the last doped heterostructures we used for the hole gas project. It featured a modulation doping boron layer in the upper barrier. Despite the assumption that this type of doping might cause screening of the top gate voltages we did not have issues in gating our heterostructures. I started fabricating rather ambitious devices featuring 18 gates and 6 ohmic contacts in a one layer process. An SEM image of a the device is depicted in Fig. 4.1a.

The idea at that time was to create two double quantum dots facing each other with charge sensors on either side for read-out. Seeing the development of other groups today [36], this design might have been promising but it was ahead of its time as the heterostructures and the fabrication process were

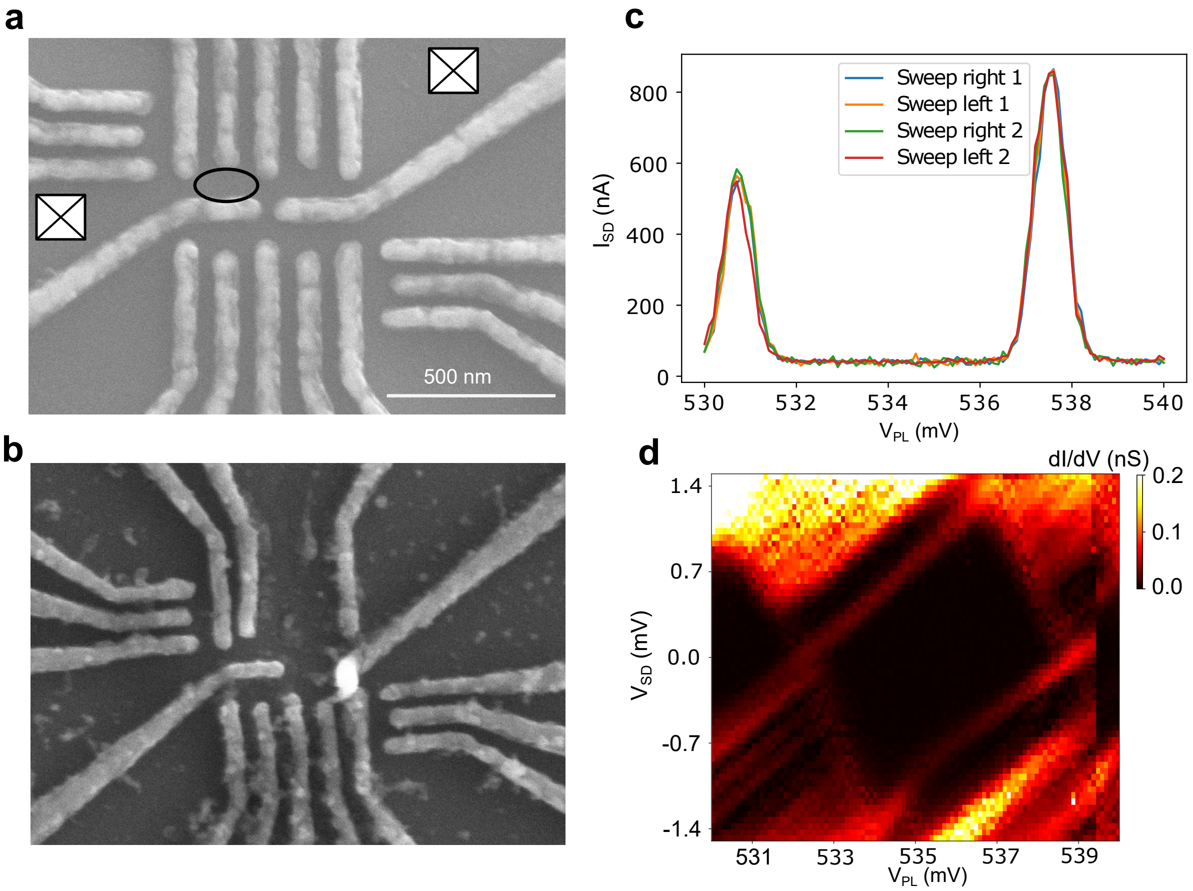

Figure 4.1: SEM and data of the first 6777 sample. a) SEM image of the device consisting of two DQDs facing each other and one charge sensor on each side. The gates were made of Al and had a width of 70 nm Al. We managed to form a quantum dot in the black circled area and measured transport through the two marked ohmic contacts (white boxes). b) SEM image of the device after unbonding and annealing. The central part of the gate layout is completely blown up. c) Coulomb peaks as a function of plunger gate voltage. Sweeping left and right in a small range shows that the peaks are stable. d) Coulomb diamond acquired sweeping the gate and bias voltage. The derivative of the current is depicted. This was the first stable Coulomb diamond in hole gases we observed in our group.

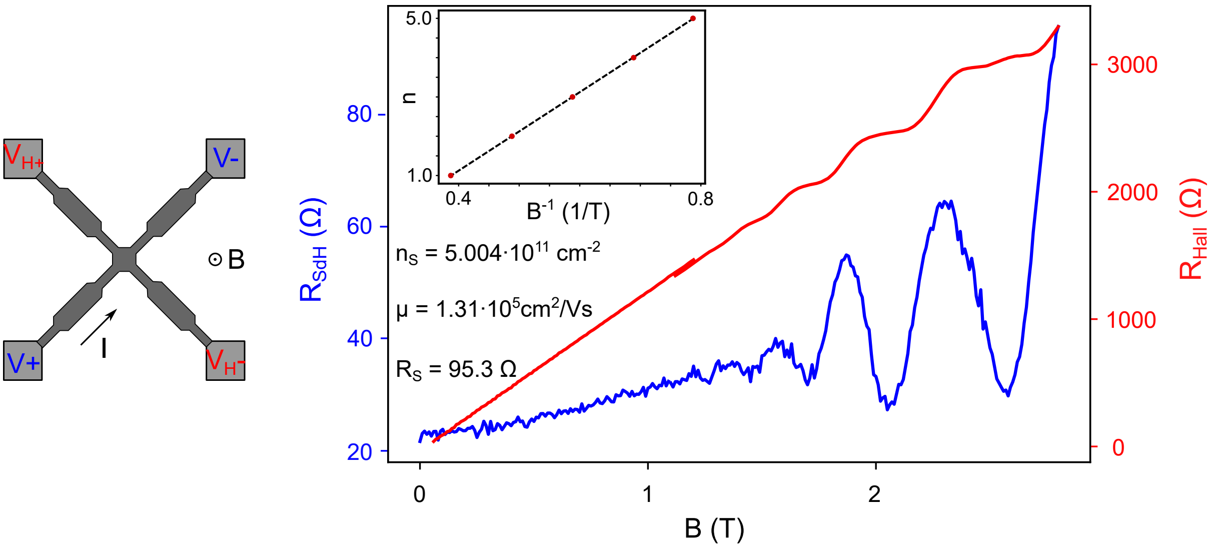

Figure 4.2: Left: the sample layout for mobility measurements on the 6777 series. The dark gray part represents the mesa while the light gray squares are the ohmic contacts. The longitudinal voltage drop is measured at $V_\pm$ while the Hall voltage is measured at $V_{H\pm}$. The magnetic field is applied in the out-of-plane direction. Right: longitudinal (blue) and transversal (red) resistance showing clear signatures of the Shubnikov de Hass as well as the quantum Hall effect, respectively. The extracted charge carrier density and mobility are reported in the figure. The inset also shows the filling factor as a function of 1/B. The red dots correspond to integer n and the dashed line is a linear fit.

not reliable enough. With such a great number of gates I was hoping for enough of them to be usable in order to form at least one quantum dot. Indeed in one sample that I called "Belle" I managed to see single hole transport features (Fig. 4.1c) and measure a beautiful Coulomb diamond (Fig. 4.1d) in June of 2017. At that time I believe there was no quantum dot in Ge hole gases published, so it was a big deal for us. I characterized the device in the Heliox (introduced in a later section and Fig. 4.13) at 300 mK and had to fight quite a bit with the switchyness of the device. Before loading it into a dilution refrigerator we therefore thought about annealing the sample to passivate potential charge traps in the oxide as was routinely done in Twente for Si devices [81]. As is clear from Fig. 4.1b, this was not a good idea as most of the gates were obliterated by the annealing step.

Motivated by the success of the first quantum dot, however, we decided to load a replica of "Belle" into one of our cryostats. The sample "Cecilia", however, featured very leaky gates, which made it impossible to tune. The design of the mesa, on the other hand, allowed basic Hall bar measurements to be performed and we decided to characterize the sample at least in terms of mobility (see Fig. 4.2). The results of the mobility measurements are summarized in Fig. 4.2. We applied a current between diagonally opposite contacts of the sample and measured the voltage drop along the current contacts (V_{SdH}) and also perpendicular to the current direction (V_H). The longitudinal Shubnikov de Haas resistance $R_{SdH} = \frac{V_{SdH}}{I}$ (blue) starts to obviously oscillate above 1.5 T. At the same time the Hall resistance $R_H = \frac{V_H}{I}$ (red) starts to show plateaus when R_{SdH} is in a local minimum in line with the QHE. We extract a density $n_S = 5.004e11$cm^{-2}, a mobility $\mu = 1.31e5$cm^2/Vs and a sample resistance of $95.3\,\Omega$. The inset further shows the linear dependence of the integer filling factor n as a function of $1/B_n$ and confirms the linear relationship between the two. The mobility results were encouraging and confirmed that the wafers are of good quality for transport. However, we quickly realized that the presence of a doping layer often leads to an unexpected and not well understood turn-on after pinch off. Therefore, we abandoned this wafer series and focused our efforts on undoped heterostructures.

4.2 The 10440 series: 2017-2018

The first undoped heterostructures arrived in summer of 2017. Undoped structures in Si/SiGe always require doping in order to obtain ohmic contacts. However, because of the fermi level pinning of most metals in Ge, ohmic contacts can be easily fabricated. Or at least that is what we thought. Indeed, the recipe we use for ohmic contacts was developed on these wafers mostly by Andrea Hofmann and Maksim Borovkov. They realized that by removing the native silicon oxide via argon milling and then evaporating the metal at an angle without breaking the vaccum resulted in reproducible and low resistance ohmic contacts. However, these heterostructures were anything but stable and gating was very troublesome. Only in late summer of 2018 we managed to obtain a quantum dot. Unfortunately, by that time quantum dots, double quantum dots, single qubits, two qubit gates and superconductivity in Ge had all been demonstrated, albeit not yet officially published. It was clear that Ge is a promising material but that the quality of our heterostructures was far from being competitive in the field. This started to change with the 10660 series.

4.3 The 10660 series: 2019-today

The 10660 series was grown in Como after a thorough cleaning of the germane and silane lines and a replacement of the germane bottle. It was immediately clear that this material batch was of much higher quality than the previous ones. Here we also investigated several different quantum well shapes, thicknesses and growth parameters. The most noteworthy wafers are the 10660, the 10662 featuring a parabolic quantum well, and the 10667. A schematic and a bandstructure simulation in NextNano is depicted in 4.4. We also outsourced the acquisition of TEM images of the wafers to the group of Jordi Arbiol which can be seen in Fig. 4.3.

From Hall bar measurements similar to the 6777 series we extracted the densities and mobilities of all the wafers which are depicted in Fig. 4.5. For all the wafers we found that at $V_{TG} = 0$ a charge carrier density was present which meant we could operate these wafers in depletion mode. The 10660 wafer had the highest mobility peaking at around $100\,000$ cm^2/Vs at a density of $n_S = 0.9 \times 10^{12}$cm^{-2}. The

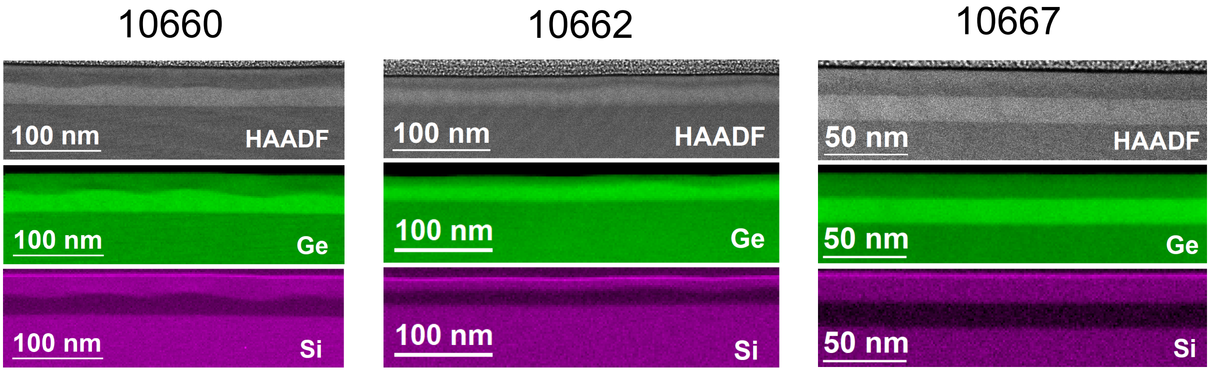

Figure 4.3: TEM images of the 1066x series. Left: The 10660 wafer displays a rather wavy upper barrier and we, therefore, did not expect it to show a high mobility, but it turned out to be one of the more successful heterostructures. Middle: The 10662 parabolic QW was also rather wavy. Here, however, the mobility reflected this. Right: the 10667 wafer looks very regular in the TEM and we would have expected it to perform better than the 10660. The growth parameters of this wafer became the standard for the next generation of wafers because of its sharp interfaces.

parabolic 10662 wafer features a rather low mobility which saturates at $8000\,\mathrm{cm}^2/\mathrm{Vs}$. The 10667 wafer, on the other hand, exhibits a slightly higher mobility than the 10662, but lower than the 10660.

The next chapter covers the measurements performed on these wafers and introduces all the building blocks necessary for a singlet-triplet qubit.

4.3.1 Double quantum dots and signatures of Pauli Spin Blockade

The first sample of the 10600 series I measured was from the parabolic 10662 wafer. We opted for a large amount of tunability which can be seen in the device design in Fig. 4.6 with a total of 4 plunger gates and an additional accumulation gate. As we soon realized the second gate layer with the accumulation gate was unnecessary as there was a charge carrier density in the QW without the need for any gate voltage. We therefore used the devices in depletion mode. The upper and lower plunger gates were always swept in pairs (left and right, respectively). As the voltage needed to define quantum dots was rather large we decided to not sweep them too often as this would decrease gate stability. We learned that fixing them at a certain voltage over longer periods of time was beneficial. The barrier gates on the other hand required only a comparably small voltage to define quantum dots and we, therefore, preferred sweeping those. Single quantum dots could be easily defined as is clear from the left and right plots in Fig. 4.6. In Fig. 4.7 we plot a series of gate vs. gate scans taken with different center barrier gate voltages V_{CB}. The stability diagrams clearly show the typical DQD features we expect from the capacitance model (chapter 2). At high tunnel coupling (low V_{CB}) the dots are so coupled that they behave more like a large single quantum dot with diagonal charge transition lines. Increasing V_{CB} (lowering the tunnel coupling) decouples the dots and we obtain the characteristic honeycomb-like pattern.

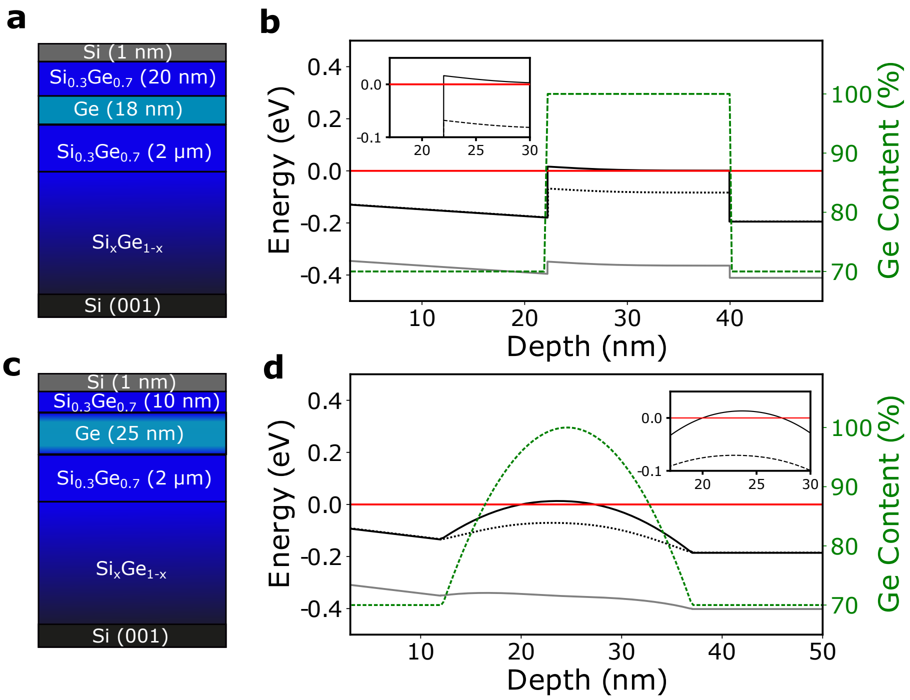

Figure 4.4: a) Layer stack of the 10660 and 10667 wafer. The Ge QW is 18 nm thick and separated by a barrier of 20 nm from the surface. A thin sacrificial layer of Si protects the sample from excessive oxidation. b) Nextnano simulation of the band-structure with small negative gate voltage applied to the top of the structure. The green dashed line marks the Ge content. The black solid (dashed) line represents the HH (LH) band energy. The red solid line is the Fermi level. The gray dashed line marks the split-off band. The inset shows a zoom in on the upper edge of the QW and highlights the region where holes are accumulated. c) Layer stack of the PQW of wafer 10662. The QW is 25 nm thick and the Si content inside is varied to produce a parabolic confinement potential for HH. d) Nextnano simulation of the PQW. The HH band is pulled above the Fermi energy in the middle of the QW as highlighted by the inset. This ensures that the hole gas is far away from interface defects.

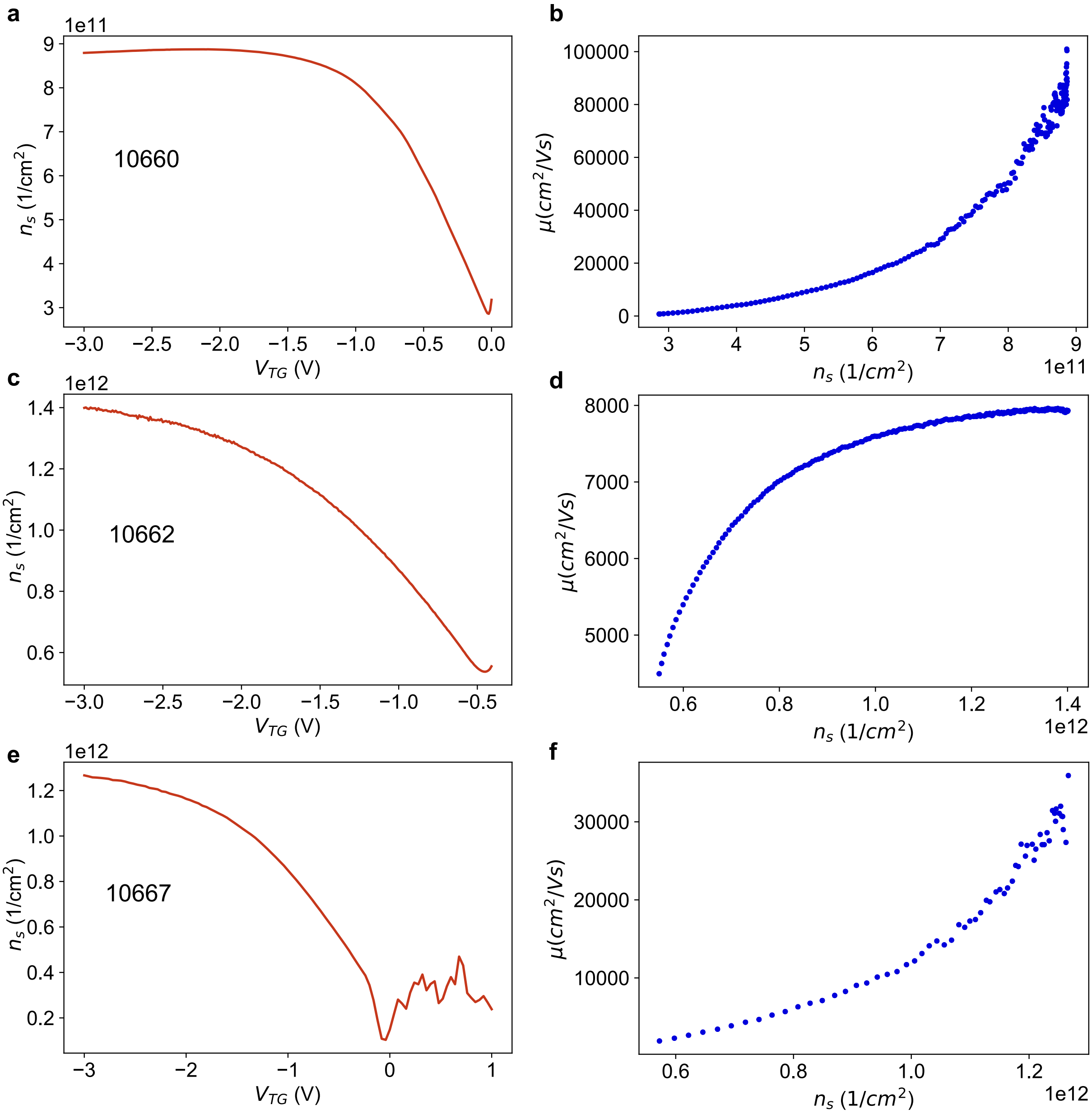

Figure 4.5: Charge carrier densities and mobilities of the 1066x wafer series. a) The density of the 10660 wafer saturates just below $1e12\text{cm}^{-2}$. b) We extracted a mobility that peaks at almost 100000 showing the high quality of this wafer. c) In the parabolic 10662 wafer we extracted a higher density than in the 10660. d) The mobility saturates quickly at 8000 suggesting a large number of scattering centers. e) The density of the 10667 wafer is exactly in between the 10660 and 10662. f) Also the mobility lies in between the other two wafers and reaches a value of 30000 at high densities.

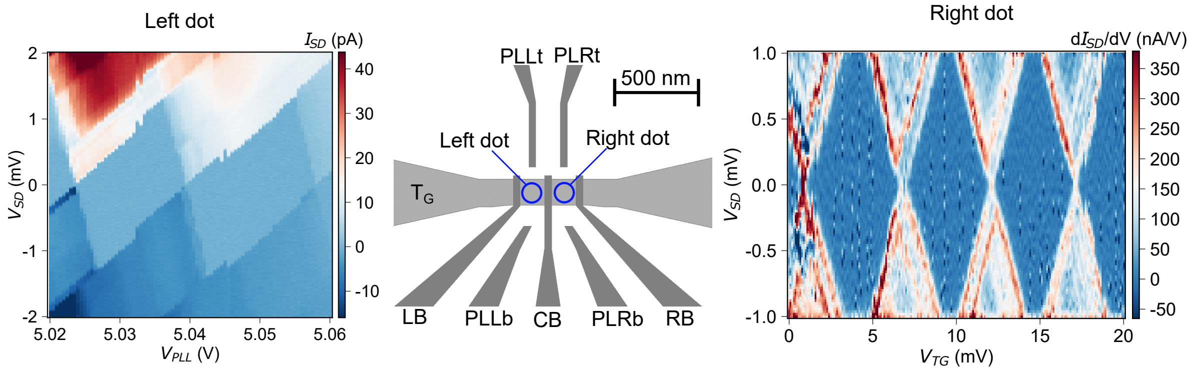

Figure 4.6: 10662 sample layout and single quantum dots. Left: V_{SD} as a function of left plunger gate voltage with $V_{RB} = 0$. PLLt and PLLb are at the same voltage denoted V_{PLL}. The gate combination formed a single quantum dot on the left side with regular Coulomb diamonds clearly visible. Middle: Device layout. We opted for a large amount of tunability with 2 dedicated plunger gates for each quantum dot. A top gate (T_G) served as charge accumulation gate which was not necessary as the sample were conductive without any top gate voltage. Right: V_{SD} as a function of V_{TG} with $V_{LB} = 0$ (in fact broken as this measurement was taken in a second cooldown). The gate combination resulted in quantum dot on the right side with very regular Coulomb diamonds appearing.

At very high center barrier voltage transport is more and more limited to the triple points as in Fig. 4.7c.

4.3.2 g-factor extraction through Kondo effect

During the tuning of the sample we stumbled upon co-tunneling and the Kondo effect. These effects arise when the tunnel barriers of a quantum dot are very transparent. The Kondo effect was first measured by DeHaas in 1934 when he discovered a resistivity minimum in Gold. It was only in 1964 that Kondo came up with a theoretical explanation of such a minimum [82]. In fact, he hypothesized the presence of magnetic impurities in metals to be the reason for an increase in resistivity below a certain temperature. In his explanation, magnetic impurities are screened by the surrounding conduction electrons which causes an increased density of states close to the impurity. This density of states appears at the Fermi level and is very effective in scattering electrons with a similar energy. As these electrons are the ones that contribute to the conductivity of a metal this scattering causes an increase in the resistance [82]. The ground state of this density of states is pinned at the Fermi level and is a many body singlet state. In quantum dots the Kondo effect can be observed as well since an unpaired spin can be trapped and act as a magnetic impurity [83]. For the Fermi sea in the leads to "see" this impurity the tunnel barriers have to be very transparent. However, contrary to metal pieces, in quantum dots the resistivity decreases at the Fermi level in the presence of the Kondo effect. The reason is that the increased density of states at the source and drain side allows electrons (or holes) to flow through the quantum dot (see Fig. 4.9a). In Fig. 4.9b we plot the derivative of the measured current in a coulomb

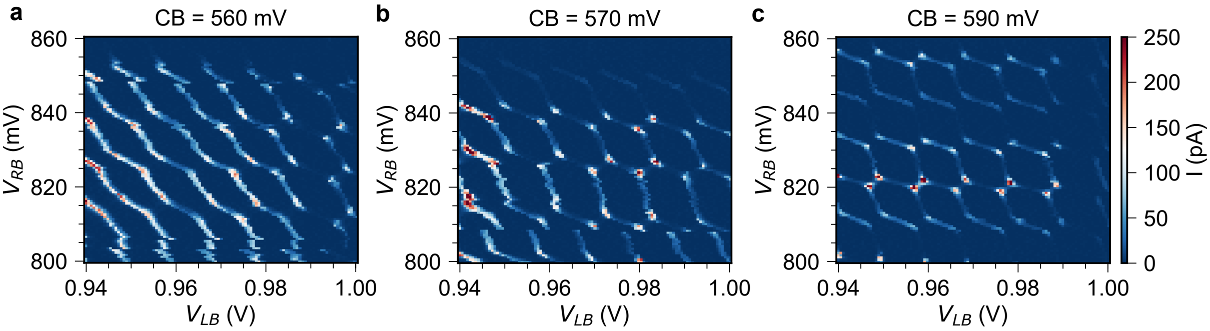

Figure 4.7: Current measured through the DQD at different center barrier voltages. a) $V_{CB} = 560\,\text{mV}$. The tunnel coupling between the dots is so large that they behave almost like a large single dot. b) $V_{CB} = 570\,\text{mV}$. The typical honeycomb pattern starts to emerge as the tunnel coupling is lowered. The overall tunneling rate still allows to measure the transitions of the left and right barrier. c) $V_{CB} = 590\,\text{mV}$. As the tunnel coupling is further lowered transport starts to take place mainly at the triple points.

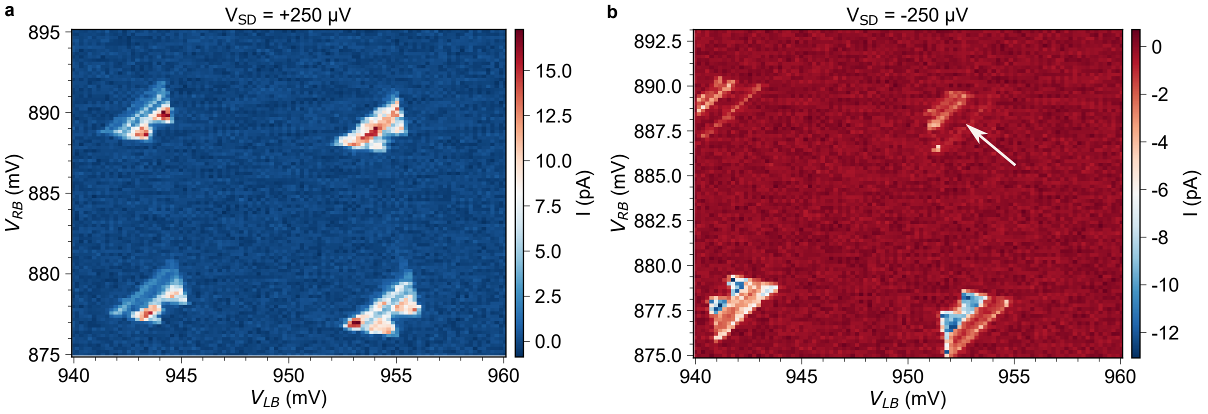

Figure 4.8: Bias triangles with positive and negative bias. a) $V_{Bias} = 250\,\mu\text{V}$. b)$V_{Bias} = -250\,\mu\text{V}$. The arrow points to a pair of bias triangles where the base line transport is suppressed. Such feature is a signature of Pauli spin blockade.

diamond in the left quantum dot of Fig. 4.6. We can clearly observe an increase of dI/dV at zero bias corresponding to the alignement of the Fermi levels of source and drain. At higher bias also more co-tunneling features can be observed but we will focus only on the feature at zero bias. Fig. 4.9c displays a slightly larger region of the stability diagram measured with a Stanford Research Lock-In amplifier. Here, we directly measure differential conductance and we see that in two adjacent diamonds there is a feature at zero bias. While this deviation from the even-odd filling is peculiar, it is known that for holes, especially at large hole numbers, this filling rule is not always observed.

In order to prove that this zero bias conductance peak is indeed arising from the Kondo effect we recorded the peaks at different temperatures. In fact, only the Kondo peak should vanish with temperature while all other conductance features should be enhanced with temperature. We fixed the gate voltage of the left barrier gate at 1.675 V for the left diamond and at 1.684 V for the right diamond and increased the temperature of the mixing chamber in the fridge. As expected in Fig. 4.10a and b we see the peak vanishing for higher temperatures in both diamonds confirming their Kondo origin.

At this point we can harvest the Kondo peak to extract information about the g-factors. Indeed, as the origin of the increased density of states is magnetic, by applying a magnetic field we are able to split the Kondo peak in a spin-up and a spin-down component (see Fig. 4.11a). The splitting is equal to the Fermi energy $\Delta E_Z = g\mu_B B$ and, hence, proportional to the effective g-factor and the applied magnetic field. We therefore have the means to extract the g-factor anisotropy for our hole system. First we sweep the magnetic field in the in plane direction ($B_{||}$) and record the evolution of the peak in the left diamond, as here the signal was a bit larger. The resulting map is displayed in Fig. 4.11b. The black dashed line is a fit to $\Delta E_{Z||} = g_{||}\mu_B B_{||}$, with $g_{||} = 0.2$, a value that is comparable to the commonly reported values in literature. In a next step, we fix the magnetic field at 600 mT and rotate it from in-plane to out-of-plane. The resulting splitting as a function of the magnetic field angle θ is plotted in Fig. 4.11c and the dashed line is a fit to the Zeeman splitting with $g(\theta) = \sqrt{(g_{||}\cos(\theta))^2 + (g_{\perp}\sin(\theta))^2}$ and we extract $g_{\perp} = 6.2$. The anisotropy $g_{\perp}/g_{||} = 30$ is a confirmation that our holes are of mainly HH character but that a considerable mixing with the LH component is present as the theoretical value of $g_{\perp} \approx 15$ is not reached. Another factor for the g-factor reduction is the leaking of the wavefunction into the SiGe barrier layer. Nevertheless, such a large g-factor in the out-of-plane direction is attractive for spin qubit implementations as far smaller fields are required to obtain a considerable spin splitting.

4.3.3 Charge sensing

We carried out this charge sensing experiment in the small probe of Smurf. The setup is basically identical to the 4 K-setup but we are able to cool down the sample to 20 mK. The wafer we used was

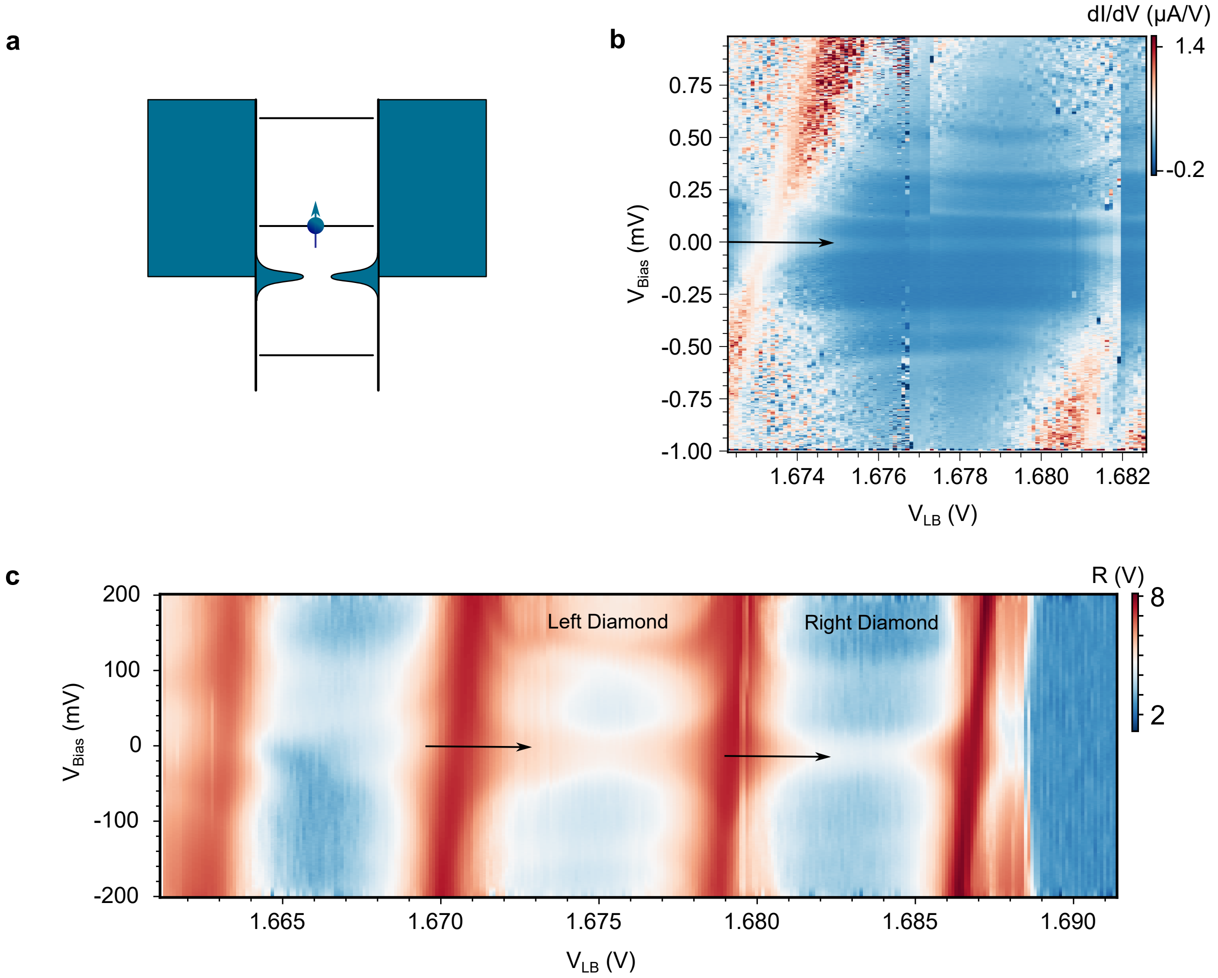

Figure 4.9: a) Schematics of the Kondo effect for a hole QD. The unpaired hole spin in the quantum dot is screened by the charges in the leads and causes a density of states to appear at the Fermi level. b) Derivative of the current through a quantum dot in the high tunnel coupling regime. The Kondo peak is visible as a line of increased conductivity pinned at 0 bias. Several other cotunneling lines appear at larger bias. c) High resolution Lock-in measurement showing the differential conductance of two adjacent Coulomb diamonds exhibiting a Kondo peak. This unexpected appearance of Kondo peaks in adjacent diamonds can be attributed to a deviation from Hund's rule.

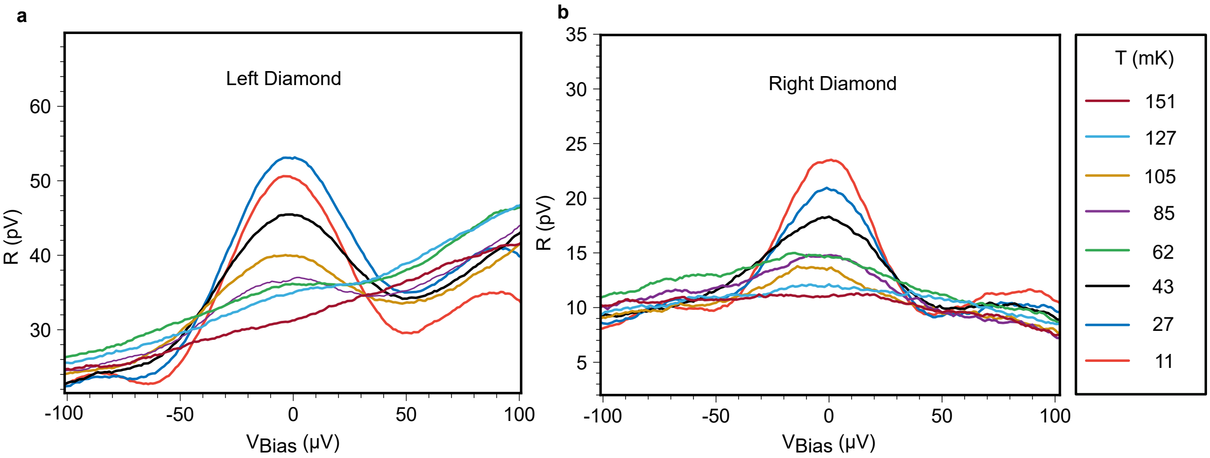

Figure 4.10: Temperature dependence of the Kondo peak. In both diamonds (a Left and b Right) the Kondo peak vanishes at higher temperatures. Any other peak should increase with temperature as thermal broadening increases the current. This confirms the Kondo nature of the two observed peaks.

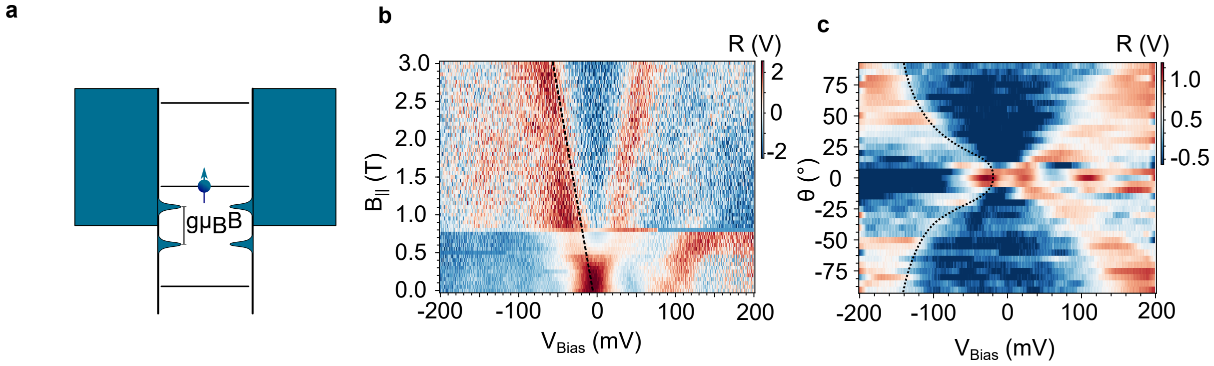

Figure 4.11: Kondo effect in a magnetic field. a) Schematics of the splitting of the Kondo peak with applied magnetic field. The Kondo peak splits according to the Zeeman energy. b) Differential conductance as a function of bias voltage and parallel magnetic field. Clearly, the Kondo peak splits with B. The dashed line is a fit to $g_{\parallel}\mu_B B$ and yields $g_{\parallel} = 0.2$. c) Differential conductance as a function of bias voltage and magnetic field direction at $B = 600\,\mathrm{mT}$. The black dashed line is a fit to $g(\theta)\mu_B B$ with $g(\theta) = \sqrt{(g_{\parallel}\cos(\theta))^2 + (g_{\perp}\sin(\theta))^2}$. We extracted $g_{\perp} = 6.2$.

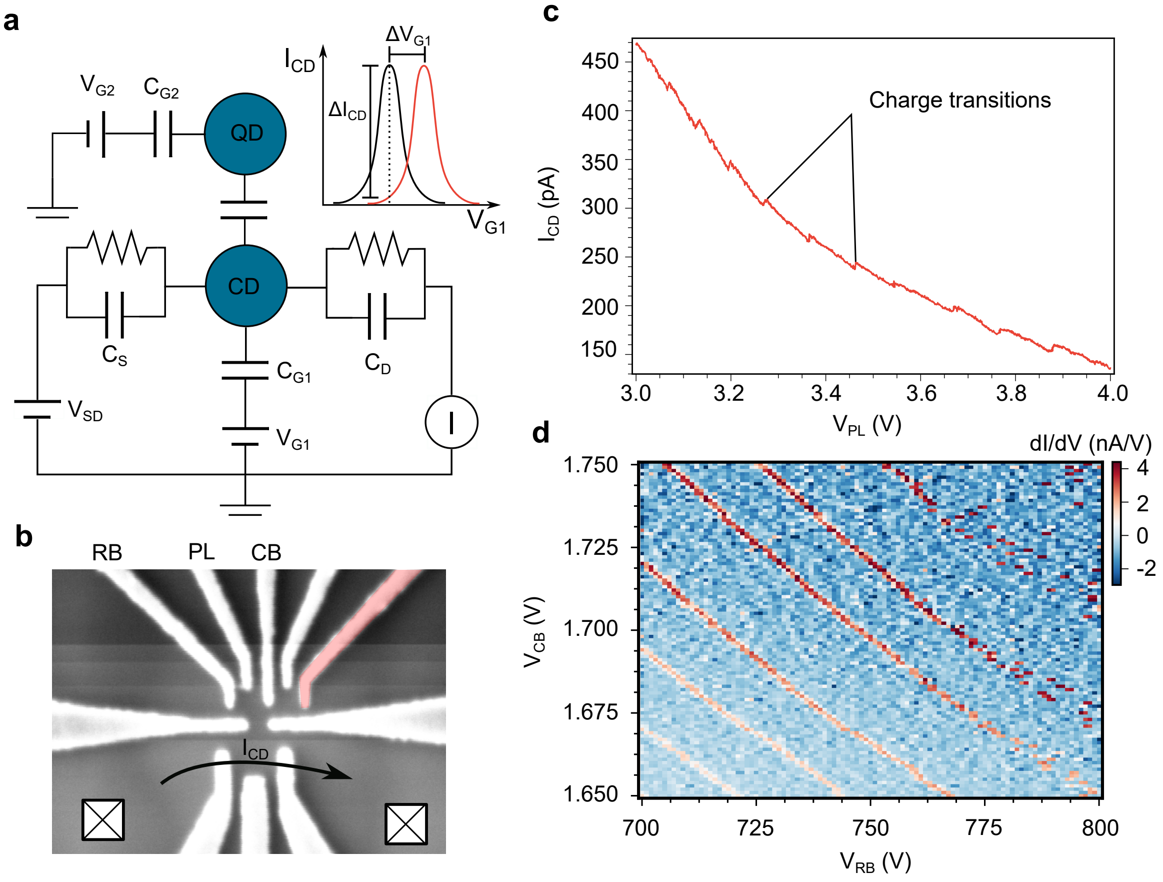

Figure 4.12: Charge sensing. a) Schematics of the circuit. The charge detector (CD) is connected to source and drain and controlled by a gate voltage V_{G1}. A QD is capacitively coupled to the CD and is itself controlled by a gate V_{G2}. Inset: The charges in the QD act as a gate voltage on the CD and shift its Coulomb peaks by an amount ΔV_{G1}. Depending on the steepness of the Coulomb peaks the current change ΔI_{CD} can amplify the charge shift significantly. b) SEM image of the device. The gate marked in red was broken. Hence, we could only form a single quantum dot in the upper part and sense it with the CD in the lower part. c) Current through the charge sensor as a function of the plunger gate voltage of the dot. Charge transitions appear as abrupt steps in I_{CD}. d) Gate vs gate plot of the QD while recording I_{CD}. Here we report the derivative of the current and clearly see the charge transitions. The current through the QD was already too small to be measured.

the 10667 and an SEM of the device is depicted in Fig. 4.12b. The gate marked in red was not working which meant we could only form a single QD in the upper part. The principle of charge sensing can be explained by the schematic in Fig. 4.12a. It is very similar to a DQD picture with the difference that the QD of interest is only capacitively coupled to the charge detector (CD). The charges in the QD act as an additional gate voltage on the CD and can shift its Coulomb peaks. This method is particularly useful when steep Coulomb peaks are available in the CD and a variation in the QD charge leads to a big change in the current through the CD. For example in Fig. 4.12c we reported the current through the charge detector (I_{CD}) as a function of the plunger gate voltage V_{PL} of the QD. Charge transitions in the QD can be observed as steps in I_{CD} that at first might look like switches. But also in Fig. 4.12d, in a gate vs gate plot, one can observe the charge transitions in the derivative of I_CD as diagonal red lines. for larger gate voltages the diagonal lines become more and more switchy as a result of slow tunneling times. Basically, the tunneling times become of the same order of magnitude as the sweep rate of the gates.

The charge sensing was a rather straight forward experiment but it required us to adapt the design to incorporate the horizontal separation gates in order to control the coupling between CD and QD. Once this was working it was only a matter of increasing the voltage on the plunger gate until no current through the dot could be measured anymore. That is typically also the region where the charge detector becomes sensitive to the transitions in the dot. Having learned how to perform charge sensing in DC we now look at how to read out at higher frequencies with reflectometry.

4.3.4 Reflectometry

The measurements in this section were carried out mostly by Oliver Sagi under my supervision. The setup used here is the same as for the 6777 series the Heliox equipped with a reflectometry circuit. The complete setup is schematically depicted in Fig. 4.13a. The reflectometry circuit consists of an attenuated excitation line, a directional coupler fixed at the 300 mK stage, an LC circuit mounted on the PCB, a superconducting cable connecting the output port of the directional coupler to a room temperature rf-amplifier and an ultra high frequency lock-in (UHFLI) amplifier from Zurich Instruments. The excitation line is attenuated by 20 dB at the 1 K plate and further two 0 dB attenuators serve as thermal anchors. This ensures that thermal noise from room temperature is sufficiently attenuated to not detrimentally affect the device. Fig. 4.13b displays a schematic of the device we used for testing. It consists of two single quantum dots separated by the gates SepL and SepR. The gates LBb (LBt) and RBb (RBt) control the left bottom (top) and right bottom (top) tunnel barrier, respectively. The pluger gate PLb (PLt) controls the levels inside the lower (upper) quantum dot. The reflectometry circuit is connected either to a gate, in our case PLt, or to an ohmic contact to allow gate or ohmic reflectometry, respectively. The schematic of the circuit is depicted in Fig. 4.13c. L represents the inductance of the board. We can choose from 4 values: 390 nH, 560 nH, 890 nH, 1200 nH. Each of these inductors has a parasitic capacitance C_P to ground and the combination of L and C_P determines the resonant frequency of the cirucit $f = \frac{1}{2\pi\sqrt{LC}}$. The sample is modeled as a capacitance C_S to ground in parallel with a resistance R_S.

The principles of reflectometry are very nicely explained in Josip Kukucka's thesis and here only the main points are highlighted. The interested reader should refer to his work for further details.

The reflection coefficient is defined as

$$\Gamma = \frac{Z - Z_0}{Z + Z_0}$$

where Z_0 is the impedance of the coaxial line, typically 50 Ω, and Z is the impedance of interest and is given by the combination of L, C_P, C_S and R_S. When $Z = Z_0$ no reflection occurs and the circuit is said to be matched.

Gate reflectometry attempt

Gate reflectometry is an attractive sensing technique for spin qubits as it does not require any additional sensing dot [84]. The appropriate confining gate is simply connected to the reflectometry circuit and is sensitive to capacitive changes in the hole gas underneath. For qubit devices based on self-assembled structures on the surface of a semiconductor, this approach is feasible due to the large lever arm which greatly increases the sensitivity [35]. In 2 dimensional hole gases buried below the surface such an approach is much more challenging and we will see that in our case it failed to produce the desired result.

To test gate reflectometry we bonded one of the 4 LC-resonators to a plunger gate (PLt) of the device. We first compared the reflected signal to the one without sample at room temperature (Fig. 4.14a). Indeed the presence of the sample changed the shape of the reflected signal as one resonance disappeared. At 300 mK we also clearly see that one resonance is missing (Fig. 4.14b). Bonding a gate to the resonator changes the parasitic capacitance to ground since there will be cross capacitances between adjacent gates. Unfortunately this seems to lead to a complete loss of the resonance as the resonant frequency might be even shifted below the MHz region ($2\pi f = \frac{1}{\sqrt{L(C_P + C_S)}}$). Ultimately, this hindered any experiment involving the detection of the reflectometry signal to infer properties of the device as there is no tuning knob to achieve matching in situ. One workaround demonstrated in Copenhagen [85] is to increase the impedance of any leakage path for the rf-signal. A large parallel impedance to ground favors the rf signal to follow the path of least impedance and, therefore, produce the wanted response. We did not implement this change on the PCBs so far.

Ohmic reflectometry

A more tunable way of performing reflectometry is through a connection to an ohmic contact of a sensor dot [86]. In this configuration the reflected signal is sensitive to changes in the resistance of the device. This is particularly advantageous for gate defined QDs as the high level of tunability allows one to

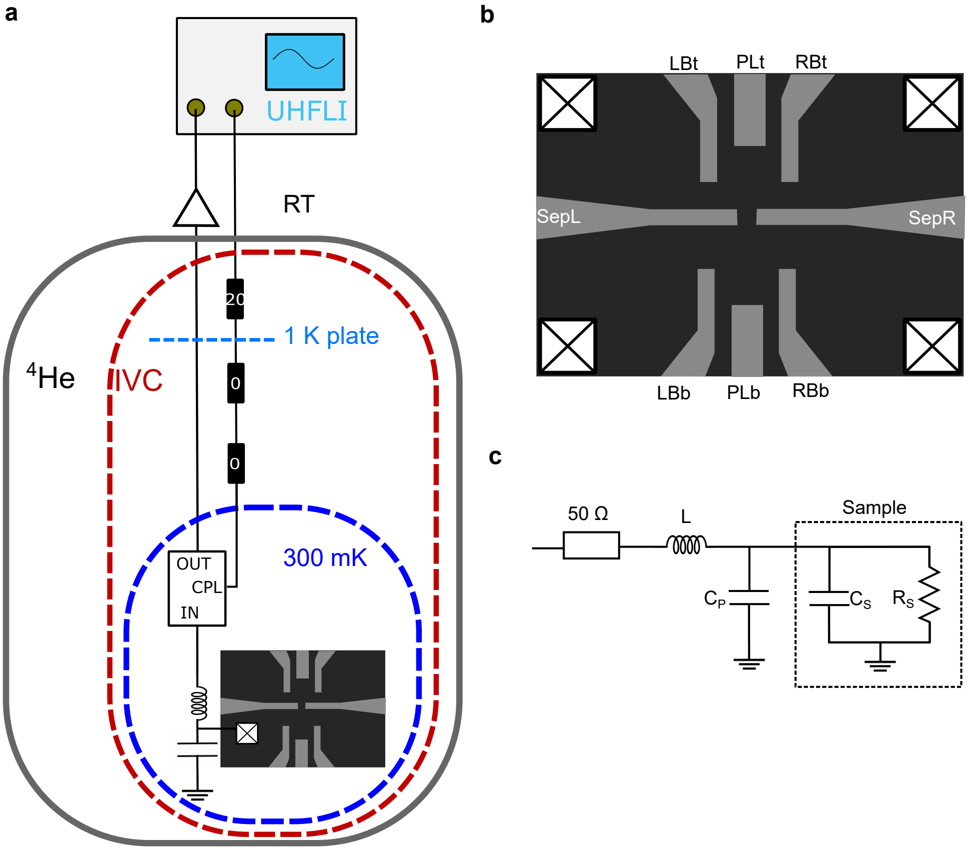

Figure 4.13: Heliox and reflectometry setup. a) The heliox is a ^{3}He cryostat capable of reaching a sample temperature of 300 mK. As the 4 K probe, it is inserted in a liquid ^{4}He dewar where helium is pumped through a small needle valve. The resulting underpressure cools the ^{4}He to about 1.2 K. This temperature is sufficient to liquify the ^{3}He encapsulated in a closed circuit. The temperature of the liquid ^{3}He can be lowered by pumping the vapour above the liquid. A directional coupler mounted on the back of the sample holder allows ohmic and gate reflectometry. The signal is supplied by the UHFLI, attenuated at various stages, reflected at the sample and routed back to the UHFLI. The rf-amplifier is situated at RT because of a lack of space in the probe. b) Schematics of the sample used for reflectometry. It consists of two single quantum dots arranged in a face-to-face architecture. We connected the reclectometry circuit (c) either to an ohmic contact or to a gate. c) Schematics of the reflectometry circuit. The signal is supplied from a 50 Ω coaxial line. The inductor L and the parasitic capacitance C_P form an LC-resonator. The sample capacitance C_S and resistance R_S alter the resonant condition of the LC-circuit.

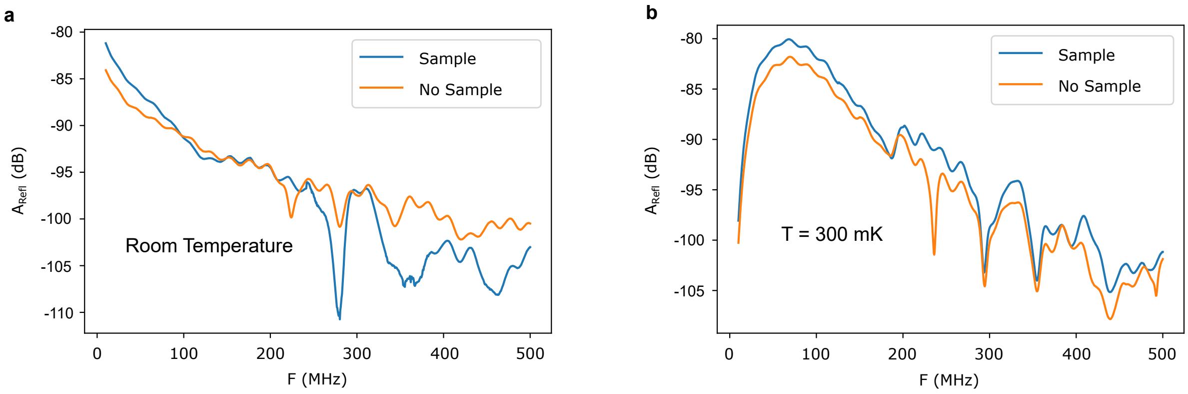

Figure 4.14: Gate reflectometry attempt. a) Response of the LC-circuit with no bond to the sample (orange) and a bond to the gate (blue) at room temperature. The presence of the sample indeed changes the reflected signal. b) Same as a) but at 300 mK. The resonance at the lowest frequency (corresponding to the largest inductor) completely disappeared. Hence, gate reflectometry was not possible in this configuration.

engineer transparent tunnel barriers and tune the device to match the $50\,\Omega$ impedance of the coaxial cables. We proceeded similarly to the previous section by comparing the reflected signal at room temperature between no sample and bonded to one ohmic contact (Fig. 4.15a). Again we observed that one dip was missing. At low temperature, on the other hand, we can observe all 4 dips once the device is tuned into the dot regime (Fig. 4.15a). Indeed, we observe that one dip is shifted to lower frequencies indicating an increase in total capacitance caused by the presence of the sample. The frequency with no sample connected to the circuit is $f = 250\,\mathrm{MHz}$. Therefore, knowing the inductance $L = 1200\,\mathrm{nH}$ we can extract the parasitic capacitance $C_P = \frac{1}{L(2\pi f)^2} = 0.34\,\mathrm{pF}$. From the shift in frequency between the condition with and without sample at low temperatures we can extract a sample capacitance of $C_s = \frac{1}{L(2\pi f_S)^2} - C_p = 0.27\,\mathrm{pF}$, where $f_S = 186\,\mathrm{MHz}$ is the resonant frequency with the sample connected.

After tuning the upper gates into a QD we can compare the reflected signal amplitude A_{Refl} to the measured current I. in Fig. 4.16a we plot the measured current as a function of the plunger gate voltage V_{PLt}. We clearly see that the Coulomb peaks in current are also reproduced in reflectometry and that the peaks in amplitude appear exactly on the flanks of the current peaks. We note that above 1800 mV the Coulomb peaks become very small and regular spaced. In this region the reflectometry circuit is not sensitive to resistance changes anymore and the reflected amplitude is flat. We proceeded and fixed V_{PLT} at 1430 mV, a region of high sensitivity for reflectometry, and swept the two barrier gates LBt and RBt. The resulting current, reflected amplitude and phase are plotted in Fig. 4.16b, c and d, respectively. We again observe that for low gate voltages the reflectometry circuit is sensitive to resistance changes as the current pattern is reproduced also here. At larger gate voltage both amplitude and phase are insensitive. This can be explained by considering the circuit in Fig. 4.13c and the formulas for the sensitivity. Around resonance $\omega C_{tot} R_S >> 1$ because R_S is normally high. C_{tot} is just the sum of the

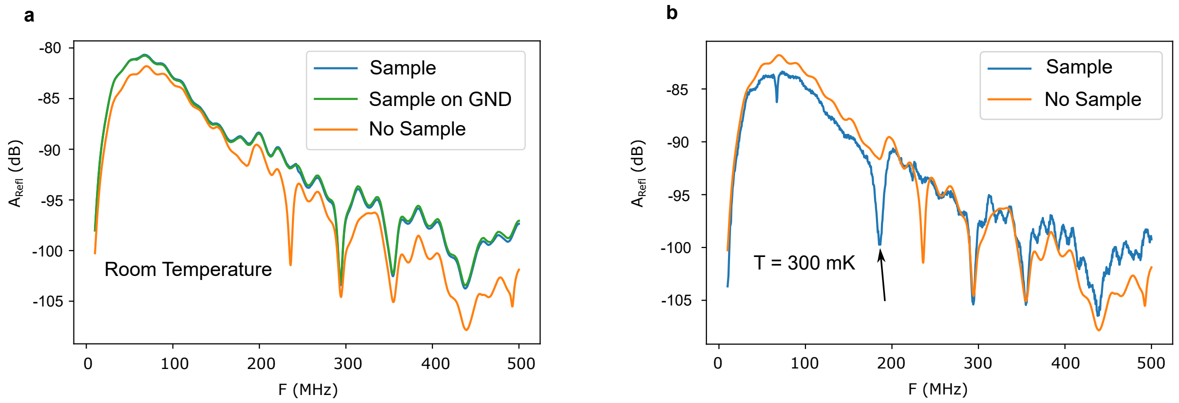

Figure 4.15: Response of the LC circuit for ohmic reflectometry. a) Including the sample into the circuit via a bond of the IC resonator to an ohmic contact changed the response of the circuit at room temperature also when the sample is grounded. b) At 300 mK we clearly observed a shifted resonance dip which allowed us to perform ohmic reflectometry.

capacitances. We define the effective resistance of the circuit as $R_{eff} = R_l + \frac{L}{C_{tot}R_S}$, where R_l is the resistance of the line. The loaded Q-factor is $Q = \frac{\sqrt{\frac{L}{C_{tot}}}}{R_{eff}+Z_0}$. The sensitivity around resonance then becomes:

$$\frac{\delta|\Gamma|}{\delta R_S}|_{\omega=\omega_0} = \frac{2Z_0Q^2}{R_S^2},$$

which shows that by having low sample resistance the sensitivity increases. This is true until the condition $\omega C_{tot}R_S >> 1$ is valid. When R_S becomes too small (few kΩ) it becomes the lowest impedance in the parallel part with the other capacitors. This lowers the overall impedance Z and hinders matching. On the other hand, if R_S becomes too big the sensitivity also decreases, so for every parasitic capacitance and inductor there is a certain window in which we can operate reflectometry and be sensitive to changes in the device resistance. The great advantage of ohmic reflectometry is, therefore, that by tuning R_S we can try to achieve the best matching conditions. Around the matching conditions small changes in R_S can be induced, for example, by an adjacent QD. The combination of reflectometry and charge sensing can give a fast and precise read-out mechanism in this configuration.

4.3.5 Conclusions about the 10600 series

This series of wafers was a great improvement over the 10400 series and allowed us to perform several preliminary measurements and characterizations necessary for the implementation of singlet-triplet qubits. We achieved double quantum dots with a high degree of tunability, measured the g-factor anisotropy through the Kondo effect, adapted our gate geometry for charge sensing and performed preliminary reflectometry characterizations. Even more, Matthias Brauns succeeded in dispersively sensing a double quantum dot with a superconducting resonator, opening the path for spin-photon cou-

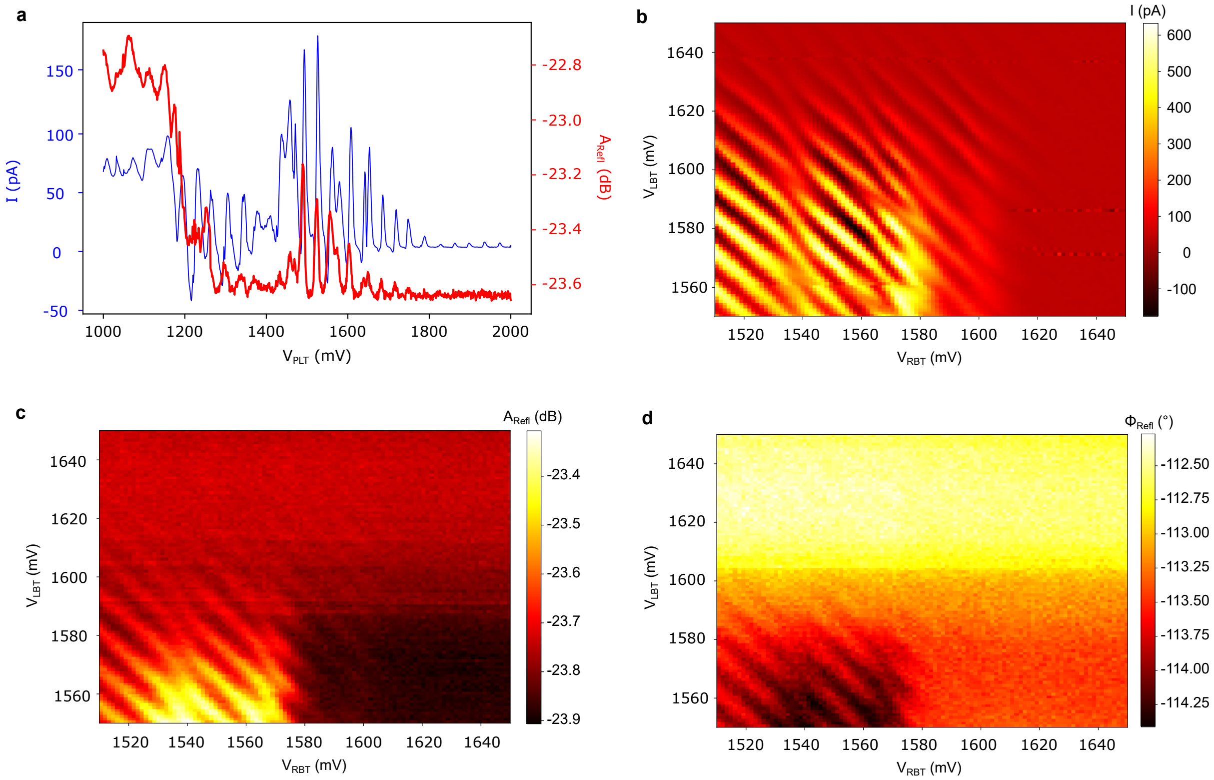

Figure 4.16: Coulomb oscillations in reflectometry. a) Comparison between current (blue) and reflected amplitude (red) of Coulomb peaks in a single QD. The peaks of the reflectometry signal appear exaclty at the flanks of the Coulomb peaks in current. b) Current as a function of left and right barrier gate voltage showing Coulomb oscillations. The pattern resembles the one of a DQD suggesting that we unintentionally formed another QD. c) Reflected amplitude of the same Coulomb oscillations as in b). The signal fades for high gate voltage as the sample resistance becomes too large. d) Phase response of the reflected signal. Similarly to c), the phase becomes less sensitive for larger gate voltages. We also note that these measurements were carried out at 1.8 K, rather than 300 mK.

pling.

4.4 The 10720 series: 2020- today

Further improvements came from the 10720 series. Here we achieved mobilities of 100k at 4K. Applying all the knowledge we gained from the previous material batches we directly fabricated a DQD with charge sensor and cooled it down in smurf. The result of this cooldown is the subject of the next chapters.

5 A hole singlet triplet qubit in Ge

This chapter is adapted from our paper with the same name recently published in Nature Materials [80]. I merged parts of the methods and supplemetary in the main text for better flow but left the overall structure the same. Moreover, the fabrication and setup parts have been discussed already in previous chapters and are, therefore, omitted. This chapter was the culmination of 3 years of work and took more than a year to complete as it was interrupted by the Corona pandemic. Luckily I managed to cool down the device 2 weeks before the first lock-down and was able to measure from home. The downside was the lack of communication with my colleagues which could have accelerated the data collection and analysis. Our main conclusion is that singlet-triplet qubits in Ge work quite well and can be incredibly fast when operated in the out-of-plane magnetic field direction. Moreover, they can be operated at extremely low fields owing to the large out-of-plane g-factors which push the T_+ and T_- states away in energy.

5.1 Overview

Spin qubits are considered to be among the most promising candidates for building a quantum processor [87]. Group IV hole spin qubits have moved into the focus of interest due to the ease of operation and compatibility with Si technology [34, 38, 39, 84, 88]. In addition, Ge offers the option for monolithic superconductor-semiconductor integration. Here we demonstrate a hole spin qubit operating at fields below 10 mT, the critical field of Al, by exploiting the large out-of-plane hole g-factors in planar Ge and by encoding the qubit into the singlet-triplet states of a double quantum dot [20, 21]. We observe electrically controlled g-factor-difference-driven and exchange-driven rotations with tunable frequencies exceeding 100 MHz and dephasing times of 1 µs which we extend beyond 150 µs with echo techniques. These results demonstrate that Ge hole singlet-triplet qubits are competing with state-of-the art GaAs and Si singlet-triplet qubits. In addition, their rotation frequencies and coherence are on par with Ge single spin qubits, but they can be operated at much lower fields underlining their potential for on chip

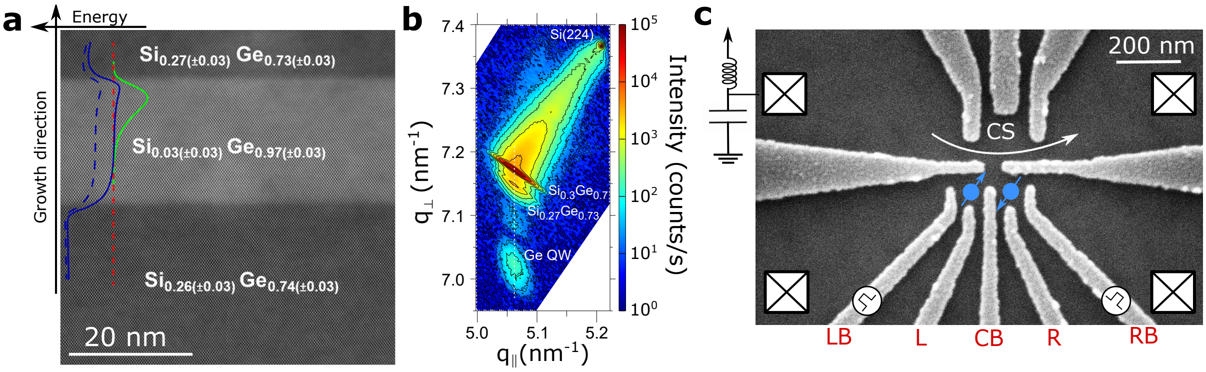

Figure 5.1: Heterostructure and gate layout. a) Atomic resolution HAADF-STEM image of the heterostructure showing sharp interfaces at the top and bottom of the quantum well. The stoichiometry of the three layers has been determined by electron energy-loss spectroscopy (see Supplementary Fig. S5). The heavy hole (solid blue line) and light hole (dashed blue line) band energies as a function of growth direction are superimposed to the picture. The red dashed line represents the fermi energy. Heavy holes are accumulated at the upper QW interface as shown by the bright green line representing the heavy hole wave function density (simulations were performed in NextNano). b) X-ray diffraction (XRD) reciprocal space map (RSM) around the Si (224) Bragg peak, present at the top right of the map. The graded buffer is visible as a diffuse intensity between the Si peak and the Si$_{0.3}$Ge$_{0.7}$ peak, while the Si$_{0.3}$Ge$_{0.7}$ peak itself corresponds to the $2\,\mu$m constant composition layer at the top of the buffer. The Ge QW peak is aligned vertically below the Si$_{0.3}$Ge$_{0.7}$ VS, as shown by the dotted line, indicating that it has the same in-plane lattice parameter, i.e. that the Ge QW is lattice-matched to the VS. The intensity just below the VS peak indicates that the true Ge content in the barriers on either side of the Ge QW is about 73%. The strain in the VS is zero, in the barrier the in-plane strain is -0.15% and in the Ge QW it is -1.18%. c) Scanning electron microscope (SEM) image of the gate layout used for this experiment. We note that without the application of any negative accumulation voltage we measure a charge carrier density of 9.7×10^{11}cm^{-2}. Secondary ion mass spectroscopy (SIMS) rules out boron doping as a source for this carrier density. We thus attribute the measured hole density to the fixed negative charges in the deposited oxide which can act as an accumulation gate [89].

integration with superconducting technologies.

5.2 Device

Holes in Ge have emerged as one of the most promising spin qubit candidates [38] because of their particularly strong spin orbit coupling (SOC) [90], which leads to record manipulation speeds [40, 91], and low dephasing rates [91]. In addition, the SOC together with the low effective mass [37] relax fabrication constrains, and larger quantum dots can be operated as qubits without the need for microstrips and micromagnets. In only three years a single Loss-DiVincenzo qubit [18], 2-qubit and most recently even 4-qubit devices have been demonstrated [35, 36, 39]. Here we show that by implementing Ge hole spin qubits in a double quantum dot (DQD) device they have the further appealing feature that operation below the critical field of aluminium becomes possible.

In order to realize such a qubit a strained Ge quantum well (QW) structure, with a hole mobility of 1.0×10^5cm^2/Vs at a density of 9.7×10^{11}cm^{-2}, was grown by low-energy plasma-enhanced chemical vapor deposition (LEPECVD). Starting from a Si wafer a 10 µm thick strain-relaxed Si$_{0.3}$Ge$_{0.7}$ virtual substrate (VS) is obtained by linearly increasing the Ge content during the epitaxial growth. The $\approx$ 20 nm thick strained Ge QW is then deposited and capped by 20 nm of Si$_{0.3}$Ge$_{0.7}$. In Fig. 5.1a we show the aberration corrected (AC) high-angle annular dark-field scanning transmission electron microscopy (HAADF-STEM) image of our heterostructure. The HAADF Z-contrast clearly draws the sharp interfaces between the QW and the top and bottom barriers. In addition, x-ray diffraction (XRD) measurements highlight the lattice matching between the virtual substrate and the QW (Fig. 5.1b). Holes confined in such a QW are of mainly heavy-hole (HH) type because compressive strain and confinement move light-holes (LHs) to higher hole energies [92]. The related Kramers doublet of the spin $S_z = \pm 3/2$ states therefore resembles an effective spin-1/2 system, $|\uparrow\rangle$ and $|\downarrow\rangle$.

In a singlet-triplet qubit the logical quantum states are defined in a 2-spin 1/2 system with total spin along the quantization axis $\mathrm{S_Z} = 0$ [20, 21]. This is achieved by confining one spin in each of two tunnel coupled quantum dots, formed by depletion gates (Fig. 5.1c). The lower gates (LB, L, CB, R, RB) form a double quantum dot (DQD) system and the upper gates tune a charge sensor (CS) dot. The separation gates in the middle are tuned to maximize the CS sensitivity to charge transitions in the DQD. An LC-circuit connected to a CS ohmic contact allows fast read-out through microwave reflectometry.

5.3 Pauli spin blockade and spin funnel

We tune our device into the single hole transport regime, as shown by the stability diagram in Fig. 5.2a where the sensor dot reflected phase signal (Φ_{refl}) is displayed as a function of the voltage on L and R. Each Coulomb blocked region corresponds to a fixed hole occupancy, and is labeled by (N_L, N_R), with N_L (N_R) being the equivalent number of holes in the left (right) quantum dot; interdot and dot-lead charge transitions appear as steep changes in the sensor signal. Fast pulses are applied to the outer barrier gates LB and RB which eases pulse calibration since the cross capacitance to the opposite dot is negligible (see also Fig. 5.8). By pulsing in a clockwise manner along the E-S-M vertices (Fig. 5.2b) we observe a triangular region leaking inside the upper-left Coulomb blocked region. Such a feature identifies the metastable region where Pauli spin blockade (PSB) occurs: once initialized in E (‘empty’), the pulse to S loads a charge and the spins are separated forming either a spin singlet or a triplet. At the measurement point M within the marked triangle, the spin singlet state leads to tunnel events, while the triplet states remain blocked, which allows spin-to-charge conversion. We repeat the experiment with a counter-clockwise ordering (E-M-S) and no metastable region is observed, as expected (Fig. 5.2a was acquired while pulsing in the counter-clockwise ordering). We thus consider the interdot line across the detuning (ϵ) axis of Fig. 5.2a equivalent to the $(2, 0) \leftrightarrow (1, 1)$ effective charge transitions. The system

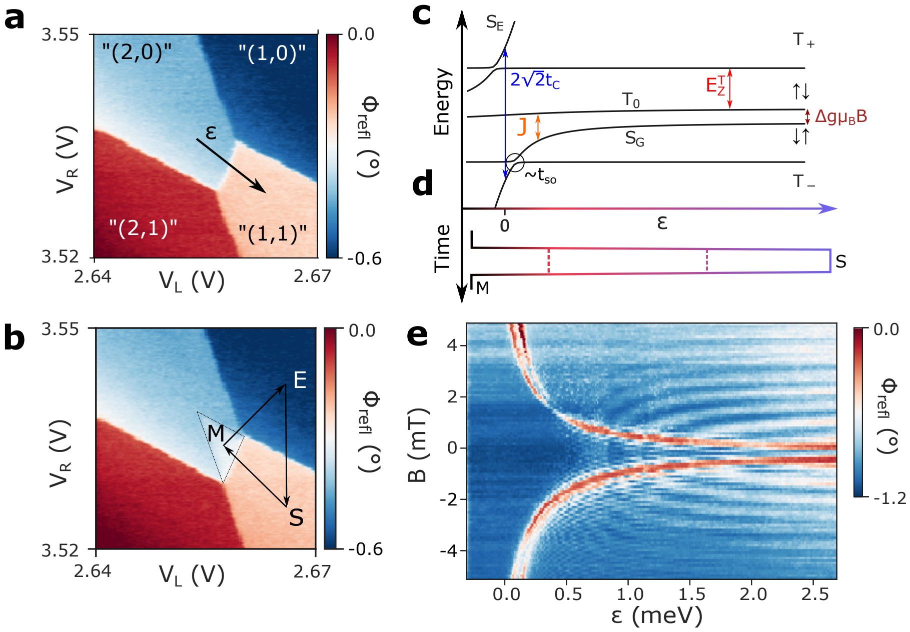

Figure 5.2: Pauli spin blockade and dispersion relation. a) Stability diagram of the region of interest. The effective number of holes in each Coulomb blocked island is defined as "(N_L,N_R)". The quotes symbolize an equivalent hole number. The real hole number is $N_L = 3$ or 4 depending on the blockade region, and $N_R = 2n$ or $2n+1$ where n is an integer (see also Fig. 5.9). We will omit the quotes in the following. The diagonal arrow highlights the detuning (ϵ) axis. bluePulses are added on gates LB and RB because of reduced cross coupling to the opposite dot. The pulse amplitudes are calibrated with respect to the stability diagram acquired with L and R (Fig. 5.9). b) Stability diagram acquired while pulsing in a clockwise manner following the arrows. The system is emptied (E) in (1,0) and pulsed to (1,1) (separation point S) where either a singlet or a triplet will be loaded. Upon pulsing to the measurement point (M) in (2,0) the triplet states are blocked leading to the marked triangular blockade region. c) Energy dipsersion relation as a function of ϵ at finite magnetic field. $\epsilon = 0$ is defined at the $(2,0) \leftrightarrow (1,1)$ resonance. At high ϵ the Hamiltonian has four eigenstates: two polarized triplets $|T_-\rangle = |{\downarrow\downarrow}\rangle$, $|T_+\rangle = |{\uparrow\uparrow}\rangle$ and two anti-parallel spin states $|{\uparrow\downarrow}\rangle$, $|{\downarrow\uparrow}\rangle$. The triplet Zeeman energy $E_Z^T = \pm\Sigma g\mu_B B/2$ (red) lifts the degeneracy of the triplets. The singlet energy $E_S = \frac{\epsilon}{2} - \sqrt{\frac{\epsilon^2}{4} + 2t_C^2}$, where t_C is the tunnel coupling between the dots, anti-crosses with the polarized triplet states due to spin-orbit interaction parametrized by t_{SO}. The singlet $S_G := S$ and triplet T_0 are split in energy by the exchange interaction $J = |E_S - E_{T_0}|$ which decreases with increasing ϵ. d) Pulse sequence adopted to acquire e). Starting from (2,0) the system is pulsed to (1,1) at varying ϵ, left evolving for 100 ns and then pulsed back to measure in M. e) Spin funnel confirming c) and the validity of assuming an effective hole number of (2,0) and (1,1). When $J(\epsilon) = E_Z^T$ the triplet signal (red) increases as a result of $S - T_-$ intermixing. Around the funnel $S - T_-$ oscillations can be observed while at higher detuning $S - T_0$ oscillations become more prominent. In order to distinguish between $S - T_0$ and $S - T_-$ oscillations we have applied detuning pulses with different ramp rates (see next chapter).

is tuned along the detuning axis from (2,0) to (1,1) by applying opposite pulses of amplitude V_{rf} on LB and RB: $\epsilon = V_{rf}\sqrt{\alpha^2_{rfLB} + \alpha^2_{rfRB}}$ (see Fig. 5.9), where α_{rfLB} (α_{rfRB}) is the rf-lever arm of the left (right) barrier gate. The DQD spectrum for a finite B field is reported in Fig. 5.2c (the triplet states T(2,0) lie high up in energy and are not shown; the model Hamiltonian is derived in the Supplemetary). We set $\epsilon = 0$ at the $(2,0) \leftrightarrow (1,1)$ crossing. Starting from (2,0) increasing ϵ mixes (2,0) and (1,1) into two molecular singlets; the ground state $S_G := S$ and the excited state S_E, neglected in the following, which are split at resonance by the tunnel coupling $2\sqrt{2}t_C$. The triplet states are almost unaffected by changes in ϵ. We define the exchange energy J as the energy difference between $S = \frac{1}{\sqrt{2}}(|\uparrow\downarrow\rangle - |\downarrow\uparrow\rangle)$ and the unpolarized triplet $T_0 = \frac{1}{\sqrt{2}}(|\uparrow\downarrow\rangle + |\downarrow\uparrow\rangle)$. At large positive detuning J drops due to the decrease of the wavefunction overlap for the two separated holes; importantly, different g-factors for the left (g_L) and the right dot (g_R) result in four (1,1) states: two polarized triplets $|T_-\rangle = |\downarrow\downarrow\rangle$, $|T_+\rangle = |\uparrow\uparrow\rangle$ and two anti-parallel spin states $|\uparrow\downarrow\rangle$, $|\downarrow\uparrow\rangle$ split by $\Delta E_Z = g^-\mu_B B$, where $g^- = |g_L - g_R|$, μ_B is the Bohr magneton and B is the magnetic field applied in the out-of-plane direction. However, as noticed later, even at large positive ϵ a residual J persists, which leads to the total energy splitting between $|\uparrow\downarrow\rangle$ and $|\downarrow\uparrow\rangle$ being $E_{tot} = \sqrt{J(\epsilon)^2 + (g^-\mu_B B)^2}$.

By applying a pulse with varying ϵ (Fig. 5.2d) and stepping the magnetic field we obtain the plot in Fig. 5.2e drawing a funnel. The experiment maps out the degeneracy between $J(\epsilon)$ and $E_Z^T = \pm\frac{\Sigma g \mu_B B}{2}$, where E_Z^T is the Zeeman energy of the polarized triplets and $\Sigma g = g_L + g_R$. The doubling of the degeneracy point can be attributed to fast spin-orbit induced $S - T_-$ oscillations [93]. At larger detuning $S - T_0$ oscillations become visible.

5.4 g^--driven oscillations

The effective Hamiltonian of the qubit subsystem is:

$$H = \begin{pmatrix} -J(\epsilon) & \frac{g^-\mu_B B}{2} \\ \frac{g^-\mu_B B}{2} & 0 \end{pmatrix} \tag{5.1}$$

in the $\{|S\rangle, |T_0\rangle\}$ basis, with $J(\epsilon)$ being the detuning-dependent exchange energy, common to all $S - T_0$ qubits. Implementations of $S - T_0$ qubits in GaAs typically harvest the local field gradient induced by the nuclear overhauser field to drive $S - T_0$ oscillations [21, 94]. Due to the near absence of nuclear spins in Si, only slow oscillations could be achieved in natural Si/SiGe structures [65]. Hence, micromagnets have been successfully used to enhance and stabilize the magnetic field gradient [66, 78]. In Si metal-oxide-semiconductor devices $S - T_0$ oscillations can be driven by spin-orbit induced g-factor differences in the two dots [67, 68] and values of 20 MHz/T have been reported. Here, similarly, we realize $S - T_0$ oscillations through g-factor differences. However, we expect a larger g^- since our holes are of mainly HH character [95, 96]. Indeed, as shown below, g-factor differences exceeding 20 GHz/T can be obtained. Pulsing on ϵ influences J and the ratio between J and $g^{-}\mu_B B$ determines the rotation axis tilted by an angle $\theta = \arctan\left(\frac{g^{-}\mu_B B}{J(\epsilon)}\right)$ from the Z-axis. For large detuning $\theta \rightarrow 90°$ corresponding to X-rotations while for small detuning $\theta \rightarrow 0°$ enabling Z-rotations.

A demonstration of coherent g^{-}-driven rotations at a center barrier voltage $V_{\mathrm{CB}} = 910\,\mathrm{mV}$ is depicted in Fig. 5.3c with the pulse sequence shown in Fig. 5.3b. The system is first initialized in (2,0) in a singlet, then pulsed quickly deep into (1,1) where the holes are separated. Here the state evolves in a plane tilted by θ (Fig. 5.3a, Fig. 5.3d). After a separation time τ_S the system is brought quickly to the measurement point in (2,0) where PSB enables the distinction of triplet and singlet. Varying τ_S produces sinusoidal oscillations with frequency $f = \frac{1}{h}\sqrt{J^2 + (g^{-}\mu_B B)^2}$ (Fig. 5.3e), where h is the Planck constant. We extract $g^{-} = 2.04 \pm 0.04$ and $J(\epsilon = 4.5\,\mathrm{meV}) \approx 21\,\mathrm{MHz}$. We attribute the large g^{-} to the different QD sizes which directly affects the HH-LH splitting determining thus the effective g-factor [92]. In addition, the different QD charge occupation can lead to further g-factor differences [95, 98] We approach frequencies of $100\,\mathrm{MHz}$ at fields as low as $3\,\mathrm{mT}$. We observed similar values of g^{-} in the range of 1.0 to 2.7 in two additional devices with similar gate geometries (see Fig. 5.13). Fig. 5.3f shows the extracted singlet probability $\mathrm{P_S}$ at different magnetic fields. The black solid line is a fit to $\mathrm{P_S} = A\cos(2\pi f \tau_s + \phi)\exp\big(-(t/T_2^*)^2\big) + C$, where T_2^* is the inhomogeneous dephasing time. $\mathrm{P_S}$ only oscillates between 0.5 and 1 as a direct consequence of $J(\epsilon = 4.5\,\mathrm{meV}) \neq 0$ and the tilted rotation axis. One would expect an increase in the oscillation amplitude with higher magnetic field. However, at large ΔE_Z the T_0 state quickly decays to the singlet during read-out due to relaxation processes [97], reducing the visibility as is clearly shown by the curve at $2\,\mathrm{mT}$ in Fig. 5.3f. This can be circumvented by different read-out schemes such as latching [99] or shelving [100] but this is out of the scope of the present work, which focuses on the low magnetic field behavior.

We, furthermore, observe a dependence of g^{-} on the voltage on CB (Fig. 5.3g) confirming electrical control over the g-factors. As the voltage is decreased by $50\,\mathrm{mV}$, g^{-} varies from ≈ 1.5 to more than 2.2 which conversely increases the frequency of X-rotations. Concurrently we measure a similar trend in T_2^* reported at $B = 1\,\mathrm{mT}$ in Fig. 5.3h; as the center barrier is lowered the coherence of the qubit is enhanced. The origin and consequences of this observation are discussed later.

5.5 Exchange-driven rotations and noise

Next, we demonstrate full access to the Bloch sphere achieved by Z-rotations leveraging the exchange interaction. We change the pulse sequence (Fig. 5.4b) such that after initialization in a singlet the system is pulsed to large detuning but is maintained in this position only for $t = t_{\pi/2}$ corresponding to a $\pi/2$ rotation, bringing the system close to $i\left|\uparrow\downarrow\right\rangle$. Now we let the state evolve for a time τ_S at a smaller detun-

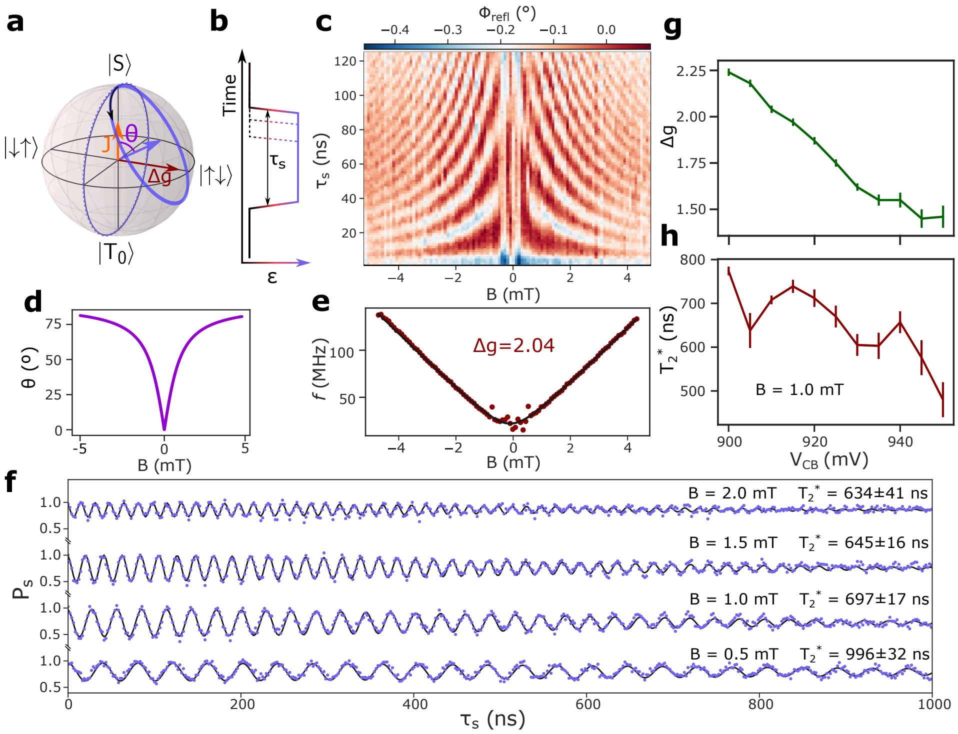

Figure 5.3: g^--driven rotations. a) State evolution on the Bloch sphere. X-rotations are controlled by g^- and the applied magnetic field. The ideal rotation axis is depicted as a dark red arrow. The dashed purple trajectory corresponds to a perfect X-rotation while the effective rotation axis is tilted by an angle θ from the z-axis due to a finite residual J (orange arrow pointing along the Z-axis) resulting in the state evolution depicted by the solid purple curve. b) Pulse sequence used for performing the g^--driven rotations. After initialization in a singlet the separation time τ_S is varied while the amplitude is $\epsilon = 4.5\,\mathrm{meV}$. The system is then diabatically pulsed back to the measurement point. c) g^--driven oscillations as a function of magnetic field and separation time at $V_\mathrm{CB} = 910\,\mathrm{mV}$. The average of each column has been substracted to account for variations in the reflectometry signal caused by magnetic field. A low (high) signal corresponds to a higher singlet (triplet) probability. Each point is integrated for $100\,\mathrm{ms}$ under continuous pulsing (see section 5.9.5). d) $\theta = \arctan\frac{g^-\mu_B B}{J(2.8meV)}$ versus magnetic field. The effective oscillation axis is magnetic field dependent and approaches 80° for B = 5 mT. e) Frequency of g^-- driven oscillations as a function of magnetic field. The black line is a fit to $f = \frac{1}{h}\sqrt{J^2 + (g^-\mu_B B)^2}$ where we extract a g-factor difference $g^- = 2.04 \pm 0.04$ and a residual exchange interaction $J(\epsilon = 4.5\,\mathrm{meV}) = 20 \pm 1\mathrm{MHz}$. We reach frequencies of 100 MHz at fields as low as 3 mT.f) Singlet probability $\mathrm{P_S}$ as a function of τ_S at different B-fields for $V_\mathrm{CB} = 910\,\mathrm{mV}$ extracted through averaged single shot measurements (see Supplementary section 5.9.6). The solid lines are a fit to $\mathrm{P_S} = A\cos(2\pi f \tau_S + \phi)\exp(-(t/T_2^*)^2) + C$. Because of the tilted angle $\mathrm{P_S}$ oscillates only between 0.5 and 1. Moreover, we observe a further decrease in visibility at higher magnetic fields due to decay mechanisms during the read-out process [97]. The extracted T_2^* shows a magnetic field dependence explainable by equation (5.2). g) g-factor difference as a function of the center barrier voltage V_CB. By opening the center barrier the g-factor difference increases from 1.50 to 2.25. h) T_2^* vs V_CB. A near doubling in coherence time with lower center barrier voltage is consequence of an increased tunnel coupling (Fig. 5.4h) as explained in the main text.

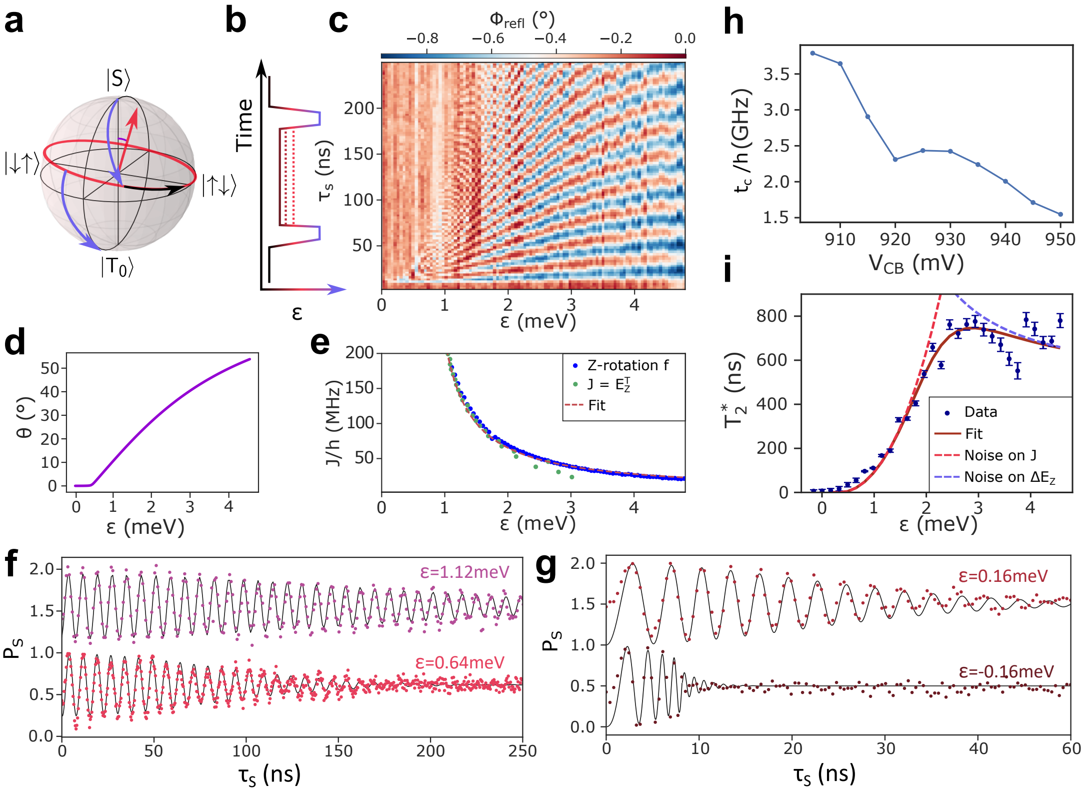

Figure 5.4: Exchange-rotations at $B = 1\,\mathrm{mT}$ and $V_{\mathrm{CB}} = 910\,\mathrm{mV}$. a) State evolution on the Bloch sphere. The purple arrows represent $\frac{\pi_x}{2}$-pulses applied at maximum detuning while the red trajectory corresponds to the free evolution at smaller ϵ. b) Pulse sequence used to probe Z-rotations. A $\frac{\pi_x}{2}$-pulse prepares the state close to the equator of the Bloch sphere, where it subsequently precesses under the influence of J. Another $\frac{\pi_x}{2}$-pulse maps the final state on the qubit basis for read-out. c) Z-rotations as a function of τ_S and ϵ. The acquisition method is the same as in Fig. 5.3c). d) Rotation angle θ as a function of ϵ for B = 1 mT and J extracted from c). e) $J/h = \sqrt{f(\epsilon)^2 - (g^- \mu_B B/h)^2}$ as a function of ϵ as extracted from the oscillation frequency in c) (blue markers). Green dots correspond to the spin funnel (Fig. 5.2e) condition $J(\epsilon) = E_Z^T$ with $\Sigma g = 11$ and the red dashed line is the best fit to $J(\epsilon) = \left|\frac{\epsilon}{2} - \sqrt{\frac{\epsilon^2}{4} + 2t_C^2}\right|$. f,g) $\mathrm{P_S}$ as a function of τ_S for different ϵ and offset of +1 for clarity. The pulse sequence adopted here increases the amplitude of oscillations as compared to Fig. 5.3f enabling full access to the Bloch sphere. At very low ϵ we observe the signal to chirp towards the correct frequency as a direct consequence of a finite pulse rise time. As a result, the coherence time is overestimated. h) tunnel coupling t_C/h as a function of V_{CB} demonstrating good control over the tunnel barrier between the two quantum dots. i) T_2^* as a function of ϵ. The dark red solid line is a fit to equation (5.2). We find $\delta\epsilon_{rms} = 7.59 \pm 0.49\,\mu\mathrm{eV}$, in line with comparable experiments, and $\delta E_{Zrms} = 1.78 \pm 0.01\,\mathrm{neV}$, smaller by a factor 2 than in a comparable natural Si qubit [66]. The bright red (violet) dashed line represents the noise on J (ΔE_Z). For low detuning clearly detuning charge noise on J dominates. At higher ϵ the sum of electric noise acting on g^- and magnetic noise acting on B limit coherence.

ing, increasing J and changing the rotation angle θ (Fig. 5.4d), before applying another $\pi/2$ rotation at high detuning and pulsing back to read-out. The state evolution on the Bloch sphere in Fig. 5.4a shows that full access to the qubit space can be obtained by a combination of appropriately timed pulses. The resulting oscillation pattern is depicted in Fig. 5.4c. From the inferred frequency we find the dependence of J on ϵ and extract $t_C/h = 3.64\,\mathrm{GHz}$ as a free fitting parameter. The extracted values of J are plotted in Fig. 5.4e with the blue markers obtained from the exchange oscillation frequency. The green dots, on the other hand, correspond to $J(\epsilon) = E_Z^T = \frac{\Sigma g \mu_B B}{2}$ extracted from the funnel experiment (Fig. 5.2e). We find that the two sets of data points coincide when $\Sigma g = 11.0$. Together with the g-factor difference already reported we obtain the two out-of-plane g-factors to be 4.5 and 6.5, comparable to previous studies [96]. In Fig. 5.4f and g we plot $\mathrm{P_S}$ as a function of separation time at different values of ϵ. $\mathrm{P_S}$ now oscillates between 0 and 1 due to the combination of $\pi/2$-pulses and free evolution time at lower detuning. From the fits (black solid lines) at different detunings we extract T_2^* as a function of ϵ (Fig.5.4i). For low ϵ the coherence time is shorter than $10\,\mathrm{ns}$, while it increases for larger ϵ and saturates at around $2\,\mathrm{meV}$. This is explained by a simple noise model [66, 94] where T_2^* depends on electric noise on J and a combination of electric and magnetic noise affecting ΔE_Z:

$$\frac{1}{T_2^*} = \frac{\pi\sqrt{2}}{h}\sqrt{\left(\frac{J(\epsilon)}{E_{tot}}\frac{dJ}{d\epsilon}\delta\epsilon_{rms}\right)^2 + \left(\frac{\Delta E_Z}{E_{tot}}\delta\Delta E_{Zrms}\right)^2}, \tag{5.2}$$

where $\delta\epsilon_{rms}$ is the rms noise on detuning, $\delta\Delta E_{Zrms}$ describes the combination of electric noise on g^- and magnetic noise affecting B. We assume $\frac{d\Delta E_Z}{d\epsilon} \approx 0$ as we observe almost no change in g^- with detuning (see Fig. 5.10). From the fit (dark red solid line) we find $\delta\epsilon_{rms} = 7.59 \pm 0.35\,\mathrm{\mu eV}$, in line with comparable experiments [66, 94], and $\delta\Delta E_{Zrms} = 1.78 \pm 0.10\,\mathrm{neV}$. Although $\delta\Delta E_{Zrms}$ is much smaller than $\delta\epsilon_{rms}$ we find that at large detuning coherence is still limited by noise on ΔE_Z because $\frac{dJ}{d\epsilon} \to 0$ (see red and violet dashed lines in Fig. 5.4i). We attribute the magentic noise to randomly fluctuating hyperfine fields caused by spin-carrying isotopes in natural Ge but a distinction from charge noise affecting g^- can not be made here. Eq. (5.2) also gives insight into the trends observed in Fig. 5.3f and h. With B we now affect ΔE_Z and, thereby, its contribution to the total energy. The higher the ratio $\Delta E_Z/E_{tot}$ the more the coherence is limited by this term as confirmed by the drop in T_2^* with magnetic field in Fig. 5.3f. Similarly one would expect that by increasing g^-, T_2^* should be lower. But, as shown in Fig. 5.4h, the raising g-factor difference is accompanied by an increase of the tunnel coupling by $2\,\mathrm{GHz}$. Hence, J is larger at lower V_{CB} and $\frac{\Delta E_Z}{E_{tot}}$ is reduced leading to a longer T_2^*. While V_{CB} affects both t_C and g^-, we see that V_{LB} and V_{RB} affect mostly t_C and leave g^- unaltered (see Fig. 5.11). This exceptional tunability enables electrical engineering of the potential landscape to favor fast operations without negatively affecting the coherence times, thus enhancing the quality factor of this qubit. We find a quality factor $Q = f \times T_2^*$ that increases with magnetic field reaching $Q = 52$ at $3\,\mathrm{mT}$ (see Fig. 5.14). While the longest T_2^* reported here is already comparable to electron singlet-triplet qubits in natural

Si [78], a reduction in the magnetic noise contribution by isotopic purification could further improve qubit dephasing and quality [67, 68].

5.6 Echo

We now focus on extending the coherence of the qubit by applying refocusing pulses similar to those developed in nuclear magnetic resonance (NMR) experiments. We investigate the high ϵ region where charge noise on detuning is lowest. Exchange pulses at $\epsilon = 0.64$ meV are adopted as refocusing pulses. We note, however, that to obtain a perfect correcting pulse, it would be necessary to implement a more complex pulse scheme [74]. We choose convenient τ_S values ($\tau_S = (2n + \frac{1}{2})t_{\pi_x}$) such that, if no decoherence has occurred, the system will always be found in the same state after τ_S. The refocusing pulse is then calibrated to apply a π-pulse that brings the state on the same trajectory as before the refocusing pulse (Fig. 5.5a and Fig. 5.16). The free evolution time after the last refocusing pulse $\tau_{s'}$ is varied in length from $\tau_s - \delta t$ to $\tau_s + \delta t$ (Fig. 5.5b,c) and we observe the amplitude of the resulting oscillations (Fig. 5.5e). Also, we increase the number of applied pulses from $n_\pi = 2$ to $n_\pi = 512$, thereby increasing the total free evolution time of the qubit and performing a Carr-Purcell-Meiboom-Gill echo. The decay is fit to a Gaussian decay and we extract a T_2^{Echo} of 4.5 µs for $n_\pi = 2$ and $T_2^{Echo} = 158$ µs for $n_\pi = 512$, the longest T_2^{Echo} reported so far in this material. Furthermore, we observe a power law dependence of T_2^{Echo} as a function of the number of refocusing pulses and find $T_2^{Echo} \approx n_\pi^\beta$ with $\beta = 0.56$ suggesting a limitation by low frequency $1/f$ noise [26]. We note that for $n_\pi < 32$ we extract $\beta = 0.72$ being a signature of quasi-static noise with spectral density $\approx 1/f^2$.

5.7 Conclusion

In conclusion we have shown coherent 2-axis control of a hole singlet-triplet qubit in Ge with an inhomogeneous dephasing time of 1 µs at 0.5 mT. We have taken advantage of an intrinsic property of heavy hole states in Ge, namely their large and electrically tunable out-of-plane g-factors. We achieved electrically driven g^--rotations of 150 MHz at fields of only 5 mT. Compared to g^- driven singlet-triplet qubits in isotopically purified Si metal-oxide-semiconductor structures [67, 68] we find a g-factor difference that is 3 orders of magnitude larger. Moreover, we demonstrate an electrical tunability of the g-factor difference ranging from 50% to more than 200% over a gate range of 50 mV in different devices. The large g-factor differences were confirmed in 2 additional devices underlining the reproducibility of the Ge platform. Echo sequences revealed a noise spectral density dominated largely by low frequency $1/f$ noise. The results and progress of singlet-triplet qubits, especially in the GaAs platform, will largely be applicable

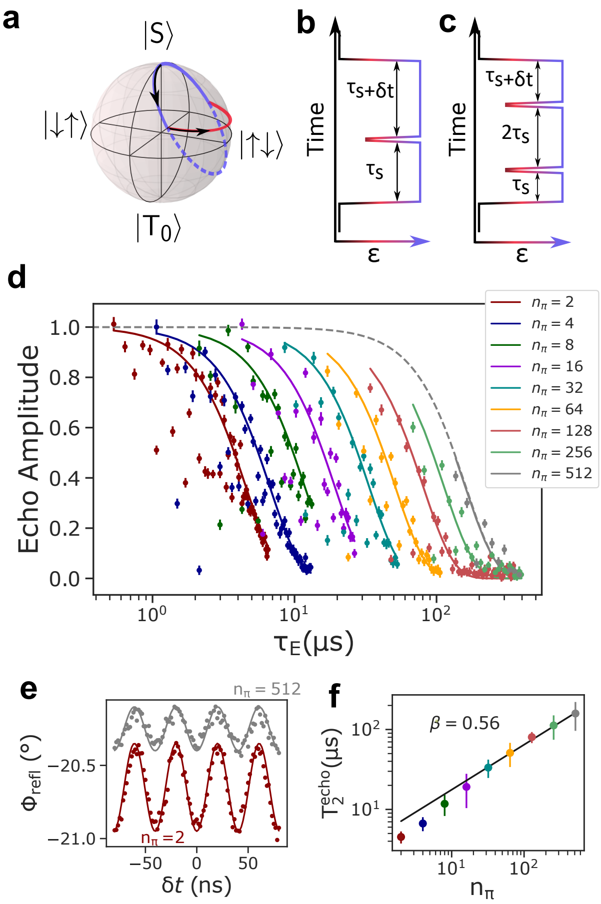

Figure 5.5: Spin Echo at B = 1 mT. a) State evolution on the Bloch sphere. The state evolves on the violet trajectory. At appropriate times a short exchange pulse is applied and the state follows the red trajectory followed by another free evolution on the violet trajectory. The free evolution times are chosen as $\tau_s = (2n + 1/2)t_{\pi_x}$ where t_{π_x} is the time needed for a π-rotation along the violet trajectory. b,c) Pulse sequence for one and two refocusing pulses. The last free evolution is $\tau_\mathrm{s}' = \tau_\mathrm{s} + \delta\mathrm{t}$. d) Normalized echo amplitude as a function of total separation time. Solid lines are a fit to $A_E \exp\left(-t/T_2^{Echo}\right)$ with A_E being the normalized echo amplitude. By increasing the number of π-pulses from 2 to 512 the coherence time increases accordingly from $\mathrm{T}_2^{\mathrm{Echo}}(\mathrm{n}_\pi = 2) = 4.5 \pm 0.7\,\mu\mathrm{s}$ to $\mathrm{T}_2^{\mathrm{Echo}}(\mathrm{n}_\pi = 512) = 158.7 \pm 6.2\,\mu\mathrm{s}$. e) Examples of $S - T_0$ oscillations as a function of δt taken for the points highlighted by arrows in d). For $\mathrm{n}_\pi = 2$ $\Sigma\tau_S = 533\,\mathrm{ns}$ while for $\mathrm{n}_\pi = 512$ $\Sigma\tau_S = 136\,\mu\mathrm{s}$. Solid lines are fit to the data with the amplitude and phase as free parameters. f) Power law dependence of $\mathrm{T}_2^{\mathrm{Echo}} = {\mathrm{n}_\pi}^{\beta}$. β (black solid line) can be used to extract the noise spectral density dominated by low frequency $1/f$ noise [26] .

in Ge as well. Real time Hamiltonian estimation [101] can boost T_2^*, a deeper understanding of the noise mechanisms might result in prolonging coherence even further [23] and feedback controlled gate operation could push gate fidelity beyond the threshold for fault tolerant computation [75].
In the future, latched or shelved read-out could circumvent the decay of T_0 to singlet during read-out opening the exploration of the qubit's behavior at slightly higher magnetic fields where the g^--rotation frequencies could surpass the highest electron-dipole spin-resonance Rabi frequencies reported so far [40, 91], without suffering from reduced dephasing times. Furthermore, by moving towards symmetric operation or resonant driving the quality of exchange oscillations can be increased since the qubit is operated at an optimal working point [76–78, 102]. The operation of Ge qubits at very low fields can further improve their prospects in terms of scalability and high fidelity fast readout, as it will facilitate their integration with superconducting circuits such as Josephson parametric amplifiers, superconducting resonators and superconducting quantum interference devices [103–108] The long coherence times combined with fast and simple operations at extremely low magnetic fields make this qubit an optimal candidate for integration into a large scale quantum processor.

5.8 Methods

Quantum well growth: In contrast with Ge QWs previously employed for qubit fabrication [38], in the present study the strained Ge QW structure was grown by low-energy plasma-enhanced chemical vapor deposition (LEPECVD) [109] instead of thermal CVD. The buffer between the Si(001) wafer and the Ge QW structure is a graded region approximately $10\,\mu\text{m}$ thick in which the Ge content was increased linearly from pure Si up to the desired final composition of $\text{Si}_{0.3}\text{Ge}_{0.7}$. Thermal CVD grown buffers typically exploit a reverse-graded approach starting from a thick pure-Ge layer on the Si(001) wafer [110]. As a consequence the Ge content in the SiGe spacers used here is approximately 70 %, a lower value than the 80 % used in previous reports. This will induce larger strain in the Ge QW [111] and therefore a larger energy difference between HH and LH states, an important feature in order to engineer as pure as possible HH states with large out of plane g-factors and g-factor differences. In the case of Ge QWs grown by thermal CVD on reverse-graded buffers, the buffer and SiGe spacers tend to display a small residual tensile strain [112]. The substrate temperature was reduced from 760 to 550°C with increasing Ge content. The buffer was completed with a $2\,\mu\text{m}$ region at a constant composition of $\text{Si}_{0.3}\text{Ge}_{0.7}$. This part is concluded in about $30\,\text{min}$, with a growth rate of 5-$10\,\text{nm/s}$ due to the efficient dissociation of the precursor gas molecules by the high-density plasma. The graded VS typically presents a threading dislocation density of about $5 \times 10^6\text{cm}^{-2}$ [113]. The substrate temperature and plasma density was then reduced without interrupting the growth. The undoped $\text{Si}_{0.3}\text{Ge}_{0.7}$/Ge/$\text{Si}_{0.3}\text{Ge}_{0.7}$ QW stack was grown at $350\,°\text{C}$ and a growth rate of about $0.5\,\text{nm}^{-1}$ to limit Si intermixing and interface diffusion. A $2\,\text{nm}$ Si cap was deposited after a short ($60\,\text{s}$) interruption to facilitate the formation of the native oxide (the interruption reduces Ge contamination in the Si cap from residual precursor gases in the growth chamber). SIMS analysis indicates that boron levels are below the detection limit of 10^{15}cm^{-3} to a depth of at least 200 nm.

5.9 Supplementary information

The following sections contain all the relevant information to understand the previous section. The TEM characterization was performed by J. Arbiol and M. Botifoll while the XRD measurements were carried out by D. Chrastina. They also wrote the respective sections which I left (almost) untouched.

5.9.1 Simulations

I calculated the time evolution of our system with a python package called qutip. The code to calculate the funnel is available in the appendix, $S-T_0$ and Exchange oscillation codes are essentially identical except for the variables that are swept so I did not report any additional code. I simply defined the system Hamiltonian and provided the parameters which we previously extracted. The resulting plots in Fig. 5.6 nicely reproduce the $S-T_0$ and exchange oscillations as well as the funnel.

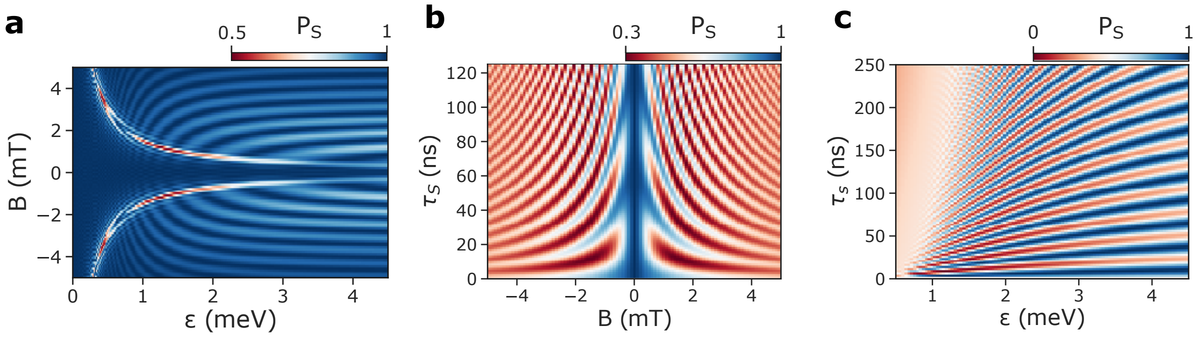

Figure 5.6: Simulations performed in Qutip. The time evolution is calculated with a master equation solver. a) Funnel simulation with the values for J, Σg, g^- extracted from the measurements of the main text (Figs. 3 and 4) and $t_{SO} = 100$ neV. All the main features of the funnel in Fig.2e are visible. b) Simulation of $S-T_0$ oscillations with the experimental values of Fig. 3c. We model the reduction in visibility with magnetic field as $V = V_0 \exp\{-B/B_0\}$ with $B_0 = 2.5$ mT. c) Simulation of the exchange oscillation experiment in Fig.4c. The decay is modelled with collapse operators σ_Z with a rate proportional to $\frac{dJ}{d\epsilon}$ as in Fig. 4i of the main text.

5.9.2 Structural characterizations

TEM

Structural characterization was performed on the samples by means of aberration corrected (AC) high-angle annular dark-field scanning transmission electron microscopy (HAADF-STEM) in a probe corrected Titan FEI microscope operated at 300 kV. The cross-section lamellae have been obtained by Focused Ion Beam in a FEI HELIOS 600 FIB. Electron energy loss spectra (EELS) were obtained in a GATAN Quantum spectrometer coupled to a field emission gun FEI F20 microscope operated at 200 kV. In order to map the atomic lattice dilatation and calculate the strain present at the QW, we have used geometric phase analyses (GPA), developed by Hytch [114, 115].

XRD

High-resolution X-ray diffraction (HR-XRD) was carried out using Cu Kα1 radiation in a PANalytical X'Pert Pro MRD system equipped with a hydrid mirror and two-bounce Ge(220) monochromator on the primary beam, precision Euler cradle, and three-bounce analyser crystal in front of the detector. An ω–2θ scan through the (004) Bragg peak (Fig. 5.7) was dynamically simulated [116] to confirm that the Ge QW is 18 nm thick, as shown in the profile in the inset.

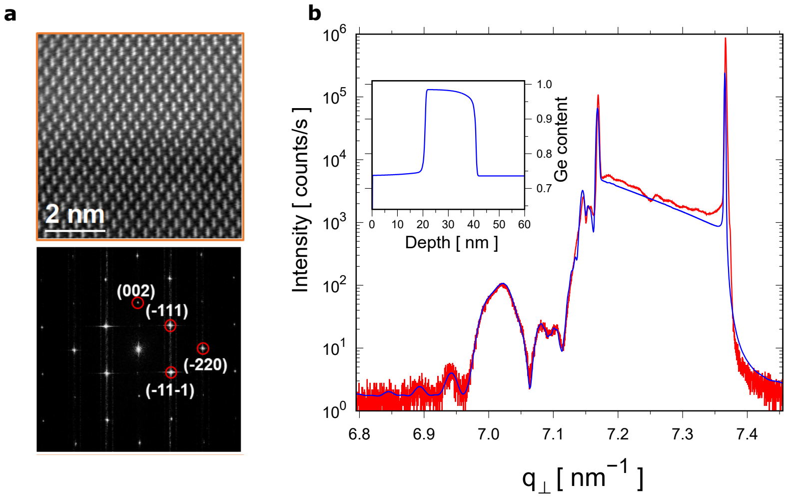

Figure 5.7: a)Atomic resolution aberration corrected (AC) high-angle annular dark-field scanning transmission electron microscopy (HAADF-STEM) image. We observe in-plane lattice matching between the ($\bar{2}$20) vertical planes that can be seen in the upper image (zoom in on bottom interface of Fig. 1a of the main text), which is quantitatively proven by Geometrical Phase Analysis (GPA) (not shown). The atomic stacking is in good agreement with the expected (002) growth. Notice that the Ge-Ge dumbbells are perfectly visible showing a perfect diamond structure. The power spectrum or fast Fourier transform (FFT) obtained on the atomic resolution HAADF-STEM image, shown in the bottom, gives us information on the frequency (reciprocal) space, nearly equivalent to a diffraction pattern, which confirms the planes and directions directly observed in the image. b) Triple-axis ω–2θ scan through Si(004) and dynamical simulation. The inset shows the simulated QW profile, designed to match the profile found by TEM (Fig. 1a of the main text).

5.9.3 Device characterization

This section contains all the relevant measurements and calibrations necessary for the qubit experiment. We start with the determination of the lever arms [55] and the pulse calibration 5.8. To obtain the bias triangles we apply a bias of $V_{SD} = 500\,\mu\text{eV}$. By drawing the parallel lines in the plot and following section (DQDs) we can extract the lever arm of the left and right gate. We then apply a pulse to the barrier gates and observe the shift of the stability diagram. From here we can directly extract the rf-lever arm of the outer barriers and determine the detuning ϵ. This step was probably the hardest one and was only necessary because one of the rf connections did not work. It was not possible to pulse gate L and, therefore, we had to pulse on the outer barriers.

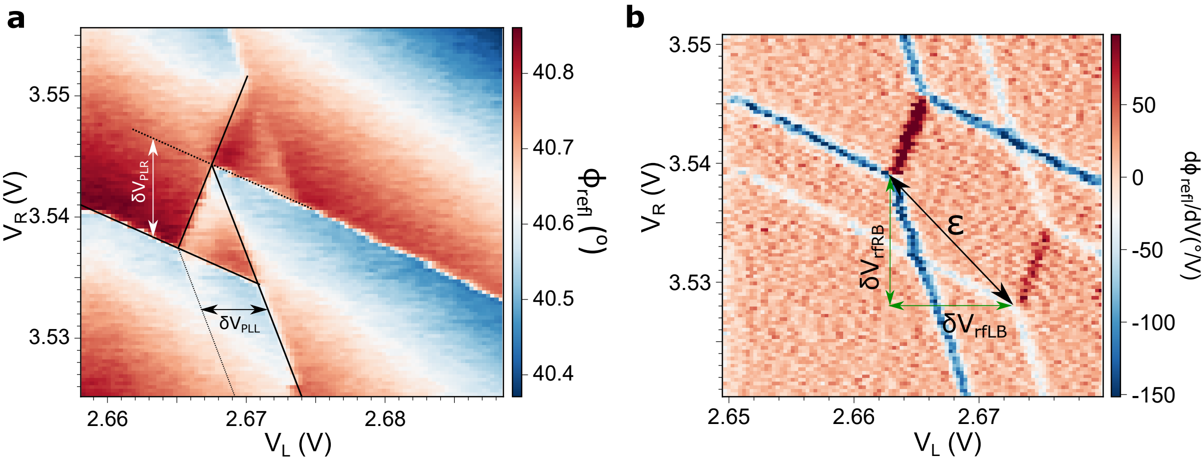

Figure 5.8: a) Bias triangles acquired with $500\,\mu\text{eV}$ bias. $\delta V_L = 5\,\text{mV}$ and $\delta V_R = 8\,\text{mV}$ leading to the lever arms [55] $\alpha_L \approx 0.10\,\text{eV/V}$ and $\alpha_R \approx 0.06\,\text{eV/V}$. b) Derivative of reflected phase as a function of plunger gate voltages. During acquisition a pulse of $Amp = 1.3\,\text{V}$ was applied to gates LB ($-Amp$) and RB ($+Amp$) for 25% of the duty cycle while 75% of it had no pulse applied. As a consequence the stability diagram shifts diagonally and doubles since the data acquisition averages over both charge configurations. The diagonal black arrow is equivalent to the detuning axis and connects two corresponding triple points. This allows us to extract the rf lever arms for the gates LB and RB: $\delta V_{rfLB} = 11.1\,\text{mV}$, $\delta V_{rfRB} = 9.8\,\text{mV}$, $\alpha_{rfLB} = \frac{\delta V_{rfLB}}{Amp}\alpha_L \approx 854\,\mu\text{eV/V}$ and $\alpha_{rfLB} = \frac{\delta V_{rfRB}}{Amp}\alpha_R \approx 454\,\mu\text{eV/V}$. The maximum pulse amplitude we can apply is 5 V on each barrier gate corresponding to a maximum detuning $\epsilon_{max} = 5\sqrt{\alpha_{rfLB}^2 + \alpha_{rfRB}^2} \approx 4.8\,\text{meV}$.

In order to show that we can deplete the left dot completely we recorded a stability diagram for a larger gate range Fig. 5.9. While we see the last transition in the left dot (black arrow) below 2.8 V we still observe transitions in the right dot all the way above 3.5 V (and beyond, not shown).

To prove our statement in equation 5.2 that g^- is not influenced by ϵ too much we plot exchange oscillations at very small tunnel coupling (Fig. 5.10). This means that g^- will be the dominant term

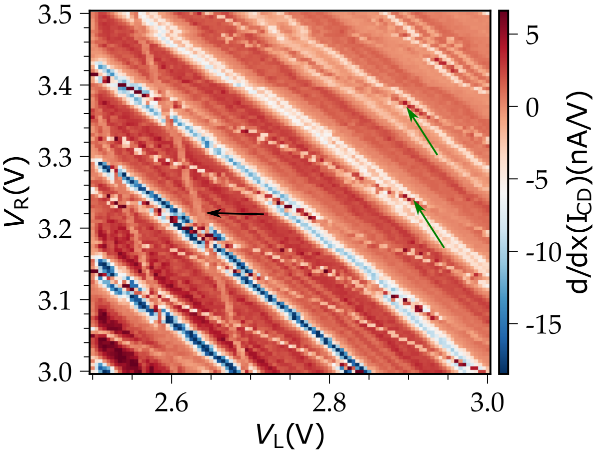

Figure 5.9: Stability diagram recorded from the current through the charge sensor and differentiated. The black arrow points to the last observable transition in the left dot, allowing precise determination of the hole number in this dot. Green arrows highlight two transitions of the right dot. We are not able to completely deplete the right dot such that the hole number determination is not possible here.

in the time evolution at large enough ϵ. we indeed see that the oscillation frequency does not change significantly above 3 meV and conclude that $\frac{g^-}{\delta\epsilon} \to 0$.

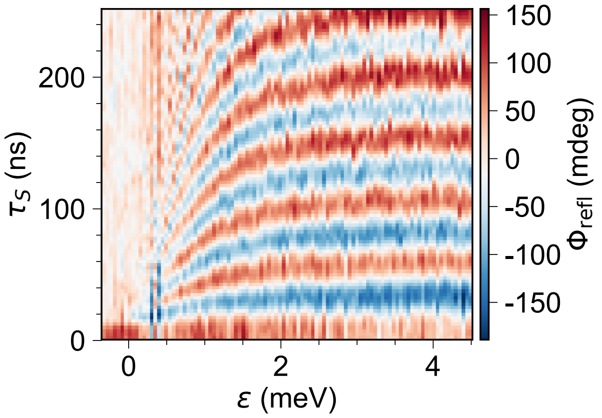

Figure 5.10: Exchange oscillations for $V_{CB} = 950$ mV at 1 mT. Here the tunnel coupling is tuned to a very small value by CB. Hence, J is reduced and $g^-\mu_B B$ dominates at very high values of detuning. From 2 to 4.5 meV detuning we observe no big change in the oscillation period. Therefore, we assume $\frac{g^-}{\delta\epsilon} \to 0$ and justify the form of equation (2) of the main text.

We also recorded g^- as a function of V_{LB} and V_{RB} and found only a small dependence on the outer barrier gate voltages. At the same time, however, the tunnel coupling is influenced by these gates as can be seen in Fig. 5.11. One can, therefore, envision to tune t_C independently of g^-.

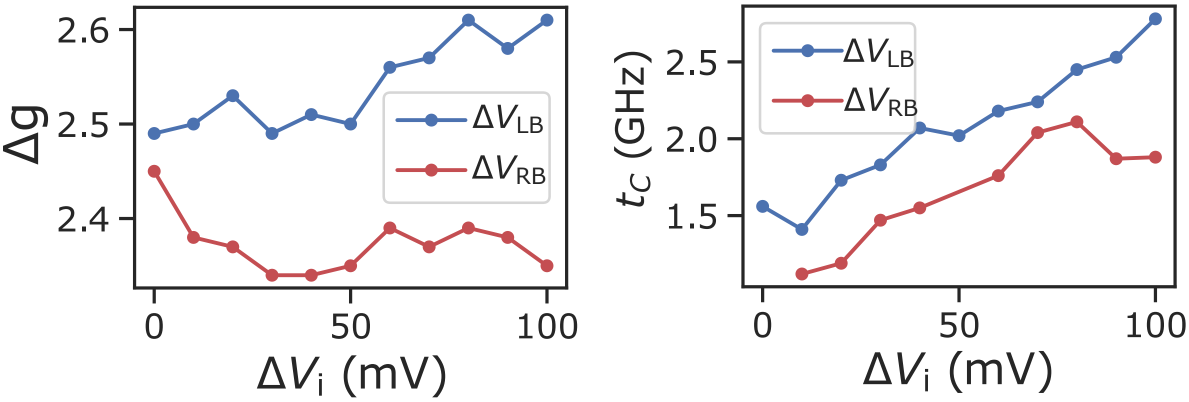

Figure 5.11: Left: g^- as a function of the voltages on LB (blue) and RB (red). Compared to Fig. 3g of the main text here we only see a change of 0.1 in the g-factor difference over a range of 100 mV for both gates. Right: t_C as a function of the voltages on LB (blue) and RB (red). The tunnel coupling can be changed by more than 1 GHz by applying 100 mV more on LB. Although the influence of LB and RB on the tunnel coupling is not as large as CB (see Fig. 4h of the main text) the combination with the g-factor dependences for these two gates allows to tune t_C and g^- almost independently. This ultimately enables precise control over the potential landscape of the dots facilitating the search for noise sweet spots (see discussion of equation (2) of the main text).

Next, we turn to test if the transition $(3, 2n+1) \leftrightarrow (2, 2n+2)$ also shows PSB and could be used as a $S-T_0$ qubit. Indeed in Fig. 5.12 we can see both a funnel and $S-T_0$ oscillations confirming the validity of the equivalent hole number assumption.

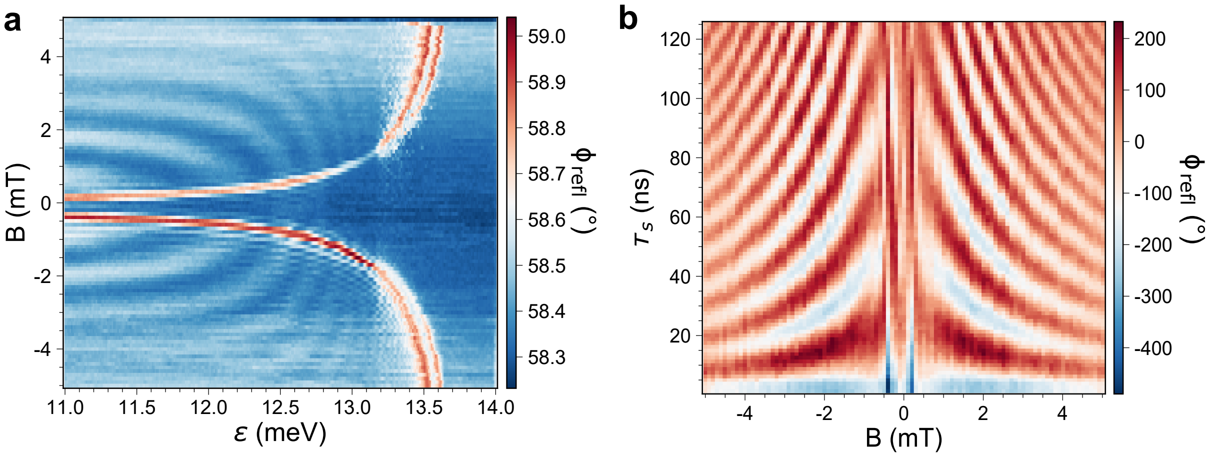

Figure 5.12: a) Spin-funnel acquired at the transition $(3, 2n+1) \leftrightarrow (2, 2n+2)$ (equivalent to $(1, 1) \leftrightarrow (0, 2)$) with the measurement point fixed at $\epsilon = 22\,\mathrm{meV}$ and same center barrier voltage as in Fig. 2e of the main text. b) X-oscillations at the transition in a) at $\epsilon = 17.2\,\mathrm{meV}$. The rotation frequency is slightly lower than in Fig. 3c of the main text and we extract $g^- = 1.4$.

Moreover, Josip Kukucka showed in two more devices that fast $S-T_0$ oscillations are reproducible. He similarly saw that the left dot could be emptied while the right was not. In all cases we measured g-factor differences >1. Interestingly, he measured an opposite trend for g^- vs V_{CB}. As we do not yet understand the mechanisms responsible for the g-factor mismatch we can also not make any conclusion and prediction about the trends.

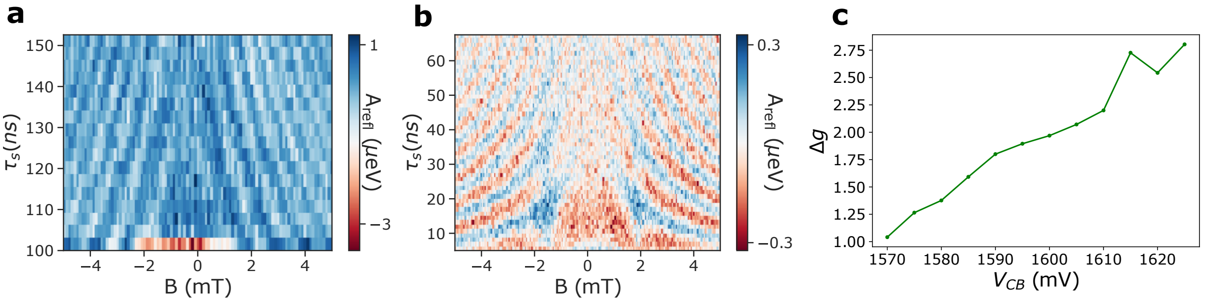

Figure 5.13: a) $S-T_0$ oscillations in a second device. The g-factor difference we extract from this plot is 1.8. b) $S-T_0$ oscillations in a third device. c) From oscillations at different center barrier voltage we extract the g^- dependence on V_{CB}. We find an opposite trend to the one observed in Fig.3g: now g^- increases with V_{CB}. Nevertheless, the reproducibly large and tunable g^- make Ge singlet-triplet qubits an interesting candidate for qubit integration.

Another reproducible quality of our samples is the ability to increase our Q-factor, that is the number of complete rotations within the dephasing time. in Fig. 5.14a we see that the oscillation frequency linearly increases with B but in Fig. 5.14b we see that T_2^* does not deteriorate as quickly. Therefore $Q = f * T_2^*$ also increases with B. Due to the short T_1 (see next section) we could not investigate regions at higher magnetic fields.

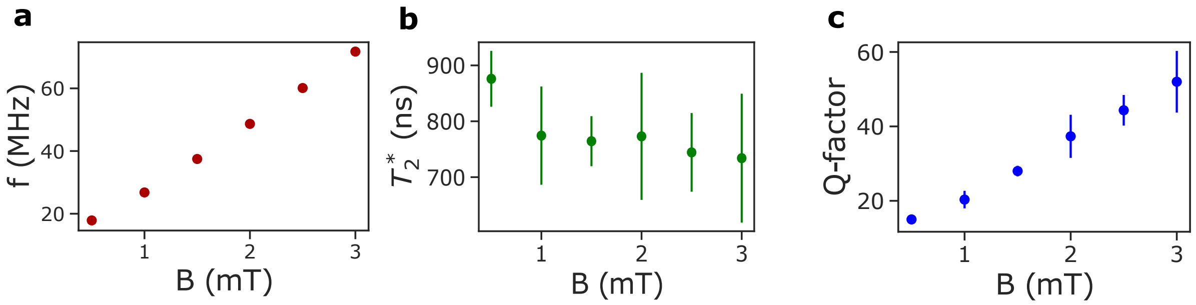

Figure 5.14: Frequency, T_2^* and Q-factor reported for a different gate configuration than in the main text averaged over 3 measurements taken at different time points over the course of 3 days. a) Frequency as a function of magnetic field strength. b) T_2^* as a function of B. We observe a slight decrease of T_2^* with magnetic field. The errors correspond to one standard deviation. For field values bigger than 2 mT the errors are larger as a result of a smaller oscillation amplitude and correspondingly worse fitting conditions. c) $Q = f \times T_2^*$ as extracted from a) and b). A linear increase of Q with B becomes evident. This means that it is possible to enhance the quality of the qubit by increasing the $S - T_0$ oscillation frequency, without affecting the dephasing time too strongly. At 3 mT we extract a Q-factor of 52.

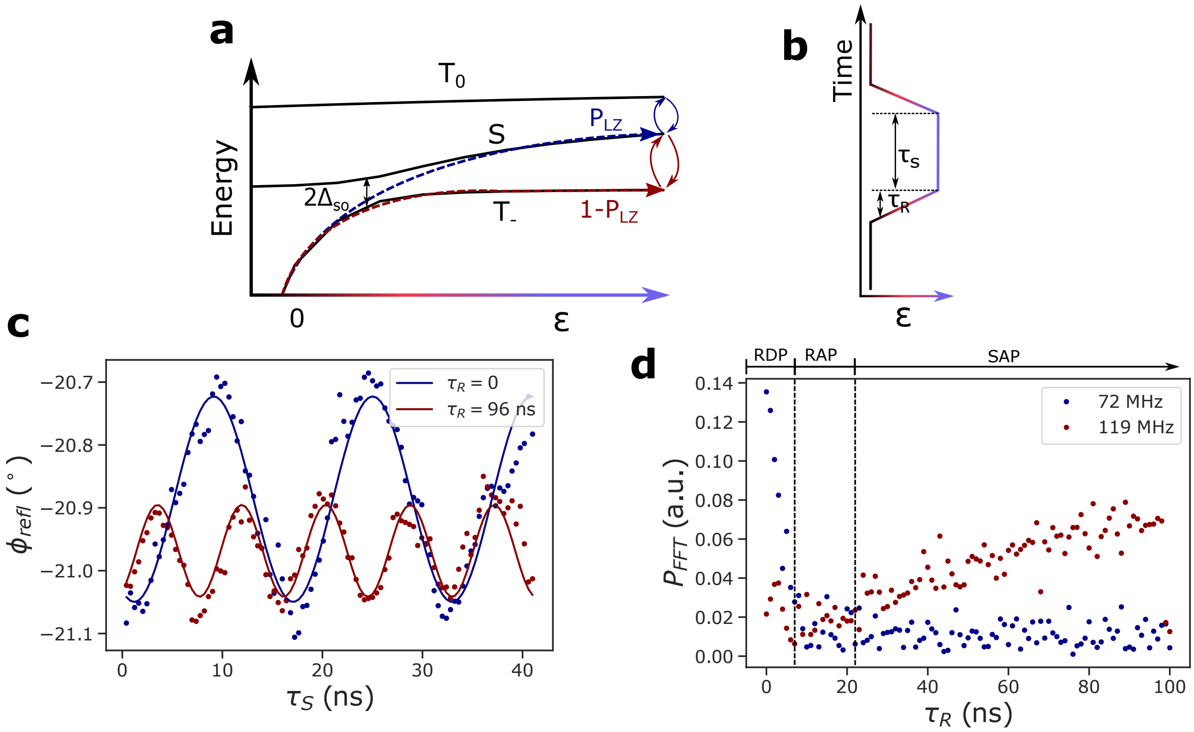

Figure 5.15: a) Dispersion relation close to the $S-T_{-}$ avoided crossing. The size of the anticrossing is determined by $\Delta_{SO} = t_{SO}\mathit{sin}(\Omega/2)$, where Ω is the mixing angle. A fast pulse from low ϵ (left) to high ϵ (right) causes the system to remain in the singlet state (blue trajectory). A slow pulse will cause the system to remain in the ground, which at high ϵ is T_{-}. The probability of maintaining a singlet or evolving to a triplet is determined by the Landau-Zener probability $P_{LZ} = \exp\left\{\frac{2\pi\Delta_{SO}^2}{\hbar v}\right\}$, with $v = \frac{dE}{dt} = \frac{dE}{d\epsilon}\frac{d\epsilon}{dt}$ being the velocity (how fast the energies are changed, e.g. how fast ϵ is ramped), $dE = |E_Z^T/2 - J|$ is the energy difference between T_{-} and S and $\frac{d\epsilon}{dt}$ is the ramp rate. b) Pulse sequence to discriminate $S-T_0$ and $S-T_{-}$ oscillations. After initializing in singlet in (2,0) the system is ramped to (1,1) in a ramp time τ_R. After a separation time τ_S the system is ramped to (2,0) again at the same ramp speed. The resulting oscillations are depicted in c). c) $S-T_0$ oscillations (blue) are evident when the system is pulsed over the anticrossing quickly ($\tau_R = 0$, we note, however, that the AWG has a nominal rise time of $1.1\,\text{ns}$). $S-T_{-}$ oscillations (red) emerge when the ramp time is longer and $S-T_{-}$ mixing occurs. The amplitude of these oscillations depends on τ_R as confirmed by the Fourier amplitude in d). d) Power of the Fourier transform as a function of ramp time for the $S-T_0$ (blue) and $S-T_{-}$ (red) oscillation frequency. For ramp times smaller than $10\,\text{ns}$ the $S-T_0$ frequency dominates, in line with the observations in c). The slower the ramp the more the $S-T_{-}$ frequency becomes prominent because the slow passage over the anticrossing mixes S with T_{-}. In fact, the speed of a pulse on ϵ will lead to 3 different regimes: the rapid diabatic passage (RDP), the rapid adiabatic passage (RAP) and the slow adiabatic passage (SAP). The passage with respect to the charge anticrossing determined by t_C is always adiabatic. In RDP the system passes rapidly over the $S-T_{-}$ anticrossing and the state remains a singlet also at high detuning. This happens for $\tau_R < 10\,\text{ns}$. In RAP the passage over the anticrossing is still diabatic but the ramprate is now slow enough to allow the singlet to evolve to $\uparrow\downarrow$ at high detuning. This means that the system is in an eigenstate state of the Hamiltonian and no oscillations will be observed ($10\,\text{ns} < \tau_R < 40\,\text{ns}$). Gradually increasing τ_R will make the passage over the anticrossing more and more adiabatic (SAP). Now $S-T_{-}$ mixing causes oscillations to appear at a frequency $f = \frac{\Sigma g\mu_B B/2 - J}{h}$ with an amplitude that still depends on τ_R and, therefore, the degree of mixing.

5.9.4 Calibrating the refocusing pulse

Spin echo techniques like Hahn echo and Carr-Purcell-Meiboom-Gill (CPMG) are easily implemented when two perpendicular rotation axis are available. The singlet-triplet qubit, however, comes with the constraint of $J(\epsilon) > 0$ for every ϵ, and $g^{-}\mu_B B \neq 0$. This means that the rotation angle $\theta = \arctan(\frac{g^{-}\mu_B B}{J(\epsilon)})$ can neither be 0 nor 90 degrees. This leads to complications when trying to perform the known echo techniques. Here we implement a spin echo by applying a refocusing pulse calibrated to a specific initial and final state. We let the system evolve freely at large detuning (ϵ_f), on the trajectory depicted in Fig. 3a of the main text and Fig. 5.16c. The initial state for the refocusing pulse is $|\Psi_i\rangle = \exp(-iH(\epsilon_f)\tau_S/\hbar)\,|\Psi_0\rangle$, where $H(\epsilon_f)$ is the hamiltonian defined in equation 1 of the main text with $\epsilon_f = 4.5\,\mathrm{meV}$, and $\Psi_0 = S$. The evolution time τ_S is chosen as $(2n + 1/2)t_\pi$ where t_π is the time needed for a π-rotation at ϵ_f. The refocusing pulse is calibrated to obtain the final state $|\Psi_1\rangle = \exp(-iH(\epsilon_f)(\tau_S + t_\pi)/\hbar)\,|\Psi_0\rangle$. Then the system is left to evolve freely again for a time $\tau_S + \delta t$ at ϵ_f. The total evolution time $\Sigma\tau_S = 2(2n+1/2)t_\pi + \delta t$ leads to a minimum in $\mathrm{P_S}$ at $\delta t = 0$ if no refocusing pulse has been applied, and to a maximum in $\mathrm{P_S}$ at $\delta t = 0$ if a correct refocusing pulse has been applied. In Fig. 5.16 we demonstrate a bad (a)) and a good (b)) calibration of τ_S and the refocusing pulse and illustrate the respective state evolution on the Bloch sphere in Fig. 5.16c-e. In a) the blue curve is obtained with no refocusing pulse. The state evolves on the trajectory in Fig. 5.16c. At $\delta t = 0$ we would expect to find a small singlet probability. However, we observe a maximum in the singlet probability suggesting that the total free evolution time is $(4n+2)t_\pi$ instead of $(4n+1)t_\pi$. The red dots correspond to the trace obtained from the same free evolution time but with a refocusing pulse applied. The state evolution is depicted in Fig. 5.16d. We observe a change in the oscillation amplitude and average value. This indicates that after the refocusing pulse, the state is not evolving on the same trajectory as before the pulse. The red trajectory on the Bloch sphere shows that a higher triplet probability is expected than for the blue trajectory because the refocusing pulse is not applied at the correct time. In b) we adjusted the free evolution time to obtain a high triplet probability after $\Sigma\tau_S$ without refocusing pulse (blue). The refocusing pulse is now calibrated to obtain a singlet state at $\delta t = 0$ (red). The state evolution on the Bloch sphere in Fig. 5.16e shows that the red and blue trajectory coincide meaning that the refocusing pulse is applied at the right time and has the correct length. With this calibration we can perform the echo sequences and extract the decay times displayed in Fig. 5d of the main text.

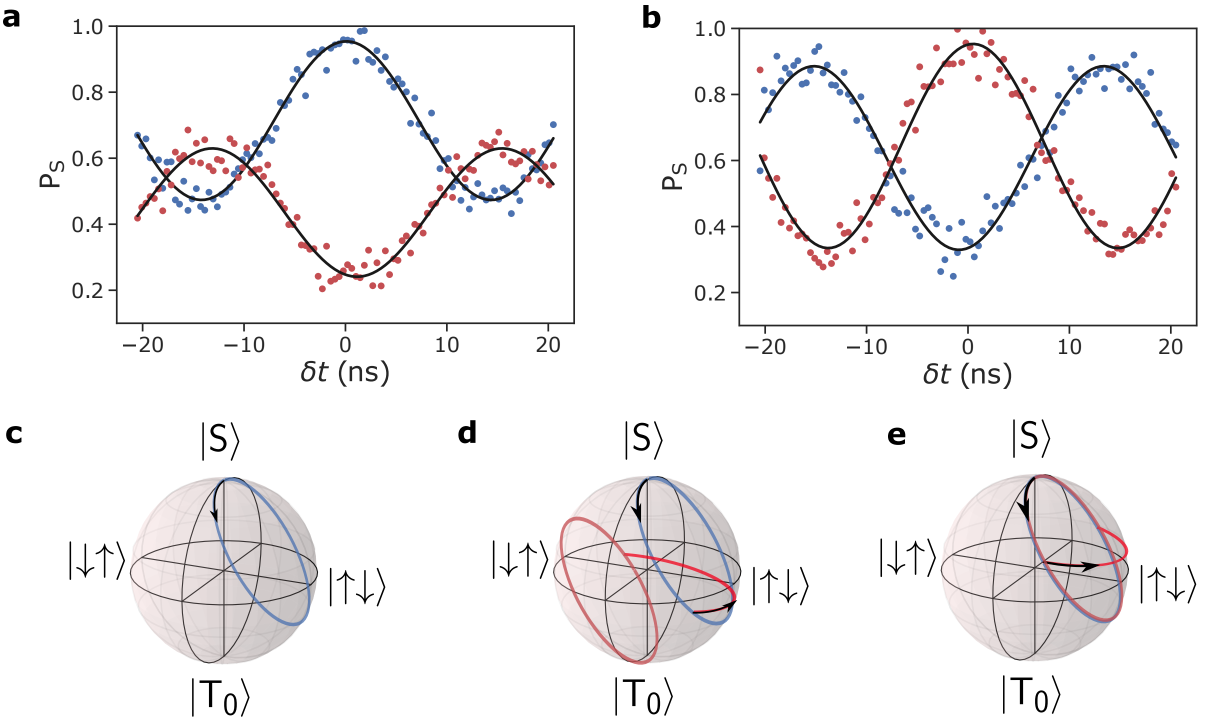

Figure 5.16: Echo oscillations as a function of δt for no (blue) or one (red) recovery pulse. The aim is to generate an echo sequence that recovers the singlet state at the end of a sequence. Because of the tilted oscillation angle during free evolution at high detuning and also during exchange pulses the typical Hahn echo sequence cannot be applied. We, therefore, need to calibrate the exchange pulse but also the free evolution time. We choose $\tau_S = (2n + 1/2)t_{\pi_x}$. We either apply no exchange pulse after τ_S or apply one. Then we let the system evolve again for a time $\tau_S \pm \delta t$. For the sequence with no exchange pulse applied we expect that for $\delta t = 0$ the system will be at the minimum singlet probability. The exchange pulse, on the other hand, should add a phase of π to the state such that we recover the maximum singlet probability at the end of the sequence for $\delta t = 0$. a) Blue dots correspond to $\Sigma\tau_S = 580$ ns without exchange pulse and red dots are with an exchange pulse of 4.5 ns at $\epsilon_r = 0.72$ meV. We obtain a maximum at $\delta t = 0$ for the blue curve meaning that $2\tau_S \neq (2n + 1/2)t_{\pi_X}$. The red curve on the other hand shows that, while we obtain a phase shift of $\approx \pi$ with respect to the blue curve, the average singlet probability is smaller (see Fig. 5.16d). This means that we over rotated the state during exchange. Both τ_S and the exchange pulse need further calibration. b) Calibrated pulses. Blue dots correspond to $\Sigma\tau_S = 600$ ns and no refocusing pulse has been applied. Red dots are also $\Sigma\tau_S = 600$ ns but exactly in between a refocusing pulse of 4.5 ns at $\epsilon_r = 0.64$ meV was applied corresponding to a phase shift of π and a consequent maximum at $\delta t = 0$. This indicates that the singlet has been recovered. c) State evolution on the Bloch sphere at ϵ_f. d) State evolution on the Bloch sphere at ϵ_f with a refocusing pulse applied at $\epsilon_r = 0.72$ meV. Because the refocusing pulse is applied at the wrong time the trajectory of the state after the recovery (red) evolves in a different plane than before recovery. This leads to an increased triplet probability. e) State evolution on the Bloch sphere at ϵ_f with a refocusing pulse applied at $\epsilon_r = 0.64$ meV. Here the refocusing pulse is applied at the correct time and the refocused trajectory coincides with the initial trajectory. In this way spin-echo can be performed.

5.9.5 Pulsing and T_1

During the acquisition of Fig. 2a,b,e, Fig. 3c and Fig. 4c of the main text the signal was integrated over 100 ms for each data point under continuous pulsing (Fig. 5.17 Left). The time spent in the measurement point $t_M \gg \tau_s$ meaning that the largest portion of the signal is actually taken at the M point. Figures 3f, 4f, 4g and 5e of the main text on the other hand are obtained by averaging 500 single shot measurements. The signal is integrated from the moment the system is returned to the measurement point. Before the next pulse starts, the system is left for 100 µs at the measurement point and the average signal Φ_{offset} (see Fig. 5.18a) is substracted from the previously integrated signal to account for fluctuations in the charge sensor. The phase signal is then transformed to probability by considering the signal difference between (1,1) and (2,0) $\delta\Phi_{\text{refl}}$. $\mathrm{P_S} = 1 - \frac{\Phi_{\text{refl}} - \Phi_{\text{offset}}}{\delta\Phi_{\text{refl}}}$. The signal to noise ratio did not allow us to distinguish singlet and triplet states in single shot measurements, only after averaging the distinction becomes clear.

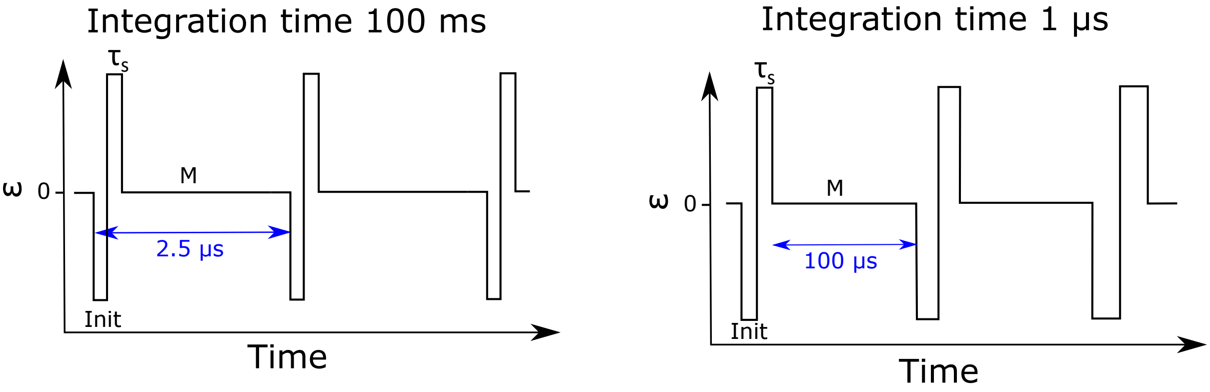

Figure 5.17: Left: Continuous pulsing. The integration time is 100 ms and the same pulse is repeated 4000 times. Since most of the duty cycle is spent in the measurement point M, the resulting signal can be interpreted as the signal in the measurement point. The intialization (Init) pulse has the same amplitude but opposite sign as the separation pulse and the same length τ_S. This ensures that there is no DC offset on the pulse. Right: averaged single shot. The integration time is 1 µs. The separation time is stepped for consecutive pulses and only the signal in the measurement point is considered (see Fig. 5.18). During the whole pulse train the data is recorded and averaged 500 times. The singlet and triplet probabilities are then extracted in post-processing.

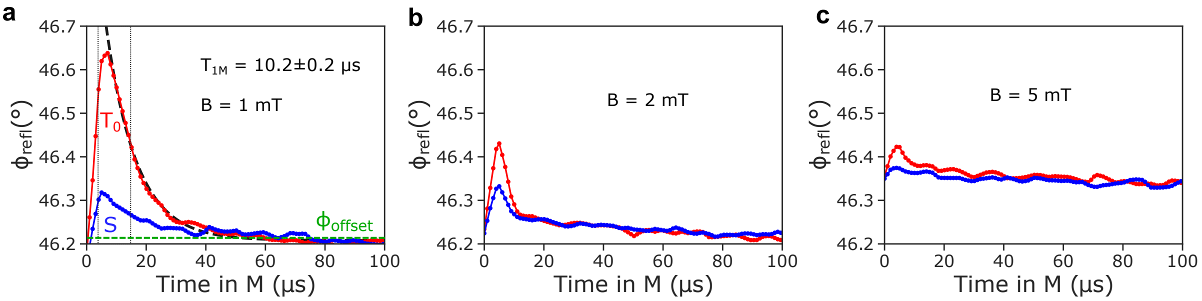

Figure 5.18: T_1 in the measurement point at different magnetic field. a) Averaged single shot traces of a singlet (blue) and a T_0 (red) state as a function of time in the measurement point. The black dashed line is a fit to $A\exp\left(\frac{-(t-t_0)}{T1}\right)+C$. At 1 mT we extract $T_1 = 10.2 \pm 0.2$µs. The signal inside the dashed region is averaged giving the difference between the T_0 and the S state. ϕ_{offset} (green) is substracted from the signal to account for drifts in the charge sensor signal over time. b) At 2 mT the amplitude of the triplet signal is greatly reduced as a consequence of decay from T_0 to S during measurement. c) At 5 mT S and T_0 states become almost indistinguishable.

5.9.6 T_2^* extraction for V_{CB} and ϵ dependence

The inhomogeneous dephasing time (T_2^*) is extracted from fits to X-rotations and Z-rotations. We find that generally a gaussian decay can be observed ($\exp(-(t/T_2^*)^2)$). Fig. 5.19 displays the traces used to determine the values of Fig. 3h of the main text. Figures 5.20,5.21 and 5.22 display Z-rotations at different detuning values. The coherence times extracted here are depicted in Fig. 4i of the main text.

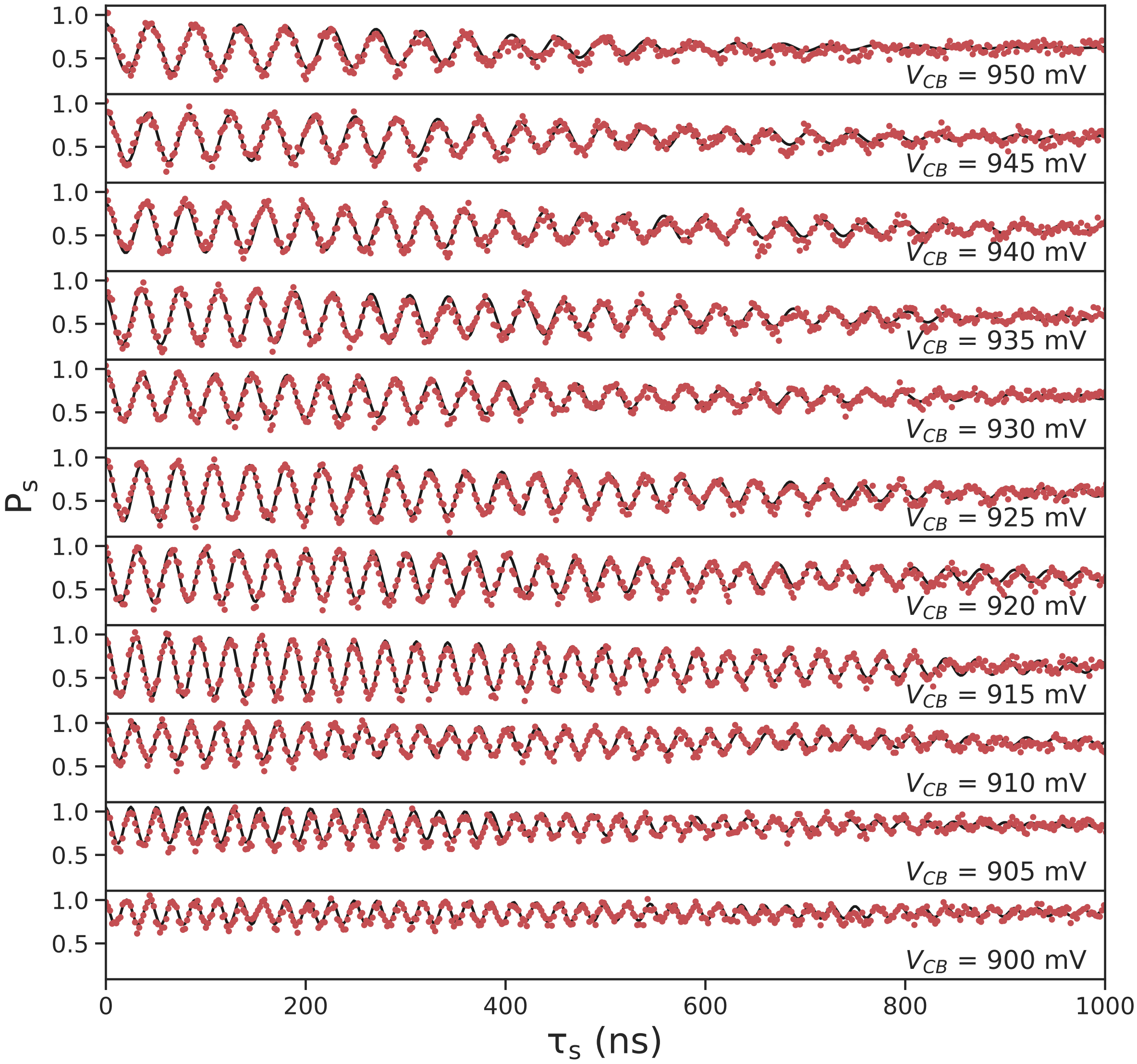

Figure 5.19: X-rotations. $\mathrm{P_S}$ as a function of τ_S at $B = 1\,\mathrm{mT}$ and $\epsilon = 2.8\mathrm{meV}$ for the center barrier voltages reported in the inset. Black lines are fit to $\mathrm{P_S} = A\cos(2\pi f + \phi)\exp\left(-(t/T_2^*)^2\right) + C$. The extracted T_2^* is reported in the main text (Fig. 3h).

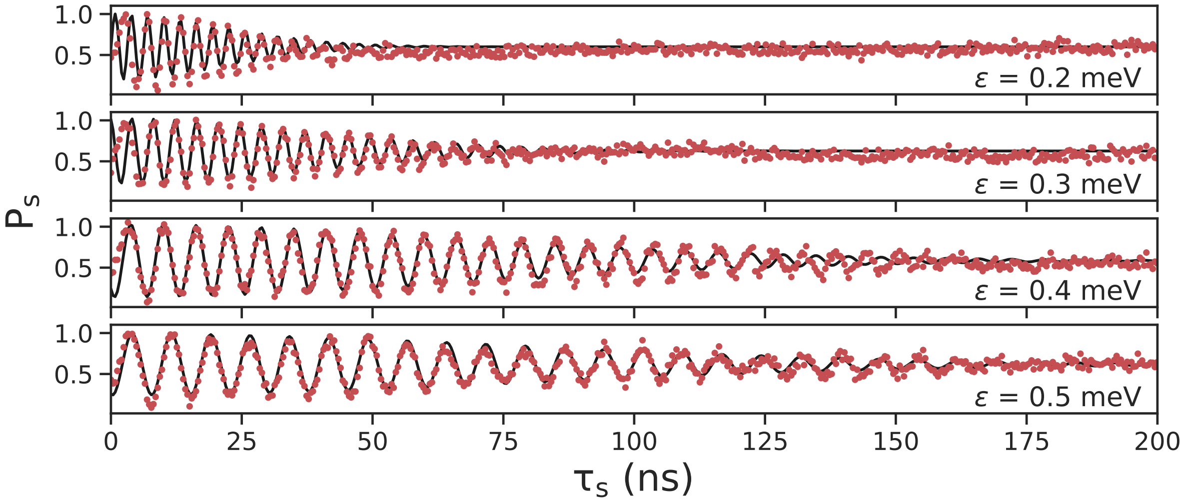

Figure 5.20: Z-rotations. $\mathrm{P_S}$ as a function of τ_S at $B = 1\,\mathrm{mT}$ and $V_{CB} = 910\,\mathrm{mV}$ for low detuning. The extracted T_2^* is reported in the main text (Fig. 4i)

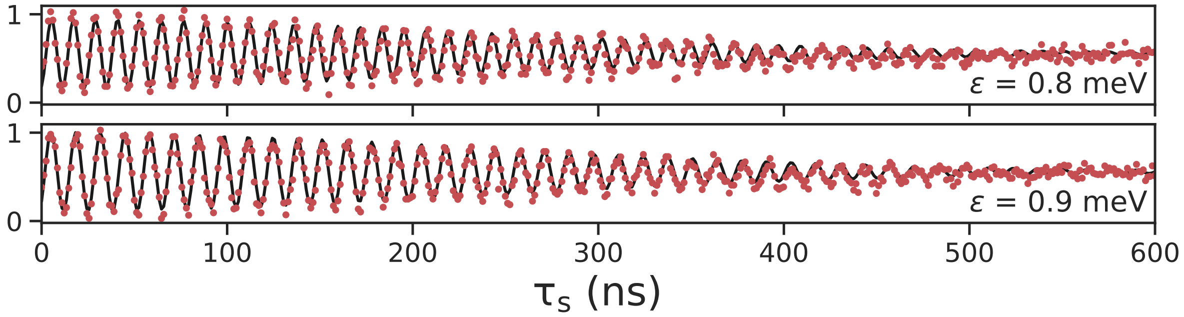

Figure 5.21: Z-rotations. $\mathrm{P_S}$ as a function of τ_S at $B = 1\,\mathrm{mT}$ and $V_{CB} = 910\,\mathrm{mV}$ for medium detuning. The extracted T_2^* is reported in the main text (Fig. 4i)

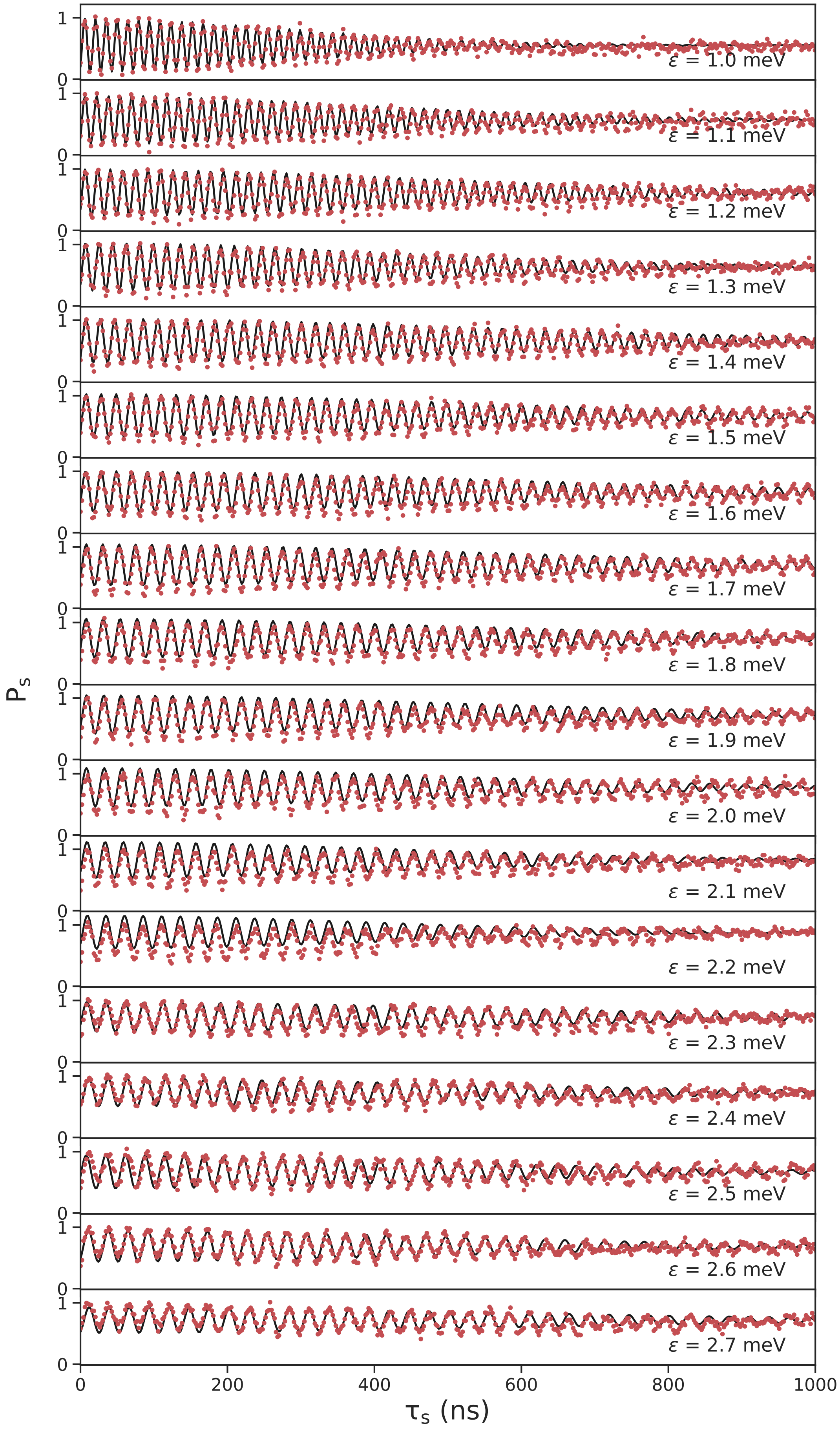

Figure 5.22: Z-rotations. $\mathrm{P_S}$ as a function of τ_S at $B = 1\,\mathrm{mT}$ and $V_{CB} = 910\,\mathrm{mV}$ for high detuning. The extracted T_2^* is reported in the main text (Fig. 4i).

6 Dynamics of hole singlet triplet qubits with large g-factor differences

This chapter is adapted from a paper with the same name which we finished writing just as I completed my thesis so it has not been reviewed at the time of writing. I personally found this experiment even more interesting and challenging than the previous chapter as here we discovered things unknown in the literature. In particular, we wanted to investigate the properties of the $S-T_0$ qubit for in-plane fields, or actually for any field direction, in the same device as in the previous chapter. However, we quickly found that it was not possible to operate this qubit the same way as in the out-of-plane direction because the $S-T_-$ splitting became too large and drastically affected the dynamics of the system. We struggled a lot to find an explanation for this on the basis of a spin-orbit spin-flip tunneling term. However, the angular anisotropy suggested that the HH g-factors might be the key to understand it. Indeed, we found that the splitting featured almost the opposite anisotropy as the HH g-factor. However, it was still not clear why the g-factors would cause such a large splitting until we realized that this could indeed happen if the absolute value of the in-plane g-factor difference is larger than the sum, meaning the in-plane g-factors must have opposite signs. Because of the small zeroth order value of the in-plane g-factor we speculated that this could happen because of the confinement potentials. The theory indeed confirms that corrections to the g-factors could arise due to elliptical confinement potentials which, for the gate configuration we had, could lead to opposite corrections which can change the sign of one g-factor with respect to the other.

6.1 Introduction

The spin-orbit interaction (SOI) allows electrical manipulation of individual spins and has therefore become a key ingredient for the realization of fully electrically controlled spin qubits [31,117]. For electrons in Si it is rather weak and synthetically boosted by means of micromagnets [26,66]. For holes, on the other hand, it is an intrinsic property which allows to perform electron dipole spin resonance (EDSR) measurements [31,34,35,39,60,117,118]. In Ge it is particularly strong leading to Rabi frequencies beyond 100MHz [35, 40, 91]. SOI for holes can be linear or cubic in k, with nanowire qubits favoring the former type while planar qubits the latter [111, 119]. The SOI is not only important for single spin but also for singlet-triplet qubits as it causes an intrinsic mixing between the heavy hole (HH) and light hole bands and thereby locally affects the g-factors of the individual spins allowing to drive $S-T_0$ oscillations [80]. In combination with an extrinsic Rashba type SOI caused by the structural inversion asymmetry induced by the heterostructure, it also mixes the S and T_- states contributing therefore to the observed avoided crossing. This singlet-triplet splitting Δ_{ST_-} has been extensively studied in GaAs structures. Different regimes dominated either by the SOI or the hyperfine interaction have been investigated and optimized for dynamical nuclear polarization [120, 121]. In Si, where the hyperfine contribution is much weaker [65], the relatively weak SOI is found to be the decisive factor for the size of the anticrossing [68, 122]. Indeed, the SOI arising from the presence of multiple valleys causes both a g-factor difference as well as a spin coupling term to emerge [69, 70].

Here we study a double quantum dot singlet triplet hole qubit realized in planar Ge. We characterize the complete spectrum of our system by observing the dynamics under different pulsing schemes and magnetic field directions. We investigate the $S-T_-$ avoided-crossing by means of Landau-Zener tunneling and find that a typical cubic SOI parametrized by an in-plane spin-flip tunneling term t_{SO} is insufficient to describe the observed angular B-field dependence. In fact, the different g-factor anisotropy in the two quantum dots greatly enhances Δ_{ST_-} in the in-plane magnetic field direction and influences the system dynamics.

6.2 Funnel as a function of magnetic field angle

A scanning electron microscope (SEM) image of the device under consideration is depicted in Fig. 6.1a and further details can be found in [80]. A hole gas confined in a Ge quantum well is buried 20 nm below the surface. A charge sensor (CS) connected to a radio-frequency (rf) reflectometry circuit is used to read out the charge state of the gate defined DQD. For qubit state selective read-out we rely on Pauli spin blockade. Fast detuning pulses are applied to gates LB and RB with an arbitrary waveform generator (AWG) which has a pulse-rise time of $\tau_{rise} \approx 2$ ns (inset of Fig. 6.1a). Throughout this work we apply a small magnetic field in a plane perpendicular to the quantum dot axis, **B** $= (B\cos(\theta), 0, B\sin(\theta))$, where θ describes the tilt angle from the in-plane direction. We tune the DQD to an effective charge transition (2,0)↔(1,1), with (n_L, n_R) where n_L (n_R) denotes the effective hole number in the left (right) quantum dot (see Supplementary Fig. 6.5). We emphasize that the real hole number in the left dot is n_L+2 while in the right dot we cannot determine the exact hole number. The tunnel coupling between the dots is described by t_C while the energy detuning between the $S(2,0)$ and $S(1,1)$ state is parametrized by ϵ. Each quantum dot is characterized by an out-of-plane and an in-plane g-factor. However, the dynamics of singlet-triplet qubits is only sensitive to differences in, or the average of, the

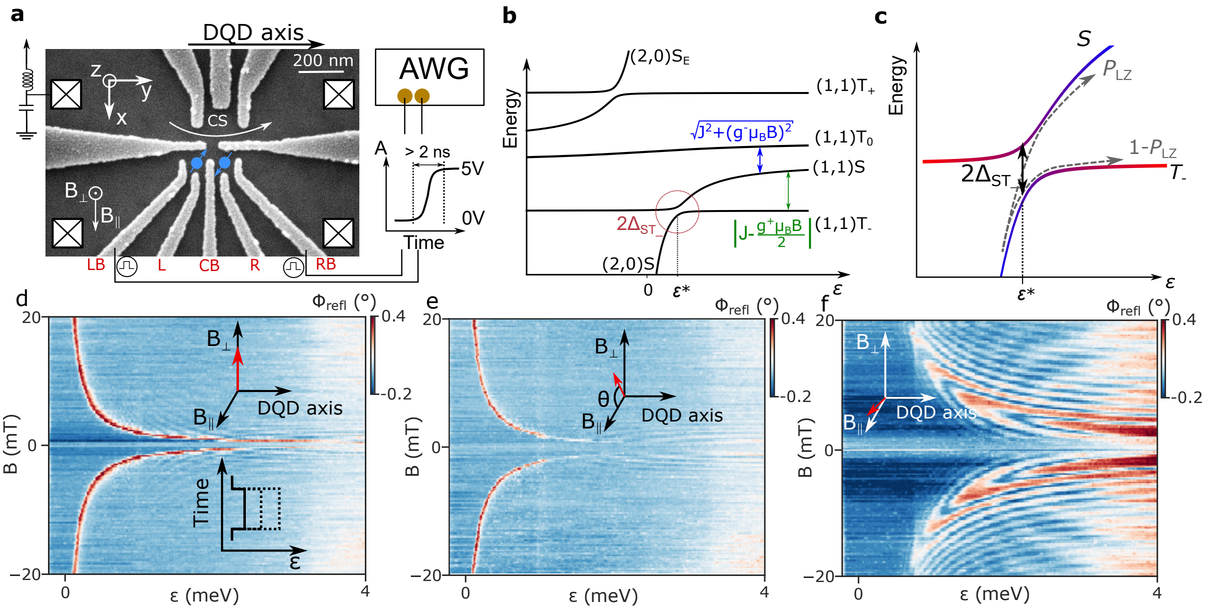

Figure 6.1: a) SEM image of the device consisting of a double dot electrostatically defined by gates LB, L, CB, R and RB. The charge sensor (CS) is coupled to an LC-resonator for Ohmic-reflectometry via a lock-in amplifier. Pulses are applied to gates LB and RB via an arbitrary waveform generator with a minimum rise time of 2 ns (inset). b) The energy level diagram as a function of detuning arising from our model highlights the relevant energy splittings between S and T_0 and S and T_-. At $\epsilon = \epsilon^*$, S and T_- anticross with a splitting $2\Delta_{ST_-}$. c) Energy level diagram of the states involved in the passage over the avoided crossing (red circle in b)). The probability P_{LZ} to maintain the initial state after a single passage over the avoided crossing is given by the Landau-Zener formula. d) Pulsing ϵ over the $S - T_-$ degeneracy will result in a mixing of the two states when $\epsilon = \epsilon^*$. Here we show the resulting return signal for a magnetic field applied at an angle $\theta = 90°$ from the in-plane direction. A high signal corresponds to a larger triplet return probability. The lower inset displays the pulse sequence where only the amplitude ϵ is varied. e) At $\theta = 60°$ compared to d) the degeneracy is sharper indicating a smaller value of Δ_{ST_-}. f) For $\theta = 10°$ the degeneracy is not a funnel-like sharp line but rather an oscillation pattern resembling a butterfly shape. Such features appear when the $S - T_-$ mixing term becomes substantial. At low ϵ $S - T_-$-like oscillations are prominent. At higher detuning also $S - T_0$-like oscillations become visible.

Zeeman energy between the dots, and hence we define $g^{\pm}_{\perp} = g^{L}_{\perp} \pm g^{R}_{\perp}$ ($g^{\pm}_{\parallel} = g^{L}_{\parallel} \pm g^{R}_{\parallel}$) as the out-of-plane (in-plane) g-factor difference and sum. The energy dispersion relation of the system (the complete Hamiltonian H_{tot} is derived in Supplementary section 6.7.6) is depicted in Fig. 6.1b as a function of ϵ. At $\epsilon = \epsilon^*$ the S and T_- states anticross.

We start by mapping out the $S - T_-$ degeneracy as a function of magnetic field angle with the funnel technique [21]. Here, mixing between S and T_- is induced by pulsing the system close to $\epsilon = \epsilon^*$. Mixing depends both on the size of the avoided crossing and the mixing time τ_S. We apply a rapid pulse of duration $\tau_S = 65$ ns and varying ϵ (inset of Fig. 6.1d). Fig.6.1d,e and f depict the phase response of the charge sensor in the measurement point as a function of the pulse amplitude on ϵ and the magnetic field strength for $\theta = 90$°, 60° and 10°, respectively. A high return signal corresponds to a larger triplet probability. In the out of plane direction we observe the expected funnel shape of the $S - T_-$ degeneracy. At 60° we similarly observe a typical funnel shape, however, we notice the line to be fainter which indicates a smaller Δ_{ST_-}. The picture drastically changes towards the in-plane direction where the $S - T_-$ degeneracy evolves into a buttefly pattern; an obvious oscillation pattern with 2 main components which can be attributed to $S - T_-$ oscillations at low detuning and $S - T_0$ oscillations becoming more prominent at high detuning can be observed. The prominent $S - T_-$ oscillations are an indication of a large coupling term in the in-plane direction, not predicted by any SOI model [123]. The angular anisotropy of Δ_{ST_-}, further exemplified in Fig. 6.9, is the main focus of this work and requires the knowledge of all parameters entering the Hamiltonian and therefore understand the interplay between the g-factor anisotropy and the spin-flip element t_{SO}.

6.3 g-factor anisotropy extraction through singlet-triplet oscillations

In order to extract the g-factor anisotropy we rely on singlet-triplet oscillations. After initialization in $S(2,0)$, appropriate pulses to (1,1) induce either $S - T_0$ or $S - T_-$ oscillations. The probability to maintain the initial eigenstate of the system after a sweep with ramp time τ_R is given by the Landau-Zener formula $P_{LZ} = \exp\left(-\frac{2\pi\Delta^2_{ST_-}}{\hbar v}\right)$, where $\hbar$ is the reduced Planck constant and $v = |\frac{dE}{dt}| = |\frac{dE}{d\epsilon}\frac{d\epsilon}{dt}| = |\frac{dJ(\epsilon)}{d\epsilon}|_{\epsilon=\epsilon^*}\frac{\Delta\epsilon}{\tau_R}$ is the velocity calculated at $\epsilon = \epsilon^*$ and $J(\epsilon) = \sqrt{\frac{\epsilon^2}{4} + 2t_C^2} - \frac{\epsilon}{2}$ is the exchange interaction (Fig. 6.1b and c). If v satisfies the diabatic condition ($P_{LZ} \approx 1$) $S - T_0$ oscillations with a frequency $f = \frac{1}{\hbar}\sqrt{J^2 + (g^-\mu_B B)^2}$ will be favored. With $P_{LZ} < 1$ $S - T_0$ oscillations are suppressed and the qubit is initialized in a superposition of S and T_-. After a time τ_S the system is pulsed back to the measurement point where another non-diabatic passage will cause an interference between the two states similar to a Mach-Zhender interferometer [124]. The accumulated phase difference is then given by $\phi = 2\pi f_{S-T_-}\tau_S \approx \frac{\tau_S}{\hbar}|J - \frac{1}{2}g^+\mu_B B|$ [93] (see Fig. 6.1b). As the oscillation frequency of the $S - T_0$

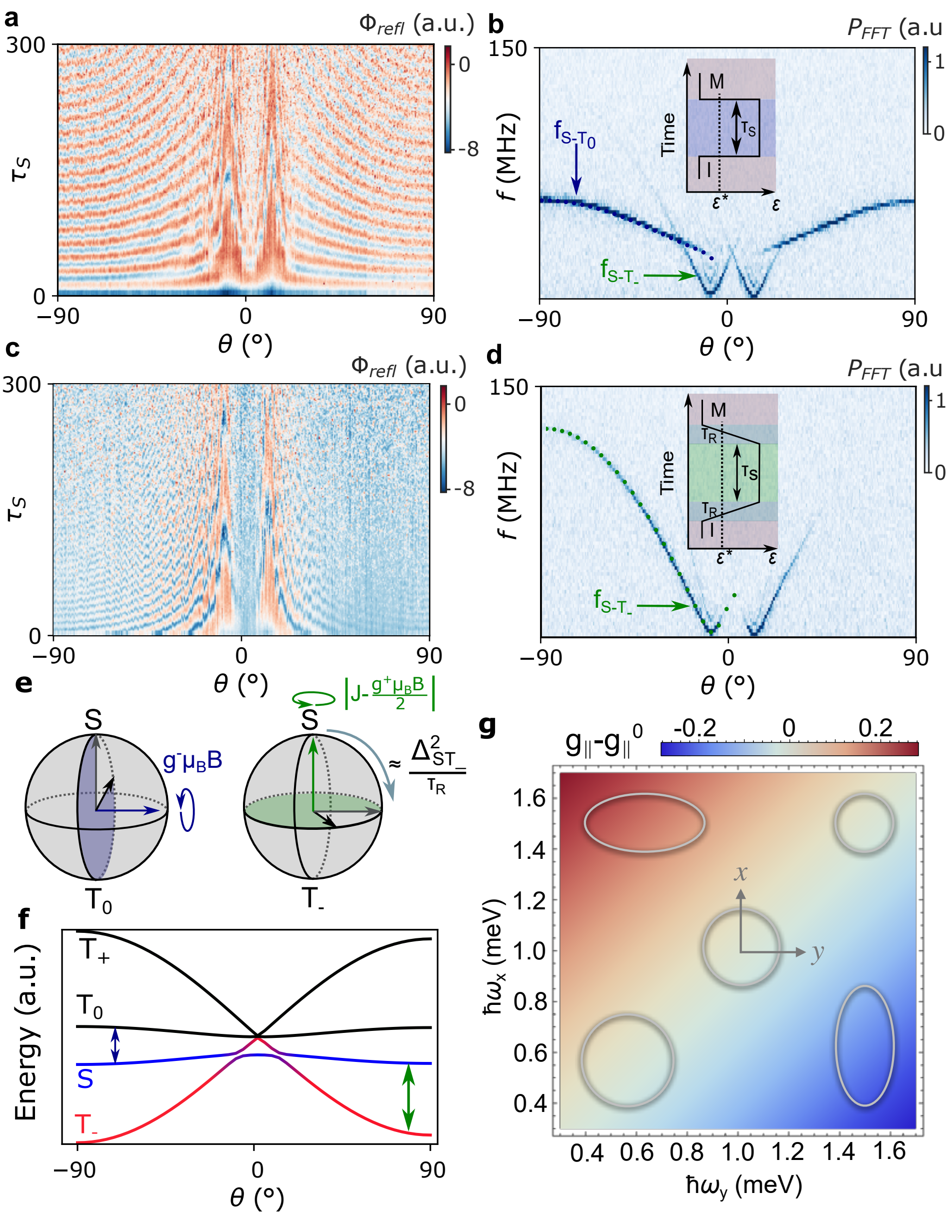

Figure 6.2: a) Oscillation amplitude of the singlet state in the measurement point as a function of separation time and magnetic field angle at $B = 2\,\mathrm{mT}$. b) FFT of a) revealing the oscillation frequency anisotropy. The blue dotted line is a fit to our model. The inset shows the pulse shape where the system is swept to $\epsilon = 4\,\mathrm{meV}$ in the shortest time enabled by the AWG. c) $S - T_-$ oscillations under the same conditions as a) but with a longer ramp time ($\tau_R = 100\,\mathrm{ns}$). d) FFT of c) showing f_{S-T_-} as the green dotted fit line. The $S - T_0$ oscillations are completely suppressed by the slow ramping to high ϵ highlighted by the pulse sequence in the inset. e) Schematic of the time evolution at high ϵ for the $S - T_0$ ($S - T_-$) qubit on the left (right). Mixing between S and T_- depends on $\frac{\Delta^2_{ST_-}}{\tau_R}$ (light blue arrow) and constitutes a second rotation axis for the qubit. f) The energy dispersion of the eigenstates of H_{tot} at $\epsilon = 4\,\mathrm{meV}$ as a function of θ reproduce the frequencies seen in b (d) with the blue (green) arrow highlighting the visible transition. g) Effect of the confinement on the in-plane g-factors for a quantum well width of $20\,\mathrm{nm}$ according to Eq. (6.1). On top, we schematically show possible dot geometries in real space.

qubit is proportional to g^- while the one of the $S-T_-$ qubit is proportional to g^+ (Fig. 6.1b and 6.2e) we can extract the individual g-factors without the need for EDSR. We fix the magnetic field at $|B| = 2\,\text{mT}$ and observe the oscillations resulting from a fast pulse ($\tau_R = \tau_{rise}$) in Fig. 6.2a and a ramped pulse with ramp time $\tau_R = 100\,\text{ns}$ of amplitude $\epsilon = 4\,\text{meV}$ and duration τ_S in Fig. 6.2c as we rotate the field. From the fast Fourier transform (FFT) in Fig. 6.2b and d we extract the oscillation frequency f_{S-T_0} (blue dots) and f_{S-T_-} (green dots). We notice that for $\theta \in [-25°, +25°]$ in both FFT plots the $S-T_-$ frequency is visible suggesting that a large coupling term is present at these magnetic field directions inducing a non-diabatic passage, in line with the observations in Fig. 6.1f. Moreover, in Fig. 6.2d the FFT power vanishes for $\theta \approx 60°$ indicating that the ramp time τ_R induces a completely adiabatic passage over the avoided crossing. This is in line with Fig. 6.1e where we observed a sharper $S-T_-$ degeneracy characteristic of a smaller mixing term.

The lines arising in the FFT plots can be fit by the energy splitting between the three lowest lying states of the system depicted in Fig. 6.2f with $g_\perp^+ = 12.00$, $g_\perp^- = 2.04$, $g_\parallel^+ = 0.10$ and $g_\parallel^- = 0.43$ and $t_C = 11.38\,\mu\text{eV}$. The latter is extracted from exchange oscillation measurements (see Supplementary Fig. 6.6). We find a small offset of $100\,\mu\text{T}$ in the perpendicular field which leads to a small asymmetry in the FFT plots. We further validate our model by observing the dynamics of the system under fast pulsing for magnetic field angles close to the in-plane direction (see Supplementary Sec. 6.7.2). We find excellent agreement between the observed frequency lines and our predictions.

Interestingly $|g_\parallel^-| > |g_\parallel^+|$ while $|g_\perp^-| < |g_\perp^+|$. This means that the g-factors in the out of plane direction have the same sign while they exhibit opposite signs in the in plane direction. To understand this observation we investigate the effect of the dot geometry on the g-factors, anticipating a particularly accentuated effect on the in-plane g-factor due to its small zeroth order value of $g_\parallel^0 \sim 0.2$. This value is considered to be phenomenological in the sense that it incorporates corrections due to system specific influences such as strain and material composition [125–127]. As is shown in Supplementary Sec. 6.7.8 by using the semi microscopic Luttinger-Kohn Hamiltonian as a starting point, the effects of the intrinsic HH-LH mixing and an elliptical confinement potential can combine to yield g-factor renormalizations. While the correction to the out-of-plane g-factor is $|\delta g_\perp| < 10^{-2}$ for the values considered and hence negligible, the in-plane g-factor can be altered considerably,

$$g_\parallel = g_\parallel^0 - \xi_1 \frac{\hbar(\omega_x - \omega_y)}{\hbar(\omega_x + \omega_y) - \xi_2 \Delta}. \tag{6.1}$$

Here, $\xi_1 \approx 20.3$ and $\xi_2 \approx 6.0$ are material specific constants, Δ is the HH-LH splitting and $\hbar\omega_{x,y}$ are the in-plane confinement energies. It can be seen from Fig. 6.2g that the in-plane g-factor corrections can be negative in one dot but not in the other for opposite elliptical confinement.

6.4 t_{SO} extraction with single Landau-Zener passages

We now turn to extract t_{SO} by analyzing Δ_{ST_-} in more detail. After calibrating the sweep rate and position of the $S - T_-$ degeneracy (Supplemetary Fig. 6.9), we perform Landau-Zener sweeps at $|B| = 20\,\mathrm{mT}$ and extract Δ_{ST_-} from P_{LZ} (Fig. 6.3a). We vary τ_R during the first passage over the avoided crossing, creating a superposition of S and T_-, and keep the return sweep diabatic in order to maintain this superposition (inset of Fig. 6.3a). The extracted Δ_{ST_-} is reported in Fig. 6.3b. In general, Δ_{ST_-} may depend on effects influencing the hole spins such as the g-factor differences in the two dots, the SOI and possible effective magnetic field gradients caused by the hyperfine interaction [128]. While the hyperfine interaction can result in a strong out-of-plane hyperfine component δb_Z for HH states due to a special Ising-type form [32], the inhomogeneous dephasing times extracted for $B_\perp$ of $\approx 700\,\mathrm{ns}$ at $1\,\mathrm{mT}$ in Ref. [80] give an upper limit for the hyperfine component $\delta b_Z < 2\,\mathrm{neV}$, suggesting that the effects of the nuclear spin bath may safely be neglected. In planar HH DQD systems the SOI can be parametrized by a real in-plane spin-orbit vector $\mathbf{t}_{SO} = (t_x, t_y, 0)$. Such in-plane spin-flip tunneling terms stem from the cubic Rashba SOI [129], while this type of SOI does not induce out-of-plane terms t_z. In a basis in which the total Hamiltonian is diagonal in the absence of the SOI and g-factor differences, the $S - T_-$ splitting has the form [130]

$$\Delta_{ST_-} = \left|\Delta_{SO} \sin\left(\frac{\Omega}{2}\right) + \Delta E_Z \cos\left(\frac{\Omega}{2}\right)\right|, \tag{6.2}$$

where the spin-orbit splitting Δ_{SO} and the Zeeman splitting ΔE_Z due to anisotropic site-dependent g-tensors read

$$\Delta_{SO} = t_y + i t_x \frac{g_\perp^+ \sin\theta}{\sqrt{(g_\parallel^+ \cos\theta)^2 + (g_\perp^+ \sin\theta)^2}}, \tag{6.3}$$

$$\Delta E_Z = \frac{\mu_B B}{4\sqrt{2}} \frac{(g_\parallel^- g_\perp^+ - g_\parallel^+ g_\perp^-)\sin(2\theta)}{\sqrt{(g_\parallel^+ \cos\theta)^2 + (g_\perp^+ \sin\theta)^2}}, \tag{6.4}$$

and $\Omega = \arctan\left(2\sqrt{2}t_C/\epsilon^*\right)$ is the mixing angle at the anticrossing. The analytical result (6.2) agrees well with the numerical results obtained by exact diagonalization of the system Hamiltonian for all θ except in a narrow region around $\theta = 0$ ($|\theta| \lesssim 2°$, Fig. 6.3d). We attribute these deviations to the small in-plane Zeeman energies which violate the assumption of an isolated two-level system made when deriving (6.2) (see Supplementary Section 6.7.6). Due to the opposite sign g-factor corrections in the dots the Zeeman splitting ΔE_Z can be the dominant contribution to Δ_{ST_-}, exceeding the spin-orbit splitting by one order of magnitude at small angles. Even when the magnetic field has a large out-of-plane component, the effect of different g-factors can contribute crucially to Δ_{ST_-} (Fig. 6.3c).

The extracted Δ_{ST_-} in Fig. 6.3b can be fit by the model with t_x and t_y as free parameters and t_C, $g_\perp^+$,$g_\perp^-$,$g_\parallel^+$,$g_\parallel^-$ extracted from previous measurements. Between -25 and 25° the splitting seems to drop to zero as the Landau-Zener assumptions of diabatic return sweeps are not met and an extraction of

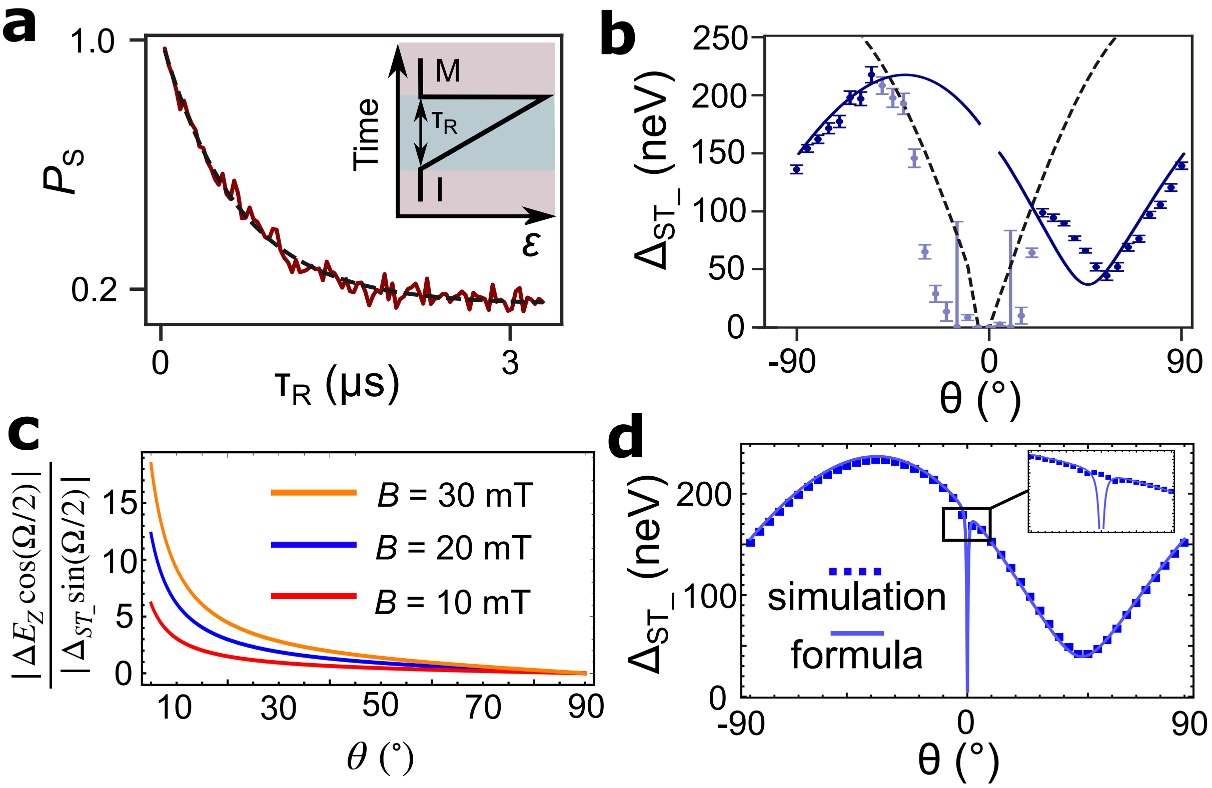

Figure 6.3: a) The single LZ passage pulse sequence (inset) leads to a singlet return probability P_S that decays exponentially with the ramp time τ_{R}. A fit to the Landau-Zener transition formula (black dashed line) allows to extract the values of Δ_{ST_-}. b) Δ_{ST_-} as a function of magnetic field angle. The extracted Δ_{ST_-} is fit to Eq. 6.2 with t_x and t_y as fitting parameters. The black dashed line represents the maximum Δ_{ST_-} as a function of θ that can be reliably measured by a single LZ passage. The light colored data points are, therefore, excluded from the fit. c) Comparison between the two contributions to Δ_{ST_-}. At small angles, the Zeeman splitting ΔE_Z can exceed the spin-orbit splitting Δ_{SO} by one order of magnitude even at $B = 20\,\mathrm{mT}$. d) Comparison between the analytical result (solid line, Eq. (6.2)) and numerical simulations (squares) for the $S - T_-$ splitting Δ_{ST_-}. We find excellent agreement except for a narrow region around $\theta = 0$ (inset), where the analytical expression fails due to the small in-plane Zeeman energies. We use the values of the g-factors and the spin-orbit vector extracted in the text in panels c) and d).

Δ_{ST_-} is not accurate. The black dashed line corresponds to the maximum Δ_{ST_-} that allows a diabatic passage with a rise time of 2 ns of our pulses ($P_{LZ,max} = 0.99 = \exp\left(-\frac{2\pi\Delta^2_{ST,max}}{\hbar v}\right)$). The model fits the dark blue datapoints with $t_x = 129.0 \pm 18.0$ neV and $t_y = -369.8 \pm 13.8$ neV, yielding the total spin-flip tunneling element $t_{SO} = \sqrt{t_x^2 + t_y^2} =$ 392.0 neV.

6.5 Funnel Simulations and l_{SO}

Having characterized all the elements in the Hamiltonian from independent measurements we can now reproduce the Funnel plots in Fig.6.1 exactly (Fig. 6.4). In particular the sharper line at $\theta = 60$° (Fig. 6.4b) as well as the $S - T_-$ oscillations for $\theta = 10$° (Fig. 6.4c) reflect what we observe in the data. Even with $t_{SO} = 0$ the in-plane g-factor difference induces $S - T_-$ oscillations (Fig. 6.4d) further confirming its dominant role in determining the size of Δ_{ST_-}.

Finally, we remark that in systems with a nonlinear SOI the spin-orbit length inferred from t_{SO} cannot be regarded as a good figure of merit for material comparison anymore. Following Ref. [128], we express t_{SO} in terms of the spin-conserving tunneling element t_C using the explicit expressions obtained in Ref. [129]. We find

$$t_{SO} = \frac{4t_C}{3}\frac{d}{l_{SO}}, \tag{6.5}$$

where d is the interdot distance and the spin-orbit length for a cubic Rashba SOI reads

$$l_{SO} = \frac{1}{\lambda_R}\frac{4\hbar\omega_0 + d^2 m\omega_0^2}{\sqrt{1 - S^2}d^2 m^3\omega_0^3} \tag{6.6}$$

for circular dots. Here, $\hbar\omega_0$ is the in-plane confinement energy, m is the in-plane HH mass, S is the overlap between the left and right dot states, and λ_R is the effective cubic Rashba coefficient with units $[\lambda_R] =$ energy/momentum^3. One can see that it depends not only on material parameters via λ_R but also on the dot geometry via ω_0, d and S (see Supplementary Sec. 6.7.7).

6.6 Conclusion

In conclusion, we have extracted all the relevant parameters of our system from the dynamics of singlet-triplet oscillations. Especially the in-plane dynamics are largely dominated by the coupling between S and T_-. We have mapped the $S - T_-$ splitting as a function of magnetic field and found that both the SOI and the Zeeman energy are influencing the observed complex angular dependence. We have furthermore demonstrated, that the g-factor anisotropy and in particular the in-plane g-factor sign difference can lead to a considerable contribution to Δ_{ST_-} in the in-plane direction. Such a large avoided

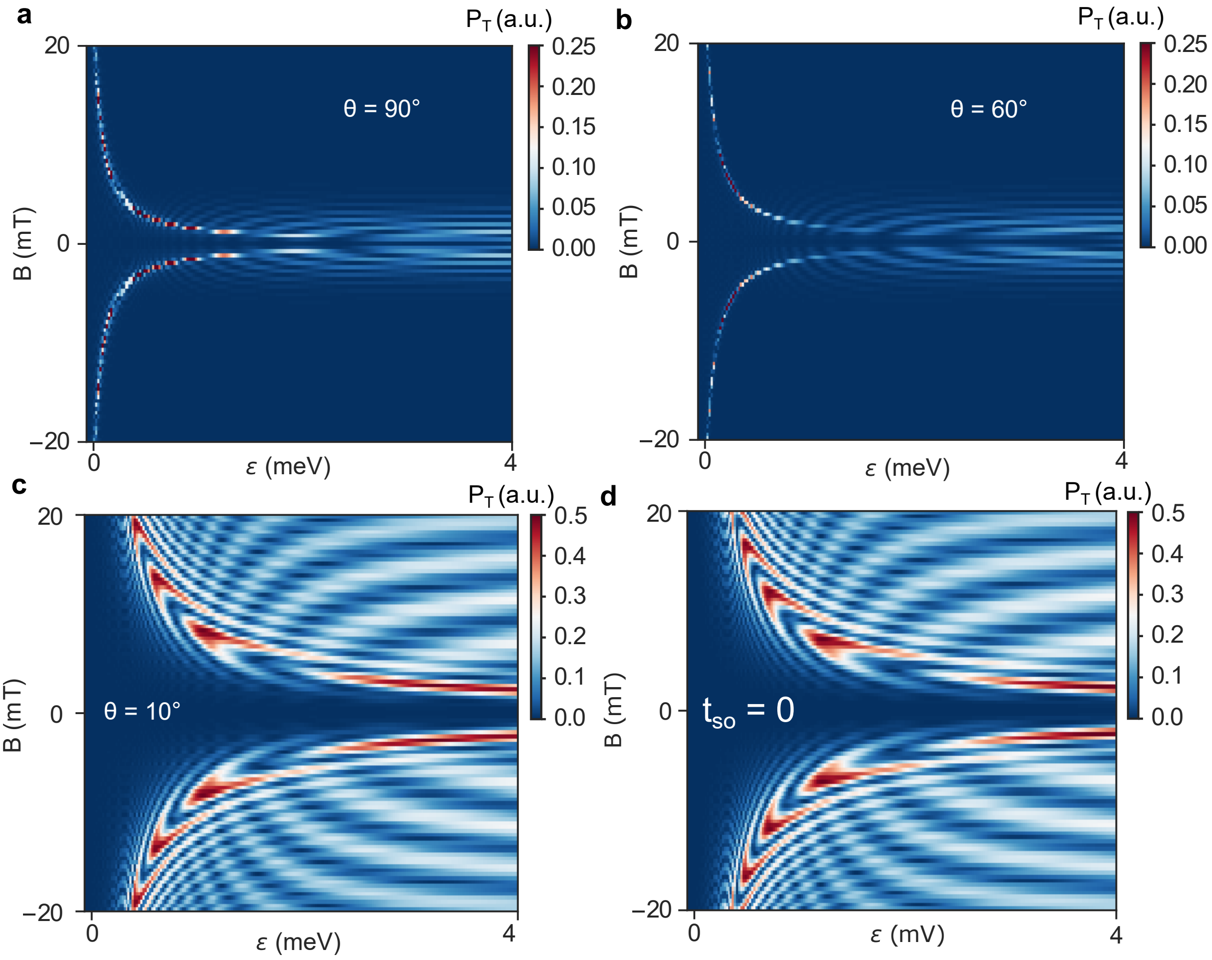

Figure 6.4: Funnel simulations with the master equation approach using qutip. a) Funnel for $\theta = 90°$ showing the $S - T_-$ degeneracy as an increased triplet return probability. For large ϵ $S - T_0$ oscillations are visible but decay at higher fields due to relaxation processes [97]. b) Funnel for $\theta = 60°$. Here the $S - T_-$ degeneracy is fainter than in a) because the interplay t_{SO} and $g_{\parallel}^-$ reduces the $S - T_-$ splitting. c) Funnel for $\theta = 10°$ which now resembles a butterfly. The $S - T_-$ degeneracy evolves into an obvious oscillation pattern which interferes at large ϵ with the $S - T_0$ oscillations. The simulations take the model Hamiltonian with the experimentally extracted parameters as input and perform the time evolution calculation returning the combined triplet return probability $((P_{T_+} + P_{T_-} + P_{T_0}))$. All the simulations nicely reproduce the experimental data observed in Fig. 6.1. d) A simulation with $t_{SO} = 0$ but with all the other values of the model as in c) again reveals the butterfly shape of the $S - T_-$ degeneracy. Now even more oscillations can be seen as the t_{SO} term does not reduce the size of Δ_{ST_-} caused by the g-factor difference at $\theta = 10°$.

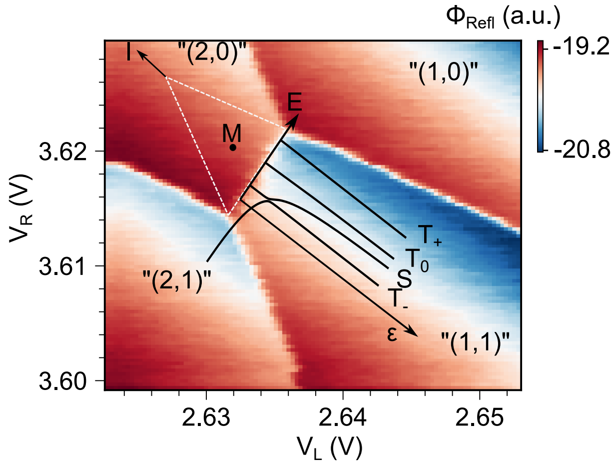

Figure 6.5: The effective hole numbers are labelled “(n_L, n_R)”. The real hole number is $(n_L+2, 2n+n_R)$ since we do not know the exact number of holes in the right dot. The dashed triangle marks the region in which Pauli spin blockade occurs and the measurement point (M) is located at the center of it at $\epsilon = \epsilon_M$. “I” marks the initialization point. The dispersion relation is overlaid on top of the “(1,1)” region. The avoided $S-T_-$ crossing occurs at $\epsilon = \epsilon^*$

crossing is beneficial for the operation of Loss-DiVincenzo qubits [18] as it reduces initialization times and increases initialization fidelity (see Fig. 6.10) [61, 131]. On the other hand, the interplay between t_{SO} and the g-factors also results in a small avoided crossing at $\theta = 60°$. This constitutes a sweet spot for $S-T_0$ qubit operation as the main driving terms ($g_\perp^- \sin\theta$) are still large but the leakage to T_- during initialization and read-out is suppressed. Our results emphasize that a detailed understanding of the g-factor anisotropy and the SOI are key in designing future qubit experiments in two-dimensional Ge hole gases and other systems where a strong SOI renormalizes the g-factors.

6.7 Supplementary Information

6.7.1 Stability diagram, pulsing, tunnel coupling

The stability diagram around the transition of interest is reported in Fig. 6.5. The effective hole numbers are labelled “(n_L, n_R)” while the real hole number is (n_L+2, n_R+2n). The dispersion relation is overlaid and highlights the 4 states involved in the dynamics of the system. When pulsing we initialize (I) deep in “(2,0)” with a short pulse knowing that the short relaxation time T_1 ensures decay to a singlet. Only for the in-plane field direction this is not true as is further discussed below.

We extract the tunnel coupling from exchange oscillations. A typical pulse sequence to probe the exchange interaction J is depicted in the inset of Fig. 6.6a. After initialization in $S(2,0)$ the system is pulsed rapidly to large ϵ and left to evolve for a time corresponding to a $\pi/2$ rotation around the x-axis of the Bloch-sphere. A subsequent pulse at lower ϵ for a time τ_S increases the exchange interaction

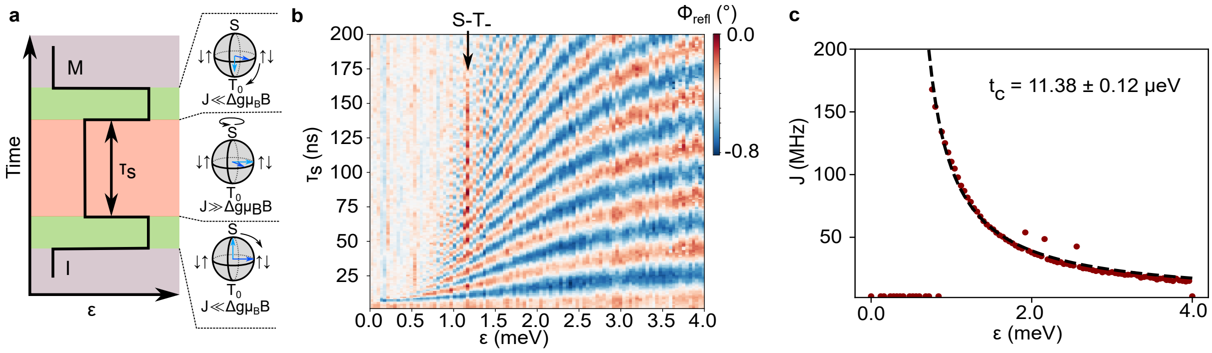

Figure 6.6: a) The pulse sequence to obtain exchange oscillations features two short pulses at high ϵ (green) where the exchange interaction $J \ll \Delta g \mu_B B$. Here, the system rotates around the x-axis of the Bloch sphere. The exchange interaction can be turned on by pulsing to lower ϵ (orange). Here $J \gg g_\perp^- \mu_B B$ and the system evolves around the z-axis of the Bloch sphere. b) The exchange oscillations as a function of ϵ and separation time τ_S at $B_\perp = 1\,\mathrm{mT}$ display the expected frequency increase for lower detuning as the exchange interaction becomes dominant. Around $1.2\,\mathrm{meV}$ the $S - T_-$ degeneracy is visible as an increase in triplet return signal (red). c) The magnitude of J in MHz can be fit by $J(\epsilon, t_C) = \sqrt{\frac{\epsilon^2}{4} + 2t_C^2} - \frac{\epsilon}{2}$ (black dashed line) and we extract $t_C = 11.38\,\mu\mathrm{eV}$.

$J(\epsilon) = \sqrt{\frac{\epsilon^2}{4} + 2t_C^2} - \frac{\epsilon}{2}$. Therefore, the oscillation frequency $f = \sqrt{J(\epsilon)^2 + (g_\perp^- \mu_B B)^2}$ will reflect the change in J and increase for lower ϵ. The fit in Fig. 6.6, therefore, allows to extract the tunnel coupling. As the coherence time for very low ϵ tends to 0, all the points at $\epsilon < \epsilon^*$ are not considered in the fit. ϵ^* is highlighted by the black arrow where the $S - T_-$ mixing is prominently visible.

6.7.2 Singlet-triplet dynamics for small angles

We probe singlet-triplet oscillations at small angles by rapidly pulsing to large ϵ and observing the signal of the returned state. In Fig. 6.7a the resulting oscillation pattern is displayed for $\theta = 0°$. The FFT in 6.7b reveals several frequency components. The dotted lines are extracted from our model and the corresponding dispersion relation is depicted in 6.7c. The colored arrows mark the transitions we actually observe in the FFT plot. The singlet-triplet oscillation and FFT plots for $\theta = 5, 10, 20$ and 30° are further depicted in Fig. 6.8. We generally find a good agreement with our theoretical model.

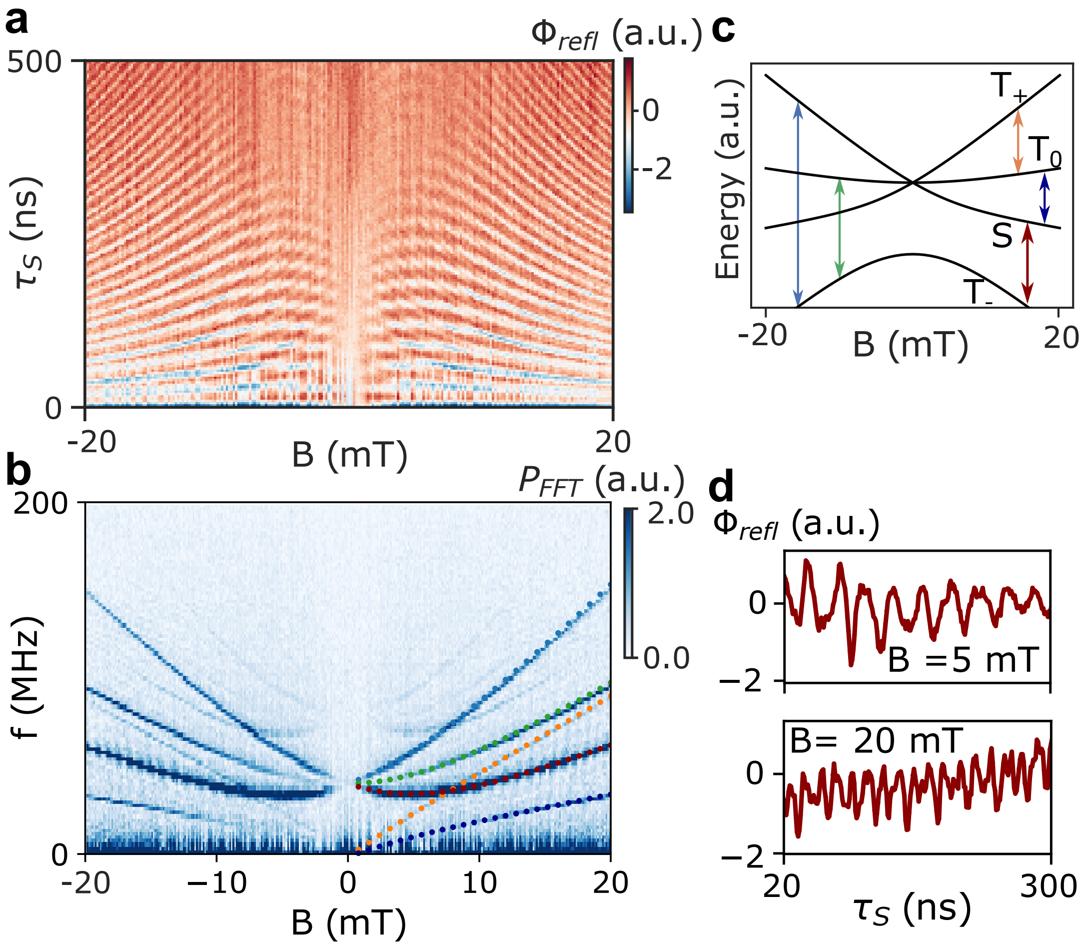

Figure 6.7: a) Singlet oscillations as a function of in-plane magnetic field and free evolution time under fast pulsing revealing a complicated oscillation pattern. b) A FFT of a) unveils many frequency components. The dotted lines are fits to the transition frequencies highlighted in c). We find good agreement between the data and the model. An additional set of lines appears at slightly higher frequencies which we attribute to spectral leakage due to the imperfect initialization [132]. c) The arrows point out the transition frequencies between the eigenstates for the in-plane dispersion relation.

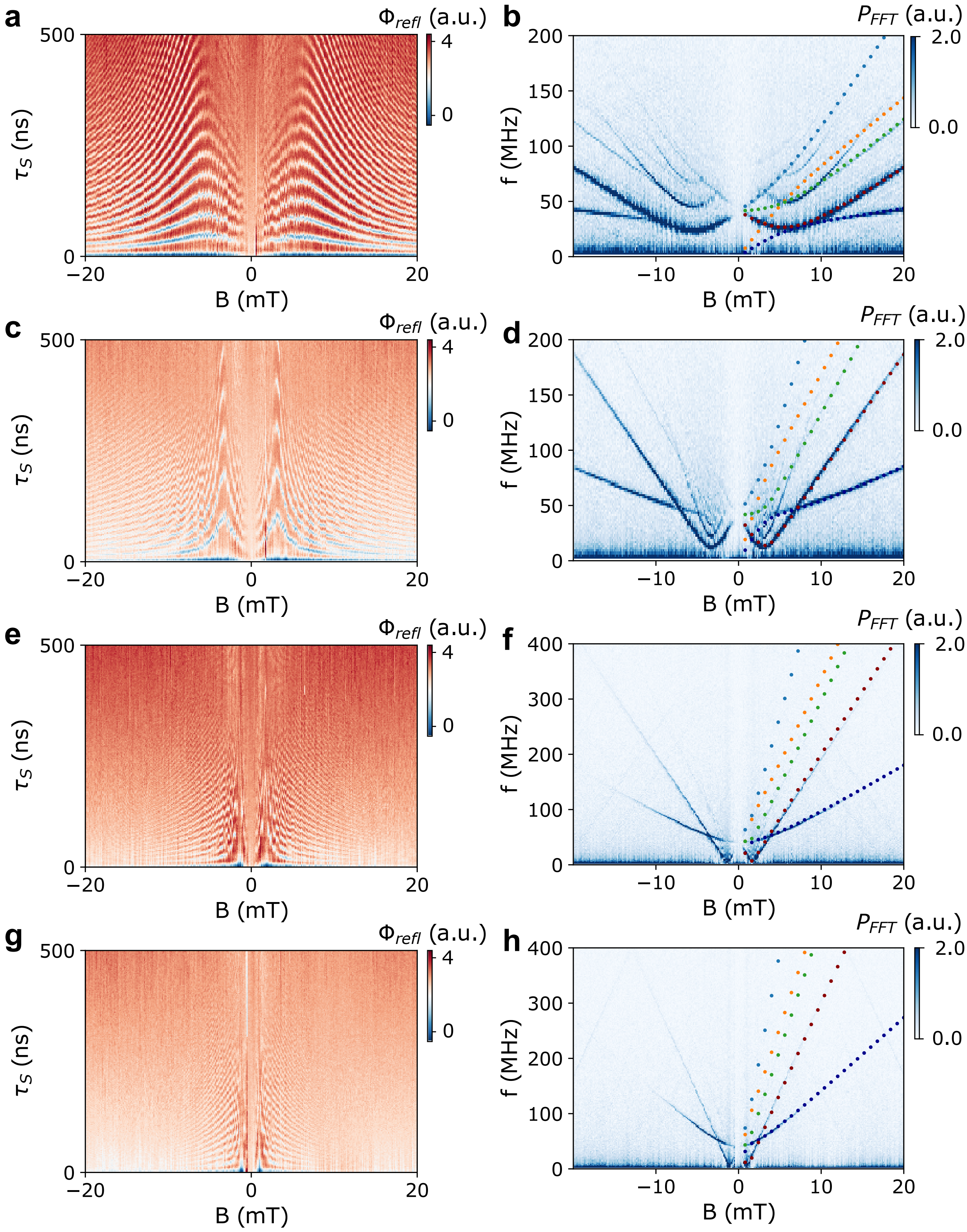

Figure 6.8: Singlet-triplet oscillations as a function of B at different θ. a) Oscillations at $\theta = 5°$. b) FFT of a) with overlaid frequency lines for positive fields as extracted from the model. c) Oscillations at $\theta = 10°$. d) FFT of c) with overlaid frequency lines as extracted from the model. e) Oscillations at $\theta = 20°$. f) FFT of e) with overlaid frequency lines as extracted from the model. g) Oscillations at $\theta = 30°$. h) FFT of g) with overlaid frequency lines as extracted from the model.

6.7.3 $S - T_-$ degeneracy as a function of magnetic field direction

We report the $S - T_-$ degeneracy for different magnetic field directions in Fig. 6.9. For the out-of-plane direction the typical funnel shape can clearly be observed. Towards the in-plane direction the $S - T_-$ degeneracy evolves into an oscillation pattern suggesting a large coupling term between S and T_-. This anisotropy, which follows the g-factor anisotropy of confined HH states, indicates a dependence related to the Zeeman terms in H_{tot}. Indeed, our model can reproduce the plots assuming $g_{\|}^{-} > g_{\|}^{+}$.

We furthermore report the effective level velocity $v = |\frac{dJ(\epsilon)}{d\epsilon}|_{\epsilon=\epsilon^*} \frac{\Delta\epsilon}{\tau_R}$ with $\Delta\epsilon = 4\,\text{meV}$, $\tau_R = 2\,\text{ns}$ as a function of the magnetic field angle θ for a magnetic field strength of $20\,\text{mT}$ (Fig. 6.10). Towards the in-plane direction the velocity is reduced as the Zeeman splitting is lowered due to the g-factor anisotropy. As a result, for small angles, the shortest possible ramp time does not allow a diabatic passage over the avoided crossing as pointed out in Fig. 6.3b. Incidentally, this is a favorable property for single spin qubits where fast initialization in the $|\downarrow\downarrow\rangle$ state is required. Indeed, for $\theta = 0$ the ground state in (1,1) can be initialized with fidelity $F = 1 - P_{LZ} \approx 1$ at a ramp time of 20 ns (Fig. 6.10).

6.7.4 Decay of T_0 state

The relaxation time of the T_0 state does not depend on the SOI (Eq. 6.21)and, therefore, displays a different anisotropy than the relaxation for the T_- state. To probe this, we perform diabatic pulses and fit the decay of the return signal to $\Phi_{refl}(\tau_M = 0)\exp\left(-\frac{\tau_M}{T_1}\right)$. As shown in Fig. 6.11 the relaxation time follows $\approx \frac{1}{g_\perp^- \mu_B B \sin\theta}^2$ and is generally $< 10\,\mu\text{s}$ making read-out at large fields challenging. Therefore, shelved read-out [100] could be harvested where the read-out distinguishes between S and T_-. At $\theta = 60°$ the relaxation of the T_- state is maximised offering a sweet spot for shelved read-out.

6.7.5 Initialization and spectral leakage

The fast Fourier transform plots in Fig. 6.7 and Fig. 6.8 display additional frequency components not predicted by our model which are especially evident at $\theta = 5°$ and $10°$ and can be attributed to improper initialization of the singlet state prior to a pulse. In [132] a similar system is analyzed and a general formula for the singlet return probability P_S of non-properly initialized state (a superposition of S and T_-) is extracted as

$$P_S = P_S' P + [1 - P_S'](1 - P), \tag{6.7}$$

where P is the return probability with correct singlet initialization and

$$P_S' = \frac{P\exp\left(-\frac{\tau_M}{T_1}\right) - 1}{(2P-1)\exp\left(-\frac{\tau_M}{T_1}\right) - 1}. \tag{6.8}$$

Here, τ_M is the measurement time and T_1 is the relaxation time of the T_- state in the read-out point. It is clear that for $\tau_M \gg T_1$ we find $P_S = P$. However, when $\tau_M \approx T_1$ the singlet return probability deviates

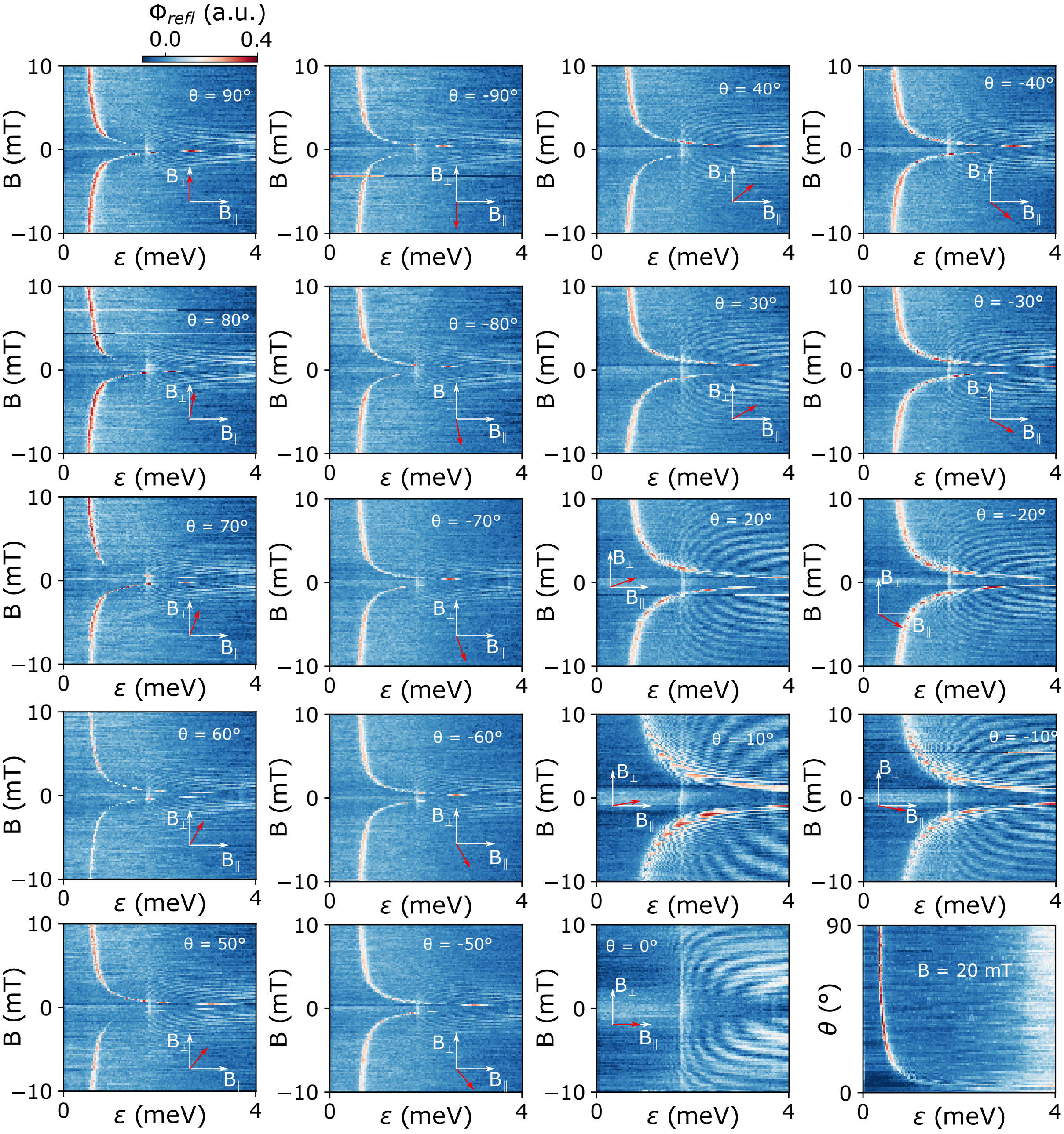

Figure 6.9: $S - T_-$ degeneracy funnel for different angles for $\tau_S = 250\,\mathrm{ns}$. Clearly the funnel is well defined for out-of-plane fields and evolves into an oscillation pattern for in-plane fields. This suggests a dependence stemming from the g-factor anisotropy of HH states. In fact, our model fits the experimentally observed funnel shapes with $g_\perp^+ = 12$, $g_\perp^- = 2.05$, $g_\parallel^+ = 0.1$, $g_\parallel^- = 0.43$. Moreover, the spin-orbit vector pointing along $\theta = 60°$ gives rise to an asymmetry between the sharpness of the funnel at $+60°$ and $-60°$, also confirmed by single Landau-Zener sweeps. The bottom right plot shows the $S - T_-$ degeneracy at 20 mT for positive angles. This is used to calibrate the pulse amplitude necessary to overcome the $S - T_-$ degeneracy in the single Landau-Zener sweeps.

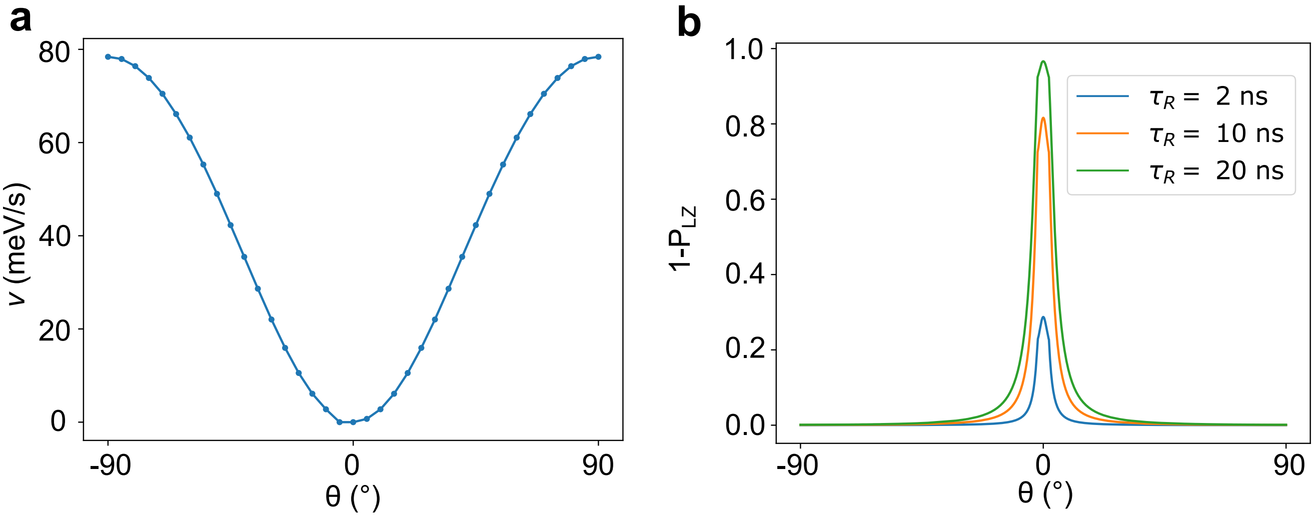

Figure 6.10: a) Velocity v as a function of θ for a magnetic field strength of 20 mT. Because of the g-factor anisotropy the Zeeman energy in the in-plane direction is lower. Consequently the velocity is reduced as $|dJ/d\epsilon|_{\epsilon=\epsilon^*}$ becomes smaller. b) $1 - P_{LZ}$ as a function of θ for different ramp times. For a ramp time of 20 ns the ground state in (1,1) can be initialized with fidelity close to 1. Hence, the g-factor difference in the in-plane direction allows fast and high fidelity initialization for single spin qubits.

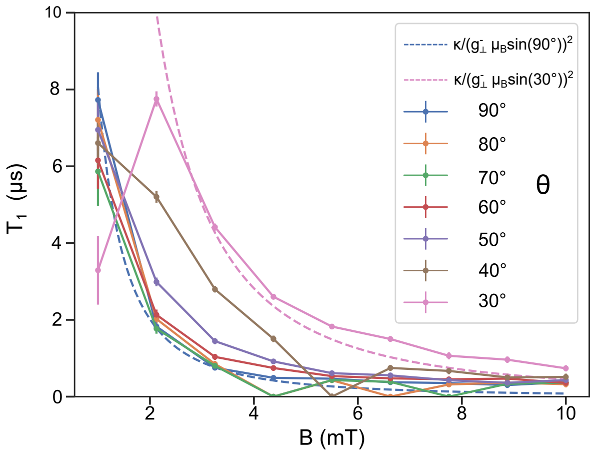

Figure 6.11: Relaxation time of the $|T_0\rangle$ state as a function of magnetic field strength and angle. In contrast to the decay of the T_- state the relaxation of the T_0 state is proportional to $\kappa/\Delta E_Z^2$ (dashed lines) wiht κ a proportionality constant. T_1 generally decreases for larger magnetic fields. Only for $\theta = 30°$ the relaxation time maximizes at 2 mT. This occurs because for lower magnetic fields the presence of the $S - T_-$ avoided crossing lowers the T_0 return probability as a diabatic passage can not be achieved with the finite rise time of our AWG. For angles $\theta < 30°$ no diabatic passage can be achieved. Therefore we cannot extract T_1 of the T_0 state.

significantly from P. In Fig. 6.12a we show a line trace of Fig. 6.8 at $\theta = 5°$ and $B = 8.5\,\mathrm{mT}$. We clearly see that the oscillations are not sinusoidal. Fig. 6.12b displays the FFT of the line trace and 3 distinct peaks can be observed. However, more peaks are present but buried in the background. Fig. 6.12c shows a simulation of the time evolution of the state. The red trace assumes perfect initialization whereas the blue trace depicts the corrected singlet return probability according to Eq. 6.7 and 6.8 with $\tau_M \approx T_1$. The blue trace indeed resembles what we measure. Furthermore, we inspect the FFT of the simulated data and find that indeed for the improperly initialized curve we observe additional frequency components. In the red trace we find only the frequency components corresponding to the transitions highlighted in Fig. 6.7 of the main text. The FFT plot extracted from the simulation of the properly initialized state is depicted as a function of magnetic field in Fig. 6.12e. On the other hand, the improperly initialized simulated FFT is plotted in Fig. 6.12f. Here, several additional lines are clearly visible and follow what we measure in Fig. 6.8b albeit with altered Fourier amplitudes.

6.7.6 The model

We consider a tunnel coupled double quantum dot in the presence of an external magnetic field and the spin-orbit interaction (SOI). The system is modelled by the Hamiltonian

$$H_{tot} = H_{orb} + H_Z + H_{SO}, \tag{6.9}$$

where H_Z is the Zeeman Hamiltonian and H_{SO} describes the SOI. The orbital part H_{orb} reads

$$H_{orb} = \epsilon|S_{20}\rangle\langle S_{20}| + \sqrt{2}t_C\left(|S_{11}\rangle\langle S_{20}| + |S_{20}\rangle\langle S_{11}|\right), \tag{6.10}$$

where $|S_{20}\rangle$ is the singlet with double occupancy in the left dot which is detuned by an amount ϵ from the $(1,1)$ configuration, t_C is the tunnel element in the one-particle picture, and $|S_{11}\rangle$ is the singlet with one hole in each dot. Diagonalizing (6.10) yields the hybridized singlet states

$$|S_E\rangle = \cos\left(\frac{\Omega}{2}\right)|S_{20}\rangle + \sin\left(\frac{\Omega}{2}\right)|S_{11}\rangle, \tag{6.11a}$$

$$|S_G\rangle = \cos\left(\frac{\Omega}{2}\right)|S_{11}\rangle - \sin\left(\frac{\Omega}{2}\right)|S_{20}\rangle, \tag{6.11b}$$

where $\Omega = \arctan\bigl(2\sqrt{2}t_C/\epsilon\bigr)$ is the orbital mixing angle and the corresponding energies are $E(S_{E/G}) = \epsilon/2 \pm \sqrt{\epsilon^2/4 + 2t_C^2}$. In the following we consider a regime where the excited singlet is far detuned and may be neglected. Defining $|S\rangle \equiv |S_G\rangle$, we may focus on the four dimensional space spanned by the states $|S\rangle$, $|T_+\rangle$, $|T_0\rangle$ and $|T_-\rangle$, where $|T_{0,\pm}\rangle$ denote the triplet states in the (1,1) configuration.

For a magnetic field of magnitude B and angle θ as measured from the plane defined by the heterostruc-

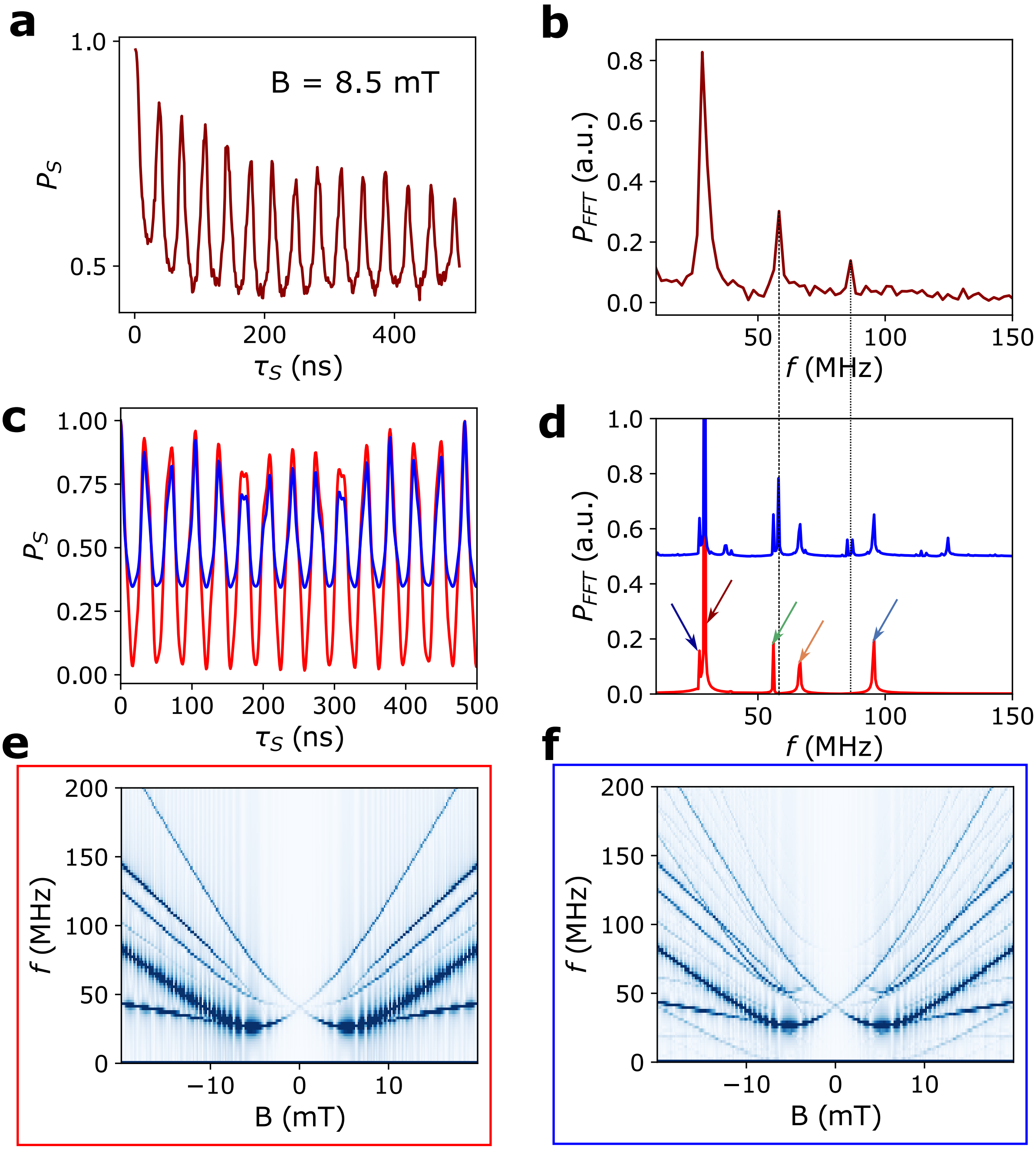

Figure 6.12: a) Line trace at 8 mT from Fig. 6.8a featuring a non-sinusoidal oscillation pattern. b) FFT of a) highlighting its frequency components. c) Simulated time evolution for the conditions in a) with proper initialization in a singlet (red) and improper initialization (blue). d) FFT of c) highlighting the frequency components of the blue and red trace (blue is offset for clarity). Comparing the 2 curves we notice additional frequency components arising in the blue one which can be mapped to the observed spectral peaks of b). The red and blue trace, however, both display peaks at the transition frequencies expected from our model. e) FFT of the simulated time evolution with proper initialization. All the transitions highlighted in Fig. 6.7c are visible. f) FFT of the simulated time evolution under improper initialization. The additional frequency lines resemble what we measure in Fig. 6.8b.

ture, the Zeeman Hamiltonian H_Z reads,

$$\begin{aligned} H_Z = \frac{\mu_B B}{2}\Bigg\{ &\sin\theta \left[\sum_{\pm} \pm g_{\perp}^{+} |T_{\pm}\rangle\langle T_{\pm}| + g_{\perp}^{-} \left(|S\rangle\langle T_0| + |T_0\rangle\langle S|\right) \cos\left(\frac{\Omega}{2}\right)\right] \\ &+ \frac{\cos\theta}{\sqrt{2}} \left[\sum_{\pm} \left(g_{\parallel}^{+} |T_0\rangle\langle T_{\pm}| \mp g_{\parallel}^{-} |S\rangle\langle T_{\pm}| \cos\left(\frac{\Omega}{2}\right) + \text{H.c.}\right)\right]\Bigg\}, \end{aligned} \tag{6.12}$$

where $g_j^{\pm} = g_j^L \pm g_j^R$. Note that the axes are labelled such that y is the double quantum dot axis, and the magnetic field is applied in the x-z-plane.

Finally, we consider a SOI parametrized by an in-plane spin-orbit vector, $\mathbf{t}_{SO} = (t_x, t_y, 0)$, where all entries are real. Such in-plane spin-flip tunneling terms stem from the cubic Rashba SOI [129], while this type of SOI does not induce out-of-plane terms t_z. Consequently, the spin-orbit Hamiltonian H_{SO} reads,

$$H_{SO} = \sin\left(\frac{\Omega}{2}\right) \sum_{\pm} (t_x \pm i t_y) |T_{\pm}\rangle\langle S| + \text{H.c.}, \tag{6.13}$$

An appropriate basis for studying the singlet-triplet anticrossing is given by the eigenstates of the total Hamiltonian (6.9) for equal g-factors and in the absence of the SOI. Transforming the total Hamiltonian in the presence of the SOI and g-factor differences into this basis, we find for the singlet-triplet splitting,

$$\Delta_{ST_-} = \left| \Delta_{SO} \sin\left(\frac{\Omega}{2}\right) + \Delta E_Z \cos\left(\frac{\Omega}{2}\right) \right|, \tag{6.14}$$

where the spin-orbit splitting Δ_{SO} and the Zeeman splitting ΔE_Z are given by

$$\Delta_{SO} = t_y - i t_x \frac{g_{\perp}^{+} \sin\theta}{\sqrt{(g_{\parallel}^{+} \cos\theta)^2 + (g_{\perp}^{+} \sin\theta)^2}}, \tag{6.15a}$$

$$\Delta E_Z = \frac{\mu_B B}{4\sqrt{2}} \frac{\left(g_{\parallel}^{-} g_{\perp}^{+} - g_{\parallel}^{+} g_{\perp}^{-}\right) \sin(2\theta)}{\sqrt{(g_{\parallel}^{+} \cos\theta)^2 + (g_{\perp}^{+} \sin\theta)^2}}. \tag{6.15b}$$

In Landau-Zener measurements the mixing angle Ω is a function of the detuning at the anticrossing between the singlet and the low-energy polarized triplet, which is described by the equation

$$\frac{\epsilon}{2} - \sqrt{\frac{\epsilon^2}{4} + 2t_C^2} = -\frac{\mu_B B}{2} G(\theta), \tag{6.16}$$

where $G(\theta) = \sqrt{(g_{\parallel}^{+} \cos\theta)^2 + (g_{\perp}^{+} \sin\theta)^2}$. Rearranging gives the detuning at which the anticrossing is located,

$$\epsilon_* = \frac{8t_C^2 - (\mu_B B G(\theta))^2}{2\mu_B B G(\theta)}, \tag{6.17}$$

and consequently the mixing angle at the anticrossing reads

$$\Omega_* = \Omega(\epsilon_*) = \arctan\left(\frac{4\sqrt{2} t_C \mu_B B G(\theta)}{8t_c^2 - (\mu_B B G(\theta))^2}\right). \tag{6.18}$$

In Fig. 6.3d we show a comparison between the analytical result for Δ_{ST_-} evaluated at the detuning at the anticrossing and simulated results obtained by exact numerical diagonalization of the total system Hamiltonian (6.9). For the latter, we obtain the splitting as the minimum difference between the two lowest eigenenergies. We find excellent agreement for all angles except in a narrow region around $\theta = 0$. The dip predicted by the analytical formula is not present in the simulations. We attribute this deviation to the small in-plane Zeeman energies $\sim g_{\parallel}^{+}$ which violate the assumption of a well separated two-level system. In this case the splitting is not given by the simple expression (6.14) which describes the coupling between the ground state singlet and the low-energy polarized triplet. Instead, the contributions of the remaining two triplet states must be taken into account near $\theta = 0$, and the coupling is altered.

6.7.7 Spin-orbit vector, field and length

In Eq. (6.13) we model the SOI using the spin-orbit vector $\mathbf{t}_{\text{SO}} = (t_x, t_y, t_z)$ [123] which contains genuine spin-flip tunneling terms. In our structure we consider an in-plane spin-orbit vector, but different forms with $t_z \neq 0$ are possible in other systems. The most general effective form in the basis $\mathcal{B}$ defined in Sec. 6.7.6 is

$$H_{SO} = \sin\left(\frac{\Omega}{2}\right)\left(i\sqrt{2}t_z|T_0\rangle\langle S| + \sum_{\pm}(t_x \pm it_y)|T_\pm\rangle\langle S| + \text{H.c.}\right). \tag{6.19}$$

Often, however, the SOI is parametrized by a spin-orbit field $\mathbf{M}_{SO}^{d}$ in dot $d \in \{L, R\}$,

$$H_{SO} = \cos\left(\frac{\Omega}{2}\right)\frac{\mu_B}{2}\sum_{d}\mathbf{M}_{SO}^{d}\cdot\boldsymbol{\sigma}^{d}, \tag{6.20}$$

where $\boldsymbol{\sigma}^{d}$ is a vector containing the Pauli matrices in dot d, and we include the factor $\cos(\Omega/2)$ to make the similarity with the Zeeman term in (6.12) more explicit. A general argument shows that the spin-orbit vector $\mathbf{t}_{SO}$ cannot be mapped to the spin-orbit field $\mathbf{M}_{SO}$. On the one hand, the Hamiltonian in Eq. (6.13) is time reversal invariant while the Zeeman type Hamiltonian (6.20) with a real spin-orbit field is not. On the other hand, a complex spin-orbit field would make (6.20) non Hermitian, and hence the two quantities $\mathbf{t}_{SO}$ and $\mathbf{M}_{SO}$ cannot be related. Taking the spin-orbit field to be a function of the crystal momenta, $\mathbf{M}_{SO}^{d}(\mathbf{k})$, can restore time reversal symmetry but is not an appropriate description for the confined hole spin states considered here. Another quantity is based on an effective approach to first order in the SOI, explicitly taking into account phonons [133],

$$\mathbf{M}_{SO}^{d} = 2\mathbf{B} \times \boldsymbol{\Omega}_{SO}^{d}, \tag{6.21}$$

where $\mathbf{B}$ is the applied magnetic field, and $\boldsymbol{\Omega}_{SO}$ contains the effect of the SOI in dot d. However, with this definition one has $\mathbf{M}_{SO} = 0$ at zero magnetic field, in contrast to Eq. (6.13) which is independent of the magnetic field. Rather, a Zeeman term (6.20) with a spin-orbit field of the form (6.21) complements the spin-flip tunneling terms appearing in the spin-orbit vector with additional intra-dot processes stemming from higher orbital contributions. These are expected to be negligible when the orbital energies $\hbar\omega_{x,y}$ are large compared to the spin-orbit parameters (in the present system we find $|\mathbf{t}_{SO}| \lesssim 500$ neV, $\hbar\omega_{x,y} \sim 1$ meV).

Yet another quantity commonly used in the literature is the spin-orbit length l_{SO}. It is shown in Ref. [129] that the spin-conserving and spin-flip tunneling terms in a Ge double quantum dot with cubic Rashba SOI and a locally harmonic double quantum well potential are given by

$$\begin{aligned} t_C &= \frac{3N\gamma}{4}\left(\hbar\omega_0 + \frac{d^2 m\omega_0^2}{4}\right), \\ t_{SO} &= \lambda_R N(S-\gamma)\frac{d^3 m^3\omega_0^3}{4}, \end{aligned} \tag{6.22}$$

where $\hbar\omega_0$ is the in-plane confinement energy, m is the in-plane HH mass, d is the interdot distance, S is the overlap between the left and right dot states, $\gamma = (1-\sqrt{1-S^2})/S$, and λ_R is the effective cubic Rashba coefficient with units $[\lambda_R] =$ energy/momentum^3. We neglect the effect of excited orbitals and orbital magnetic contributions which are expected to be valid simplifications at the confinement energies and low magnetic fields considered in this paper. Following Ref. [128], we express the spin-flip tunneling element in terms of the spin-conserving tunneling element,

$$t_{SO} = \frac{4t_C}{3}\frac{d}{l_{SO}}, \tag{6.23}$$

and use this expression as a working definition of the spin-orbit length,

$$l_{SO} = \frac{1}{\lambda_R}\frac{\gamma}{S-\gamma}\frac{4\hbar\omega_0 + d^2 m\omega_0^2}{d^2 m^3\omega_0^3} = \frac{1}{\lambda_R}\frac{1}{\sqrt{1-S^2}}\frac{4\hbar\omega_0 + d^2 m\omega_0^2}{d^2 m^3\omega_0^3}. \tag{6.24}$$

Ref. [128] considers a DQD with a linear SOI, and we find that the spin-orbit length is rather different for systems with a cubic Rashba SOI. In particular, it depends not only on material parameters via λ_R but also on the dot geometry via ω_0, d, S and γ.

This dependence on the dot geometry can be understood from the definition of the spin-orbit length as the distance travelled by a particle before its spin is flipped. Assume for simplicity a particle travelling along x (e.g. the DQD axis) and an nth order Rashba type SOI of the form

$$H_{SO} = \alpha_n(\hbar k_x)^n\sigma_y, \tag{6.25}$$

where the real number α_n is the coupling strength with units energy/momentum^n, k_x the crystal momentum along x and σ_y a Pauli matrix. We may then work with an effective spin Hamiltonian by averaging over the crystal momentum,

$$\langle H_{SO}\rangle_\psi = \alpha_n\hbar^n\langle k_x^n\rangle_\psi\sigma_y, \tag{6.26}$$

where the state ψ is only required to satisfy the condition $\langle k_x^n\rangle_\psi \neq 0$ to allow for finite spin flip times. In this case the time evolution generated by this Hamiltonian in spin space will cause a spin flip in time $\tau = \pi/(2\alpha_n\hbar^{n-1}\langle k_x^n\rangle_\psi)$. The spin-orbit length along x is then defined to be

$$l_{SO} := \frac{\langle p_x\rangle_\psi}{m}\tau = \frac{\hbar\langle k_x\rangle_\psi}{m}\tau = \frac{\pi}{2}\frac{\hbar^{2-n}}{m\alpha_n}\frac{\langle k_x\rangle_\psi}{\langle k_x^n\rangle_\psi}. \tag{6.27}$$

For $n = 1$, the final fraction equals one and the spin-orbit length is a well defined quantity which only depends on material parameters. However, for $n > 1$ the expectation values must be evaluated given a specific state of the system. This introduces two problems: Firstly, since the state must be chosen by hand there is a degree of arbitrariness in the definition of the spin-orbit length. Secondly, given a specific setup, the state chosen for computing the expectation value will depend on the system geometry, and hence the spin-orbit length loses its character as a geometry independent quantity as was explicitly shown above for the case of the cubic ($n = 3$) Rashba SOI. It is therefore necessary to treat the spin-orbit length with caution for nonlinear SOI as it can possibly no longer be considered a good figure of merit for material comparison.

6.7.8 Effect of the dot geometry on the g-factors

Heavy-hole (HH) and light-hole (LH) states confined in a germanium heterostructure in the presence of a magnetic field $\mathbf{B}$ are well described by the Hamiltonian

$$H = -\frac{\hbar^2}{2m_0}\left[\left(\gamma_1 + \frac{5}{2}\gamma_s\right)\mathbf{k}^2 - 2\gamma_s\left(\mathbf{k}\cdot\mathbf{J}\right)^2\right] + 2\mu_B\left(\kappa\mathbf{B}\cdot\mathbf{J} + q\sum_{n=1}^{3} B_n J_n^3\right) + V(z) + U(x,y). \quad (6.28)$$

Here, the first term is the Luttinger-Kohn Hamiltonian in spherical approximation featuring the Luttinger parameters γ_1 and γ_s, the bare electron mass m_0 and the spin $3/2$ matrices J_n. The second term describes the effect of a magnetic field in the context of the envelope function approximation, κ and q being constants that depend on system specific influences such as strain and material composition [125–127]. We model the heterostructure by an infinite hard wall potential $V(z)$ in the out-of-plane direction, and realize the quantum dot in the x-y-plane by an elliptical harmonic confinement potential,

$$U(x,y) = \frac{m}{2}\left(\omega_x^2 x^2 + \omega_y^2 y^2\right). \quad (6.29)$$

Note that the confinement energies ω_x and ω_y are defined with respect to the in-plane HH mass $m = m_0/(\gamma_1 + \gamma_s)$. In the following we assume small magnetic fields in the mT range and neglect orbtial effects arising from the canonical momentum. This is valid for in-plane fields $B_{x,y}$ if $\epsilon_\parallel = \hbar e B_{x,y}/2m \ll \Delta = 2\gamma_s\hbar^2\pi^2/m_0 d^2$, where Δ is the HH-LH splitting with the quantum well width d. At $d \approx 20$ nm one finds $\Delta \approx 17$ meV and hence $\epsilon_\parallel \ll \Delta$ for $B_{x,y} \lesssim 1$ T. On the other hand, for out-of-plane fields B_z we require $\epsilon_\perp = \hbar e B_z/2m \ll \text{min}\{\hbar\omega_x, \hbar\omega_y\}$. For a typical minimal in-plane confinement energy $\text{min}\{\hbar\omega_x, \hbar\omega_y\} \approx 0.5$ meV, we have $\epsilon_\perp/\text{min}\{\hbar\omega_x, \hbar\omega_y\} < 0.05$ at $B_z = 20$ mT which is the maximal field applied in this work.

The eigenstates of the Hamiltonian (6.28) in the absence of HH-LH mixing and at zero in-plane magnetic field have the form $|\Psi_h\rangle|j_z\rangle$ ($|\Psi_l\rangle|j_z\rangle$) for $j_z = \pm 3/2$ ($j_z = \pm 1/2$), where j_z is the magnetic quantum number of the total angular momentum, and the position states $|\Psi_{h/l}\rangle$ are a product of simple harmonic oscillator states in x and y and trigonometric functions satisfying the boundary conditions set by $V(z)$ at

$\pm d/2$. We proceed to project the Hamiltonian (6.28) onto the space spanned by the orthonormal orbital ground state basis $\{|\Psi_h^0\rangle|3/2\rangle, |\Psi_l^0\rangle|1/2\rangle, |\Psi_l^0\rangle|-1/2\rangle, |\Psi_h^0\rangle|-3/2\rangle\}$ with

$$\begin{aligned} &\Psi_{h/l}^0(x,y,z) = \psi_{h/l}(x,y)\phi(z), \\ &\psi_{h/l}(x,y) = \sqrt{\frac{m_{h/l}\sqrt{\omega_x\omega_y}}{\hbar\pi}} \exp\left(-\frac{m_{h/l}}{2\hbar}\left[\omega_x x^2 + \omega_y y^2\right]\right), \quad \phi(z) = \sqrt{\frac{2}{d}}\cos\left(\frac{\pi z}{d}\right)\Theta\left(\frac{d}{2} - |z|\right), \end{aligned} \tag{6.30}$$

where Θ is the Heaviside step function, $m_h = m$ and $m_l = \sqrt{Mm}$ with in-plane LH mass $M = m_0/(\gamma_1 - \gamma_s)$. Note that $m < M$ for in-plane motion. One obtains a 4×4 matrix (labelled by angular momentum) in which the HH and LH spaces are separated in energy by the HH-LH splitting Δ and can mix due to the intrinsic SOI,

$$\langle H \rangle = \begin{pmatrix} \left(3\kappa + \frac{27}{4}q\right)\mu_B B_z & \sqrt{3}\left(\kappa + \frac{7}{4}q\right)\mu_1\mu_B b^* & -\sqrt{3}\gamma_s\mu_2\hbar(\omega_x - \omega_y) & \frac{3}{2}q\mu_B b \\ \sqrt{3}\left(\kappa + \frac{7}{4}q\right)\mu_1\mu_B b & \epsilon + \left(\kappa + \frac{1}{4}q\right)\mu_B B_z & (5q + 2\kappa)\mu_B b^* & -\sqrt{3}\gamma_s\mu_2\hbar(\omega_x - \omega_y) \\ -\sqrt{3}\gamma_s\mu_2\hbar(\omega_x - \omega_y) & (5q + 2\kappa)\mu_B b & \epsilon - \left(\kappa + \frac{1}{4}q\right)\mu_B B_z & \sqrt{3}\left(\kappa + \frac{7}{4}q\right)\mu_1\mu_B b^* \\ \frac{3}{2}q\mu_B b^* & -\sqrt{3}\gamma_s\mu_2\hbar(\omega_x - \omega_y) & \sqrt{3}\left(\kappa + \frac{7}{4}q\right)\mu_1\mu_B b & -\left(3\kappa + \frac{27}{4}q\right)\mu_B B_z \end{pmatrix}, \tag{6.31}$$

where we introduce the quantities

$$b = B_x + iB_y, \quad \epsilon = \frac{\hbar(\omega_x + \omega_y)}{2}\left(\sqrt{\frac{m}{M}} - 1\right) + \Delta, \quad \mu_1 = \langle\psi_h|\psi_l\rangle = \frac{2(mM)^{1/4}}{\sqrt{m} + \sqrt{M}}, \quad \mu_2 = \frac{m^{3/2}(mM)^{3/4}}{m_0(m + \sqrt{mM})^2}. \tag{6.32}$$

Note that any additional part of the Hamiltonian that is linear in the momentum (e.g. a Rashba type SOI) vanishes upon projection onto the space spanned by the symmetric ground state wave functions. Assuming the HH-LH splitting to be the largest relevant energy scale, $\Delta \gg \mu_B|\mathbf{B}|, \hbar\omega_x, \hbar\omega_y$, we may perform a Schrieffer-Wolff transformation to decouple the LH subspace. We find an effective 2×2 HH Hamiltonian with a Zeeman term (i.e., a term linear in $\mathbf{B}$) containing the renormalized g-factors

$$g_x = g_x^0 - \xi_1 \frac{\hbar(\omega_x - \omega_y)}{\hbar(\omega_x + \omega_y) - \xi_2\Delta}, \tag{6.33a}$$

$$g_y = g_y^0 + \xi_1 \frac{\hbar(\omega_x - \omega_y)}{\hbar(\omega_x + \omega_y) - \xi_2\Delta}, \tag{6.33b}$$

$$g_z = g_z^0 - \xi_1 \left[\frac{\hbar(\omega_x - \omega_y)}{\hbar(\omega_x + \omega_y) - \xi_2\Delta}\right]^2, \tag{6.33c}$$

where $g_x^0 = g_y^0 = 3q$, $g_z^0 = 6\kappa + 27q/2$ are the effective zeroth order values and

$$\xi_1 = (12\kappa + 21q)\frac{\sqrt{\gamma_1^2 - \gamma_s^2}}{\gamma_1 + \sqrt{\gamma_1^2 - \gamma_s^2}}, \quad \xi_2 = \frac{2\sqrt{\gamma_1 + \gamma_s}}{\sqrt{\gamma_1 + \gamma_s} - \sqrt{\gamma_1 - \gamma_s}} \tag{6.34}$$

are material specific constants, $\xi_1 \approx 20.3$ and $\xi_2 \approx 6.0$ in (bulk) germanium. While g_z is always reduced by the HH-LH mixing, the sign of the correction to g_x and g_y depends on the relative in-plane confinement strength. In particular, $g_x \neq g_y$ due to the broken in-plane symmetry. It is therefore possible that one in-plane g-factor becomes negative. This effect can be observed even in a perturbative approach because the zeroth order in-plane g-factors in germanium are small, $g_x^0 = g_y^0 = 3q \approx 0.2$. In contrast, we find that the correction to the out-of-plane g-factor is $|\delta g_z| \lesssim 10^{-2}$ for the values considered here and hence negligible. The smallness of the correction to the out-of-plane g-factor compared to the correction to the in-plane g-factors can be understood as follows: The HH and LH subspaces are mixed by the effect of elliptical confinement ($\sim [\omega_x - \omega_y]$) and the in-plane magnetic fields, and the corrections to the matrix elements in the effective HH Hamiltonian are given by a product of these effects. The effective in-plane g-factor corrections then effectively contain only one of the two small mixing terms ($\delta g_{x,y} \sim [\omega_x - \omega_y]$) because one factor contains the in-plane magnetic field, while the out-of-plane g-factor correction contains two small factors ($\delta g_z \sim [\omega_x - \omega_y]^2$).

7 Future Directions

7.1 Gate fidelity

One point we did not address is gate fidelity. Speed and coherence are definitely desirable properties for a qubit but how well the gates work is probably even more important. Here, the Loss-DiVincenzo qubit has a definite advantage over the $S-T_0$ qubit: the control axes are orthogonal by design. This means that a quantum gate intended as a $\pi/2$ rotation around the x-axis is simply accomplished by turning on a microwave burst for a time $t_{\pi/2}$, the time it takes to rotate the state at the applied power. One only needs to calibrate $t_{\pi/2}$ correctly. Similarly, a pulse around the y-axis is achieved by applying a microwave burst but altering the phase by 90°. For $S-T_0$ qubits this is not possible as the off diagonal terms $(\Delta g\mu_B B)$ can not be switched off quickly and the exchange interaction J can be only switched quickly between $J_{MAX} \gg \Delta g\mu_B B$ and $J_{MIN} \ll \Delta g\mu_B B$. The two non-collinear axes are, therefore, never orthogonal and composite pulses are necessary to achieve the desired quantum gates. Several approached exist to tackle this problem and generate quantum gates that are also minimizing the infidelity [74, 75].

We set up a gradient ascent pulse engineering (GRAPE) method [134] where we feed the experimental parameters ($J(\epsilon)$, Δg and B) and calculate a pulse sequence that results in the highest fidelity. This work was done by Przemyslaw Zielinski during his rotation in our group. The principle of GRAPE is illustrated in Fig. 7.1. Quantum gates are obtained by concatenating a fixed number of pulses N of duration τ and amplitude ϵ_i. The duration of each segment can be conveniently chosen to be equal to, or a multiple of, the sampling rate of the AWG. The total pulse duration $N\tau$ will be equal for every quantum gate enabling the use of something like a quantum clock cycle. The amplitudes ϵ_i of each pulse segment are confined in an interval $[\epsilon_{min}, \epsilon_{max}]$, where ϵ_{min} is chosen large enough to not introduce too much charge noise and ϵ_{max} is the maximum signal we can apply to the sample. The value of ϵ_i with a fixed B and g^- determines the rotation axis for the $i-$th pulse segment ($\theta_i = \arctan\left(\frac{g^-\mu_B B}{J(\epsilon_i)}\right)$) and produces an operator $u_i = \exp\left(\frac{-i\tau H_i}{\hbar}\right)$ with $H_i = (I - J(\epsilon_i))\sigma_z + g^-\mu_B B\sigma_x$. Starting from a random initial sequence producing an operator $U_I = u_N u_{N-1}...u_i...u_2 u_1$, the GRAPE algorithm is designed to

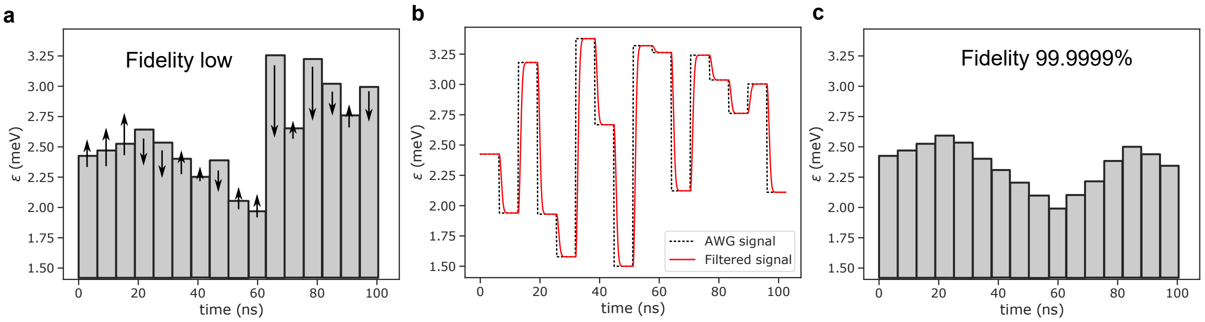

Figure 7.1: a) We start from a random pulse sequence with N segments of duration τ which are confined between $\epsilon_{min} = 1.5$ meV and $\epsilon_{max} = 4$ meV. The GRAPE algorithm then calculates how each pulse segment needs to be adapted in order to decrease the cost function (increase the fidelity). b) We need to take into account that what we apply at the AWG (black dashed line) is not what the sample experiences (red line) as a result of a finite risetime of the AWG. Adjacent pulses with large amplitude differences will therefore produce errors. c) After the pulse is optimized we reach a theoretical fidelity of 99.9999% including limited rise time.

find the sequence of ϵ_i that maximizes the fidelity of the final operator U_F to the target operator $U - T$: $1 - ||U_F - U_T||^2_{max}$. At each step the amplitudes are updated according to a cost function that needs to be maximised as well (black arrows in Fig. 7.1). The steps of the GRAPE algorithm are:

- (1) guess the initial control amplitudes ϵ_i;
- (2) calculate the fidelity $1 - ||U_F - U_T||^2$ and check if it reached the desired threshold;
- (3) update the control amplitudes according to a cost function;
- (4) re-iterate from step (2).

Fig. 7.1b highlights one of the main issues. The AWG signal has a finite rise time which means that the amplitudes will be experienced by the sample with a time delay. Hence, we needed to adapt the algorithm to account for these delays. In order to calculate the real time evolution of the qubit we applied a low pass filter with a time constant of 2 ns to the AWG signal. We then calculated the time evolution with a granulation of 4, 8, 16 and 32. Here granulation means that we calculate the state evolution at intervals of $\tau/4$, $\tau/8$, $\tau/16$ and $\tau/32$. We found that a granulation above 16 does not improve the achievable theoretical fidelity but increases computational resources significantly. We, therefore, opted for a granularity of 16.

Fig. 7.1c shows an example of an optimized pulse with a theoretical fidelity of 99.9999% which takes an average of less than 100 iterations to complete for random initial pulses. Over several runs the algorithm tends to produce solutions with a rather smooth envelope without spikes of high amplitude. The shortest sequences to allow swift convergence of the algorithm are 51.2 ns long with $\tau = 1.66$ ns. In the near future this Algorithm will be tested on a singlet-triplet qubit.

7.2 Auto-tuning

In collaboration with the group of Natalia Ares we are also working on a machine assisted tuning algorithm. As device complexity increases it becomes more and more challenging to tune QDs into a regime where quantum algorithms can be performed. Hence, artificial intelligence can help to solve this issue and enable fully automated tuning of devices. We fabricated double quantum dot devices similar to the sample in Fig. 5.1 on a SiGe/Ge heterostructure. The devices were then tuned from scratch to the double quantum dot regime. First results showed that the heterostructures at hand can be tuned as effectively as dots in GaAs [135, 136].

8 Conclusion

Looking back at the beginning of my PhD we were struggling to fabricate quantum dots. Now, 4 years later, we perform qubit measurements on reproducible devices routinely. This once again shows how fast the Ge platform has grown to maturity and what other great things we can expect to happen.

The properties of holes in Ge are incredibly favorable for qubit implementations. We have seen that high mobility, low effective mass, low hyperfine interaction and the presence of a tunable spin orbit interaction leads to very controllable fabrication and outstanding qubit performance. The spin-orbit interaction arises as a consequence of HH-LH mixing. For 2D confinement the HH-LH mixing is dependent on the width of the quantum well as well as the composition of the barrier layers which induce strain. Moreover, electric fields for quantum dot confinement can also influence the splitting. Several theoretical proposals exist that predict ultrafast operation of Loss-DiVincenzo qubits in Ge [91]. Recently, two independent works also postulated the existence of a linear Rashba spin-orbit interaction for very elliptical dots [119, 137]. Such a term is the reason why the manipulation speed in 1D structures like core shell nanowires [40] or Ge hutwires [35] greatly exceeds what is typically observed in 2D systems where only the cubic Rashba term is present [60].

The HH-LH mixing is also responsible for the experimentally observable g-factor. In fact, the out-of-plane g-factor of HH states should be > 15 for holes in Ge but we generally observe values ranging from 4.5 to 7.5. This entails a consistent contribution of the LH character to the overall wavefunction. In previous studies in our group, Hannes Watzinger showed that by filling a QD with more and more holes the effective out-of-plane g-factor is gradually reduced [95]. In this work, we leveraged this property and used it to create a $S - T_0$ qubit. Indeed, in the out-of-plane direction we found g-factor differences 1000 times larger than reported for electrons in Si [67, 68, 122] by having unequal filling of the two quantum dots. This meant that we could operate our qubit at 1000 times smaller fields. We found that at only 4 mT we could drive $S - T_0$ oscillations at more than 100 MHz. My colleague Josip Kukucka even pushed Δg above 4.5 in another device resulting in incredibly fast oscillation frequencies approaching 600 MHz at fields of just 10 mT. We found that the large g-factor difference is reproducible for all devices we measured so far. Definitely a detailed investigation of the g-factor landscape as a function of the filling factor is necessary to fully understand and control singlet-triplet qubits.

Rotating the magnetic field into the in-plane direction revealed that the shape of the quantum dots can drastically affect the behavior of a singlet-triplet qubit as well. As the g-factors in this direction are typically very small (≈ 0.2) perturbations from the confinement potential become relevant. In fact, theoretical calculations showed that squeezing the quantum dots in the x or y direction produces corrections to the g-factor. Engineering a DQD where the dots possess opposite ellipticity can produce a large g-factor difference and can even lead to the g-factors having opposite signs. In this case, the coupling terms between singlet and triplet states become dominant over the SOI induced spin-flip term and alter the dynamics of the system. As we saw in chapter 6, this coupling term can be the dominant contribution to the singlet-triplet splitting which is typically attributed to the SOI spin-flip term or the hyperfine interaction [68, 121, 122, 128]. We showed that, in systems with large g-factor differences, this is not the case and could lead to an overestimation of the spin-orbit interaction present in the system.

Bibliography

[1] R. P. Feynman, “Simulating physics with computers,” *International Journal of Theoretical Physics*, vol. 21, pp. 467–488, jun 1982. (Cited on page 1)

[2] M. Riordan, L. Hoddeson, and C. Herring, “The invention of the transistor,” *Reviews of Modern Physics*, vol. 71, pp. S336–S345, mar 1999. (Cited on page 1)

[3] CHM, “1959: Practical monolithic integrated circuit concept patented.” (Cited on page 1)

[4] G. E. Moore, “Cramming more components onto integrated circuits, reprinted from electronics, volume 38, number 8, april 19, 1965, pp.114 ff.,” *IEEE Solid-State Circuits Society Newsletter*, vol. 11, pp. 33–35, sep 2006. (Cited on page 1)

[5] M. Gurman, D. Wu, and I. King, “Apple aims to sell macs with its own chips starting in 2021.” (Cited on page 1)

[6] A. M. Turing, “On computable numbers, with an application to the entscheidungsproblem,” *Proceedings of the London Mathematical Society*, vol. s2-42, no. 1, pp. 230–265, 1937. (Cited on page 1)

[7] A. M. Turing, “On computable numbers, with an application to the entscheidungsproblem. a correction,” *Proceedings of the London Mathematical Society*, vol. s2-43, no. 1, pp. 544–546, 1938. (Cited on page 1)

[8] P. Shor, “Algorithms for quantum computation: discrete logarithms and factoring,” in *Proceedings 35th Annual Symposium on Foundations of Computer Science*, IEEE Comput. Soc. Press, 1994. (Cited on page 1)

[9] J. Preskill, “Quantum computing in the NISQ era and beyond,” *Quantum*, vol. 2, p. 79, aug 2018. (Cited on page 2)

[10] M. Kjaergaard, M. E. Schwartz, J. Braumüller, P. Krantz, J. I.-J. Wang, S. Gustavsson, and W. D. Oliver, “Superconducting qubits: Current state of play,” *Annual Review of Condensed Matter Physics*, vol. 11, pp. 369–395, mar 2020. (Cited on page 2)

[11] I. L. C. Michael A. Nielsen, *Quantum Computation and Quantum Information*. Cambridge University Pr., 2010. (Cited on page 2)

[12] C. D. Bruzewicz, J. Chiaverini, R. McConnell, and J. M. Sage, "Trapped-ion quantum computing: Progress and challenges," *Applied Physics Reviews*, vol. 6, p. 021314, jun 2019. (Cited on page 2)

[13] S. Slussarenko and G. J. Pryde, "Photonic quantum information processing: A concise review," *Applied Physics Reviews*, vol. 6, p. 041303, dec 2019. (Cited on page 2)

[14] R. Hanson, L. P. Kouwenhoven, J. R. Petta, S. Tarucha, and L. M. K. Vandersypen, "Spins in few-electron quantum dots," *Reviews of Modern Physics*, vol. 79, pp. 1217–1265, oct 2007. (Cited on pages 2 and 10)

[15] F. A. Zwanenburg, A. S. Dzurak, A. Morello, M. Y. Simmons, L. C. L. Hollenberg, G. Klimeck, S. Rogge, S. N. Coppersmith, and M. A. Eriksson, "Silicon quantum electronics," *Reviews of Modern Physics*, vol. 85, pp. 961–1019, jul 2013. (Cited on pages 2, 3, 10, and 22)

[16] R. Aguado and L. P. Kouwenhoven, "Majorana qubits for topological quantum computing," *Physics Today*, vol. 73, pp. 44–50, jun 2020. (Cited on page 2)

[17] F. Arute, K. Arya, R. Babbush, D. Bacon, J. C. Bardin, R. Barends, R. Biswas, S. Boixo, F. G. S. L. Brandao, D. A. Buell, B. Burkett, Y. Chen, Z. Chen, B. Chiaro, R. Collins, W. Courtney, A. Dunsworth, E. Farhi, B. Foxen, A. Fowler, C. Gidney, M. Giustina, R. Graff, K. Guerin, S. Habegger, M. P. Harrigan, M. J. Hartmann, A. Ho, M. Hoffmann, T. Huang, T. S. Humble, S. V. Isakov, E. Jeffrey, Z. Jiang, D. Kafri, K. Kechedzhi, J. Kelly, P. V. Klimov, S. Knysh, A. Korotkov, F. Kostritsa, D. Landhuis, M. Lindmark, E. Lucero, D. Lyakh, S. Mandrà, J. R. McClean, M. McEwen, A. Megrant, X. Mi, K. Michielsen, M. Mohseni, J. Mutus, O. Naaman, M. Neeley, C. Neill, M. Y. Niu, E. Ostby, A. Petukhov, J. C. Platt, C. Quintana, E. G. Rieffel, P. Roushan, N. C. Rubin, D. Sank, K. J. Satzinger, V. Smelyanskiy, K. J. Sung, M. D. Trevithick, A. Vainsencher, B. Villalonga, T. White, Z. J. Yao, P. Yeh, A. Zalcman, H. Neven, and J. M. Martinis, "Quantum supremacy using a programmable superconducting processor," *Nature*, vol. 574, pp. 505–510, oct 2019. (Cited on page 2)

[18] D. Loss and D. P. DiVincenzo, "Quantum computation with quantum dots," *Physical Review A*, vol. 57, pp. 120–126, jan 1998. (Cited on pages 2, 20, 58, and 95)

[19] B. E. Kane, "A silicon-based nuclear spin quantum computer," *Nature*, vol. 393, pp. 133–137, may 1998. (Cited on page 2)

[20] J. Levy, "Universal quantum computation with spin-1/2 pairs and heisenberg exchange," *Physical Review Letters*, vol. 89, p. 147902, sep 2002. (Cited on pages 2, 23, 57, and 59)

[21] J. R. Petta, “Coherent manipulation of coupled electron spins in semiconductor quantum dots,” *Science*, vol. 309, pp. 2180–2184, sep 2005. (Cited on pages 2, 23, 57, 59, 61, and 88)

[22] F. H. L. Koppens, C. Buizert, K. J. Tielrooij, I. T. Vink, K. C. Nowack, T. Meunier, L. P. Kouwenhoven, and L. M. K. Vandersypen, “Driven coherent oscillations of a single electron spin in a quantum dot,” *Nature*, vol. 442, pp. 766–771, aug 2006. (Cited on pages 2 and 20)

[23] H. Bluhm, S. Foletti, I. Neder, M. Rudner, D. Mahalu, V. Umansky, and A. Yacoby, “Dephasing time of GaAs electron-spin qubits coupled to a nuclear bath exceeding 200 μs,” *Nature Physics*, vol. 7, pp. 109–113, dec 2010. (Cited on pages 2, 23, and 68)

[24] M. Veldhorst, J. C. C. Hwang, C. H. Yang, A. W. Leenstra, B. de Ronde, J. P. Dehollain, J. T. Muhonen, F. E. Hudson, K. M. Itoh, A. Morello, and A. S. Dzurak, “An addressable quantum dot qubit with fault-tolerant control-fidelity,” *Nature Nanotechnology*, vol. 9, pp. 981–985, oct 2014. (Cited on pages 2 and 22)

[25] J. T. Muhonen, J. P. Dehollain, A. Laucht, F. E. Hudson, R. Kalra, T. Sekiguchi, K. M. Itoh, D. N. Jamieson, J. C. McCallum, A. S. Dzurak, and A. Morello, “Storing quantum information for 30 seconds in a nanoelectronic device,” *Nature Nanotechnology*, vol. 9, pp. 986–991, oct 2014. (Cited on pages 2 and 22)

[26] J. Yoneda, K. Takeda, T. Otsuka, T. Nakajima, M. R. Delbecq, G. Allison, T. Honda, T. Kodera, S. Oda, Y. Hoshi, N. Usami, K. M. Itoh, and S. Tarucha, “A quantum-dot spin qubit with coherence limited by charge noise and fidelity higher than 99.9%,” *Nature Nanotechnology*, vol. 13, pp. 102–106, dec 2017. (Cited on pages 2, 22, 66, 67, and 85)

[27] A. G. Fowler, M. Mariantoni, J. M. Martinis, and A. N. Cleland, “Surface codes: Towards practical large-scale quantum computation,” *Physical Review A*, vol. 86, sep 2012. (Cited on page 2)

[28] I. Georgescu, “25 years of quantum error correction,” *Nature Reviews Physics*, vol. 2, pp. 519–519, sep 2020. (Cited on page 2)

[29] M. Veldhorst, C. H. Yang, J. C. C. Hwang, W. Huang, J. P. Dehollain, J. T. Muhonen, S. Simmons, A. Laucht, F. E. Hudson, K. M. Itoh, A. Morello, and A. S. Dzurak, “A two-qubit logic gate in silicon,” *Nature*, vol. 526, pp. 410–414, oct 2015. (Cited on pages 3 and 20)

[30] T. F. Watson, S. G. J. Philips, E. Kawakami, D. R. Ward, P. Scarlino, M. Veldhorst, D. E. Savage, M. G. Lagally, M. Friesen, S. N. Coppersmith, M. A. Eriksson, and L. M. K. Vandersypen, “A programmable two-qubit quantum processor in silicon,” *Nature*, vol. 555, pp. 633–637, feb 2018. (Cited on pages 3 and 22)

[31] D. V. Bulaev and D. Loss, “Electric dipole spin resonance for heavy holes in quantum dots,” *Physical Review Letters*, vol. 98, p. 097202, feb 2007. (Cited on pages 3 and 85)

[32] J. Fischer, W. A. Coish, D. V. Bulaev, and D. Loss, “Spin decoherence of a heavy hole coupled to nuclear spins in a quantum dot,” *Physical Review B*, vol. 78, p. 155329, oct 2008. (Cited on pages 3, 19, and 91)

[33] S. Studenikin, M. Korkusinski, A. Bogan, L. Gaudreau, D. G. Austing, A. S. Sachrajda, L. Tracy, J. Reno, and T. Hargett, “Single-hole physics in GaAs/AlGaAs double quantum dot system with strong spin–orbit interaction,” *Semiconductor Science and Technology*, vol. 36, p. 053001, apr 2021. (Cited on page 3)

[34] R. Maurand, X. Jehl, D. Kotekar-Patil, A. Corna, H. Bohuslavskyi, R. Laviéville, L. Hutin, S. Barraud, M. Vinet, M. Sanquer, and S. D. Franceschi, “A CMOS silicon spin qubit,” *Nature Communications*, vol. 7, p. 13575, nov 2016. (Cited on pages 3, 57, and 85)

[35] H. Watzinger, J. Kukučka, L. Vukušić, F. Gao, T. Wang, F. Schäffler, J.-J. Zhang, and G. Katsaros, “A germanium hole spin qubit,” *Nature Communications*, vol. 9, p. 3902, sep 2018. (Cited on pages 3, 51, 58, 85, 86, and 115)

[36] N. W. Hendrickx, W. I. L. Lawrie, M. Russ, F. van Riggelen, S. L. de Snoo, R. N. Schouten, A. Sammak, G. Scappucci, and M. Veldhorst, “A four-qubit germanium quantum processor,” *Nature*, vol. 591, pp. 580–585, mar 2021. (Cited on pages 3, 22, 37, and 58)

[37] M. Lodari, A. Tosato, D. Sabbagh, M. A. Schubert, G. Capellini, A. Sammak, M. Veldhorst, and G. Scappucci, “Light effective hole mass in undoped ge/SiGe quantum wells,” *Physical Review B*, vol. 100, jul 2019. (Cited on pages 3 and 58)

[38] G. Scappucci, C. Kloeffel, F. A. Zwanenburg, D. Loss, M. Myronov, J.-J. Zhang, S. D. Franceschi, G. Katsaros, and M. Veldhorst, “The germanium quantum information route,” *Nature Materials*, 2020. (Cited on pages 3, 57, 58, and 68)

[39] N. W. Hendrickx, D. P. Franke, A. Sammak, G. Scappucci, and M. Veldhorst, “Fast two-qubit logic with holes in germanium,” *Nature*, vol. 577, pp. 487–491, jan 2020. (Cited on pages 3, 22, 57, 58, and 85)

[40] F. N. M. Froning, L. C. Camenzind, O. A. H. van der Molen, A. Li, E. P. A. M. Bakkers, D. M. Zumbühl, and F. R. Braakman, “Ultrafast hole spin qubit with gate-tunable spin–orbit switch functionality,” *Nature Nanotechnology*, vol. 16, pp. 308–312, jan 2021. (Cited on pages 3, 22, 58, 68, 86, and 115)

[41] N. W. Hendrickx, D. P. Franke, A. Sammak, M. Kouwenhoven, D. Sabbagh, L. Yeoh, R. Li, M. L. V. Tagliaferri, M. Virgilio, G. Capellini, G. Scappucci, and M. Veldhorst, “Gate-controlled quantum dots and superconductivity in planar germanium,” *Nature Communications*, vol. 9, jul 2018. (Cited on page 3)

[42] K. Aggarwal, A. Hofmann, D. Jirovec, I. Prieto, A. Sammak, M. Botifoll, S. Martí-Sánchez, M. Veldhorst, J. Arbiol, G. Scappucci, J. Danon, and G. Katsaros, “Enhancement of proximity-induced superconductivity in a planar ge hole gas,” *Physical Review Research*, vol. 3, apr 2021. (Cited on page 3)

[43] J. H. Davies, *The physics of low-dimensional semiconductors : an introduction*. Cambridge, U.K. New York, NY, USA: Cambridge University Press, 1998. (Cited on pages 5 and 9)

[44] O. Wada, “Optoelectronic integration based on GaAs material,” *Optical and Quantum Electronics*, vol. 20, pp. 441–474, nov 1988. (Cited on page 6)

[45] J.-W. Luo, G. Bester, and A. Zunger, “Full-zone spin splitting for electrons and holes in bulk GaAs and GaSb,” *Physical Review Letters*, vol. 102, feb 2009. (Cited on pages 6 and 7)

[46] O. Madelung, ed., *Semiconductors*. Springer Berlin Heidelberg, 1991. (Cited on pages 6 and 7)

[47] J. R. Chelikowsky and M. L. Cohen, “Nonlocal pseudopotential calculations for the electronic structure of eleven diamond and zinc-blende semiconductors,” *Physical Review B*, vol. 14, pp. 556–582, jul 1976. (Cited on page 7)

[48] H. Lüth, *Surfaces and Interfaces of Solid Materials*. Springer Berlin Heidelberg, 1995. (Cited on page 7)

[49] E. H. Hall, “On a new action of the magnet on electric currents,” *American Journal of Mathematics*, vol. 2, p. 287, sep 1879. (Cited on page 8)

[50] L. Schubnikiv and W. J. D. Haas, “A new phenomenon in the change of resistance in a magnetic field of single crystals of bismuth,” *Nature*, vol. 126, pp. 500–500, oct 1930. (Cited on page 9)

[51] T. Ando, Y. Matsumoto, and Y. Uemura, “Theory of hall effect in a two-dimensional electron system,” *Journal of the Physical Society of Japan*, vol. 39, pp. 279–288, aug 1975. (Cited on page 9)

[52] F. Gao, J.-H. Wang, H. Watzinger, H. Hu, M. J. Rančić, J.-Y. Zhang, T. Wang, Y. Yao, G.-L. Wang, J. Kukučka, L. Vukušić, C. Kloeffel, D. Loss, F. Liu, G. Katsaros, and J.-J. Zhang, “Site-controlled uniform ge/si hut wires with electrically tunable spin–orbit coupling,” *Advanced Materials*, vol. 32, p. 1906523, feb 2020. (Cited on page 10)

[53] L. Chen, W. Lu, and C. M. Lieber, “Chapter 1. semiconductor nanowire growth and integration,” in *Smart Materials Series*, pp. 1–53, Royal Society of Chemistry, 2014. (Cited on page 10)

[54] G. Katsaros, P. Spathis, M. Stoffel, F. Fournel, M. Mongillo, V. Bouchiat, F. Lefloch, A. Rastelli, O. G. Schmidt, and S. D. Franceschi, “Hybrid superconductor–semiconductor devices made from self-assembled SiGe nanocrystals on silicon,” *Nature Nanotechnology*, vol. 5, pp. 458–464, may 2010. (Cited on pages 10 and 11)

[55] W. G. van der Wiel, S. D. Franceschi, J. M. Elzerman, T. Fujisawa, S. Tarucha, and L. P. Kouwenhoven, “Electron transport through double quantum dots,” *Reviews of Modern Physics*, vol. 75, pp. 1–22, dec 2002. (Cited on pages 12 and 72)

[56] K. Ono, “Current rectification by pauli exclusion in a weakly coupled double quantum dot system,” *Science*, vol. 297, pp. 1313–1317, jul 2002. (Cited on page 14)

[57] Y. Hu, F. Kuemmeth, C. M. Lieber, and C. M. Marcus, “Hole spin relaxation in ge–si core–shell nanowire qubits,” *Nature Nanotechnology*, vol. 7, pp. 47–50, dec 2011. (Cited on page 14)

[58] H.-A. Engel, V. N. Golovach, D. Loss, L. M. K. Vandersypen, J. M. Elzerman, R. Hanson, and L. P. Kouwenhoven, “Measurement efficiency andn-shot readout of spin qubits,” *Physical Review Letters*, vol. 93, sep 2004. (Cited on page 16)

[59] D. V. Bulaev and D. Loss, “Spin relaxation and decoherence of holes in quantum dots,” *Physical Review Letters*, vol. 95, aug 2005. (Cited on page 19)

[60] N. W. Hendrickx, W. I. L. Lawrie, L. Petit, A. Sammak, G. Scappucci, and M. Veldhorst, “A single-hole spin qubit,” *Nature Communications*, vol. 11, p. 3478, jul 2020. (Cited on pages 19, 22, 85, and 115)

[61] D. P. DiVincenzo, “The physical implementation of quantum computation,” *Fortschritte der Physik*, vol. 48, pp. 771–783, 2000. (Cited on pages 19, 20, and 95)

[62] S. Nadj-Perge, S. M. Frolov, E. P. A. M. Bakkers, and L. P. Kouwenhoven, “Spin–orbit qubit in a semiconductor nanowire,” *Nature*, vol. 468, pp. 1084–1087, dec 2010. (Cited on page 20)

[63] E. Kawakami, P. Scarlino, D. R. Ward, F. R. Braakman, D. E. Savage, M. G. Lagally, M. Friesen, S. N. Coppersmith, M. A. Eriksson, and L. M. K. Vandersypen, “Electrical control of a long-lived spin qubit in a si/SiGe quantum dot,” *Nature Nanotechnology*, vol. 9, pp. 666–670, aug 2014. (Cited on page 22)

[64] D. A. Lidar and K. B. Whaley, “Decoherence-free subspaces and subsystems,” *Springer Lecture Notes in Physics*, vol. 622, pp. 83–120, 2003. (Cited on page 23)

[65] B. M. Maune, M. G. Borselli, B. Huang, T. D. Ladd, P. W. Deelman, K. S. Holabird, A. A. Kiselev, I. Alvarado-Rodriguez, R. S. Ross, A. E. Schmitz, M. Sokolich, C. A. Watson, M. F. Gyure, and A. T. Hunter, "Coherent singlet-triplet oscillations in a silicon-based double quantum dot," *Nature*, vol. 481, pp. 344–347, jan 2012. (Cited on pages 23, 61, and 86)

[66] X. Wu, D. R. Ward, J. R. Prance, D. Kim, J. K. Gamble, R. T. Mohr, Z. Shi, D. E. Savage, M. G. Lagally, M. Friesen, S. N. Coppersmith, and M. A. Eriksson, "Two-axis control of a singlet-triplet qubit with an integrated micromagnet," *Proceedings of the National Academy of Sciences*, vol. 111, pp. 11938–11942, aug 2014. (Cited on pages 23, 61, 64, 65, and 85)

[67] R. M. Jock, N. T. Jacobson, P. Harvey-Collard, A. M. Mounce, V. Srinivasa, D. R. Ward, J. Anderson, R. Manginell, J. R. Wendt, M. Rudolph, T. Pluym, J. K. Gamble, A. D. Baczewski, W. M. Witzel, and M. S. Carroll, "A silicon metal-oxide-semiconductor electron spin-orbit qubit," *Nature Communications*, vol. 9, p. 1768, may 2018. (Cited on pages 23, 61, 66, and 115)

[68] P. Harvey-Collard, N. T. Jacobson, C. Bureau-Oxton, R. M. Jock, V. Srinivasa, A. M. Mounce, D. R. Ward, J. M. Anderson, R. P. Manginell, J. R. Wendt, T. Pluym, M. P. Lilly, D. R. Luhman, M. Pioro-Ladrière, and M. S. Carroll, "Spin-orbit interactions for singlet-triplet qubits in silicon," *Physical Review Letters*, vol. 122, p. 217702, may 2019. (Cited on pages 23, 61, 66, 86, 115, and 116)

[69] Y.-Y. Liu, L. Orona, S. F. Neyens, E. MacQuarrie, M. Eriksson, and A. Yacoby, "Magnetic-gradient-free two-axis control of a valley spin qubit in SixGe1-x," *Physical Review Applied*, vol. 16, p. 024029, aug 2021. (Cited on pages 23 and 86)

[70] R. M. Jock, N. T. Jacobson, M. Rudolph, D. R. Ward, M. S. Carroll, and D. R. Luhman, "A silicon singlet-triplet qubit driven by spin-valley coupling," *ArXiv*, 2021. (Cited on pages 23 and 86)

[71] F. N. M. Froning, M. J. Rančić, B. Hetényi, S. Bosco, M. K. Rehmann, A. Li, E. P. A. M. Bakkers, F. A. Zwanenburg, D. Loss, D. M. Zumbühl, and F. R. Braakman, "Strong spin-orbit interaction and g -factor renormalization of hole spins in ge/si nanowire quantum dots," *Physical Review Research*, vol. 3, p. 013081, jan 2021. (Cited on page 23)

[72] P. M. Mutter and G. Burkard, "g-tensor resonance in double quantum dots with site-dependent g-tensors," *Materials for Quantum Technology*, jun 2020. (Cited on page 23)

[73] R. Hanson and G. Burkard, "Universal set of quantum gates for double-dot spin qubits with fixed interdot coupling," *Physical Review Letters*, vol. 98, jan 2007. (Cited on page 24)

[74] X. Wang, L. S. Bishop, J. Kestner, E. Barnes, K. Sun, and S. D. Sarma, "Composite pulses for robust universal control of singlet–triplet qubits," *Nature Communications*, vol. 3, jan 2012. (Cited on pages 24, 66, and 111)

[75] P. Cerfontaine, T. Botzem, J. Ritzmann, S. S. Humpohl, A. Ludwig, D. Schuh, D. Bougeard, A. D. Wieck, and H. Bluhm, "Closed-loop control of a GaAs-based singlet-triplet spin qubit with 99.5% gate fidelity and low leakage," *Nature Communications*, vol. 11, aug 2020. (Cited on pages 24, 68, and 111)

[76] F. Martins, F. K. Malinowski, P. D. Nissen, E. Barnes, S. Fallahi, G. C. Gardner, M. J. Manfra, C. M. Marcus, and F. Kuemmeth, "Noise suppression using symmetric exchange gates in spin qubits," *Physical Review Letters*, vol. 116, mar 2016. (Cited on pages 25 and 68)

[77] J. M. Nichol, L. A. Orona, S. P. Harvey, S. Fallahi, G. C. Gardner, M. J. Manfra, and A. Yacoby, "High-fidelity entangling gate for double-quantum-dot spin qubits," *npj Quantum Information*, vol. 3, jan 2017. (Cited on pages 25 and 68)

[78] K. Takeda, A. Noiri, J. Yoneda, T. Nakajima, and S. Tarucha, "Resonantly driven singlet-triplet spin qubit in silicon," *Physical Review Letters*, vol. 124, p. 117701, mar 2020. (Cited on pages 25, 61, 66, and 68)

[79] M. D. Shulman, O. E. Dial, S. P. Harvey, H. Bluhm, V. Umansky, and A. Yacoby, "Demonstration of entanglement of electrostatically coupled singlet-triplet qubits," *Science*, vol. 336, pp. 202–205, apr 2012. (Cited on page 25)

[80] D. Jirovec, A. Hofmann, A. Ballabio, P. M. Mutter, G. Tavani, M. Botifoll, A. Crippa, J. Kukucka, O. Sagi, F. Martins, J. Saez-Mollejo, I. Prieto, M. Borovkov, J. Arbiol, D. Chrastina, G. Isella, and G. Katsaros, "A singlet-triplet hole spin qubit in planar ge," *Nature Materials*, jun 2021. (Cited on pages 27, 57, 86, and 91)

[81] P. C. Spruijtenburg, S. V. Amitonov, F. Mueller, W. G. van der Wiel, and F. A. Zwanenburg, "Passivation and characterization of charge defects in ambipolar silicon quantum dots," *Scientific Reports*, vol. 6, dec 2016. (Cited on page 39)

[82] L. Kouwenhoven and L. Glazman, "Revival of the kondo effect," *Physics World*, vol. 14, pp. 33–38, jan 2001. (Cited on page 44)

[83] D. Goldhaber-Gordon, H. Shtrikman, D. Mahalu, D. Abusch-Magder, U. Meirav, and M. A. Kastner, "Kondo effect in a single-electron transistor," *Nature*, vol. 391, pp. 156–159, jan 1998. (Cited on page 44)

[84] A. Crippa, R. Ezzouch, A. Aprá, A. Amisse, R. Laviéville, L. Hutin, B. Bertrand, M. Vinet, M. Urdampilleta, T. Meunier, M. Sanquer, X. Jehl, R. Maurand, and S. D. Franceschi, “Gate-reflectometry dispersive readout and coherent control of a spin qubit in silicon,” *Nature Communications*, vol. 10, jul 2019. (Cited on pages 51 and 57)

[85] C. Volk, A. Chatterjee, F. Ansaloni, C. M. Marcus, and F. Kuemmeth, “Fast charge sensing of si/sige quantum dots via a high-frequency accumulation gate,” *Nano Letters*, vol. 19, no. 8, pp. 5623–5633, 2019. (Cited on page 51)

[86] N. Ares, F. Schupp, A. Mavalankar, G. Rogers, J. Griffiths, G. Jones, I. Farrer, D. Ritchie, C. Smith, A. Cottet, G. Briggs, and E. Laird, “Sensitive radio-frequency measurements of a quantum dot by tuning to perfect impedance matching,” *Physical Review Applied*, vol. 5, mar 2016. (Cited on page 51)

[87] L. M. K. Vandersypen, H. Bluhm, J. S. Clarke, A. S. Dzurak, R. Ishihara, A. Morello, D. J. Reilly, L. R. Schreiber, and M. Veldhorst, “Interfacing spin qubits in quantum dots and donors—hot, dense, and coherent,” *npj Quantum Information*, vol. 3, sep 2017. (Cited on page 57)

[88] T. Kobayashi, J. Salfi, C. Chua, J. van der Heijden, M. G. House, D. Culcer, W. D. Hutchison, B. C. Johnson, J. C. McCallum, H. Riemann, N. V. Abrosimov, P. Becker, H.-J. Pohl, M. Y. Simmons, and S. Rogge, “Engineering long spin coherence times of spin–orbit qubits in silicon,” *Nature Materials*, vol. 20, pp. 38–42, jul 2020. (Cited on page 57)

[89] S. V. Amitonov, P. C. Spruijtenburg, M. W. S. Vervoort, W. G. van der Wiel, and F. A. Zwanenburg, “Depletion-mode quantum dots in intrinsic silicon,” *Applied Physics Letters*, vol. 112, p. 023102, jan 2018. (Cited on page 58)

[90] C. Kloeffel, M. Trif, and D. Loss, “Strong spin-orbit interaction and helical hole states in ge/si nanowires,” *Physical Review B*, vol. 84, nov 2011. (Cited on page 58)

[91] K. Wang, G. Xu, F. Gao, H. Liu, R.-L. Ma, X. Zhang, T. Zhang, G. Cao, T. Wang, J.-J. Zhang, X. Hu, H.-W. Jiang, H.-O. Li, G.-C. Guo, and G.-P. Guo, “Ultrafast operations of a hole spin qubit in ge quantum dot,” *ArXiV*, 2020. (Cited on pages 58, 68, 86, and 115)

[92] G. Katsaros, V. N. Golovach, P. Spathis, N. Ares, M. Stoffel, F. Fournel, O. G. Schmidt, L. I. Glazman, and S. D. Franceschi, “Observation of spin-selective tunneling in SiGe nanocrystals,” *Physical Review Letters*, vol. 107, dec 2011. (Cited on pages 59 and 62)

[93] J. R. Petta, H. Lu, and A. C. Gossard, “A coherent beam splitter for electronic spin states,” *Science*, vol. 327, pp. 669–672, feb 2010. (Cited on pages 61 and 88)

[94] O. E. Dial, M. D. Shulman, S. P. Harvey, H. Bluhm, V. Umansky, and A. Yacoby, “Charge noise spectroscopy using coherent exchange oscillations in a singlet-triplet qubit,” *Physical Review Letters*, vol. 110, apr 2013. (Cited on pages 61 and 65)

[95] H. Watzinger, C. Kloeffel, L. Vukušić, M. D. Rossell, V. Sessi, J. Kukučka, R. Kirchschlager, E. Lausecker, A. Truhlar, M. Glaser, A. Rastelli, A. Fuhrer, D. Loss, and G. Katsaros, “Heavy-hole states in germanium hut wires,” *Nano Letters*, vol. 16, pp. 6879–6885, oct 2016. (Cited on pages 61, 62, and 115)

[96] A. Hofmann, D. Jirovec, M. Borovkov, I. Prieto, A. Ballabio, J. Frigerio, D. Chrastina, G. Isella, and G. Katsaros, “Assessing the potential of ge/sige quantum dots as hosts for singlet-triplet qubits,” *ArXiv*, 2019. (Cited on pages 61 and 65)

[97] C. Barthel, J. Medford, H. Bluhm, A. Yacoby, C. M. Marcus, M. P. Hanson, and A. C. Gossard, “Relaxation and readout visibility of a singlet-triplet qubit in an overhauser field gradient,” *Physical Review B*, vol. 85, jan 2012. (Cited on pages 62, 63, and 94)

[98] S. D. Liles, R. Li, C. H. Yang, F. E. Hudson, M. Veldhorst, A. S. Dzurak, and A. R. Hamilton, “Spin and orbital structure of the first six holes in a silicon metal-oxide-semiconductor quantum dot,” *Nature Communications*, vol. 9, aug 2018. (Cited on page 62)

[99] S. A. Studenikin, J. Thorgrimson, G. C. Aers, A. Kam, P. Zawadzki, Z. R. Wasilewski, A. Bogan, and A. S. Sachrajda, “Enhanced charge detection of spin qubit readout via an intermediate state,” *Applied Physics Letters*, vol. 101, p. 233101, dec 2012. (Cited on page 62)

[100] L. A. Orona, J. M. Nichol, S. P. Harvey, C. G. L. Bøttcher, S. Fallahi, G. C. Gardner, M. J. Manfra, and A. Yacoby, “Readout of singlet-triplet qubits at large magnetic field gradients,” *Physical Review B*, vol. 98, p. 125404, sep 2018. (Cited on pages 62 and 99)

[101] M. D. Shulman, S. P. Harvey, J. M. Nichol, S. D. Bartlett, A. C. Doherty, V. Umansky, and A. Yacoby, “Suppressing qubit dephasing using real-time hamiltonian estimation,” *Nature Communications*, vol. 5, oct 2014. (Cited on page 68)

[102] M. Reed, B. Maune, R. Andrews, M. Borselli, K. Eng, M. Jura, A. Kiselev, T. Ladd, S. Merkel, I. Milosavljevic, E. Pritchett, M. Rakher, R. Ross, A. Schmitz, A. Smith, J. Wright, M. Gyure, and A. Hunter, “Reduced sensitivity to charge noise in semiconductor spin qubits via symmetric operation,” *Physical Review Letters*, vol. 116, mar 2016. (Cited on page 68)

[103] A. Wallraff, D. I. Schuster, A. Blais, L. Frunzio, R.-S. Huang, J. Majer, S. Kumar, S. M. Girvin, and R. J. Schoelkopf, “Strong coupling of a single photon to a superconducting qubit using circuit quantum electrodynamics,” *Nature*, vol. 431, pp. 162–167, sep 2004. (Cited on page 68)

[104] J. Stehlik, Y.-Y. Liu, C. Quintana, C. Eichler, T. Hartke, and J. Petta, “Fast charge sensing of a cavity-coupled double quantum dot using a josephson parametric amplifier,” *Physical Review Applied*, vol. 4, jul 2015. (Cited on page 68)

[105] G. Burkard, M. J. Gullans, X. Mi, and J. R. Petta, “Superconductor–semiconductor hybrid-circuit quantum electrodynamics,” *Nature Reviews Physics*, vol. 2, pp. 129–140, jan 2020. (Cited on page 68)

[106] E. Leonard, M. A. Beck, J. Nelson, B. Christensen, T. Thorbeck, C. Howington, A. Opremcak, I. Pechenezhskiy, K. Dodge, N. Dupuis, M. Hutchings, J. Ku, F. Schlenker, J. Suttle, C. Wilen, S. Zhu, M. Vavilov, B. Plourde, and R. McDermott, “Digital coherent control of a superconducting qubit,” *Physical Review Applied*, vol. 11, jan 2019. (Cited on page 68)

[107] F. J. Schupp, F. Vigneau, Y. Wen, A. Mavalankar, J. Griffiths, G. A. C. Jones, I. Farrer, D. A. Ritchie, C. G. Smith, L. C. Camenzind, L. Yu, D. M. Zumbühl, G. A. D. Briggs, N. Ares, and E. A. Laird, “Sensitive radiofrequency readout of quantum dots using an ultra-low-noise SQUID amplifier,” *Journal of Applied Physics*, vol. 127, p. 244503, jun 2020. (Cited on page 68)

[108] F. Vigneau, R. Mizokuchi, D. C. Zanuz, X. Huang, S. Tan, R. Maurand, S. Frolov, A. Sammak, G. Scappucci, F. Lefloch, and S. D. Franceschi, “Germanium quantum-well josephson field-effect transistors and interferometers,” *Nano Letters*, vol. 19, pp. 1023–1027, jan 2019. (Cited on page 68)

[109] B. Rössner, D. Chrastina, G. Isella, and H. von Känel, “Scattering mechanisms in high-mobility strained ge channels,” *Applied Physics Letters*, vol. 84, pp. 3058–3060, apr 2004. (Cited on page 68)

[110] V. A. Shah, A. Dobbie, M. Myronov, D. J. F. Fulgoni, L. J. Nash, and D. R. Leadley, “Reverse graded relaxed buffers for high ge content SiGe virtual substrates,” *Applied Physics Letters*, vol. 93, p. 192103, nov 2008. (Cited on page 68)

[111] Z. Wang, E. Marcellina, A. R. Hamilton, J. H. Cullen, S. Rogge, J. Salfi, and D. Culcer, “Optimal operation points for ultrafast, highly coherent ge hole spin-orbit qubits,” *npj Quantum Information*, vol. 7, p. 54, apr 2021. (Cited on pages 68 and 86)

[112] A. Sammak, D. Sabbagh, N. W. Hendrickx, M. Lodari, B. P. Wuetz, A. Tosato, L. Yeoh, M. Bollani, M. Virgilio, M. A. Schubert, P. Zaumseil, G. Capellini, M. Veldhorst, and G. Scappucci, “Shallow and undoped germanium quantum wells: A playground for spin and hybrid quantum technology,” *Advanced Functional Materials*, vol. 29, p. 1807613, jan 2019. (Cited on page 68)

[113] S. Marchionna, A. Virtuani, M. Acciarri, G. Isella, and H. von Kaenel, “Defect imaging of SiGe strain relaxed buffers grown by LEPECVD,” *Materials Science in Semiconductor Processing*, vol. 9, pp. 802–805, aug 2006. (Cited on page 68)

[114] M. Hÿtch, E. Snoeck, and R. Kilaas, “Quantitative measurement of displacement and strain fields from HREM micrographs,” *Ultramicroscopy*, vol. 74, pp. 131–146, aug 1998. (Cited on page 70)

[115] M. de la Mata, C. Magén, P. Caroff, and J. Arbiol, “Atomic scale strain relaxation in axial semiconductor III–v nanowire heterostructures,” *Nano Letters*, vol. 14, pp. 6614–6620, oct 2014. (Cited on page 70)

[116] D. Kriegner, E. Wintersberger, and J. Stangl, “xrayutilities: a versatile tool for reciprocal space conversion of scattering data recorded with linear and area detectors,” *Journal of Applied Crystallography*, vol. 46, pp. 1162–1170, jul 2013. (Cited on page 70)

[117] V. N. Golovach, M. Borhani, and D. Loss, “Electric-dipole-induced spin resonance in quantum dots,” *Physical Review B*, vol. 74, p. 165319, oct 2006. (Cited on page 85)

[118] A. Crippa, R. Maurand, L. Bourdet, D. Kotekar-Patil, A. Amisse, X. Jehl, M. Sanquer, R. Laviéville, H. Bohuslavskyi, L. Hutin, S. Barraud, M. Vinet, Y.-M. Niquet, and S. D. Franceschi, “Electrical spin driving by g -matrix modulation in spin-orbit qubits,” *Physical Review Letters*, vol. 120, p. 137702, mar 2018. (Cited on page 85)

[119] S. Bosco, M. Benito, C. Adelsberger, and D. Loss, “Squeezed hole spin qubits in ge quantum dots with ultrafast gates at low power,” *ArXiv*, 2021. (Cited on pages 86 and 115)

[120] C. Dickel, S. Foletti, V. Umansky, and H. Bluhm, “Characterization of $s-t_+$ transition dynamics via correlation measurements,” *Physical Review B*, vol. 92, p. 125402, sep 2015. (Cited on page 86)

[121] J. M. Nichol, S. P. Harvey, M. D. Shulman, A. Pal, V. Umansky, E. I. Rashba, B. I. Halperin, and A. Yacoby, “Quenching of dynamic nuclear polarization by spin–orbit coupling in GaAs quantum dots,” *Nature Communications*, vol. 6, p. 7682, jul 2015. (Cited on pages 86 and 116)

[122] T. Tanttu, B. Hensen, K. W. Chan, C. H. Yang, W. W. Huang, M. Fogarty, F. Hudson, K. Itoh, D. Culcer, A. Laucht, A. Morello, and A. Dzurak, “Controlling spin-orbit interactions in silicon quantum dots using magnetic field direction,” *Physical Review X*, vol. 9, p. 021028, may 2019. (Cited on pages 86, 115, and 116)

[123] J. Danon and Y. V. Nazarov, “Pauli spin blockade in the presence of strong spin-orbit coupling,” *Physical Review B*, vol. 80, p. 041301(R), jul 2009. (Cited on pages 88 and 105)

[124] S. Shevchenko, S. Ashhab, and F. Nori, “Landau–zener–stückelberg interferometry,” *Physics Reports*, vol. 492, pp. 1–30, jul 2010. (Cited on page 88)

[125] X. Marie, T. Amand, P. L. Jeune, M. Paillard, P. Renucci, L. E. Golub, V. D. Dymnikov, and E. L. Ivchenko, “Hole spin quantum beats in quantum-well structures,” *Physical Review B*, vol. 60, pp. 5811–5817, aug 1999. (Cited on pages 90 and 107)

[126] R. Winkler, *Spin—Orbit Coupling Effects in Two-Dimensional Electron and Hole Systems*. Springer Berlin Heidelberg, 2003. (Cited on pages 90 and 107)

[127] A. V. Trifonov, I. A. Akimov, L. E. Golub, E. L. Ivchenko, I. A. Yugova, A. N. Kosarev, S. E. Scholz, C. Sgroi, A. Ludwig, A. D. Wieck, D. R. Yakovlev, and M. Bayer, “Strong enhancement of heavy-hole landé factor q in ingaas symmetric quantum dots revealed by coherent optical spectroscopy,” *ArXiv*, 2021. (Cited on pages 90 and 107)

[128] D. Stepanenko, M. Rudner, B. I. Halperin, and D. Loss, “Singlet-triplet splitting in double quantum dots due to spin-orbit and hyperfine interactions,” *Physical Review B*, vol. 85, p. 075416, feb 2012. (Cited on pages 91, 93, 106, and 116)

[129] P. M. Mutter and G. Burkard, “Pauli spin blockade with site-dependent g tensors and spin-polarized leads,” *Physical Review B*, vol. 103, p. 245412, jun 2021. (Cited on pages 91, 93, 104, and 106)

[130] P. M. Mutter and G. Burkard, “All-electrical control of hole singlet-triplet spin qubits at low leakage points,” *ArXiv*, 2021. (Cited on page 91)

[131] M. Veldhorst, H. G. J. Eenink, C. H. Yang, and A. S. Dzurak, “Silicon CMOS architecture for a spin-based quantum computer,” *Nature Communications*, vol. 8, p. 1766, dec 2017. (Cited on page 95)

[132] G. Granger, G. C. Aers, S. A. Studenikin, A. Kam, P. Zawadzki, Z. R. Wasilewski, and A. S. Sachrajda, “Visibility study of $s - t_+$ landau-zener-stückelberg oscillations without applied initialization,” *Physical Review B*, vol. 91, p. 115309, mar 2015. (Cited on pages 97 and 99)

[133] V. N. Golovach, A. Khaetskii, and D. Loss, “Phonon-induced decay of the electron spin in quantum dots,” *Physical Review Letters*, vol. 93, p. 016601, jun 2004. (Cited on page 105)

[134] N. Khaneja, T. Reiss, C. Kehlet, T. Schulte-Herbrüggen, and S. J. Glaser, “Optimal control of coupled spin dynamics: design of NMR pulse sequences by gradient ascent algorithms,” *Journal of Magnetic Resonance*, vol. 172, pp. 296–305, feb 2005. (Cited on page 111)

[135] H. Moon, D. T. Lennon, J. Kirkpatrick, N. M. van Esbroeck, L. C. Camenzind, L. Yu, F. Vigneau, D. M. Zumbühl, G. A. D. Briggs, M. A. Osborne, D. Sejdinovic, E. A. Laird, and N. Ares, “Machine learning enables completely automatic tuning of a quantum device faster than human experts,” *Nature Communications*, vol. 11, aug 2020. (Cited on page 113)

[136] B. Severin, D. T. Lennon, L. C. Camenzind, F. Vigneau, F. Fedele, D. Jirovec, A. Ballabio, D. Chrastina, G. Isella, M. de Kruijf, M. J. Carballido, S. Svab, A. V. Kuhlmann, F. R. Braakman, S. Geyer, F. N. M. Froning, H. Moon, M. A. Osborne, D. Sejdinovic, G. Katsaros, D. M. Zumbühl, G. A. D. Briggs, and N. Ares, “Cross-architecture tuning of silicon and sige-based quantum devices using machine learning,” *ArXiv*, 2021. (Cited on page 113)

[137] J.-X. Xiong, S. Guan, J.-W. Luo, and S.-S. Li, “Emergence of strong tunable linear rashba spin-orbit coupling in two-dimensional hole gases in semiconductor quantum wells,” *Physical Review B*, vol. 103, feb 2021. (Cited on page 115)

A Appendix

A.1 Simulations and scripts

The simulations are performed with the package qutip (https://qutip.org/) in Python. To simulate the dynamics of the system we need to know all the values of the full Hamiltonian including in-plane and out-of-plane g-factor terms as well as the spin-flip tunneling term. The individual Hamiltonians H_{orb}, H_Z and H_{SO} can be found in chapters 5 and 6. The total Hamiltonian in the basis $\{S, T_+, T_0, T_-\}$ reads:

$$H = \begin{pmatrix} \frac{\epsilon}{2} - \sqrt{\frac{\epsilon^2}{4} + 2t_c^2} & (t_y + it_x)\sin\frac{\Omega}{2} - \frac{g_\parallel^- \mu_B B\cos\theta}{2\sqrt{2}}\cos\frac{\Omega}{2} & \frac{g_\perp^- \mu_B B\sin\theta}{2}\cos\frac{\Omega}{2} & (t_y - it_x)\sin\frac{\Omega}{2} + \frac{g_\parallel^- \mu_B B\cos\theta}{2\sqrt{2}}\cos\frac{\Omega}{2} \\ (t_y - it_x)\sin\frac{\Omega}{2} - \frac{g_\parallel^- \mu_B B\cos\theta}{2\sqrt{2}}\cos\frac{\Omega}{2} & \frac{g_\perp^+ \mu_B B\sin\theta}{2} & \frac{g_\parallel^+ \mu_B B\cos\theta}{2\sqrt{2}} & 0 \\ \frac{g_\perp^- \mu_B B\sin\theta}{2}\cos\frac{\Omega}{2} & \frac{g_\parallel^+ \mu_B B\cos\theta}{2\sqrt{2}} & 0 & \frac{g_\parallel^+ \mu_B B\cos\theta}{2\sqrt{2}} \\ (t_y + it_x)\sin\frac{\Omega}{2} + \frac{g_\parallel^- \mu_B B\cos\theta}{2\sqrt{2}}\cos\frac{\Omega}{2} & 0 & \frac{g_\parallel^+ \mu_B B\cos\theta}{2\sqrt{2}} & -\frac{g_\perp^+ \mu_B B\sin\theta}{2} \end{pmatrix} \tag{A.1}$$

As can be seen from Eq. (A.1) in the presence of an in-plane magnetic field component the S and $T_\pm$ states are coupled by the in-plane g-factor difference $g_\parallel^-$ while T_0 couples to $T_\pm$ via $g_\parallel^+$. We substitute the values for $g_\perp^+$, $g_\perp^-$, $g_\parallel^+$, $g_\parallel^-$, t_x, t_y and t_C found in previous chapters and perform a time evolution with the master equation approach provided by qutip. The code can be found below. To obtain the correct plots one has to substitute the values for θ and t_x and t_y.

```
# -*- coding: utf-8 -*-
"""
Created on Thu Sep  9 09:15:26 2021

@author: djirovec
"""


import matplotlib.pyplot as plt
import numpy as np
```

```
from qutip import *
mpl.rcParams['font.size'] = 20
mpl.rcParams['axes.labelsize'] = 15
mpl.rcParams['xtick.labelsize'] = 13
mpl.rcParams['ytick.labelsize'] = 13
#%%
muB = 5.57e-5 #bohr magnetron in eV
h = 4.13e-15 # Planck constant in eV*s
hbar = h/(2*np.pi) #reduced Planck constant in eV*s

#Define basis states with qutip function basis()
Tplus = basis(5,0)
T0 = basis(5,1)
Tminus = basis(5,2)
SG = basis(5,3)
SE = basis(5,4)

#define Hamiltonain
def SOIhamiltionianInPlaneDiag(epsilon, tc, B, deltag, sumg ,tx, tz,t0, theta, Sgp, dgp):
    Omega = np.arctan(2*np.sqrt(2)*tc/epsilon) #mixing angle
    J = np.sqrt(epsilon**2/4+2*tc**2)-epsilon/2 #exchange interaction for SG
    Jplus = np.sqrt(epsilon**2/4+2*tc**2)+epsilon/2 #exchange interaction for SE
    Bx = B*np.sin(theta)-B0 #magnetic filed in out of plane, B0 is an offset
    bz = B*np.cos(theta) #magnetic field in plane
    deltaEz = 0.5*deltag*muB*Bx #Zeeman energy difference out of plane
    Ez = 0.5*sumg*muB*Bx #Zeeman energy of triplet states out of plane
    H0 = -J*(SG*SG.dag()) #orbital part
    Hso = np.sin(Omega/2)*((ty+1.0j*tx)*Tplus*SG.dag()+(ty-1.0j*tx)*SG*Tplus.dag()+(ty-1.0j*tx)*Tminus*SG.
     dag()+(ty+1.0j*tx)*SG*Tminus.dag()) #spin orbit part
    #Zeeman part
    Hz = Ez*(Tplus*Tplus.dag()-Tminus*Tminus.dag())+np.cos(Omega/2)*(+deltaEz*(T0*SG.dag()+SG*T0.dag())
     +0.5*(dgp*muB*bz/np.sqrt(2))*np.cos(Omega/2)*(-(SG*Tplus.dag()+Tplus*SG.dag())+(SG*Tminus.dag()+Tminus*
     SG.dag()))+0.5*Sgp*muB*bz/np.sqrt(2)*((T0*Tplus.dag()+Tplus*T0.dag())+(T0*Tminus.dag()+Tminus*T0.dag())
     ))

    return H0+Hso+Hz

B = np.linspace(-20e-3,20e-3,101) #magnetic field values in T
epsilon = np.linspace(0e-3,3e-3,201) #detuning in eV
theta = np.deg2rad(10) #theta in rad
tc = 3.6e9*h #tunnel coupling in eV

#initialize expectation values
ExpectvalS = []
ExpectvalT0 = []
ExpectvalTminus = []
ExpectvalTplus = []
dg = 2.04 #out of plane
Sgp = 0.1 #in plane
dgp = 0.43 #in plane
Sg = 12 #out of plane
tx = 0#129e-9 insert spin orbit values
ty = 0#-369e-9
for b in B:
```

```
    for det in epsilon:
        H = SOIhamiltionianInPlaneDiag(det, tc, b, dg, Sg, tx, ty,t0, theta,Sgp, dgp)/hbar #calculate
     Hamiltonian
        psi0 = SG #define initial state
        times = np.linspace(0.0, 55e-9, 51) #define time points
        result = mesolve(H, psi0, times, [], [Tplus*Tplus.dag(), Tminus*Tminus.dag(), T0*T0.dag(), SG*SG.
     dag()]) #simulate with collapse operatorS*S.dag()
        ExpectvalTplus.append(result.expect[0])
        ExpectvalTminus.append(result.expect[1])
        ExpectvalT0.append(result.expect[2]*(np.exp(-np.abs(b/b0))))
        ExpectvalS.append(result.expect[3])
    print(b)
#%%
Expectval = (np.array(ExpectvalT0)+np.array(ExpectvalTplus)+np.array(ExpectvalTminus))/2 #sum up all
     triplet expectation values
FinalState = Expectval[:,-1]
FinalState = np.reshape(FinalState, (len(B),len(epsilon))) #reshape to matrix
#plot
pos = plt.imshow(FinalState, aspect = 'auto', cmap = 'RdBu_r', extent = (-0.05, 3, np.min(B)*1e3, np.max(B)
     *1e3), vmin = -0., vmax = 0.5)
cbar = plt.colorbar(pos)
cbar.set_label('$P_T$ (a.u.)')
plt.xlabel('$\\epsilon$ (mV)')
plt.ylabel('B (mT)')
plt.xticks([0,3])
plt.yticks([-20,0,20])
```